

Development of Li sensors for its application in fusion technology

Marc Nel-lo Pascual

<http://hdl.handle.net/10803/676028>

ADVERTIMENT. L'accés als continguts d'aquesta tesi doctoral i la seva utilització ha de respectar els drets de la persona autora. Pot ser utilitzada per a consulta o estudi personal, així com en activitats o materials d'investigació i docència en els termes establerts a l'art. 32 del Text Refós de la Llei de Propietat Intel·lectual (RDL 1/1996). Per altres utilitzacions es requereix l'autorització prèvia i expressa de la persona autora. En qualsevol cas, en la utilització dels seus continguts caldrà indicar de forma clara el nom i cognoms de la persona autora i el títol de la tesi doctoral. No s'autoritza la seva reproducció o altres formes d'explotació efectuades amb finalitats de lucre ni la seva comunicació pública des d'un lloc aliè al servei TDX. Tampoc s'autoritza la presentació del seu contingut en una finestra o marc aliè a TDX (framing). Aquesta reserva de drets afecta tant als continguts de la tesi com als seus resums i índexs.

ADVERTENCIA. El acceso a los contenidos de esta tesis doctoral y su utilización debe respetar los derechos de la persona autora. Puede ser utilizada para consulta o estudio personal, así como en actividades o materiales de investigación y docencia en los términos establecidos en el art. 32 del Texto Refundido de la Ley de Propiedad Intelectual (RDL 1/1996). Para otros usos se requiere la autorización previa y expresa de la persona autora. En cualquier caso, en la utilización de sus contenidos se deberá indicar de forma clara el nombre y apellidos de la persona autora y el título de la tesis doctoral. No se autoriza su reproducción u otras formas de explotación efectuadas con fines lucrativos ni su comunicación pública desde un sitio ajeno al servicio TDR. Tampoco se autoriza la presentación de su contenido en una ventana o marco ajeno a TDR (framing). Esta reserva de derechos afecta tanto al contenido de la tesis como a sus resúmenes e índices.

WARNING. The access to the contents of this doctoral thesis and its use must respect the rights of the author. It can be used for reference or private study, as well as research and learning activities or materials in the terms established by the 32nd article of the Spanish Consolidated Copyright Act (RDL 1/1996). Express and previous authorization of the author is required for any other uses. In any case, when using its content, full name of the author and title of the thesis must be clearly indicated. Reproduction or other forms of for profit use or public communication from outside TDX service is not allowed. Presentation of its content in a window or frame external to TDX (framing) is not authorized either. These rights affect both the content of the thesis and its abstracts and indexes.

DOCTORAL THESIS

Title	Development of Li sensors for its application in fusion technology
Presented by	Marc Nel-lo Pascual
Centre	IQS School of Engineering
Department	Analytical and Applied Chemistry
Directed by	Dr. Jordi Abellà and Dr. Sergi Colominas

Acknowledgments

First of all, I would like to acknowledge the support that IQS has provided to be able to accomplish this Thesis, conceding me a three-year predoctoral contract.

I would also like to express my gratitude to Dr. Jordi Abellà, who has given me the opportunity to accomplish this work in the Electrochemical Methods Laboratory. Thank you for your time and counseling which has certainly made this a higher-quality project. Many thanks also for the support and trust deposited in me throughout the years.

I would also like to thank Dr. Sergi Colominas for the guidance, follow-up, and continued interest shown in the research. Thank you for those enjoyable moments inside and outside the laboratory and for always encouraging a healthy atmosphere that has helped expand our family of electrochemists.

I am grateful to Dr. Carles Colominas, who has lent me numerous times his X-ray diffraction equipment, and to Dr. Anna Ramos and Mrs. Neus Sala for all the help received in this area.

Thank you also to Mr. César Alquézar for all his help that has allowed me to continue my research.

Thanks also to Dr. Eduard Juhera and Dr. Margalida Artigues, who started as my senior Ph.D. Students, and have enlightened me on the path to follow. Especially to you, Marga, for your knowledge and comprehension, you are one of my biggest rewards during this Thesis.

I am also very grateful to Toni and Enric, once TFM students and now my Ph.D. colleagues. Both of you are excellent people, both professionally and personally. I hope I have been able to help you a fraction of what you have aided me.

I would also like to thank all the TFG and TFM students with whom I have shared the laboratory. Thank you, especially to those of you who helped me with the progress of my work. I really appreciate that you made the days more enjoyable: Xavier, Itsaso, Iago, Gerard, Àlex, Òscar, Aniol, Iván, José, Victor, Eloi, Santi, and Laura.

I would also like to express my sincere gratitude to my parents for all the support they have shown me all these years. Thank you for the concern, advice, and trust placed in your son. To my brother, Lluís, the best friend and brother I could wish for, always ready to listen and distract me from my worries.

A special acknowledgment deserves my life-partner Teresa. She has always encouraged me and has helped me through the tough moments. Thank you, Teresa, for your love and concern that have helped me never lose my spirit and keep me motivated.

ABSTRACT

One of the challenges to be tested in future fusion reactors is tritium generation through the nuclear reaction of lithium-6 with high-energy neutrons. This tritium production will take place in the Tritium Breeding Modules (TBM) of the future fusion reactors. Different breeding concepts are being considered, some of which will use the molten eutectic alloy Lead-Lithium ($T_m = 235\text{ °C}$). However, since lithium will be consumed, this alloy's physical and chemical properties will vary as its composition changes. Thus, lithium concentration is a key parameter that must be monitored in real-time. For that, electrochemical sensors based on solid electrolytes are devices that could allow real-time monitoring of the Li concentration at high temperatures in highly reactive media.

In this Doctoral Thesis, electrochemical sensors based on solid Li-ion conducting electrolytes have been developed. For this, $\text{Li}_6\text{BaLa}_2\text{Ta}_2\text{O}_{12}$ (LBLTO) and $\text{Li}_6\text{La}_3\text{Ta}_{1.5}\text{Y}_{0.5}\text{O}_{12}$ (LLTYO) electrolytes were selected since they present characteristics such as stability at high temperatures, and low reactivity in contact with metallic Li, humidity, and air, as well as high ionic conductivity. The selected electrolytes have been satisfactorily synthesized and sintered, evaluating both their microstructure and the crystalline phases formed in the process.

The ionic conductivity of sintered electrolytes has been determined. For this purpose, an experimental set-up for impedance measurements at high temperatures has been designed and built. The ionic conductivities of the electrolytes were measured up to 200-300 °C. From the results, it has been observed that the electrolytes presented sufficiently high ionic conductivities to be used in electrochemical sensors. Furthermore, conductivities similar to those described in the bibliography were obtained, demonstrating that they had been produced with excellent quality.

For the construction of the electrochemical sensors, the sintered disc-shaped electrolytes have been bonded to an alumina tube. From these sensors, potentiometric measurements have been performed at high temperatures (400-600 °C) in different Pb-Li alloys. The results obtained have been compared to theoretical values and relationships. During this process, the reference system, the linear range, and the precision of the sensors have been studied, as well as their repeatability, reproducibility, and intermediate precision. After their evaluation, sensors based on both LBLTO and LLTYO electrolytes have shown excellent results. In addition, the sensors have successfully determined the lithium nominal concentration of prepared Pb-Li samples. Therefore, it was concluded that analytical instruments capable of monitoring the concentration of lithium in molten Pb-Li alloys have been developed.

RESUMEN

Uno de los retos a probar en los futuros reactores de fusión es la generación de tritio mediante la reacción nuclear del litio-6 con neutrones de alta energía. Esta producción de tritio se realizará en los *Tritium Breeding Modules* (TBM) de los futuros reactores de fusión. De los diferentes diseños de regeneración de tritio que se están considerando, algunos de ellos utilizarán la aleación eutéctica fundida Plomo-Litio ($T_m = 235\text{ °C}$). Sin embargo, dado que el litio se consumirá, las propiedades físicas y químicas de esta aleación variarán a medida que cambie su composición. Por lo tanto, la concentración de litio es un parámetro clave que debe monitorizarse en tiempo real. Para ello, los sensores electroquímicos basados en electrolitos sólidos son dispositivos que podrían permitir monitorizar en tiempo real la concentración de Li a altas temperaturas en medios altamente reactivos.

En esta Tesis Doctoral se han desarrollado sensores electroquímicos basados en electrolitos sólidos conductores de iones de litio. Para ello se seleccionaron los electrolitos $\text{Li}_6\text{BaLa}_2\text{Ta}_2\text{O}_{12}$ (LBLTO) y $\text{Li}_6\text{La}_3\text{Ta}_{1.5}\text{Y}_{0.5}\text{O}_{12}$ (LLTYO) ya que presentan características como estabilidad a altas temperaturas, y baja reactividad en contacto con Li metálico, humedad y aire, así como alta conductividad iónica. Los electrolitos seleccionados han sido sintetizados y sinterizados satisfactoriamente, evaluando tanto su microestructura como las fases cristalinas formadas en el proceso.

Se ha determinado la conductividad iónica de electrolitos sinterizados. Para ello se ha diseñado y construido un montaje experimental para medidas de impedancia a altas temperaturas. Las conductividades iónicas de los electrolitos se midieron hasta $200\text{-}300\text{ °C}$. A partir de los resultados se ha observado que los electrolitos presentaron conductividades iónicas suficientemente altas para ser utilizados en sensores electroquímicos. Además, se obtuvieron conductividades similares a las descritas en la bibliografía, demostrando que habían sido producidos con una calidad excelente.

Para la construcción de los sensores electroquímicos, los electrolitos sinterizados en forma de disco se han unido a un tubo de alúmina. A partir de estos sensores se han realizado medidas potenciométricas a altas temperaturas ($400\text{-}600\text{ °C}$) en diferentes aleaciones de Pb-Li. Los resultados obtenidos se han comparado con valores y relaciones teóricas. Durante este proceso se ha estudiado el sistema de referencia, el rango lineal y la precisión del sensor, así como su repetibilidad, reproducibilidad y precisión intermedia. Después de su evaluación, los sensores basados en electrolitos LBLTO y LLTYO han mostrado excelentes resultados. Además, los sensores han determinado con éxito la concentración nominal de litio en muestras preparadas de Pb-Li. Por estos motivos, se concluyó que se han desarrollado instrumentos analíticos capaces de monitorizar la concentración de litio en aleaciones de Pb-Li fundidas.

RESUM

Un dels reptes a provar en els futurs reactors de fusió és la generació de triti mitjançant la reacció nuclear del liti-6 amb neutrons d'alta energia. Aquesta producció de triti es realitzarà als *Tritium Breeding Modules* (TBM) dels futurs reactors de fusió. Dels diferents dissenys de regeneració de triti que s'estan considerant, alguns d'ells utilitzaran l'aliatge eutèctic fos Plom-Liti ($T_m = 235 \text{ }^\circ\text{C}$). No obstant això, atès que el liti es consumirà, les propietats físiques i químiques d'aquest aliatge variaran a mesura que canviï la seva composició. Per tant, la concentració de liti és un paràmetre clau que cal monitoritzar en temps real. Per a això, els sensors electroquímics basats en electròlits sòlids són dispositius que podrien permetre monitoritzar en temps real la concentració de Li a altes temperatures en mitjans altament reactius.

En aquesta Tesi Doctoral s'han desenvolupat sensors electroquímics basats en electròlits sòlids conductors d'ions de liti. Per això es van seleccionar els electròlits $\text{Li}_6\text{BaLa}_2\text{Ta}_2\text{O}_{12}$ (LBLTO) i $\text{Li}_6\text{La}_3\text{Ta}_{1.5}\text{Y}_{0.5}\text{O}_{12}$ (LLTYO), ja que presenten característiques com estabilitat a altes temperatures, i baixa reactivitat en contacte amb Li metàl·lic, humitat i aire, així com alta conductivitat iònica. Els electròlits seleccionats han estat sintetitzats i sinteritzats satisfactòriament, avaluant tant la seva microestructura com les fases cristal·lines formades en el procés.

S'ha determinat la conductivitat iònica dels electròlits sinteritzats. Per a això s'ha dissenyat i construït un muntatge experimental per a mesures d'impedància a altes temperatures. Les conductivitats iòniques dels electròlits es van mesurar fins a $200\text{-}300 \text{ }^\circ\text{C}$. A partir dels resultats s'ha observat que els electròlits van presentar conductivitats iòniques prou altes com per a ser utilitzats en sensors electroquímics. A més, es van obtenir conductivitats similars a les descrites en la bibliografia, demostrant que havien estat produïts amb una qualitat excel·lent.

Per a la construcció dels sensors electroquímics, els electròlits sinteritzats en forma de disc s'han unit a un tub d'alúmina. A partir d'aquests sensors s'han realitzat mesures potenciomètriques a altes temperatures ($400\text{-}600 \text{ }^\circ\text{C}$) en diferents aliatges de Pb-Li. Els resultats obtinguts s'han comparat amb valors i relacions teòriques. Durant aquest procés s'ha estudiat el sistema de referència, el rang lineal i la precisió del sensor, així com la seva repetibilitat, reproductibilitat i precisió intermèdia. Després de la seva avaluació, els sensors basats en electròlits LBLTO i LLTYO han mostrat excel·lents resultats. A més, els sensors han determinat amb èxit la concentració nominal de liti en mostres preparades de Pb-Li. Per aquests motius, es va concloure que s'han desenvolupat instruments analítics capaços de monitoritzar la concentració de liti en aliatges de Pb-Li fosos.

ACRONYMS

AAS: Atomic Absorption Spectroscopy

ANOVA: Analysis of Variance

AOAC: Association of Analytical Communities

BSS: Back Supporting Structure

BZ: Breeding Zone

CPE: Constant-Phase Element

CV: Coefficient of Variation

DCLL: Dual Coolant Lithium Lead

DFLL: Dual Functional Lithium Lead

DSC: Differential scanning calorimetry

DWT: Double-Walled Tubes

EC: Equivalent Circuit

EDS: Energy Dispersive X-Ray Spectroscopy

EIS: Electrochemical Impedance Spectroscopy

FW: First Wall

HCLL: Helium Cooled Lithium Lead

ICP-OES: Inductively Coupled Plasma-Optical Emission Spectrometry

ITER: International Thermonuclear Experimental Reactor

KK: Kronig-Kramer

LBLTO: $\text{Li}_6\text{BaLa}_2\text{Ta}_2\text{O}_{12}$

LISICON: Lithium Superionic Conductor

LLCB: Lithium Lead Ceramic Breeder

LLTO: Lithium-Lanthanum Titanate

LLTYO: $\text{Li}_6\text{La}_3\text{Ta}_{1.5}\text{Y}_{0.5}\text{O}_{12}$

MHD: Magnetohydrodynamic

NASICON: Sodium Superionic Conductor

OCP: Open Circuit Potential

PWR: Pressurized Water Reactors

RE: Reference Electrode

SD: Standard Deviation

SEM: Scanning Electron Microscope

SW: Side Wall

TBB: Tritium Breeding Blanket

TBM: Tritium Breeding Modules

WE: Working Electrode

WCLL: Water-Cooled Lithium Lead

XRD: X-Ray Diffraction

LIST OF FIGURES

Figure 1.1. Aerial view of ITER construction site in Saint Paul-lès-Durance, southern France (April 14 th , 2022).....	2
Figure 1.2. Tokamak reactor [7].	3
Figure 1.3. Lithium activity and hydrogen solubility as a function of the Li molar fraction in Pb-Li alloy [15].	5
Figure 1.4. Breeding blankets concepts of the A) HCLL [24], B) WCLL [25] and C) DCLL [26].	6
Figure 1.5. Pb-Li phase diagram [29].	8
Figure 1.6. Design of the electrical resistivity monitor developed by Hubberstey et al. [33].	10
Figure 1.7. Resistivity-temperature data for Pb-Li alloys with at% Li concentrations of: A – 0.00; B – 2.03; C - 4.04; D - 6.13; E - 8.21; F - 10.16; G - 11.96; H - 13.89; I - 15.60; J - 17.11 [33].	11
Figure 1.8. Electrochemical Li sensor [40].	13
Figure 1.9. Experimental ΔE as a function of the temperature and the lithium concentration [34].	14
Figure 1.10. Cell assembly of the Li electrochemical sensor proposed by Wu et al. [37].	15
Figure 1.11. Experimental ΔE and $\ln \gamma_{Li}$ versus x_{Li} for Zn-Li alloys at 600 °C [37].	16
Figure 1.12. Ion transportation mechanisms in solid electrolytes: A) vacancy and B) interstitial mechanisms [50].	18
Figure 1.13. $Li_{11}AlP_2S_{12}$ crystallographic structure [56].	20
Figure 1.14. Crystal structure of A) a cubic perovskite-type LLTO, and B) an AO_{12} cuboctahedron [61].	21
Figure 1.15. NASICON-type structure of $LiM_2(PO_4)_3$ [69].	22
Figure 1.16. Crystal garnet structure of $Li_3B_3C_2O_{12}$ [69].	23
Figure 3.1. Scheme of the collinear four-point probe method.	34
Figure 3.2. Nyquist and Bode plots [101].	36

Figure 3.3. Equivalent circuit and the corresponding Nyquist and Bode impedance plots, for a typical electrode/electrolyte system without diffusion [89].	37
Figure 3.4. Circuit used for Kronig-Kramer test [114].	39
Figure 4.1. XRD patterns corresponding to A) synthesized LBLTO powder at 700°C for 6h and B) bibliographic data [79,141]. The black arrow designates an anomalous signal.	49
Figure 4.2. XRD peak pattern from A) $\text{Li}_6\text{BaLa}_2\text{Ta}_2\text{O}_{12}$ synthesized ceramic at 700 °C for 6h and B) $\text{Li}_2\text{Ba}_3\text{Ta}_2\text{O}_9$ ceramic.	50
Figure 4.3. SEM micrographs of the synthesized LBLTO powder at 700 °C for 6h at different magnifications: A) 500x and B) 3500x.	51
Figure 4.4. EDS spectrum of the synthesized LBLTO ceramic powder at 700 °C for 6h.	52
Figure 4.5. XRD patterns corresponding to A) sintered LBLTO pellet at 900 °C for 24h and B) bibliographic data [79,141].	54
Figure 4.6. SEM micrographs of the LBLTO sintered pellet at 900°C for 24h at different magnifications: A) 100x and B) 2000x.	55
Figure 4.7. EDS spectrum of the LBLTO pellet.	56
Figure 4.8. SEM micrographs at A) 100x and B) 2000x magnifications of the sintered pellet at 900 °C for 48h.	58
Figure 4.9. EDS analysis of the sintered pellet at 900 °C for 48h.	59
Figure 4.10. XRD patterns corresponding to A) sintered LBLTO pellet at 900 °C for 48h and B) bibliographic data [79,141]. The black arrow designates an unexpected signal.	60
Figure 4.11. SEM micrographs (2000x) of LBLTO sintered pellets at A) 950 °C for 24h and B) 1000 °C for 24h.	61
Figure 4.12. EDS spectra of the LBLTO sintered pellets at A) 950 °C for 24h and B) 1000 °C for 24h.	62
Figure 4.13. XRD patterns corresponding to LBLTO sintered pellets at A) 950 °C for 24h and B) 1000 °C for 24h. Black arrows designate anomalous signals.	63
Figure 4.14. A) SEM micrograph (1000x) and B) EDS spectrum of the cross-section of an LBLTO pellet sintered at 950 °C for 24h.	65

Figure 4.15. A) Scheme and B) Constructed experimental set-up for EIS measurements....	67
Figure 4.16. Complete assembly for the EIS measurements, composed of the measuring set-up and the heating system.	69
Figure 4.17. Basic and Advanced parameters in NOVA® software for an EIS measurement.	70
Figure 4.18. Nyquist plots of an LBLTO sintered pellet at 30 °C, 100 °C, 175 °C, and 250 °C.	72
Figure 4.19. Equivalent circuit used to fit EIS data.....	73
Figure 4.20. Nyquist plot of an LBLTO pellet at 200 °C A) before and B) after removing the impedance data from 1 MHz to 10 kHz.....	75
Figure 4.21. Equivalent circuit used to fit the impedance data when values from 1Mhz to 10 kHz had been discarded.	76
Figure 4.22. A) Nyquist plot of the electrical connections of the measuring set-up at 200 °C, and B) the equivalent circuit used to fit this impedance data.	77
Figure 4.23. Nyquist plots of A) LBLTO pellet at 200 °C and B) of the same LBLTO pellet at 200 °C after the inductance’s correction was applied.	79
Figure 4.24. Equivalent circuit used to fit EIS data.....	80
Figure 4.25. Total lithium-ion conductivities as a function of the temperature and strategy for an LBLTO electrolyte. Bibliographic data from V. Thangadurai et al. were also included [79].....	82
Figure 4.26. Arrhenius plots of the total lithium-ion conductivities obtained from each of the three applied strategies and bibliographic data [79] of the LBLTO electrolyte.	83
Figure 4.27. Total lithium-ion conductivities against temperature from two LBLTO pellets and bibliographic data [79].	85
Figure 4.28. Arrhenius plots of the total lithium-ion conductivities from two LBLTO pellets and bibliographic data [79].	86
Figure 4.29. XRD patterns corresponding to A) synthesized LLTO electrolyte at 700 °C for 6h [150] and B) bibliographic data [125,149]. The black arrow designates an unexpected signal.	88

Figure 4.30. EDS of the synthesized LLTYO powder at 700 °C for 6h [150].....	89
Figure 4.31. XRD patterns corresponding to A) synthesized LLTYO powder at 700°C for 5h and 900 °C for 1h and B) bibliographic data [125,149].	90
Figure 4.32. SEM micrograph of the synthesized LLTYO powder at 700 °C for 5h and 900 °C for 1h at different magnifications: A) 500x and B) 1500x.	91
Figure 4.33. EDS spectrum of the synthesized LLTYO ceramic powder at 700 °C for 5h and 900 °C for 1h.	92
Figure 4.34. Corresponding XRD patterns to A) sintered LLTYO pellet at 900 °C for 24h and 1100 °C for 6h, and B) bibliographic data [125,149].	94
Figure 4.35. SEM micrograph of the LLTYO sintered pellet at 900 °C for 24h and 1100 °C for 6h at different magnifications: A) 50x and B) 750x.	95
Figure 4.36. EDS spectrum of the LLTYO pellet	96
Figure 4.37. A) SEM micrograph of the cross-section and B) EDS spectrum of a sintered LLTYO pellet at 900 °C for 24h and 1100 °C for 6h.....	98
Figure 4.38. Nyquist plots of a LLTYO sintered pellet at 30 °C, 75 °C, 125 °C, and 175 °C. .	100
Figure 4.39. Total lithium-ion conductivities as a function of the temperature and strategy for an LLTYO electrolyte. Bibliographic data from S. Narayanan et al. [149] were also included.	102
Figure 4.40. Arrhenius plots of the total lithium-ion conductivities of the LLTYO electrolyte from each of the three applied strategies and bibliographic data [149].	103
Figure 4.41. Total lithium-ion conductivities against temperature for the LLTYO electrolyte [149].....	104
Figure 4.42. Arrhenius plots of the total lithium-ion conductivities from two LLTYO pellets and bibliographic data [149].....	105
Figure 4.43. Pb-Li phase diagram [29].	111
Figure 4.44. Pb-Li ingot sample preparation procedure.....	112
Figure 4.45. DSC curve of a 15.9at% Li Pb-Li alloy.....	115
Figure 4.46. Scheme of the Li sensor.....	117

Figure 4.47. Developed ceramic binder treated for 30 minutes at A) 1200 °C, B) 1300 °C, and C) 1400 °C [173].	118
Figure 4.48. Mixtures of ceramic cement and conventional glass A) 4:1, B) 1:1, C) 1:4, and D) 0:1 respectively, treated at 950 °C for 1 hour [173].	119
Figure 4.49. Conventional glass binder treated at A) 900 °C for 1 hour, B) 950 °C for 1 hour, and C) 1050 °C for 30 minutes [173].	120
Figure 4.50. Binding thermal process.	121
Figure 4.51. Binding result after the final thermal process (Figure 4.50).	121
Figure 4.52. SEM micrograph of a cross-sectional cut showing the union interface of a solid electrolyte's pellet to an alumina tube merged with the glass binder. The electrolyte and binder interface is pointed with a blue dashed line and the binder and alumina interface is pointed with a green dashed line.	122
Figure 4.53. EDS spectrum of the alumina tube (Spectrum 1)	123
Figure 4.54. EDS spectrum of the LBLTO electrolyte (Spectrum 2)	123
Figure 4.55. EDS spectrum of the glass binder (Spectrum 3).	124
Figure 4.56. Schematic illustration of the assembly for permeation testing.	125
Figure 4.57. Experimental set-up for sensors testing.	126
Figure 4.58. Schematic representation of the Li sensor.	127
Figure 4.59. OCP measurements in Pb-Li 3.1at% alloy at 400 °C, 500 °C, and 600 °C. Pb-16.1Li was used in the reference electrode.	129
Figure 4.60. Plotted OCPs versus the logarithm of the lithium activity in the working electrode at 400 °C, 500 °C, and 600 °C. Pb-16.1Li was used in the reference electrode.	131
Figure 4.61. OCP measurements in Pb-Li 3.3at% alloy at 400 °C, 500 °C, and 600 °C. Pb-15.9Li was used in the reference electrode.	132
Figure 4.62. Plotted OCPs versus the logarithm of the lithium activity in the working electrode at 400 °C, 500 °C, and 600 °C. Pb-15.9Li was used in the reference electrode.	134
Figure 4.63. OCP measurements in Pb-Li alloys with Li concentrations of 3.3at%, 5.3at%, 9.3at% and 15.4at% at 400 °C. Pb-3.1Li was used in the reference electrode.	136

Figure 4.64. Plotted OCPs versus the logarithm of the lithium activity in the working electrode at 400 °C, 500 °C, and 600 °C. Pb-3.2Li was used in the reference electrode.....	138
Figure 4.65. Phase diagram of the lithium-tin system [183].	140
Figure 4.66. OCP measurements in Pb-Li alloys with Li concentrations of 3.0at%, 5.4at%, 9.4at% and 15.5at% at 400 °C. Sn-3.0Li was used in the reference electrode.....	141
Figure 4.67. Plotted OCPs versus the logarithm of the lithium activity in the working electrode at 400 °C, 500 °C, and 600 °C. Sn-3.04Li was used in the reference electrode...	144
Figure 4.68. OCP measurements in Pb-Li alloys with Li concentrations of 3.1at%, 5.3at%, 9.3at%, 15.4at%, and 25.0at% Li at 400 °C. Pb-3.2Li was used in the reference electrode.	147
Figure 4.69. The logarithm of the lithium activity against the logarithm of lithium atomic fraction in Pb-Li alloys at 400 °C, 500 °C, and 600 °C.....	149
Figure 4.70. The logarithm of the lithium activity plotted against the logarithm of lithium atomic fraction in Pb-Li alloys with $x_{Li} \geq 0.17$ at 400 °C, 500 °C, and 600 °C.	152
Figure 4.71. OCP measurements in Pb-Li alloys samples with Li concentrations of 15.8at%, 18.2at%, 21.1at%, and 25.0at% Li at 400 °C. Pb-15.8Li was used in the reference electrode.	153
Figure 4.72. OCP measurement of three replicates in a Pb-Li alloy with Li concentration of 16.0at% at 500 °C. Pb-3.0Li was used in the reference electrode.....	156
Figure 4.73. OCP measurement on three different days in the same Pb-Li alloy with a Li concentration of 16.0at% at 500 °C. Pb-3.0Li was used in the reference electrode.....	157
Figure 4.74. OCP measurement with three different lithium sensors in the same 16.0at% Li Pb-Li alloy at 500 °C. Pb-3.0Li was used in the reference electrode.	158
Figure 4.75. OCP measurements of five Pb-Li sample alloys with Li concentrations of 13.1at%, 14.5at%, 16.0at%, and 17.5at% Li at 500 °C. Pb-3.0Li was used in the reference electrode.	159
Figure 4.76. OCP measurements in a Pb-Li alloy with a varying Li concentration of 17.5at%, 16.0at%, 14.5at%, and 13.1at% Li at 500 °C. Pb-3.0Li was used in the reference electrode.	161

Figure 4.77. OCP measurements in Pb-Li 2.9at% alloy at 400 °C, 500 °C, and 600 °C. Pb-17.0Li was used in the reference electrode.....	163
Figure 4.78. OCP potentials plotted versus the logarithm of the lithium activity in the working electrode at 400 °C, 500 °C, and 600 °C. Pb-17.0Li was used in the reference electrode. .	165
Figure 7.1. Confidence intervals of the A) slope and B) constant term of each obtained linear correlation from the different strategies and bibliographic data [79].....	197
Figure 7.4. Contour map of the PGSTAT302N/FRA2 combination.....	198
Figure 7.5. Confidence intervals of the A) slope and B) constant term of each obtained linear correlation from two LBLTO pellets and bibliographic data [79].	199
Figure 7.6. Confidence intervals of the A) slope and B) constant term of each obtained linear correlation from the different strategies and bibliographic data [149].....	200
Figure 7.7. Confidence intervals of the A) slope and B) constant term of each obtained linear correlation from two LLTYO pellets and bibliographic data [149].	201
Figure 7.1. Lithium calibration curve for the AAS-Flame analysis.	202
Figure 7.8. Probability plot of each of the analyzed Pb-Li ingots.	203
Figure 7.9. Confidence intervals of the linear correlations' slopes for each preparation method at A) 400 °C, B) 500 °C, and C) 600 °C.	205
Figure 7.10. Confidence intervals of the linear correlations' slopes for each reference system at A) 400 °C, B) 500 °C and C) 600 °C.	206

LIST OF TABLES

Table 1.1. Coefficients for [Eq. 1.6] describing the concentration and temperature dependence on the resistivity [33].....	12
Table 3.1. Common electrical elements.....	37
Table 3.2. Description of the Warburg and the CPE components.....	38
Table 4.1. Electrolyte candidates for the development of lithium sensors.	45
Table 4.2. Representation of the selection process for the lithium-ion conducting solid electrolytes candidates.....	47
Table 4.3. Experimental and theoretical atomic relationship for each identified metallic element forming the LBLTO electrolyte.	53
Table 4.4. Experimental and theoretical atomic relationship for each identified metallic element forming the LBLTO electrolyte.	57
Table 4.5. Description, references, and suppliers for the components of the EIS measuring set-up (Figure 4.15).	68
Table 4.6. R_0 and L_s obtained values at each of the studied temperatures.	77
Table 4.7. Determined resistances and ionic conductivities by each of the strategies as a function of the temperature.	81
Table 4.8. Experimental and theoretical atomic relationship for each identified metallic element forming the LLTYO electrolyte.	92
Table 4.9. Experimental and theoretical atomic relationship for each identified metallic element forming the LLTYO sintered electrolyte.	97
Table 4.10. Resistances and ionic conductivities for the LLTYO electrolyte as a function of the temperature from each of the strategies.....	101
Table 4.11. AAS-Flame characterization results of Pb-Li ingots with different Li concentrations.....	113
Table 4.12. Determined melting points for a Pb-15.9Li ingot. The upper, middle, and bottom parts of the ingot were evaluated separately.	116

Table 4.13. Experimental and calculated potentials in Pb-Li with 3.1at%, 10.14at%, and 16.10at% Li, at 400 °C, 500 °C, and 600 °C. Pb-16.1Li was used in the reference electrode.	130
Table 4.14. Experimental and calculated potentials in Pb-Li with 3.27at%, 5.83at%, 10.00at%, and 15.90at% Li, at 400 °C, 500 °C, and 600 °C. Pb-15.9Li was used in the reference electrode.	133
Table 4.15. Experimental and calculated potentials in Pb-Li alloys with different Li concentrations (WE) at 400 °C, 500 °C, and 600 °C. Pb-3.2Li was used in the reference electrode.....	137
Table 4.16. Experimental and calculated potentials in Pb-Li with 3.0at%, 5.4at%, 9.4 at%, and 15.5at% Li, at 400 °C, 500 °C, and 600 °C. Sn-3.0Li was used in the reference electrode...143	143
Table 4.17. Experimental and calculated potentials in Pb-Li alloys with different Li concentrations (WE) at 400 °C, 500 °C, and 600 °C. Pb-3Li was used in the reference electrode.....	148
Table 4.18. Slope and y-intercept divergences between experimental and Hubberstey's correlations at 400 °C, 500 °C, and 600 °C.....	150
Table 4.19. Experimental potentials and calculated lithium activities' logarithm in Pb-Li alloys with different Li concentrations (WE) at 400 °C, 500 °C, and 600 °C.	151
Table 4.20. Lithium quantification results for the Pb-Li samples with concentrations: 15.8at%, 18.2at%, 21.1at%, and 25.0at% Li. The OCP measurements were performed at 400 °C.....	154
Table 4.21. Lithium quantification results for the Pb-Li samples with concentrations: 13.1at%, 14.5at%, 16.0at%, and 17.5at%. The OCP measurements were performed at 500 °C.....	160
Table 4.22. Lithium quantification results for the Pb-Li samples with concentrations: 17.5at%, 16.0at%, 14.5at%, and 13.0at% Li. The OCP measurements were performed at 500 °C, with Pb-3.0Li as the reference electrode.	162
Table 4.23. Experimental and calculated potentials in Pb-Li with 2.87at%, 5.33at%, 9.85at%, and 17.16at% Li, at 400 °C, 500 °C, and 600 °C. Pb-17.02Li was used in the reference electrode.....	164

Table 4.24. Signal stability results at 400 °C, 500 °C, and 600 °C of the LBLTO and LLTYO sensors.....	166
Table 4.25. Average accuracy results at 400 °C, 500 °C, and 600 °C.	167
Table 7.1. Grubb’s test results for outliers for each of the analyzed Pb-Li ingots.	204
Table 7.2. T-student’s test results for each of the analyzed Pb-Li ingots.....	204

INDEX

1. INTRODUCTION	1
1.1. Pb-Li in Tritium Breeding Blankets	4
1.2. Lithium Monitoring in Molten Metals	9
1.2.1. Electrical Resistivity Meter	9
1.2.2. Electrochemical Lithium Sensors.....	13
1.3. Ion-Conducting Solid-State Electrolytes.....	17
1.3.1. Ionic Conductivity	18
1.3.2. Lithium-Ion Conducting Solid-State Electrolytes.....	19
1.3.2.1. LISICON and thio-LISICON type.....	20
1.3.2.2. Perovskite-type.....	21
1.3.2.3. NASICON-type.....	22
1.3.2.4. Garnet-type	23
2. OBJECTIVES.....	27
3. MATERIALS AND METHODS.....	31
3.1. Characterization techniques.....	31
3.2. Ionic conductivity measurements	33
3.2.1. Four-point probe	34
3.2.2. Electrochemical Impedance Spectroscopy.....	35
4. RESULTS AND DISCUSSION	43
4.1. Selection of the Solid Electrolytes Candidates	43
4.2. Synthesis and Sintering of the Selected Solid Electrolytes.....	48
4.2.1. $\text{Li}_6\text{BaLa}_2\text{Ta}_2\text{O}_{12}$	48
4.2.1.1. Synthesis and Characterization	49

4.2.1.2. Sintering and Characterization	53
4.2.1.3. Ionic Conductivity	66
4.2.2. $\text{Li}_6\text{La}_3\text{Ta}_{1.5}\text{Y}_{0.5}\text{O}_{12}$	88
4.2.2.1. Synthesis and Characterization.....	88
4.2.2.2. Sintering and Characterization	93
4.2.2.3. Ionic Conductivity	99
4.2.3. Comparison and Discussion of the Solid Electrolytes.....	107
4.3. Pb-Li Synthesis and Characterization.....	111
4.3.1. Flame-Atomic Absorption Spectrophotometry (AAS)	112
4.3.2. DSC - Characterization	114
4.4. Electrochemical Lithium Sensors	117
4.4.1. Characterization of the $\text{Li}_6\text{BaLa}_2\text{Ta}_2\text{O}_{12}$ Sensor	127
4.4.1.1. Alloy synthesis procedure's effect on the OCP.....	128
4.4.1.2. Reference System	135
4.4.1.3. Lithium activity in Pb-Li alloys.....	145
4.4.1.4. Evaluation of the Sensor's Precision.....	155
4.4.2. $\text{Li}_6\text{La}_3\text{Ta}_{1.5}\text{Y}_{0.5}\text{O}_{12}$ Sensor	163
4.4.3. Discussion of the Lithium Sensors Results in Pb-Li	166
4.5. General Discussion.....	170
5. CONCLUSIONS.....	175
6. REFERENCES.....	179
7. ANNEXES	197
Annex 1: Statistical Study of the Three Different Strategies on LBLTO Ionic Conductivity Results.....	197
Annex 2: PGSTAT302N/FRA2 Contour Map.....	198

Annex 3: Statistical Study of the Two LBLTO Replicates' Ionic Conductivity.....	199
Annex 4: Statistical Study of the Three Different Strategies on LLTYO Ionic Conductivity Results	200
Annex 5: Statistical Study of the Two LLTYO Replicates' Ionic Conductivity.....	201
Annex 6: Lithium Calibration Curve for the AAS-Flame Analysis.....	202
Annex 7: Statistical Study of the Lithium Quantification Results In Pb-Li Samples.....	203
Annex 8: Statistical Study of the Pb-Li Preparation Method.....	205
Annex 9: Statistical Study of the Eutectic Pb-Li and Pb-3Li Reference Systems.....	206

1. INTRODUCTION

1. INTRODUCTION

Due to the growing concerns about global climate change, carbon footprint mitigation is currently a serious topic. In this regard, extensive efforts are being made internationally to control climate change by decreasing CO₂ emissions and consuming fewer fossil fuels as the primary energy resource [1]. To this end, alternative energy sources are being explored and developed.

Among these alternatives, renewal energy sources appear as the most suitable solution due to their multiple advantages: highly available resources and low waste production. However, these technologies are in a very early stage of development and depend on atmospheric factors that cannot be controlled. These facts made that these energy sources only accounted for 13% of the world's primary energy consumption in 2020 [2], so it is not projected to mainly rely upon these energies in a near future.

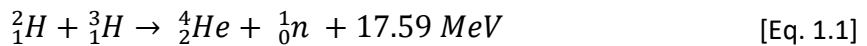
As an alternative, energy based on nuclear technology can contribute to decreasing the dependence on carbon-based energy sources. This technology is divided into two forms: fission and fusion energy. Fission energy is the nuclear source that nowadays is commercially available. This technology is based on the fission of a heavy nucleus to yield two or more smaller nuclei and energy. However, fission energy relates to two problematics that are the security of their power plants and their waste management.

By contrast, nuclear fusion is a more interesting option as an energy source. This energy concept is based on the fusion of two light atomic nuclei to yield a heavier atomic nucleus, subatomic particles, and energy. Fusion energy is projected to exhibit a high energy yield and a much lower environmental impact than fission energy. However, to achieve fusion energy profitably, difficulties arise due to the complexity of achieving fusion reactions on a large scale. In this context, 35 countries, which include the United States, China, India, Japan, Russia, and members of the European Union, work together on one of the most ambitious world projects: ITER (“International Thermonuclear Experimental Reactor”) [3]. In the ITER project, the largest Tokamak fusion reactor is under construction. An aerial view of the whole ITER construction site is shown in Figure 1.1.



Figure 1.1. Aerial view of ITER construction site in Saint Paul-lès-Durance, southern France (April 14th, 2022).

This reactor will serve to test this large-scale fusion technology, evaluating materials, different components of the reactor, and the energy produced during the fusion reactor. In this reactor, the fusion reaction between deuterium and tritium will take place at 150 million Celsius ([Eq. 1.1]).



From this reaction, an alpha particle, a neutron, and a large quantity of energy will be obtained [4]. However, ITER will require a constant supply of deuterium and tritium to generate and maintain the plasma. Deuterium supply does not entail any major difficulty, since it is a relatively abundant element on earth that can be obtained from seawater employing isotopic enrichment techniques [5]. By contrast, tritium obtention is more complex since it does not present natural sources for its direct obtention. This is due to its radioactive nature, having a short half-life (12.3 years) [6]. Tritium production is planned to be produced inside a Tokamak reactor, specifically in the Tritium Breeding Blanket (TBB) that will be surrounding the plasma (Figure 1.2).

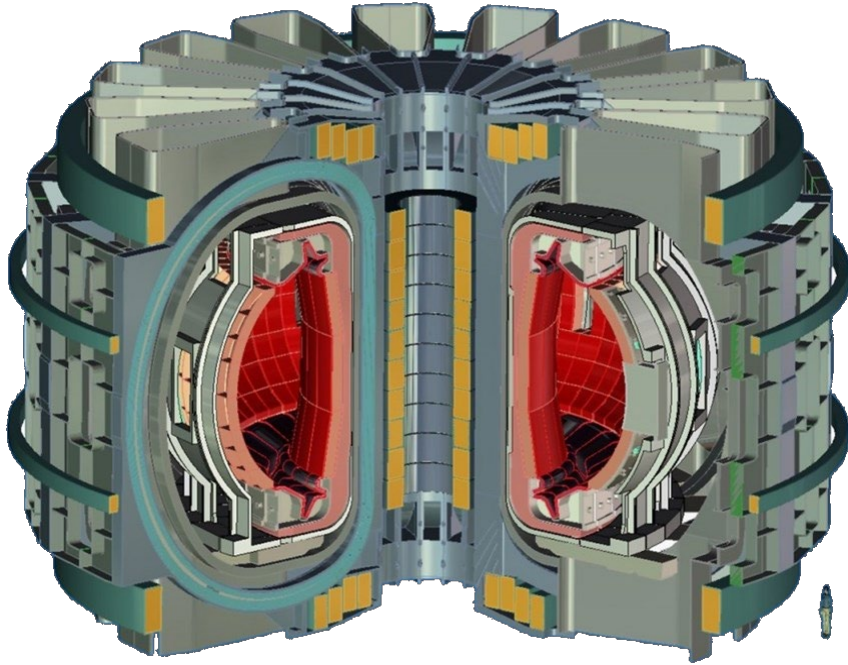
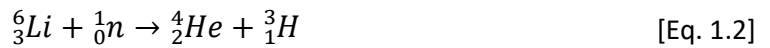


Figure 1.2. Tokamak reactor [7].

This blanket will be composed of different Tritium Breeding Modules (TBM) where the reaction of lithium-6 with high-energy neutrons will produce tritium ([Eq. 1.2]):



Among the different concepts of breeding blankets, two main designs are distinguished according to the physical state of the lithium breeder: solid or liquid [8]. The principal solid breeder candidates are Li_2O and ternary oxides, such as LiAlO_2 , Li_2SiO_3 , Li_2TiO_3 , etc. These solid breeders are relatively non-reactive and allow secure cooling with water. However, their main disadvantage is the difficulty to produce tritium due to their low lithium density, generating the need for neutron multipliers that complicates the design of the breeding blanket [8].

As an alternative, liquid lithium breeding blankets can overcome some of the disadvantages of solid breeders. Furthermore, molten metal breeders can act as coolants; with high thermal conductivity ($\sim 100 \text{ W}\cdot\text{mK}^{-1}$) and with low viscosity ($\sim 10^{-7} \text{ m}^2\cdot\text{s}^{-1}$) they are interesting options for heat removal [9]. However, these breeding blankets exhibit viability problems associated with magnetohydrodynamic interactions between their flowing high electrical conductivity ($\sim 10^6 \text{ S}\cdot\text{m}^{-1}$) and the strong magnetic field that confines the plasma.

The main liquid breeders are metallic lithium and the eutectic Pb-Li alloy. Much research is focused on the eutectic Pb-Li since it is thought to be a safer option. Its lower chemical reactivity with water, air, and structural materials, make this alloy a more interesting breeder/refrigerant candidate [9]. Furthermore, Pb (n, 2n) and Pb (n, 3n) reactions allow this material to act as a neutron multiplier [10]. Moreover, it exhibits a high breeding capability and low tritium solubility [11].

Since the lithium concentration of the eutectic Pb-Li alloy in the breeding blanket will decrease as the fusion reaction occurs [12], it is important to monitor lithium concentration in real-time. Therefore, the preservation of the eutectic composition is critical, not only because lithium is required for tritium breeding, but also because other physical and chemical properties of the alloy will get compromised [13].

It is worth noting that directly related to breeding blankets, different projects emerged exploring the use of eutectic Pb-Li as a breeder material. Among these, projects such as PICOLO at KIT [14], TRIEX at ENEA [15,16], or CLIPPER at CIEMAT [17] are assessing some of the challenges that will be faced when using this alloy in future blankets. These facilities share a common trait which is a flowing molten eutectic Pb-Li loop. On one hand, PICOLO testing loop was designed for analyzing the compatibility of steels in a flowing Pb-15.7Li environment at 550 °C. On the other hand, TRIEX and CLIPPER projects investigate tritium extraction from eutectic Pb-Li in different breeding concepts at temperatures in the 350 °C-500 °C range. A Li monitoring tool could be also relevant in all these projects since it is important to ensure the eutectic composition is preserved during all the experiments. Note that such Li indicator will be able to determine whether there is an interaction between Li and any component or compound in direct contact.

1.1. Pb-Li in Tritium Breeding Blankets

As mentioned, eutectic Pb-Li is an interesting breeding material for future breeding blankets. This eutectic composition was chosen considering several factors and reaching an equilibrium among them. First of all, this alloy is composed of lithium, which will react to form tritium ([Eq. 1.2]), and lead as a neutron multiplier, which is important to achieve an adequate tritium breeding ratio (TBR) [10,18]. Thus, both elements need to be balanced to achieve the optimum performance of the tritium breeding blanket (TBB). Moreover, there are more physicochemical properties (tritium solubility, melting point, etc.) that must be considered. For instance, in Figure 1.3, it can be observed how the hydrogen solubility

(whose behavior is not expected to differ significantly from tritium) and lithium activity relate to the lithium mole fraction in Pb-Li alloy.

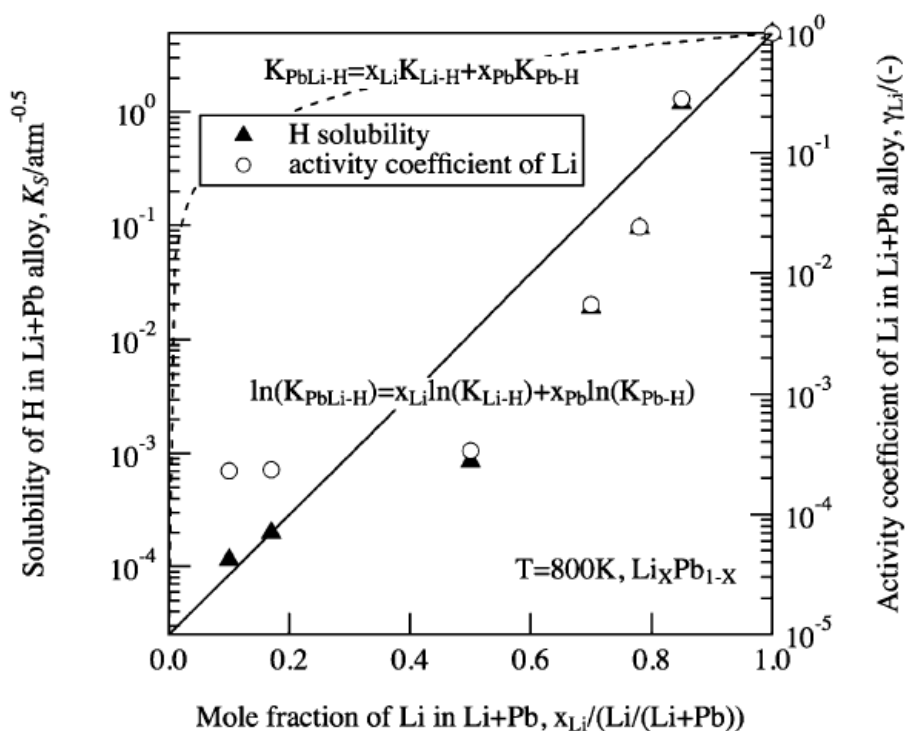


Figure 1.3. Lithium activity and hydrogen solubility as a function of the Li molar fraction in Pb-Li alloy [19].

As observed in Figure 1.3, both hydrogen solubility and lithium activity increase as the lithium mole fraction is raised in the alloy. On the one hand, a large tritium solubility is not desired, since having this hydrogen isotope dissolved would cause to diminish its partial pressure, increasing the difficulty of its extraction. On the other hand, lithium activity should be kept as low as possible, since a higher lithium activity can cause higher corrosion on the blanket structural materials [20]. Note that, eutectic Pb-Li fulfills both low lithium activity and low hydrogen solubility, those being among other reasons why it has been selected as a tritium breeder in future TBB [19,21].

Although many different breeding designs have been proposed, there is still no consensus to select the most suitable concept [22]. The proposed Pb-Li breeder blankets concepts are the Chinese Dual Functional Lithium Lead (DFLL) blanket, European Helium-Cooled Lithium Lead (HCLL), Dual Coolant Liquid Lead (DCLL), and Water-Cooled Lithium Lead (WCLL) blankets, American Dual Coolant Liquid Lead (DCLL), and Indian Lithium Lead Ceramic Breeder (LLCB) [23,24].

Among these, three strong candidates are the HCLL, WCLL, and DCLL concepts. As its name indicates, HCLL design employs He as a coolant. This breeding concept is being developed in the European Union and China [25]. The WCLL which uses water as a coolant is also a European breeding concept [24]. By contrast, the DCLL breeding design shows a dual cooling with He and Pb-Li. This breeding concept is being developed in Europe, the United States, and China [26–30]. A schematic representation of these breeding concepts is shown in Figure 1.4.

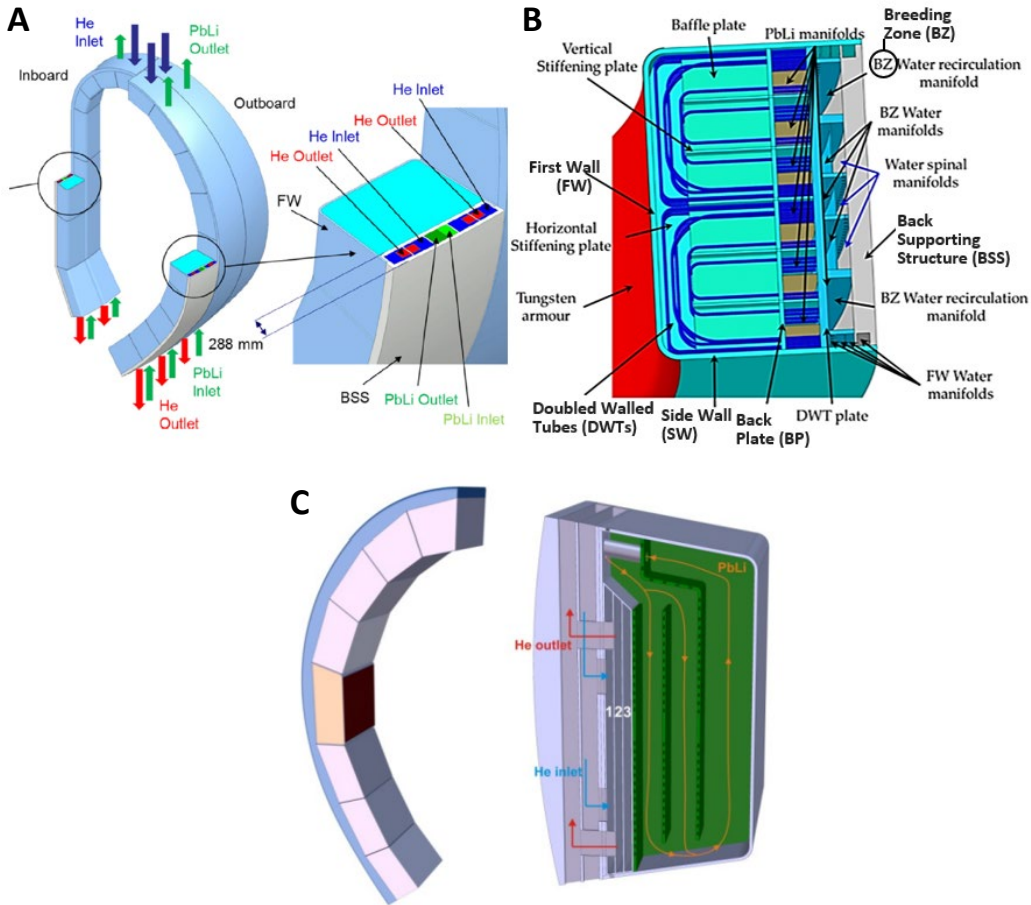


Figure 1.4. Breeding blankets concepts of the A) HCLL [31], B) WCLL [32], and C) EU-DCLL [30].

As seen in Figure 1.4A, the HCLL design uses eutectic Pb-Li as a neutron multiplier and lithium source. Its outlet and inlet are located at the top and bottom of each module. In the opposite direction of the Pb-Li flow, helium coolant will circulate at 8MPa and 300 °C (inlet)/500 °C (outlet) [25]. In Figure 1.4B, the breeding blanket concept of the WCLL is shown. In this concept, the breeding zone (BZ) is the area of the breeding blanket surrounded by the First

Wall-Side Wall (FW–SW) complex. In this area, it is contained the liquid lead–lithium eutectic alloy. The cooling of the BZ is achieved through double-walled tubes (DWT) where water flows under Pressurized Water Reactors (PWR) conditions. In these conditions, water capacity for heat extraction is increased, and it is expected to circulate at 15.5 MPa with inlet/outlet temperatures of 285/325 °C [33]. As observed from the figure, water and Pb-Li manifolds will be used to distribute the water coolant and lead–lithium alloy to the BZ and FW–SW areas and recollect them [32]. In Figure 1.4C the construction principle of the EU-DCLL blanket is shown. In this design, it can be observed that each blanket segment is subdivided into 8 independent modules. The modules are rigid large boxes with a grid structure inside, which are used as flow channels for the eutectic Pb-Li and helium. High-pressure helium gas is used to cool the FW and the entire steel structure to maintain its temperature under 550 °C. In addition, it allows the preheating of the structure before the PbLi injection into the segment [30]. In DCLL concepts, Pb-Li has the dual function of coolant and tritium breeder and neutron multiplier. In the design shown in Figure 1.4C, four independent circuits compose the BZ where the Pb-Li flows in parallel through rectangular channels. The outlet temperature must be as high as possible to maximize the thermal efficiency of the power conversion system. However, in the low-temperature version, the temperature is limited to 550°C to avoid creep of the structural material (Eurofer) and extreme corrosion rates [34,35]. Nevertheless, efforts are being focused on developing a novel TBB still based on the DCLL concept but working at higher temperatures [36].

Note that, in these designs, as tritium starts to be produced, the alloy’s lithium concentration will start to decrease. Due to this phenomenon, the physicochemical properties of the alloy will change significantly. As a result, the performance of the reactor can be influenced [13]. One of the main properties of Pb-Li alloy that will get affected is its melting point (Figure 1.5).

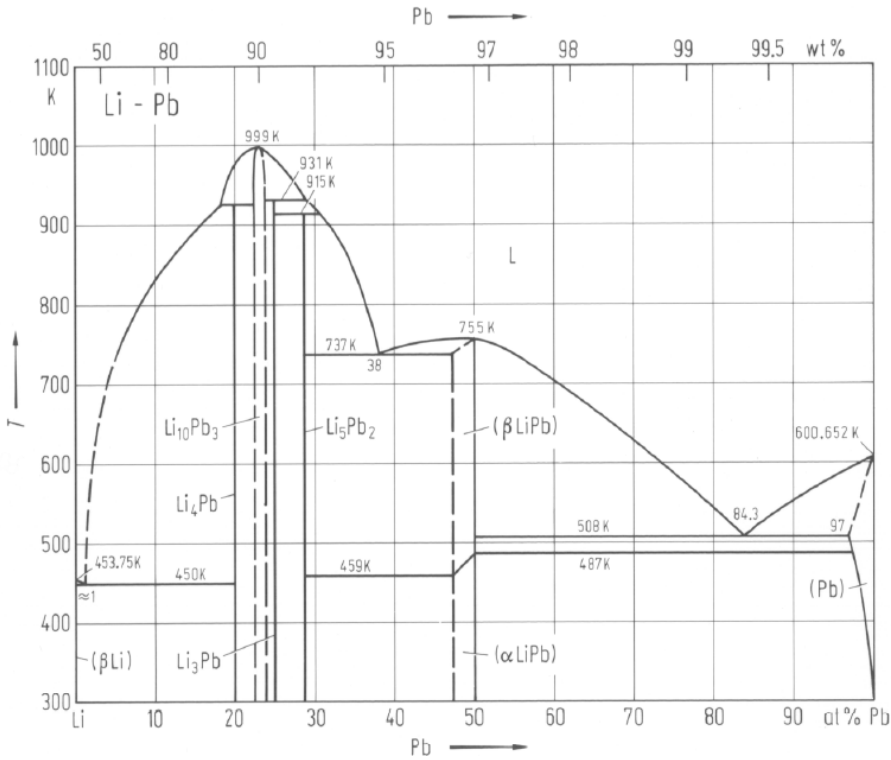


Figure 1.5. Pb-Li phase diagram [37].

It can be seen in Figure 1.5, that the melting point of a Pb-Li alloy depends on its lithium at%. Note that, the Pb-Li alloy with eutectic composition gives the lowest melting temperature, near 235 °C. Upon decreasing its lithium concentration, the melting point can significantly increase. Furthermore, if the lithium concentration is not kept homogeneous, lithium-rich phases can form such as $\text{Li}_{10}\text{Pb}_3$, Li_5Pb_2 , Li_3Pb , etc., which would exhibit melting points higher than 500 °C.

To determine Li concentration there are different analytical techniques such as atomic emission (ICP-OES [38]), atomic absorption spectroscopy (AAS [39]), and resistivity measurements [40,41]. However, these techniques require extracting the sample for its analysis. Therefore, these cannot provide real-time online monitoring of the lithium concentration in the melt. Electrochemical sensors are an alternative to these techniques since they can be used to obtain real-time measurements. However, these analytical tools are still in development, with little information published in the bibliography. Therefore, the development of electrochemical sensors is an essential research field to offer a solution to online lithium monitoring.

1.2. Lithium Monitoring in Molten Metals

To ensure the safe and efficient operation of the breeding blankets, it is necessary to have a reliable and accurate method for the determination of the lithium content. The methods to monitor the lithium concentration in Pb-Li alloys can be divided into two categories, batch methods (offline), and continuous methods (online). The former relies on the removal of a sample for its analysis (ICP-OES [38] and AAS [39]). The latter, which is still under development, is more interesting since it can be used as an online and onboard monitoring tool in Pb-Li TBMs.

Hubberstey et al. [40,41] developed an electrical resistivity meter for Li determination in molten Pb-Li. Its principle is based on the fact that the electrical resistivity of the alloy is dependent on the Li concentration and the temperature. In contrast, electrochemical lithium sensors based on lithium-ion conducting electrolytes were reported by De Schutter et al. [42–44] and Wu et al. [45]. Sodium β -alumina and LiYO_2 electrolytes were used respectively. These permitted the potentiometric comparison of the lithium activity in a liquid Li alloy to a reference system with a known lithium activity.

1.2.1. Electrical Resistivity Meter

Hubberstey and coworkers [40,41] developed an electrical resistivity meter, which was originally conceived at Nottingham University for the study of the chemistry of liquid metal solutions [46]. Furthermore, this monitoring instrument was supplied to F. Babier to further study its features in a loop system [47]. Its working principle is that the electrical resistivity of a Pb-Li alloy depends on its lithium concentration and temperature: the resistivity rises with lithium concentration or temperature. As the resistivity of the alloy can be determined from resistance measurements, at a given temperature, any changes in the lithium concentration can be measured. The design of the electrical resistivity meter is shown in Figure 1.6.

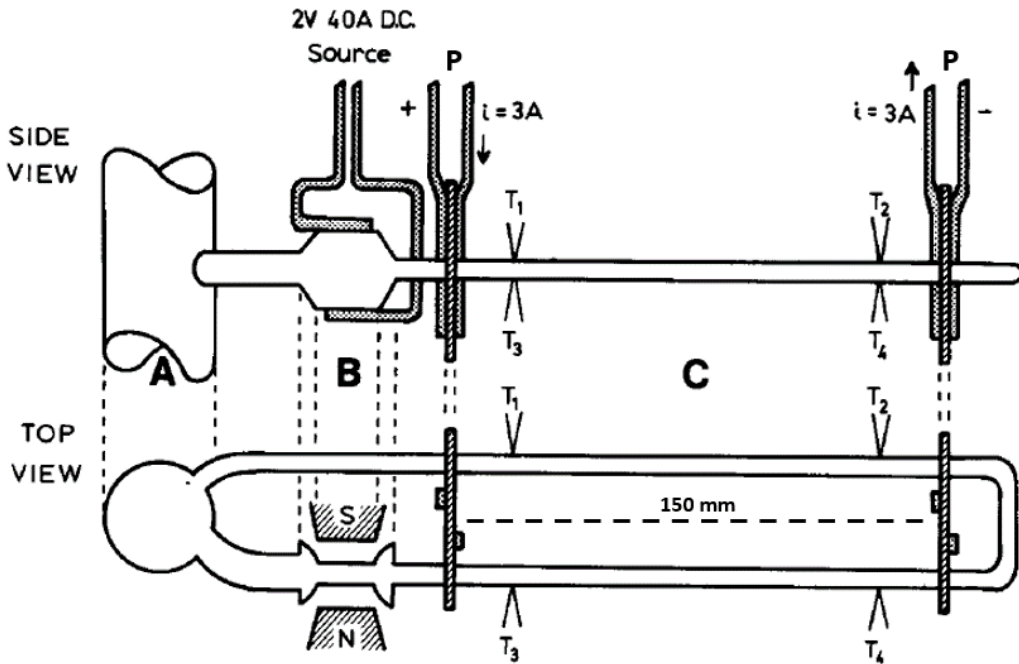


Figure 1.6. Design of the electrical resistivity monitor developed by Hubberstey et al. [41].

The body of the monitor (A) made of 316L stainless steel was connected to a loop where a capillary section (C) (outer diameter 4.8 mm; inner diameter 3.0 mm; length, 450 mm) was attached, also made of 316L stainless steel. The molten alloy was pumped around the capillary using a miniaturized electromagnetic pump (B). Two plates (P) were attached to the capillary section 150 mm apart and two silver leads were placed on each plate to supply a 3 A constant current. This current was generated by a stabilized power supply and circulated through the capillary section and a standard resistance of 0.01Ω (R_s), arranged in series. The capillary was inserted into a furnace and the temperature was controlled by four thermocouples (T_1 - T_4). The resistance of the Pb–Li alloy was obtained using a version of the four-terminal method as described by Hubberstey et al. [41]. With this aim, first, the resistance of the capillary (R_t) was calculated from the expression ([Eq. 1.3]):

$$R_t = R_s \frac{V_t}{V_s} \quad [\text{Eq. 1.3}]$$

where R_s is the 0.01Ω standard resistance, V_s is the potential difference across the standard resistance, and V_t is the potential difference across the cell. The resistance of the Pb–Li alloy (R_m) is then obtained from the resistance of the capillary (R_t) filled with alloy and the resistance of the empty capillary (R_c) using the expression of parallel conductors:

$$R_m = \frac{R_c R_t}{(R_c - R_t)} \quad [\text{Eq. 1.4}]$$

Then, the resistivity of the alloy (ρ_m) was calculated through the relationship:

$$\rho_m = R_m \frac{A}{l} \quad [\text{Eq. 1.5}]$$

where A is the cross-sectional area and l is the length of the capillary between the two plates. Before use, the resistance of the empty capillary (R_c) and the constant A/l were determined. The constant, which is specific to each monitor, could be obtained either by measurement of the internal diameter of the capillary and the distance between the plates or by calibration using a metal or alloy of known resistivity. Data concerning resistances, temperatures, and resistivities were collected for various alloy compositions. From these data, the authors plotted the resistivity-temperature and resistivity-concentration dependence for Pb-Li alloys at temperatures from 600 to 800 K and concentrations from 0.0 to 20.5 at% Li. Some of these relationships can be observed in Figure 1.7.

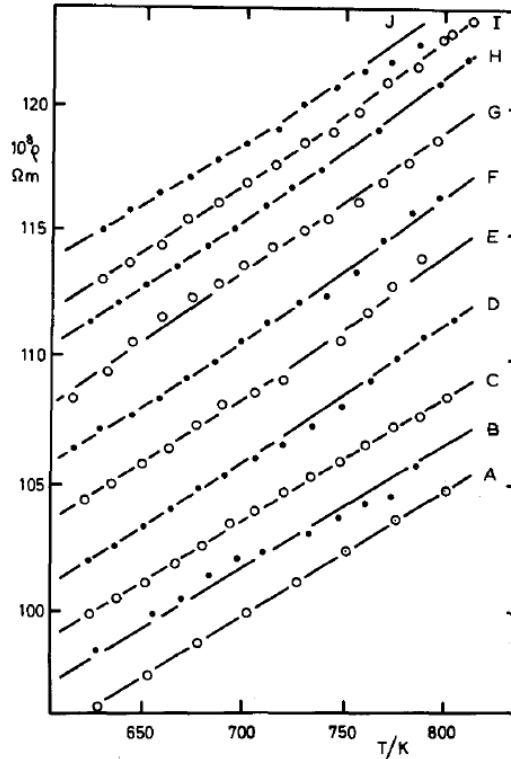


Figure 1.7. Resistivity-temperature data for Pb-Li alloys with at% Li concentrations of: A – 0.00; B – 2.03; C – 4.04; D – 6.13; E – 8.21; F – 10.16; G – 11.96; H – 13.89; I – 15.60; J – 17.11 [41].

From Figure 1.7, it was determined that the resistivity-concentration isotherms obtained for temperatures up to 500°C could be represented by the following equation:

$$10^8 \rho (\Omega m) = A + Bx_{Li} + Cx_{Li}^2 \quad [\text{Eq. 1.6}]$$

where ρ is the resistivity value, x_{Li} is the lithium concentration in at% ($0.0 < x_{Li} < 20.5$), and A, B, and C are coefficients whose values are presented in Table 1.1.

Table 1.1. Coefficients for [Eq. 1.6] describing the concentration and temperature dependence on the resistivity [41].

T / K	A	B	C
623	96.37	0.905	0.0124
648	97.43	0.934	0.0112
673	98.53	0.961	0.0099
698	99.6	0.995	0.0085
723	100.67	1.042	0.0067
748	101.73	1.095	0.0047
773	102.79	1.148	0.0028

From the coefficients, the lithium concentration of a Pb-Li alloy could be monitored upon measuring the alloy's resistivity with the described instrument. From different experiments performed it was determined that this analytical tool could detect lithium depletion in case of oxygen ingress. Furthermore, it was also observed that the device was sensitive to other concentration changes such as Pb-Li addition. The monitor exhibited a minimum detectable limit of ± 0.15 at% Li. During the tests conducted by F. Barbier in a loop system, it was also observed that the concentration change detected by the device was stabilized between 10 and 20 min. This response time was considered to only depend on the rate of Pb-Li dissolution (sampling) and the flow rate of the alloy in the loop (mixing) [47,48].

1.2.2. Electrochemical Lithium Sensors

Electrochemical sensors are another interesting analytical tool that can be used for Li monitoring in molten metal alloys. However, to be able to withstand high temperatures their design typically encounters many challenging issues, such as thermal and long-term stability, sensitivity, reproducibility, and selectivity. To overcome this matter, those based on solid-state electrolytes are expected to endure the harsh conditions of the molten Pb-Li breeding blanket and satisfy the required analytical parameters for lithium monitoring.

Electrochemical lithium sensors using sodium β -alumina electrolytes were reported for their use in molten eutectic Pb-Li [42–44] (Figure 1.8). These potentiometric sensors compared the Li activity of liquid Pb-Li alloy with a biphasic Li-Bi mixture (reference system).

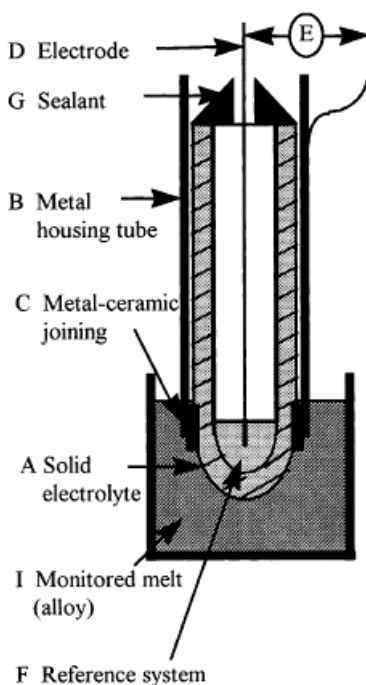


Figure 1.8. Electrochemical Li sensor [48].

The sensor design (Figure 1.8) was formed by a solid electrolyte thimble (A) sealed in a cylindrical stainless steel housing (B) using ceramic cement (C). The central electrode (D), made of stainless steel, dipped into the reference system (F) and exited the thimble through a vacuum-tight sealant (G) situated at the top of the probe. The other electrical connection (E) was made at the external surface of the steel housing (B) which contacted the Pb-Li alloy to be monitored (I). The stainless steel housing was about 30 cm long, the external diameter

of the ceramic thimble was 1 cm and its thickness was 1 mm. At equilibrium, the measured potential difference (ΔE) of the cell follows the Nernst law, which can be written:

$$\Delta E = \frac{RT}{nF} \ln \frac{a_{Li(PbLi)}}{a_{Li(ref)}} \quad [\text{Eq. 1.7}]$$

with $a_{Li(PbLi)}$ the lithium activity in the PbLi alloy to be measured, $a_{Li(ref)}$ the constant lithium activity in the reference system, R the gas constant, F the Faraday constant, n the number of electrons involved in the electrochemical reaction, and T the temperature. From ΔE and a known lithium activity in the reference system, the activity of the Pb-Li alloy monitored can be calculated.

During the experiments performed with this electrochemical sensor, a stable signal was observed 10 min after immersion of the sensor into Pb-17Li. The sensor also exhibited a reproducibility of ± 1 mV which related to a minimum measurable concentration change of 0.15 ± 0.05 at% Li. Results obtained with several of these sensors are shown in Figure 1.9. In the figure, the author also included previous data on the Pb-Li system studied by Saboungi et al. [49].

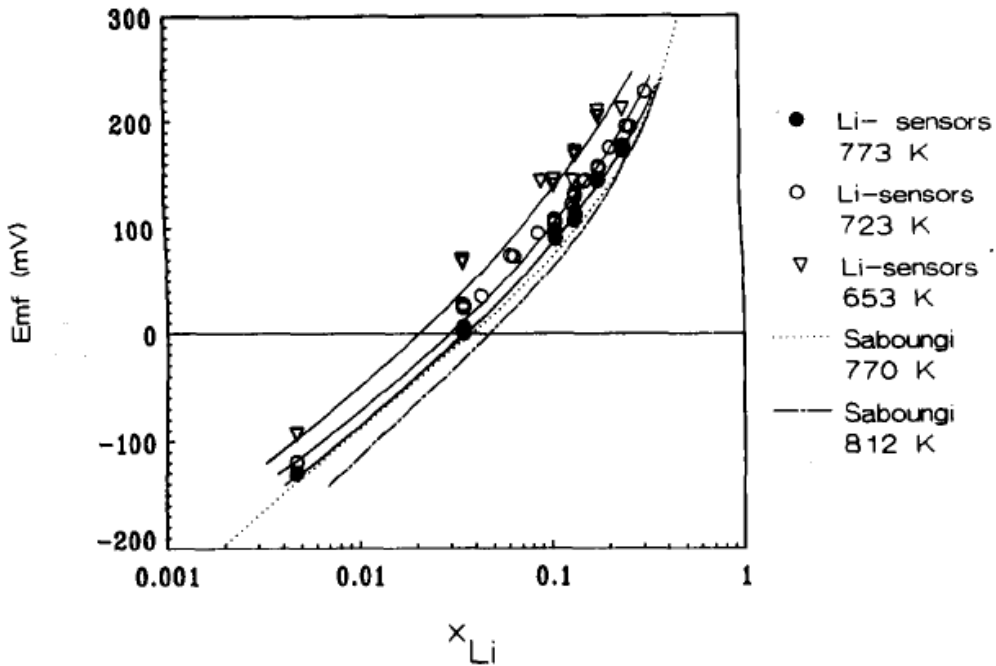


Figure 1.9. Experimental ΔE as a function of the temperature and the lithium concentration [42].

Both investigations exhibit comparable potential values versus Li concentration relationships. When the absolute values of De Schutter data obtained at 773 K were compared with Saboungi's data [49], a difference of typically 5 to 10 mV was observed. Despite the satisfactory results, most of the sensors which were tested had a very short mean lifetime because of cracks in the sodium β -alumina electrolyte. De Schutter et al. estimated that only 55% of the fabricated sensors were reliable, some of which broke after their first immersion [48]. Another unusual aspect of this lithium sensor was the fact that a sodium ion conductor instead of a lithium-ion conductor was used as a solid electrolyte. This fact made that this element required a certain period of exposure to behave as theoretically expected [43]. During the first period of exposure, a partial replacement of the sodium ions by lithium occurred to achieve the correct interface [43,50].

Another electrochemical lithium sensor used in molten metals was reported by Wu et al. [45]. In contrast to the previous sensor mentioned, it was used in Zn alloys and was based on the solid electrolyte LiYO_2 . The sensor was fabricated by reactive sintering and joining a LiYO_2 tube with a Y_2O_3 -12.5% MgO lid. The working principle of the potentiometric sensor was similar to the one previously discussed (see [Eq. 1.7]). The design of the sensor is shown in Figure 1.10.

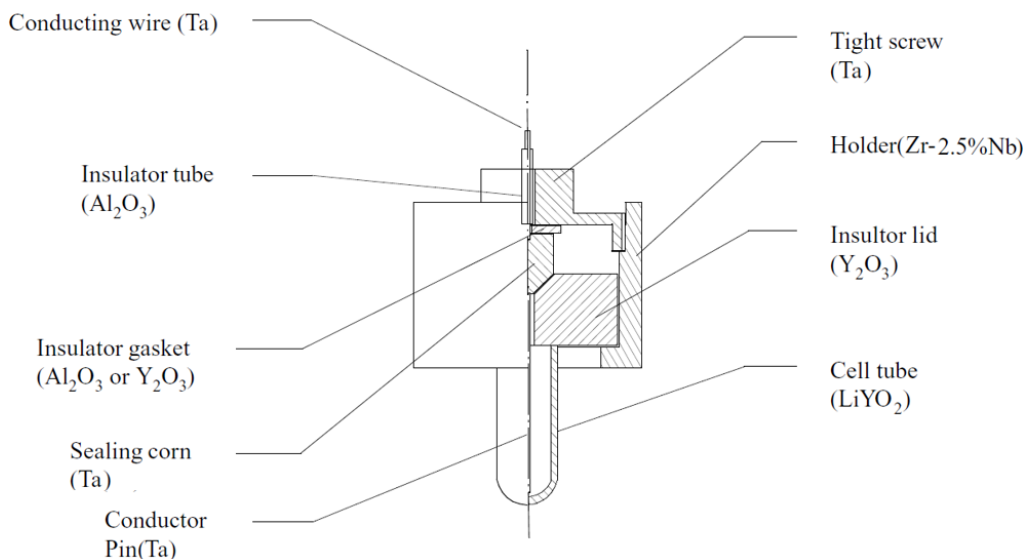


Figure 1.10. Cell assembly of the Li electrochemical sensor proposed by Wu et al. [45].

Working and reference half-cells were constructed by adding tantalum wires to the cell tube (LiYO_2) - insulator lid (Y_2O_3) assembly. A Ta sealing cone was clamped to the lid by a cell holder machined from a Zr-2.5% Nb alloy. Potentiometric measurements were taken between working and reference half-cells.

With the constructed sensor, potentiometric measurements were performed to study Zn-Li systems at 600 °C. The reference electrodes used to study this system were Sn-0.635 at% Li and 1.62 at% Li alloys. Tin was chosen as the base metal for the reference electrode because of its low melting point and low vapor pressure. The use of a dilute lithium concentration also ensured a low Li vapor pressure, reducing the chances of side reactions or leakage. The reference electrodes were calibrated against pure Li in a temperature range of 340 to 680 °C. The ΔE for each of the concentrations is given in [Eq. 1.8]-[Eq. 1.9] as a function of the temperature (T , °C):

$$0.635 \text{ at\% Li: } \Delta E \text{ (mV)} = 645.9 + 0.520T \quad [\text{Eq. 1.8}]$$

$$1.62 \text{ at\% Li: } \Delta E \text{ (mV)} = 784.1 - 0.212T + 0.0007T^2 \quad [\text{Eq. 1.9}]$$

Then, Zn-Li alloys were potentiometrically measured as a function of the concentration at 600 °C. From the ΔE measured, the Li activity coefficients (γ_{Li}) in Zn-Li alloys were determined. In Figure 1.11 the ΔE and Li activity coefficients of different Zn-Li alloys are plotted against their lithium concentration. In the figure, the author also included data from a previous potentiometric study of the Zn-Li system conducted by Gasior et al. [51]. In this study, molten LiCl-LiF was used as the electrolyte.

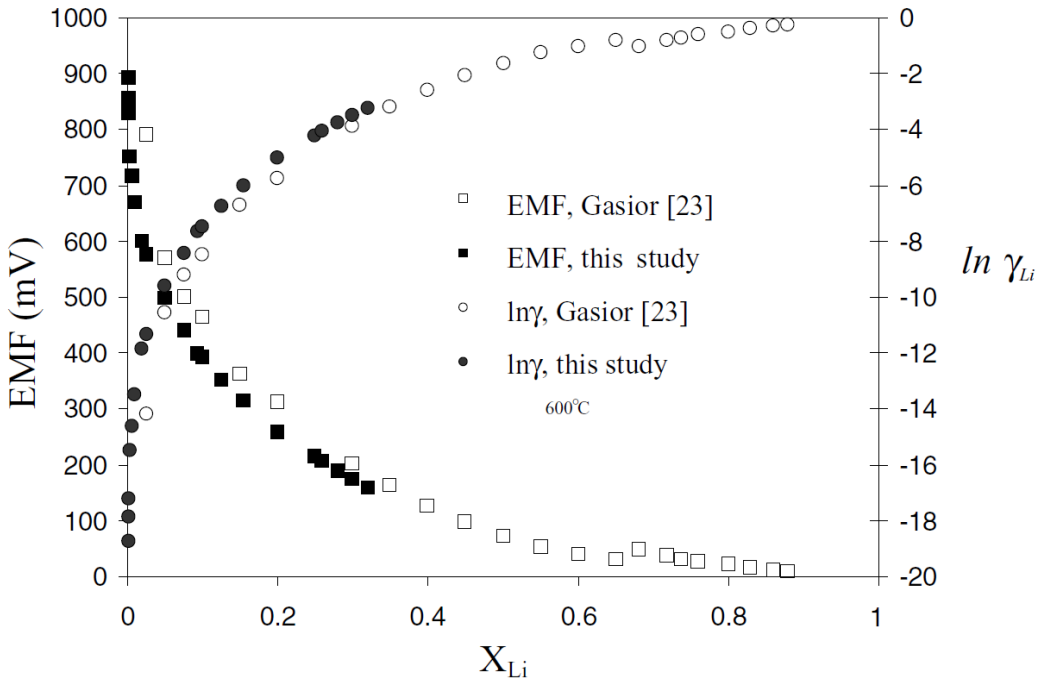


Figure 1.11. Experimental ΔE and $\ln \gamma_{Li}$ versus x_{Li} for Zn-Li alloys at 600 °C [45].

From this study, Wu et al. reported the thermodynamic properties of the Zn-Li system. Furthermore, the ΔE and Υ_{Li} measured showed good agreement with the reported data from Gasior et al. [51]. Despite the interesting results obtained from Wu et al. [45], the sensor was not tested in Pb-Li alloys.

It is worth mentioning that both, the resistivity monitor and electrochemical lithium sensors, demonstrated their capability for lithium monitoring in molten alloys. However, the resistivity monitor use and replacement on the TBMs would be more complicated than the electrochemical sensor. Furthermore, although no major impurities are expected in eutectic Pb-Li, the instrument is sensitive to any solute [52]. Due to the largest simplicity of the electrochemical sensors compared to the resistivity monitor, these analytical devices appeared as a more interesting option. Despite that, further research is needed since there were still aspects to improve from the previously developed electrochemical sensors. On the one hand, more suitable lithium-ion conducting electrolytes can be used, expecting a higher selectivity to Li than sodium β -alumina electrolytes. On the other hand, more experimentation is required to determine the analytical performance of the sensors when used in Pb-Li alloys.

To design new electrochemical sensors, the most crucial part is to adequately select the solid electrolyte. Among the different solid electrolytes, it is important to choose electrolytes capable to withstand the physicochemical conditions of the Li melts. Furthermore, these electrolytes need to exhibit high lithium-ion conduction for proper sensor functioning. This property is further discussed in the following sections.

1.3. Ion-Conducting Solid-State Electrolytes

Ion-conducting solid-state electrolytes are attractive materials due to their high thermal stabilities and low chemical reactivity. Such properties enable several emerging technologies such as micro-batteries [53], solid oxide fuel cells [54], solid-state batteries for electric vehicles [55] or sensors [56,57]. For this reason, solid electrolytes are great candidates to develop sensing devices able to withstand the operational conditions that will be found in future Pb-Li breeding blankets. Due to these characteristics, considerable research has focused on the development of new solid-state electrolytes. From these, attaining large ionic conductivities is one of the primary interests, since this property is strongly related to the performance of the electrolyte.

1.3.1. Ionic Conductivity

Ionic conductivity implies the transport of one or more types of ions across a material. In an ideal crystal, all constituent ions are arranged in a regular periodic pattern and are stacked in a close-packed form, therefore, there is little space for ions to move. Thus, crystalline defects are necessary for ions to diffuse through a solid and give rise to ionic conductivity through different mechanisms [58].

At any non-zero temperature, crystalline defects occur, which imply a positional disorder from its ideal stacking. These defects are classified according to their dimension:

- Zero-dimensional defects, which are point defects: impurities, vacancies, interstitials.
- One-dimensional defects, which are line defects: dislocations.
- Two-dimensional defects, which correspond to planar defects: interfacial defects such as surfaces, grain boundaries, and phase boundaries.
- Three-dimensional defects, which result in bulk or volume defects: voids, cracks, pores, precipitates.

As mentioned, the movement of ions across the solid structure is necessary for ionic conduction to be possible. To achieve this ionic transport across the solid, different mechanisms are described. Some of these mechanisms are shown in Figure 1.12.

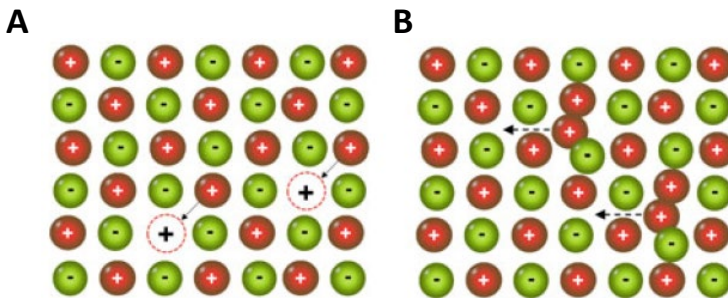


Figure 1.12. Ion transportation mechanisms in solid electrolytes: A) vacancy and B) interstitial mechanisms [58].

The vacancy migration mechanism (Figure 1.12A) takes place when point defects occurring in the crystal result in vacant sites. Consequently, these defects permit the movement of any ion in immediate proximity from a normal site to these vacant sites. Through this mechanism, ions can gradually move across the crystal. Interstitial migration, shown in Figure 1.12B, is another important conduction mechanism. This mechanism occurs when an ion moves to an interstitial site, giving rise to a defect, the ion can then subsequently jump to a neighboring interstitial site, and so on.

The total conductivity of a material is equal to the movement of charged particles across its structure: anions, cations, electrons, or holes. The conductivity due to charged particles of any of these types (i) moving through a solid is given by equation [Eq. 1.10] [59].

$$\sigma_i = c_i q_i \mu_i \quad [\text{Eq. 1.10}]$$

Where σ_i is its conductivity ($\text{S}\cdot\text{m}^{-1}$), c_i is the number of charged particles per unit volume ($\text{particles}\cdot\text{m}^{-3}$), q_i is the particle's charge (C), and μ_i is the mobility of the particles ($\text{m}^2\cdot\text{V}^{-1}\cdot\text{s}^{-1}$). When several different species (n) exhibit conductivity, σ_{total} is the sum of these various contributions ([Eq. 1.11]):

$$\sigma_{\text{total}} = \sum_i^n \sigma_i \quad [\text{Eq. 1.11}]$$

From this equation, it is deduced that the total conductivity of a material is thus equal to the sum of electronic (holes and electrons) and ionic (anions and cations) conductivities ([Eq. 1.12]):

$$\sigma_{\text{total}} = \sigma_{\text{electronic}} + \sigma_{\text{ionic}} \quad [\text{Eq. 1.12}]$$

Materials such as lithium solid-state electrolytes require that the total conductivity is only due to the movement of Li^+ ions through the material. That implies that the ionic conductivity is almost equal to the total conductivity and thus, the electronic contribution to conductivity is insignificant. Therefore, these materials are expected to be electronic insulators, where electrons and holes are highly localized and are not free to move throughout the crystal.

1.3.2. Lithium-Ion Conducting Solid-State Electrolytes

The ionic conductivity of lithium-ion conducting solid-state electrolytes is a key parameter that determines its electrochemical performance. The ionic conductivity in these electrolytes is strongly dependent on the movement of ionic point defects. Therefore, the crystal structure plays an important role in the ion's movement across the material. As a consequence, different crystalline families have been studied as lithium-ion conducting solid-state electrolytes. Among these crystalline families, crystal structures which include LISICON-like (lithium superionic conductor), perovskites-type, NASICON-like (sodium superionic conductor), and garnet-type have been extensively researched.

1.3.2.1. LISICON and thio-LISICON type

The LISICON and thio-LISICON type compounds exhibit crystalline structures similar to the γ - Li_3PO_4 , which is formed by an orthorhombic unit cell, where all cations are tetrahedrally coordinated [59]. The substitution of the P (V) ion in γ - Li_3PO_4 by aliovalent ions such as Si (IV) or Ge (IV) can create compositions such as $\text{Li}_{3+x}(\text{P}_{1-x}\text{Si}_x)\text{O}_4$ [60–62], which yield electrolytes with higher lithium-ion conduction ($\sim 3 \cdot 10^{-6} \text{ S} \cdot \text{cm}^{-1}$ at room temperature). This phenomenon is explained since an excess of lithium ions is generated due to this substitution, which cannot be accommodated in the tetrahedral sites, and hence, have to occupy interstitial sites. Therefore, the adjacent lithium–lithium ion distance is shortened, increasing the lithium-ion conductivity. Moreover, when substituting O by S, $\text{Li}_{3+x}(\text{P}_{1-x}\text{Si}_x)\text{S}_4$ structures form, giving rise to the thio-LISICON family. This compositional change further increased lithium-ion conductivities up to values of $\sim 6 \cdot 10^{-4} \text{ S} \cdot \text{cm}^{-1}$ at room temperature [63]. More recently, the high ionic conducting electrolyte $\text{Li}_{11}\text{AlP}_2\text{S}_{12}$ ($8.02 \cdot 10^{-4} \text{ S} \cdot \text{cm}^{-1}$ at 25 °C) was synthesized by Zhou et al. [64]. The high ionic conductivity of the electrolyte was attributed to the thio-LISICON analog crystalline structure and to the Al substitution, which facilitated Li ionic conduction. The crystallographic structure of $\text{Li}_{11}\text{AlP}_2\text{S}_{12}$ is represented in Figure 1.13.

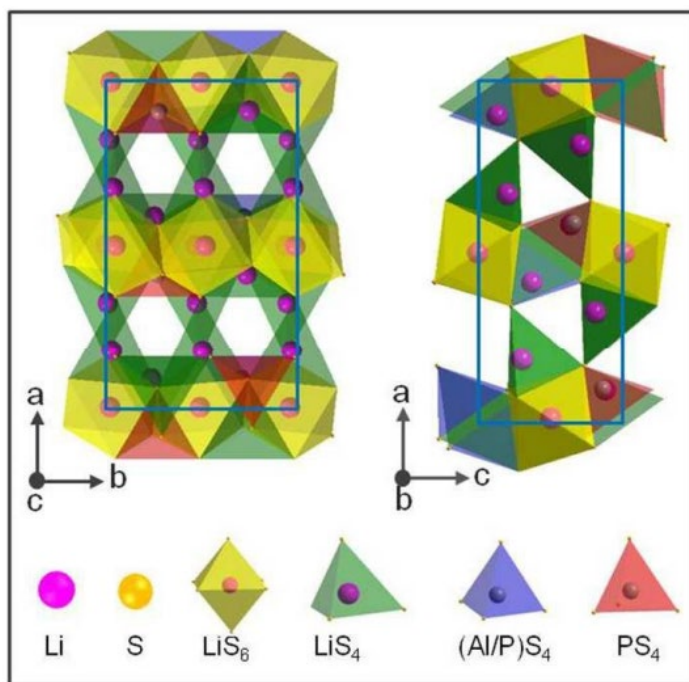


Figure 1.13. $\text{Li}_{11}\text{AlP}_2\text{S}_{12}$ crystallographic structure [64].

The compound exhibits a typical three-dimensional framework of thio-LISICON. From Figure 1.13, it is observed that PS_4 and $(Al/P)S_4$ acquire tetrahedral forms which are isolated from each other. Lithium coordinates tetrahedrally (LiS_4) or octahedrally (LiS_6). The arrangement of PS_4 or $(Al/P)S_4$ tetrahedrons connected by LiS_4 tetrahedra and LiS_6 octahedra finally forms the 3D structure. Despite the high lithium-ion conductivities of these electrolytes, it has been reported from computational studies, that some of them could be unstable in lithium [65,66].

1.3.2.2. Perovskite-type

The perovskite-type structure exhibits a general formula ABO_3 which consists of A-site ions (typically rare-earth or alkaline-earth elements) at the corners of a cube, B ions (typically transition metal ions) at the center, and oxygen atoms at the face-center positions. The A sites are twelve-fold coordinated (AO_{12}) and the B sites are six-fold coordinated (BO_6) and share corners with each other [67]. Lithium can be introduced in the perovskite on the A site through aliovalent doping, modifying the concentrations of both lithium ions and vacancies in the structure. Compounds such as lithium-lanthanum titanate (LLTO) $Li_{3-x}La_{2/3-x}TiO_3$ ($0 < x < 0.16$) can be synthesized. These electrolytes can exhibit high ionic conductivity up to $10^{-3} S \cdot cm^{-1}$ at room temperature [68]. Figure 1.14 shows a schematic representation of the LLTO structure.

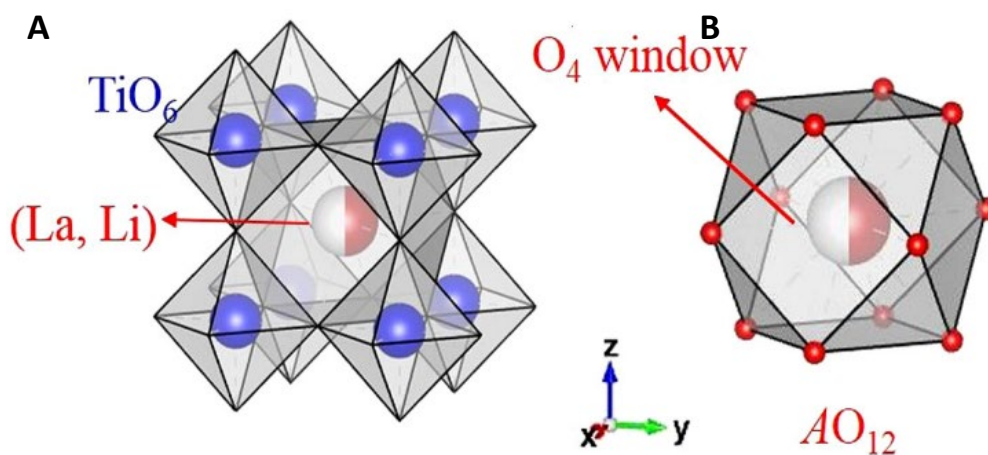


Figure 1.14. Crystal structure of A) a cubic perovskite-type LLTO, and B) an AO_{12} cuboctahedron [69].

Figure 1.14A shows the unit cell of LLTO with a conventional perovskite ABO_3 structure. Eight TiO_6 octahedrons sharing corners in pairs form an AO_{12} cuboctahedron (Figure 1.14B), in the center of which Li^+ and La^{3+} are situated. However, due to the various ordered distributions

of Li/La ions as well as the distortion of TiO_6 octahedrons, plenty of structural variations and symmetries are derived from this simple cubic perovskite-type [70,71].

Despite the high bulk ionic conductivity, the grain boundary ionic conductivity of LLTO was only in the magnitude of $10^{-5} \text{ S}\cdot\text{cm}^{-1}$ at room temperature, resulting in a relatively low total ionic conductivity [72]. At the same time, LLTO is not stable at a voltage below 1.8 V vs. Li/Li^+ , making it incompatible with many low-potential anode materials, including lithium [73]. The low electrochemical stability is caused by Ti (IV) in the LLTO structure since it can be reduced at low voltage vs. Li/Li^+ . To address this issue, new perovskite-type solid electrolytes were developed, substituting the Ti ions in their structure. For instance, Thangadurai et al. synthesized the $\text{LiSr}_{1.65}\text{Zr}_{1.3}\text{Ta}_{1.7}\text{O}_9$ solid electrolyte that was stable in contact with lithium demonstrating that Zr^{4+} and Ta^{5+} oxidation states are stable against reduction [74].

1.3.2.3. NASICON-type

The name NASICON was initiated from sodium super ion conductors with the general formula $\text{NaM}_2(\text{PO}_4)_3$, where M represents metallic cations. When replacing the Na ions with Li, NASICON-type Li-ion solid electrolytes were synthesized. The general formula for these NASICON-type lithium solid electrolytes can be described as $\text{LiM}_2^{\text{IV}}(\text{PO}_4)_3$ ($\text{M}^{\text{IV}} = \text{Ti, Zr, Ge, Hf}$). Depending on the temperature and composition, NASICON-like compounds can have monoclinic, triclinic, orthorhombic, or rhombohedral structures. However, the most common is rhombohedral [75,76] (Figure 1.15).

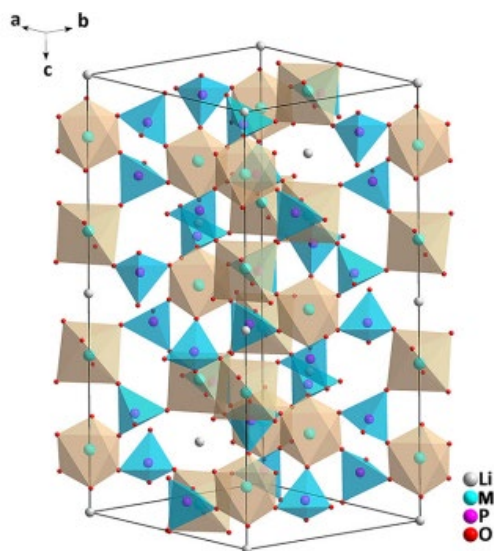


Figure 1.15. NASICON-type structure of $\text{LiM}_2(\text{PO}_4)_3$ [77].

The rhombohedral structure consists of MO_6 octahedra linked via corner-sharing with PO_4 tetrahedra to form 3D interconnected channels. The mobile cations (Li^+) are distributed in these channels in two types of interstitial positions: the sites that are six-fold coordinated with oxygen, and the sites that are ten-fold coordinated with oxygen. The six-fold coordinated sites are located between two MO_6 octahedra and the ten-fold are located between two columns of MO_6 octahedra. These interstitial positions provide the pathway for Li^+ ion conduction.

Among the different $\text{LiM}_2^{\text{IV}}(\text{PO}_4)_3$ NASICON-type electrolytes, $\text{LiTi}_2(\text{PO}_4)_3$ exhibits the highest Li^+ conductivity ($\sim 10^{-5} \text{ S}\cdot\text{cm}^{-1}$ at room temperature) [78]. Furthermore, NASICON-like conductors are typically stable with air and water and are stable at high potentials [79]. However, similar to perovskites, titanium-containing compounds can be reduced at low potentials [80,81].

1.3.2.4. Garnet-type

Garnet-type solid electrolytes are derived from the ideal garnet structure with the general formula $\text{A}_3\text{B}_2\text{C}_3\text{O}_{12}$. A sites are eight-fold coordinated (antiprismatic sites), B sites are six-fold coordinated (octahedral sites) and C sites are four-fold coordinated (tetrahedral sites) [79,82,83]. Figure 1.16 shows a schematic representation of ideal lithium garnet-type metal oxide, where A sites have been occupied by Li^+ ions.

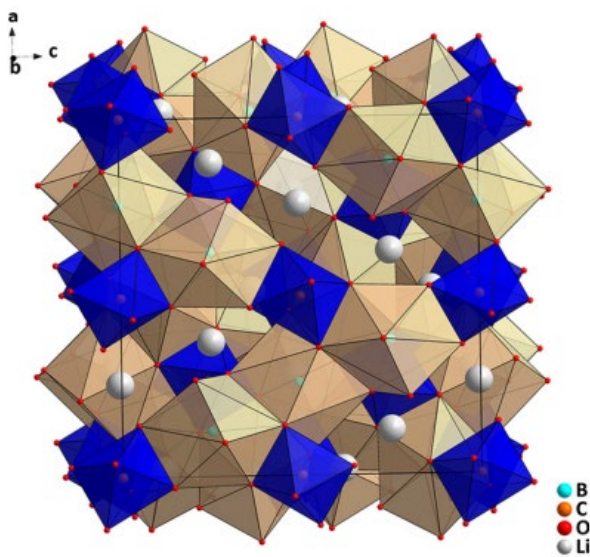


Figure 1.16. Crystal garnet structure of $\text{Li}_3\text{B}_3\text{C}_2\text{O}_{12}$ [77].

In Figure 1.16, this structure model can be viewed as a three-dimensional $B_3C_2O_{12}$ framework hosting Li^+ ions inside the interstitial sites. These sites contain Li-occupied tetrahedral sites and unoccupied octahedral sites, both of which connect by sharing faces to form a 3D network with octahedral sites as junctions. This network provides a pathway for Li^+ ion transport. In these ideal lithium garnets, lithium ions occupy tetrahedral positions such as in $Li_3Ln_3Te_2O_{12}$ ($Ln = Y, Pr, Nd, Sm - Lu$). However, these electrolytes have low ionic conductivities [84,85]. To obtain appreciable ionic conductivity more lithium can be added to the structure by adjusting the valence of the B and C cations, leading to several stoichiometries of lithium-conducting garnets [86]. For instance, adding M (V) ions in the garnet structure inserts extra lithium ions such as in $Li_5La_3M_2O_{12}$ ($M = Ta, Nb, Bi$). La and M ions occupy eight-fold (LaO_8) and six-fold (MO_6) coordination sites, respectively, and Li occupies tetrahedral and distorted octahedral sites. The MO_6 octahedra are surrounded by six lithium ions in octahedral sites (LiO_6) and two lithium-ion vacancies, causing an increase in Li-ion conductivity [87]. Moreover, replacing La (III) with divalent ions and M with Zr (IV) in $Li_5La_3M_2O_{12}$ leads to greater lithium-ion concentrations such as in $Li_6Ala_2M_2O_{12}$ ($A = Mg, Ca, Sr, Ba; M = Nb, Ta$) and $Li_7La_3M_2O_{12}$ ($M = Zr, Sn$) [67]. Among these compounds, $Li_6BaLa_2Ta_2O_{12}$ exhibited a high ionic conductivity of $4 \cdot 10^{-5} \text{ S} \cdot \text{cm}^{-1}$ at $22 \text{ }^\circ\text{C}$ [87]. These high Li^+ ion conductivities resulted from the short $Li^+ - Li^+$ distances in the edge-sharing LiO_6 octahedra and the high concentration of Li^+ ions on the octahedral sites. Generally, increasing the lithium-ion concentration in the garnet structures increases the ionic conductivity [88]. Furthermore, by aliovalent doping, many electrolytes have been synthesized searching for higher lithium-ion conductivities [89,90]. On balance, garnet lithium electrolytes appear as interesting electrolytes, since high thermal stabilities up to $900 \text{ }^\circ\text{C}$ have been determined as well as chemical stability against lithium metal [91].

2. OBJECTIVES

2. OBJECTIVES

The general objective of this Doctoral Thesis is the development of electrochemical sensors for lithium monitoring in molten Pb-Li. To achieve this general objective, the following specific objectives are proposed:

1. Synthesis and characterization of lithium-ion conductive ceramics to be used as electrolytes in electrochemical lithium sensors.
2. Electrochemical characterization of the sintered ceramics, in order to determine their suitability to be used as electrolytes in electrochemical lithium sensors.
3. Design and construction of electrochemical lithium sensors for molten alloys.
4. Electrochemical characterization and evaluation of the lithium sensors for molten alloys.

3. MATERIALS AND METHODS

3. MATERIALS AND METHODS

3.1. Characterization techniques

During this work, solid-state electrolytes were synthesized as powders to be later shaped and sintered as pellets. To do so, the synthesized ceramic powders were pressed in a mold (Specac, Ref: PT. No. 3000) up to about 10 tones for 1 hour to attain a compact ceramic disc green body. These measured about 1.5 mm in thickness and 13 mm in diameter. To ensure the desired quality for its latter application in the construction of a lithium probe, these powders and pellets were rigorously characterized. During this process, if required, the experimental procedure for each ceramic could be modified to guarantee a satisfactory and reproducible synthesis and sintering. Characterization of the solid electrolytes was performed through different techniques:

- X-ray diffraction (XRD) was used to analyze the crystalline phases of the electrolytes. Since the studied electrolytes are crystals formed by regular arrays of atoms, these can scatter incident X-rays, primarily through interaction with the atoms' electrons. Upon X-ray incidence, a regular array of scatterers produces a regular array of spherical waves. In the majority of directions, these waves cancel each other out through destructive interference, however, these add constructively in a few specific directions, as determined by Bragg's law:

$$2d\sin\theta = n\lambda \quad [\text{Eq. 3.1}]$$

Where d is the spacing between diffracting planes, ϑ is the incident angle, n is an integer, and λ is the wavelength. The specific directions appear on the diffraction pattern and are called reflections. Consequently, X-ray diffraction patterns result from electromagnetic waves impacting a regular array of scatterers.

To perform the X-ray diffractions, an X'Pert PANalytical diffractometer with Cu $K\alpha$ radiation was used. Continuous scan mode was used to collect 2θ data from 10° to 80° with a 0.02 sampling pitch and a 2° min^{-1} scan rate. The X-ray tube voltage and current were set at 40 kV and 30 mA, respectively. The HighScore Plus software was used to compare the XRD spectra of the sample with compounds presenting similar diffraction angles. In some cases, the XRD data of interest was not included in this

database (ICDD's PDF-4+). In those scenarios, the resulting XRD signals were compared with diffractograms from bibliographic sources.

- A JEOL JSM-5310 scanning electron microscope (SEM) was used to study the microstructure. The instrument uses a focused beam of high-energy electrons (20 keV) to generate a variety of signals at the surface of solid specimens. The signals that derive from electron-sample interactions reveal information about the external morphology of the sample. An electrically conductive coating must be applied to insulate electrically the samples for study. For this reason, the sintered samples were gold-coated through a sputtering process with a Polaron SC7620 Sputter Coater.

The SEM instrument was coupled with an Oxford Inca Energy 200 EDS system which was set at a working distance of 20 mm. The interaction of an electron beam with a sample target produces a variety of emissions, including X-rays. An energy-dispersive (EDS) detector can be used to separate the characteristic X-rays of different elements into an energy spectrum. Then, the EDS instrument Oxford IncaMethod software is used to analyze the energy spectrum to determine the abundance of specific elements. Consequently, EDS analysis permitted to perform elemental microanalysis to obtain a semi-quantitative atomic ratio of the sample's elements and, to detect major impurities. Note that, the lightest element that could be detected by EDS was Beryllium.

- The lithium content of the electrolyte was measured with a Perkin Elmer Analyst 200 atomic absorption spectrometer employing a lithium hollow cathode lamp (Lumina™, PerkinElmer). It was important to monitor its lithium content because of possible loss caused by volatilization at high temperatures during the synthesis or sintering processes [92]. For this purpose, samples were digested in hot aqua regia for 2 hours. Then, the solutions were filtered and diluted with deionized water until the appropriate Li concentration was attained. Spiked samples were also prepared and analyzed to observe whether matrix effects were affecting the result. The acceptance criterion was based on pharmacopeia recovery standards $100.0 \pm 15\%$ [93], within this range, it was considered that no matrix effects were altering the sample's quantification.
- Finally, electrochemical impedance spectroscopy was used to determine the ionic conductivity of the synthesized electrolytes. To perform the experiences, the experimental set-up and operational EIS conditions are described in the following

section 3.2. EIS measurements were performed with a Potentiostat/Galvanostat Autolab PGSTAT302N coupled with an impedance module FRA32M. The quality of the obtained results was verified by comparing experimental data with bibliographic values.

3.2. Ionic conductivity measurements

The ionic conductivity of solid electrolytes is a subject of great interest since it is a key property for these types of compounds. Many efforts have been focused on developing fast ion-conducting electrolytes, especially in areas such as batteries, where lithium-ion conducting electrolytes are of major importance [67,77,94,95]. The measurement of this property is important for evaluating new and existing lithium-ion conducting solid electrolytes.

Ionic conductivity (σ , $S \cdot m^{-1}$) measures the material's capability to conduct an electric current through ionic transport. This property is the reciprocal of electrical resistivity (ρ , $\Omega \cdot m$), according to the equation:

$$\sigma = \frac{1}{\rho} \quad [\text{Eq. 3.2}]$$

Moreover, if the cross-section and physical composition of the examined material is considered uniform across the sample, and the electric field and current density are both parallel and constant everywhere, the electrical resistivity ρ can be calculated by:

$$\rho = R \frac{A}{l} \quad [\text{Eq. 3.3}]$$

Where R is the electrical resistance of the material in ohms (Ω), l is the length of the sample in meters (m), and A is the cross-sectional area of the sample in square meters (m^2).

Depending on the sample, its resistance can not be determined from a simple measurement of the voltage drop using a two-point probe measurement. In dielectric samples with high impedance, the interpretation of the resulting resistance can be complex [96]. This is due to parasitic resistances, mainly of the electrodes and of Schottky barrier contacts. The obtained resistances are generally too large and highly depend on the sample materials and geometries [97]. In practice, such measurements are therefore not recommended.

Nevertheless, different techniques are available to measure the ionic conductivity of solid-state electrolytes. Among them, the four-point probe method, or Electrochemical Impedance Spectroscopy (EIS) are the most commonly used for resistance measurements.

3.2.1. Four-point probe

This technique uses four separate electrodes, and the measurement can be performed with any arrangement of these four probes. However, in most situations, a collinear (in-line) and equidistant geometry is used [97] as is shown in Figure 3.1.

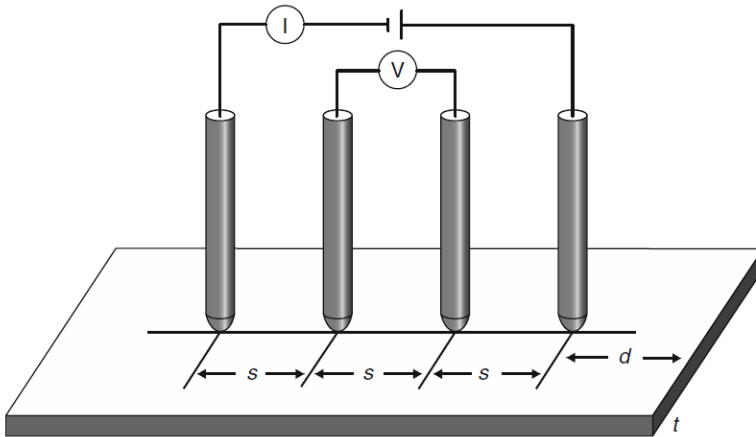


Figure 3.1. Scheme of the collinear four-point probe method.

In the collinear arrangement shown in Figure 3.1, the current passes through the two outer electrodes, and the inner two electrodes are then used to measure the voltage drop under negligible current. In this way, parasitic resistances like the probe resistance and the contact resistance (e.g., metal/semiconductor contacts) can be largely eliminated on the two voltage probes, as the passing current is negligible. For a semi-infinite sample and infinitesimal small-point contacts [96,98], the resistivity of the material generally can be described as a function of the voltage (V) and current (I) measured ([Eq. 3.4]):

$$\rho = 2\pi s \frac{V}{I} \quad [\text{Eq. 3.4}]$$

Most real samples, however, do not satisfy the precondition of semi-infinite dimensions. Therefore, a geometric correction factor ' F ' is necessary for most practical samples to obtain the true resistivity from the measured voltage and current readings, according to [Eq. 3.5]:

$$\rho = 2\pi sF \frac{V}{I} \quad [\text{Eq. 3.5}]$$

This geometric factor considers deviations from the semi-infinite geometry and is described in most cases as the product of three independent correction factors, as shown in [Eq. 3.6].

$$F = F_1 \cdot F_2 \cdot F_3 \quad [\text{Eq. 3.6}]$$

with F_1 correcting for the sample thickness, F_2 for the sample's dimensions, and F_3 for the probes' location on the sample. These correction factors have been reported for a variety of probe arrangements and sample geometries ([96,98–100]).

Although the four-point probe is a valid technique for the determination of ionic conductivities, the Electrochemical Impedance Spectroscopy technique is an alternative that exhibits a higher versatility. The technique permits to account for the resistance of the electrical connections, which, at high temperatures, was expected to be of the same order of magnitude as the electrolyte. Moreover, EIS application in lithium ion-conducting electrolytes has been extensively reported in the bibliography [101–108].

3.2.2. Electrochemical Impedance Spectroscopy

Electrochemical Impedance Spectroscopy (EIS) is used for the investigation of frequency-dependent electrical properties of materials and interfaces. It can be used to investigate the dynamics of bound or mobile charge, both in the bulk and in interfacial regions of any kind of solid material [109]. Electrochemical Impedance Spectroscopy is performed by applying an electrical stimulus (a known voltage or current) to the sample electrode to later observe its resulting response (current or voltage, respectively) at different frequencies. The most common and standard method is to apply a sinusoidal AC voltage of small amplitude (E_0 , 10–200 mV) in a single frequency (see [Eq. 3.7]) to measure the phase shift (ϕ) and current density amplitude (i_0) of the resulting current wave at that frequency (ω) ([Eq. 3.8]), as described:

$$E(t) = E_0 \sin(\omega t) \quad [\text{Eq. 3.7}]$$

$$i(t) = i_0 \sin(\omega t - \phi) \quad [\text{Eq. 3.8}]$$

where $E(t)$ and $i(t)$ are the complex AC voltage and density current, respectively. This measure is repeated at different frequencies, commonly starting at few MHz and decreases to values in the order of mHz [110]. From the obtained voltage $E(t)$ and current $i(t)$, the impedance $Z(\omega)$ can be obtained as a complex parameter through Euler's formula, as a result, the impedance value can be represented in polar and cartesian coordinates as described in [Eq. 3.9].

$$Z(\omega) = |Z|(\cos \varphi + j\sin \varphi) = Z_{re} + jZ_{im} \quad [\text{Eq. 3.9}]$$

Where $|Z|$ is the modulus of the impedance, j is the imaginary number $\sqrt{-1}$, and Z_{re} and Z_{im} are the real and imaginary components of the impedance. The most common forms of representation of the impedance $Z(\omega)$ are the Nyquist or the Bode plots (Figure 3.2).

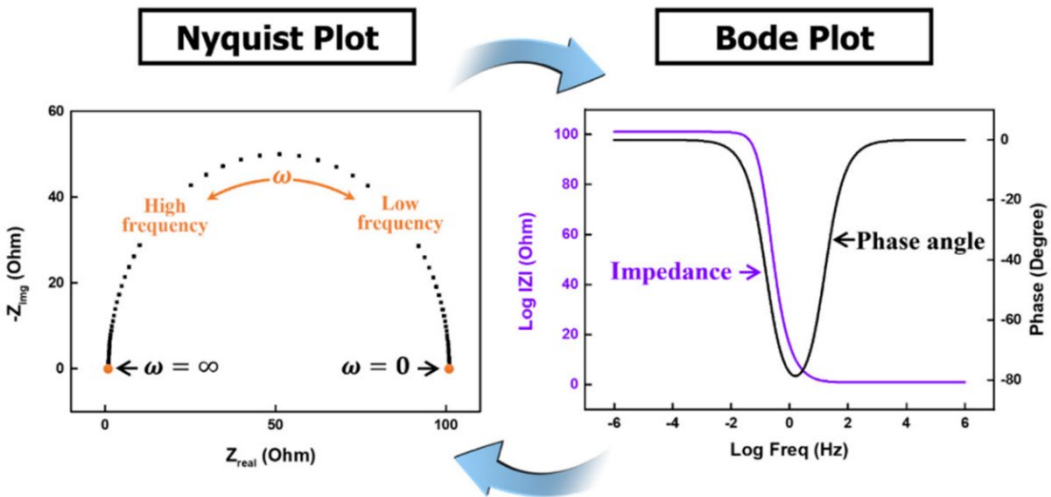


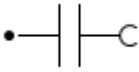


Figure 3.2. Nyquist and Bode plots [109].

In the Nyquist plot, the imaginary part $-Z_{im}$ is plotted versus the real part Z_{re} of the impedance, for different frequencies. For instance, in an RC circuit, the highest frequencies are situated on the left part of the plot, while as the frequency decreases Z_{re} tends to increase. Alternatively, the Bode plot represents both the modulus of the impedance $|Z|$ and the phase shift ϕ as a function of the frequency.

One of the different methods to interpret an impedance spectrum is by fitting an equivalent electric circuit consisting of discrete electrical elements. These elements are representative of the physicochemical processes occurring in the system. Most of the circuit components are common electrical elements such as resistors, capacitors, and inductors. In Table 3.1, the impedance of these elements is shown along with their representation.

Table 3.1. Common electrical elements

Component	Impedance	Representation
Resistor (R)	$Z(\omega) = R$	
Inductor (L)	$Z(\omega) = j\omega L$	
Capacitor (C)	$Z(\omega) = \frac{1}{j\omega C}$	

In the physicochemical interpretation, a conductive path that may account for the bulk conductivity of the material can be given by an ohmic resistor, while a space charge polarization region is generally associated with a capacitor. By variation of the frequency, processes with different dynamics can thus be separated. For instance, a simple impedance spectrum of a thin-film electrode/electrolyte system would present the following regions. At frequencies higher than 100 kHz, its impedance is mainly influenced by the resistance of the electrolyte (R_E). Then, with decreasing frequencies, the impedance increases due to the Helmholtz double-layer (charge transfer resistance R_{CT} , double-layer capacitance C_{DL}) and, at even lower frequencies, by the ionic diffusion in the film [97]. The equivalent circuit of such an electrode/electrolyte system without diffusion is shown in Figure 3.3A, its two characteristic plots (Nyquist and Bode plot) are also illustrated (Figure 3.3B and Figure 3.3C).

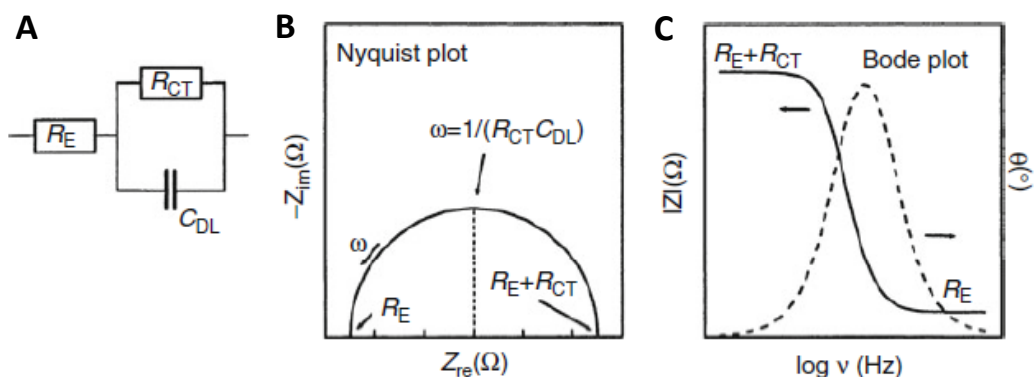


Figure 3.3. Equivalent circuit and the corresponding Nyquist and Bode impedance plots, for a typical electrode/electrolyte system without diffusion [97].

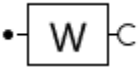
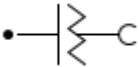
In this scenario, the equivalent circuit is composed by the electrolyte resistance R_E and a parallel RC circuit, formed by the charge transfer resistance R_{CT} plus the double layer capacitance C_{DL} . The impedance of this equivalent circuit is then given by [Eq. 3.10].

$$Z(\omega) = R_E + \frac{R_{CT}}{1 + j\omega C_{DL} R_{CT}} \quad [\text{Eq. 3.10}]$$

Then, the values of the components of the equivalent circuit are fitted to satisfactorily adjust to the experimental data. The fitting of the parameters is accomplished iteratively by an algorithm (e.g., Levenberg–Marquardt algorithm), using the nonlinear least-squares method [111–113].

Another equivalent circuit component is the Warburg diffusion element. This component is used to account for diffusion, and its impedance description is shown in Table 3.2, along with its graphical representation. In its description, W accounts for the Warburg coefficient ($\Omega \cdot s^{-1/2}$). Note that, at high frequencies, the Warburg impedance is small since diffusing species do not have to move very far. At low frequencies, the species have to diffuse farther, increasing the Warburg-impedance.

Table 3.2. Description of the Warburg and the CPE components

Component	Impedance	Representation
Warburg (W)	$Z(\omega) = \frac{W}{(j\omega)^{0.5}}$	
Constant-Phase Element (CPE)	$Z(\omega) = \frac{1}{Q(j\omega)^n}$	

One of the last equivalent circuit components that is commonly used is the constant-phase element (CPE). It is worth mentioning that in most situations capacitors deviate from ideal behavior, which can be a consequence of various phenomena, e.g., the roughness of the electrode surface, nonhomogeneous reaction rates occurring at the surface, etc. [97]. To account for this non-ideality, these can be replaced by constant-phase elements (CPE). This electrical element has intermediate characteristics between a capacitor and a resistor [114]. The impedance description of a CPE is given in Table 3.2, along with its graphical representation. In its description, Q is the CPE coefficient ($\Omega^{-1} \cdot s^n$) and n is a number between 0 and 1 ($n = 1$ for a pure capacitance). This component can also be used to account for different diffusion processes due to the flexibility given by the n value [109,114–116].

EIS has a great advantage in comparison with the four-point probe method because it permits the validation of its experimental data [117]. To perform such validation, the so-called Kronig-Kramer (KK) test has to be performed on the experimental data obtained [118–121]. During the KK test, the experimental data points are fitted using a specific model circuit. If the measured data can be represented with this circuit, then the data can be considered valid. The specific circuit used in the test is a series of RC circuits and is shown below (Figure 3.4).

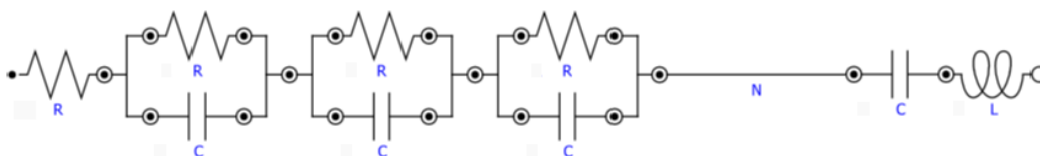


Figure 3.4. Circuit used for Kronig-Kramer test [122].

In the KK circuit, the number of RC circuits is equal to the number of data points. The result of the test is the sum of squares of the relative residuals for the real and the imaginary part, χ^2 . Large χ^2 values indicate that the data quality is low. Low values, on the other hand, usually indicate a good fit. As a rule of thumb, values lower than 10^{-6} usually mean an excellent fit, reasonable between 10^{-5} and 10^{-6} , marginal between 10^{-4} and 10^{-5} , and bad for even higher values [122]. Moreover, residuals should be small and randomly distributed around zero. To satisfy the Kronig-Kramers test, the complex function must satisfy four criteria [118–120]:

1. Linearity: a system is linear when its response to a sum of individual input signals is equal to the sum of the individual responses. In addition, linear systems responses are independent of the amplitude.
2. Causality: the response of a system must be entirely determined by the applied perturbation, that is, the output depends only on the present and past input values. This also means that the system does not generate noise independently of the applied signal for $t \geq 0$.
3. Stability: the stability of a system is determined by its response to inputs. A stable system remains stable until excited by an external source, and it should return to its original state once the perturbation is removed.

4. Finiteness: It means that the real and imaginary components of the impedance must be finite-valued over the entire frequency range $0 < \omega < \infty$.

If the investigated system changes with time due to e.g. aging, temperature change, non-equilibrium initial state, etc., the test fails. Failure of the KK test usually means that no equivalent circuit would fit adequately.

4. RESULTS AND DISCUSSION

4. RESULTS AND DISCUSSION

In this thesis, potentiometric lithium sensors based on lithium-ion conducting solid electrolytes have been developed. The obtained results during the development and testing of these analytical tools can be structured into two parts.

In the first part, suitable solid electrolytes were selected. These electrolytes had to fulfill several criteria to ensure the adequate performance of the Li sensors: thermal and chemical stabilities and high Li-ion conductivities. Furthermore, the selected electrolytes were synthesized as powders and were sintered as discs. The obtained powders and discs were thoroughly characterized to guarantee the quality of the final product. Finally, their ionic conductivity, which is one of the key properties that demonstrate their operability as lithium-ion conducting electrolytes, was determined.

The second part of this work describes the construction of the lithium sensors, the experimental set-up built for their evaluation, and the results obtained from the tests performed with these analytical tools. In the former case, an adequate binder and heat treatment had to be determined to join the sintered electrolytes' discs to an alumina tube to form the body of the sensor. Then, an adequate experimental set-up had to be built to perform the potentiometric measurements at high temperatures (400 – 600 °C). In the latter case, potentiometric measurement results performed in different Pb-Li alloys are presented and discussed. These were planned to characterize the constructed sensors, evaluating the sensors' precision, accuracy, and linear range. Furthermore, during these tests, other sensor characteristics were studied such as their stability or the effect of different reference systems.

4.1. Selection of the Solid Electrolytes Candidates

The adequate selection of the solid electrolyte is of major importance for the development of the lithium sensor. To determine the best solid electrolyte candidates, extensive bibliographic research of lithium-ion conducting electrolytes was performed. Fortunately, solid-state electrolytes have recently gained great attention as potential substitutes for liquid electrolytes in batteries, as they offer enhanced stability and safety. Since the ionic conductivity of solid-state electrolytes is a key parameter that determines electrochemical performance, great efforts have been put into developing new solid-state electrolytes with enhanced ionic conductivity.

Considerable research has focused on several crystal structures including LISICON-like (lithium superionic conductor), garnet-type, perovskites-type, and NASICON-like (sodium superionic conductor). Substitution and partial doping with optimal-sized ions have been extensively proven to be effective in the enhancement of conductivity in these crystal families [67]. Substitution and doping increase the lattice volume, which can be correlated with larger bottleneck sizes, reduced activation energies, and greater ionic conductivities by several orders of magnitude [83]. It is worth mentioning that electrolyte candidates, shown in Table 4.1, were selected among the latest developed electrolytes.

Table 4.1. Electrolyte candidates for the development of lithium sensors.

Electrolyte	References	Electrolyte	References
$\text{Li}_{10}\text{GeP}_2\text{S}_{12}$ (LGPS)	[67,123]	$\text{LiZr}_2(\text{PO}_4)_3$	[124]
$\text{Li}_{3.25}\text{Ge}_{0.25}\text{P}_{0.75}\text{S}_4$	[123,125]	$\text{LiHf}_2(\text{PO}_4)_3$	[67]
$\text{LiTi}_2(\text{PO}_4)_3$	[126]	$\text{LiTaAl}(\text{PO}_4)_3$	[127]
$\text{Li}_{1.3}\text{Al}_{0.3}\text{Ti}_{1.7}(\text{PO}_4)_3$	[67]	$\text{Li}_3\text{Sc}_{1.6}\text{Al}_{0.4}(\text{PO}_4)_3$	[128]
$\text{Na}_3\text{Zr}_2\text{Si}_2\text{PO}_{12}$	[126]	$\text{LiAlSi}_2\text{O}_6$	[129]
$\text{Li}_{0.34}\text{La}_{0.51}\text{TiO}_{2.94}$	[67,79]	$\text{LiAlSi}_4\text{O}_{10}$	[129]
$\text{LiO}_{2.11}\text{Al}_2\text{O}_3$	[128]	LiV_3O_8	[130]
Li_3N	[128]	$\text{Li}_{10.42}\text{Ge}_{1.5}\text{P}_{1.5}^{\text{e}}\text{I}_{0.08}\text{O}_{11.92}$	[95]
Li_8PbO_6	[131]	$\text{Li}_{10.42}\text{Si}_{1.5}\text{P}_{1.5}^{\text{e}}\text{I}_{0.08}\text{O}_{11.92}$	[95]
Li_8ZrO_6	[132]	$\text{Na}_3\text{P}_{0.62}\text{As}_{0.38}\text{S}_4$	[94]
Li_2MCl_4 (M= Mg, Mn, Ti, Cd, Cr, Co, Fe, Zn)	[128]	$\text{Li}_6\text{La}_3\text{Ta}_{195}\text{Y}_{0.5}\text{O}_{12}$	[133]
$\text{Li}_{3.25}\text{Ge}_{0.25}\text{P}_{0.75}\text{S}_4$	[67,79,125]	$\text{Li}_6\text{BaLa}_2\text{Ta}_2\text{O}_{12}$	[86,134]
$\text{Li}_{10}\text{Ge}_{0.95}\text{Si}_{0.05}\text{P}_2\text{S}_{12}$	[67,79,123]	LiYO_2	[45]
$\text{Li}_{10}\text{SnP}_2\text{S}_{12}$	[67,123]	$\text{Li}_{3/8}\text{Sr}_{7/16}\text{Ta}_{3/8}\text{Zr}_{1/4}\text{O}_3$	[135]
$\text{Li}_{11}\text{Si}_2\text{PS}_{12}$	[67,123]	$\text{Na}_4\text{Zr}_2\text{Si}_3\text{O}_{12}$	[126]
$\text{Li}_{3.4}\text{Si}_{0.4}\text{P}_{0.6}\text{S}_4$	[67,123]	$\text{Li}_{6.55}\text{La}_3\text{Zr}_2^{\text{e}}\text{a}_{0.15}\text{O}_{12}$	[67,86,136]
$\text{Li}_{14}\text{ZnGe}_4\text{O}_{16}$	[79]	$\text{Li}_{3.4}\text{Si}_{0.4}\text{V}_{0.6}\text{O}_4$	[128,137–139]
$\text{Li}_{3.6}\text{Ge}_{0.6}\text{V}_{0.4}\text{O}_4$	[140]	$\text{Li}_{3.6}\text{Si}_{0.6}\text{P}_{0.4}\text{O}_4$	[141]
$\text{Li}_6\text{PS}_5\text{Cl}$	[142,143]	$\text{Li}_{1.1}\text{Zr}_{1.9}\text{La}_{0.1}(\text{PO}_4)_3$	[144]
$\text{Li}_6\text{PS}_5\text{I}$	[143]	$\text{Li}_5\text{La}_3\text{Ta}_2\text{O}_{12}$	[79,86,145]
$\text{Li}_6\text{PS}_5\text{Br}$	[143]	$\text{Li}_{3.833}\text{Sn}_{0.833}\text{As}_{0.166}\text{S}_4$	[67,123]
$\text{LiGe}_2(\text{PO}_4)_3$	[67,79]		

From the different candidates a selection process was followed to determine the suitable electrolytes for the construction of potentiometric lithium sensors:

- In the first step of the process, the electrolytes' thermal stability and reactivity towards molten lithium were reviewed. The sensor will be submerged in Li alloys at the expected operational temperatures of TBM (400 °C – 600 °C). Thus, the integrity of the electrolyte must not get compromised by the operating temperature or the lithium reactivity of the tested alloys. The electrolytes (Table 4.1) that were not thermally stable up to 600 °C or did not exhibit low reactivity towards lithium were rejected since it was considered indispensable to demonstrate such properties for the correct functioning of the sensor. In Table 4.2., these firstly discarded electrolytes are shown in the first column with a red background.
- From the remaining electrolytes, those that did not exhibit low reactivity towards moisture and air were rejected. Lithium ceramics tend to react with water vapor and with carbon dioxide from the air [146,147]. Note that, the sintered electrolytes will be stored and used inside a glovebox with a high purity Ar atmosphere. Despite that, the electrolytes will occasionally be exposed to air. Therefore, highly unstable electrolytes to moisture and air should not be used. In the second column in Table 4.2, orange background, the electrolytes that did not match these criteria were downselected.
- The last step of the selection process considered the lithium-ion conductivity of the remaining electrolytes. A minimum ion conductivity is necessary to ensure that the ceramic will be able to operate as a lithium-ion conducting electrolyte. The electrolytes that did not exhibit lithium-ion conductivities higher than $10^{-5} \text{ S}\cdot\text{cm}^{-1}$ at 25 °C were discarded [148], and are shown on a yellow background in the third column of Table 4.2.

Finally, the electrolytes which fulfilled all the requirements were selected as candidates for the construction of potentiometric lithium sensors. These electrolytes are shown in a green background in the last column of Table 4.2.

Table 4.2. Representation of the selection process for the lithium-ion conducting solid electrolytes candidates.

Lithium Reactive and Thermally Unstable Electrolytes	Highly Unstable Electrolytes Towards Water or Air	Low Li-Ion Conducting Electrolytes	Selected Electrolytes
$\text{Li}_{10}\text{GeP}_2\text{S}_{12}$ (LGPS)	Li_2MCl_4 (M= Mg, Mn, Ti, Cd, Cr, Co, Fe, Zn)	$\text{Li}_{3.833}\text{Sn}_{0.833}\text{As}_{0.166}\text{S}_4$	$\text{Li}_6\text{La}_3\text{Ta}_{1.95}\text{Y}_{0.5}\text{O}_{12}$
$\text{Li}_{3.25}\text{Ge}_{0.25}\text{P}_{0.75}\text{S}_4$	$\text{Li}_{3.25}\text{Ge}_{0.25}\text{P}_{0.75}\text{S}_4$	$\text{LiZr}_2(\text{PO}_4)_3$	$\text{Li}_6\text{BaLa}_2\text{Ta}_2\text{O}_{12}$
$\text{LiTi}_2(\text{PO}_4)_3$	$\text{Li}_{10}\text{Ge}_{0.95}\text{Si}_{0.05}\text{P}_2\text{S}_{12}$	$\text{LiHf}_2(\text{PO}_4)_3$	LiYO_2
$\text{Li}_{1.3}\text{Al}_{0.3}\text{Ti}_{1.7}(\text{PO}_4)_3$	$\text{Li}_{10}\text{SnP}_2\text{S}_{12}$	$\text{LiTaAl}(\text{PO}_4)_3$	$\text{Li}_{3/8}\text{Sr}_{7/16}\text{Ta}_{3/8}\text{Zr}_{1/4}\text{O}_3$
$\text{Na}_3\text{Zr}_2\text{Si}_2\text{PO}_{12}$	$\text{Li}_{11}\text{Si}_2\text{PS}_{12}$	$\text{Li}_3\text{Sc}_{1.6}\text{Al}_{0.4}(\text{PO}_4)_3$	$\text{Na}_4\text{Zr}_2\text{Si}_3\text{O}_{12}$
$\text{Li}_{0.34}\text{La}_{0.51}\text{TiO}_{2.94}$	$\text{Li}_{3.4}\text{Si}_{0.4}\text{P}_{0.6}\text{S}_4$	$\text{LiAlSi}_2\text{O}_6$	$\text{Li}_{6.55}\text{La}_3\text{Zr}_2\text{Ta}_{0.15}\text{O}_{12}$
$\text{LiO}_{2.11}\text{Al}_2\text{O}_3$	$\text{Li}_{14}\text{ZnGe}_4\text{O}_{16}$	$\text{LiAlSi}_4\text{O}_{10}$	$\text{Li}_{3.4}\text{Si}_{0.94}\text{V}_{0.6}\text{O}_4$
Li_3N	$\text{Li}_{3.6}\text{Ge}_{0.6}\text{V}_{0.4}\text{O}_4$	LiV_3O_8	$\text{Li}_{1.1}\text{Zr}_{1.9}\text{La}_{0.1}(\text{PO}_4)_3$
Li_8PbO_6	$\text{Li}_6\text{PS}_5\text{Cl}$	$\text{Li}_{10.42}\text{Ge}_{1.5}\text{P}_{1.5}\text{I}_{0.08}\text{O}_{11.92}$	
Li_8ZrO_6	$\text{Li}_6\text{PS}_5\text{I}$	$\text{Li}_{10.42}\text{Si}_{1.5}\text{P}_{1.5}\text{I}_{0.08}\text{O}_{11.92}$	
	$\text{Li}_6\text{PS}_5\text{Br}$	$\text{Na}_3\text{P}_{0.62}\text{As}_{0.38}\text{S}_4$	
	$\text{LiGe}_2(\text{PO}_4)_3$	$\text{Li}_{3.6}\text{Si}_{0.6}\text{P}_{0.4}\text{O}_4$	
	$\text{Li}_5\text{La}_3\text{Ta}_2\text{O}_{12}$		

A total of 8 electrolytes were selected for the development of lithium probes: $\text{Li}_6\text{La}_3\text{Ta}_{1.95}\text{Y}_{0.5}\text{O}_{12}$, $\text{Li}_6\text{BaLa}_2\text{Ta}_2\text{O}_{12}$, LiYO_2 , $\text{Li}_{3/8}\text{Sr}_{7/16}\text{Ta}_{3/8}\text{Zr}_{1/4}\text{O}_3$, $\text{Na}_4\text{Zr}_2\text{Si}_3\text{O}_{12}$, $\text{Li}_{6.55}\text{La}_3\text{Zr}_2\text{Ga}_{0.15}\text{O}_{12}$, $\text{Li}_{3.4}\text{Si}_{0.4}\text{V}_{0.6}\text{O}_4$, $\text{Li}_{1.1}\text{Zr}_{1.9}\text{La}_{0.1}(\text{PO}_4)_3$. Note that these electrolytes are not commercially available, and thus had to be synthesized and sintered from the procedures described in the bibliography.

To reduce the number of selected electrolytes, those that presented more demanding synthesis and/or sintering procedures were discarded. $\text{Li}_{3/8}\text{Sr}_{7/16}\text{Ta}_{3/8}\text{Zr}_{1/4}\text{O}_3$ and $\text{Li}_{1.1}\text{Zr}_{1.9}\text{La}_{0.1}(\text{PO}_4)_3$ electrolytes required the highest sintering temperatures of 1200-1400 °C [135,144]. $\text{Li}_{6.55}\text{La}_3\text{Zr}_2\text{Ga}_{0.15}\text{O}_{12}$ electrolyte was synthesized by a citric acid-nitrate route and required a dry O_2 atmosphere during its synthesis and sintering [136]. Lastly, $\text{Li}_{3.4}\text{Si}_{0.4}\text{V}_{0.6}\text{O}_4$ electrolyte required two calcinations steps to synthesize the electrolyte [137]. Moreover, $\text{Na}_4\text{Zr}_2\text{Si}_3\text{O}_{12}$ was discarded since was the one presenting the smallest conductivity among them. Finally, from the final candidates, $\text{Li}_6\text{La}_3\text{Ta}_{1.5}\text{Y}_{0.5}\text{O}_{12}$ and $\text{Li}_6\text{BaLa}_2\text{Ta}_2\text{O}_{12}$ were selected to be used as electrolytes in the construction of the Li sensors.

Once selected, $\text{Li}_6\text{BaLa}_2\text{Ta}_2\text{O}_{12}$ and $\text{Li}_6\text{La}_3\text{Ta}_{1.5}\text{Y}_{0.5}\text{O}_{12}$ (coded as LBLTO and LLTYO) had to be synthesized as powders and had to be sintered as pellets. Note that the quality of the final product depends on the thermal conditions. Consequently, their synthesis and sintering thermal conditions would be readjusted as a function of the obtained results.

4.2. Synthesis and Sintering of the Selected Solid Electrolytes

4.2.1. $\text{Li}_6\text{BaLa}_2\text{Ta}_2\text{O}_{12}$

Although the synthesis and sintering conditions of the electrolyte are reported in the bibliography, these had to be tested and evaluated to achieve optimum synthesis and sintering. In sections 4.2.1.1 and 4.2.1.2, the details of both procedures, as well as the electrolytes characterization, are presented and discussed. The ionic conductivity measurement of the LBLTO electrolyte is discussed in section 4.2.1.3.

4.2.1.1. Synthesis and Characterization

$\text{Li}_6\text{BaLa}_2\text{Ta}_2\text{O}_{12}$ (LBLTO) ceramic powder was synthesized by a solid-state reaction according to the method described by V. Thangadurai, et al. [149]. Stoichiometric amounts of each reagent were weighted in order to obtain the desired composition. To synthesize 30 g of the ceramic, 9.67 g of La_2O_3 (Acros Organics, 99.9%), 7.76 g of BaNO_3 (Alfa Aesar, +99%), 13.12 g of Ta_2O_5 (Acros Organics, 99.99%) and 8.21 g of $\text{LiOH}\cdot\text{H}_2\text{O}$ (Scharlau, 99.5%) were weighted. $\text{LiOH}\cdot\text{H}_2\text{O}$ was added in 10 wt.% excess to compensate for lithium losses at elevated temperatures. The reagents were mixed and ground overnight in a rotary ball mill using zirconia balls and 2-propanol. The mixture was dried, and the resulting precursor powder was placed in an alumina crucible and heated at 700 °C for 6h in a J.P. SELECTA muffle-type furnace. The resulting powder was finely ground with an agate mortar.

To characterize the synthesized powder and ensure its quality, the structural phases of the solid electrolyte were determined by XRD analysis. In Figure 4.1A the XRD pattern of the sintered powder is presented along with the pattern of the $\text{Li}_6\text{BaLa}_2\text{Ta}_2\text{O}_{12}$ ceramic obtained from the bibliography [87,149] (Figure 4.1B).

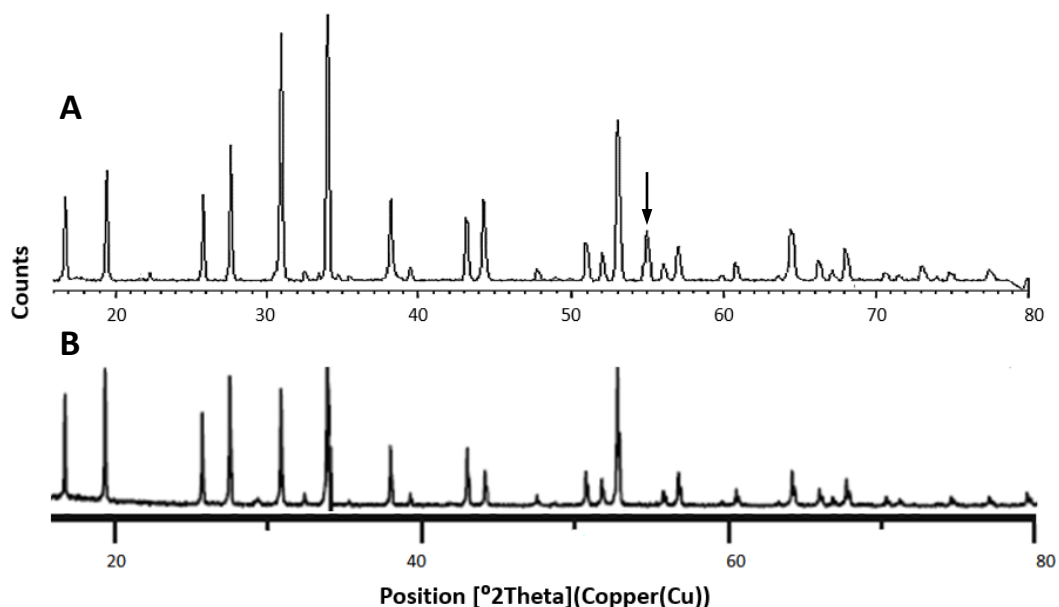


Figure 4.1. XRD patterns corresponding to A) synthesized LBLTO powder at 700°C for 6h and B) bibliographic data [87,149]. The black arrow designates an anomalous signal.

The powder showed a single phase of the garnet-type which was in good agreement with bibliography data. As shown in Figure 4.1, the main signal peaks between both diffractograms appear in the same diffraction angles. However, an anomalous peak was

detected between the 54° and 56° angles (indicated with an arrow in Figure 4.1A). A probable explanation is the formation of $\text{Li}_2\text{Ba}_3\text{Ta}_2\text{O}_9$ which presents a strong signal near this position. The XRD pattern of $\text{Li}_2\text{Ba}_3\text{Ta}_2\text{O}_9$ compared to the one obtained from the LBLTO powder is shown in Figure 4.2, which was obtained from the database of the XRD software.

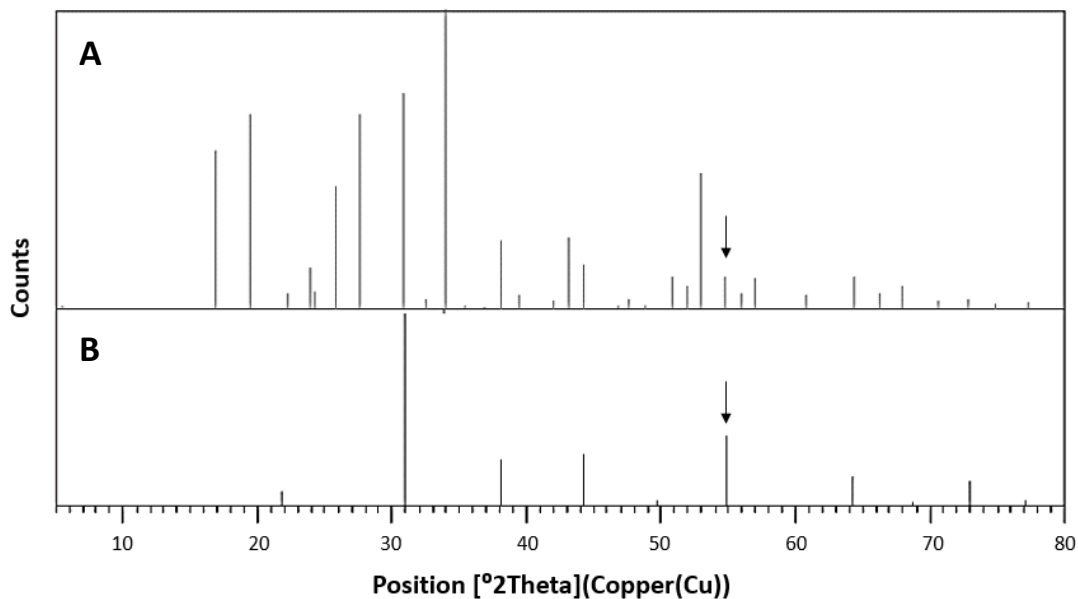


Figure 4.2. XRD peak pattern from A) $\text{Li}_6\text{BaLa}_2\text{Ta}_2\text{O}_{12}$ synthesized ceramic at 700 °C for 6h and B) $\text{Li}_2\text{Ba}_3\text{Ta}_2\text{O}_9$ ceramic.

From Figure 4.2, it was observed that $\text{Li}_2\text{Ba}_3\text{Ta}_2\text{O}_9$ could be producing this signal, since it can be observed that it matched the anomalous signal peak at 55° approximately (indicated with an arrow in the figure). Furthermore, the other signal peaks at 23°, 31°, 38°, 44°, 50°, 64°, 73°, and 84° approximately, were found in similar positions as the ones from the LBLTO electrolyte. After comparing both XRD patterns, it was concluded that the formation of the $\text{Li}_2\text{Ba}_3\text{Ta}_2\text{O}_9$ compound could be occurring. Nevertheless, since it was a minor impurity, before modifying the synthesis, the XRD spectra of the sintered ceramic should be determined.

Once the crystallographic structure of the ceramic powder was analyzed, the size of the powder's particles was analyzed with a SEM microscope. The particle size is important since it has to be small enough to obtain the necessary free surface energy to achieve proper sintering. The larger the particle size, the higher the temperature required to sinter the ceramic powder will be [150]. In Figure 4.3, two micrographs of the synthesized powder are

shown, Figure 4.3A was taken at 500x magnification, and Figure 4.3B was taken at 3500x magnification.

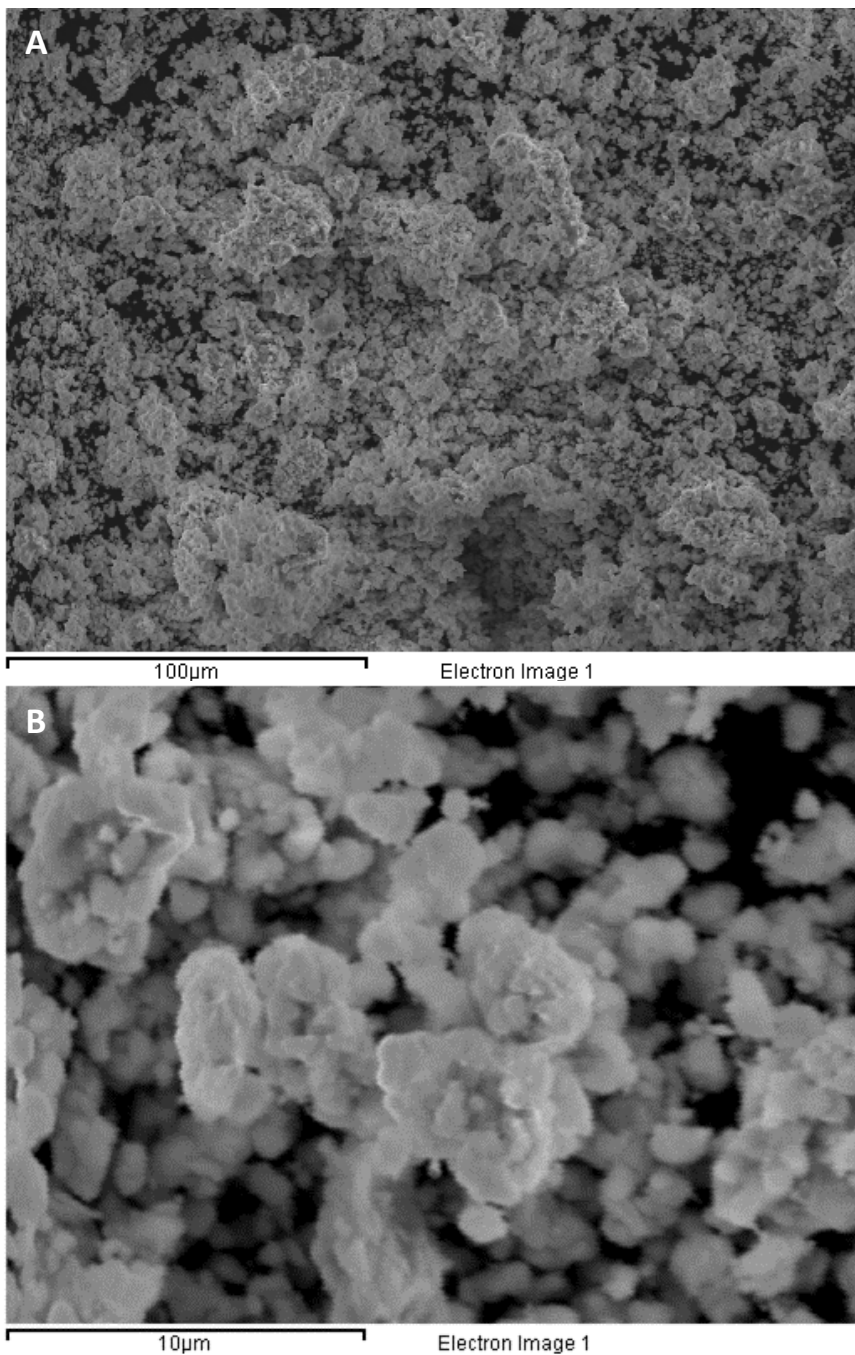


Figure 4.3. SEM micrographs of the synthesized LBLTO powder at 700 °C for 6h at different magnifications: A) 500x and B) 3500x.

SEM micrographs show a homogeneous particle size distribution between 1 to 5 μm approximately. In Figure 4.3, particle agglomeration in the powder can also be observed. EDS analysis was also performed to check for possible impurities and check the presence of the elements forming the ceramic powder (Figure 4.4).

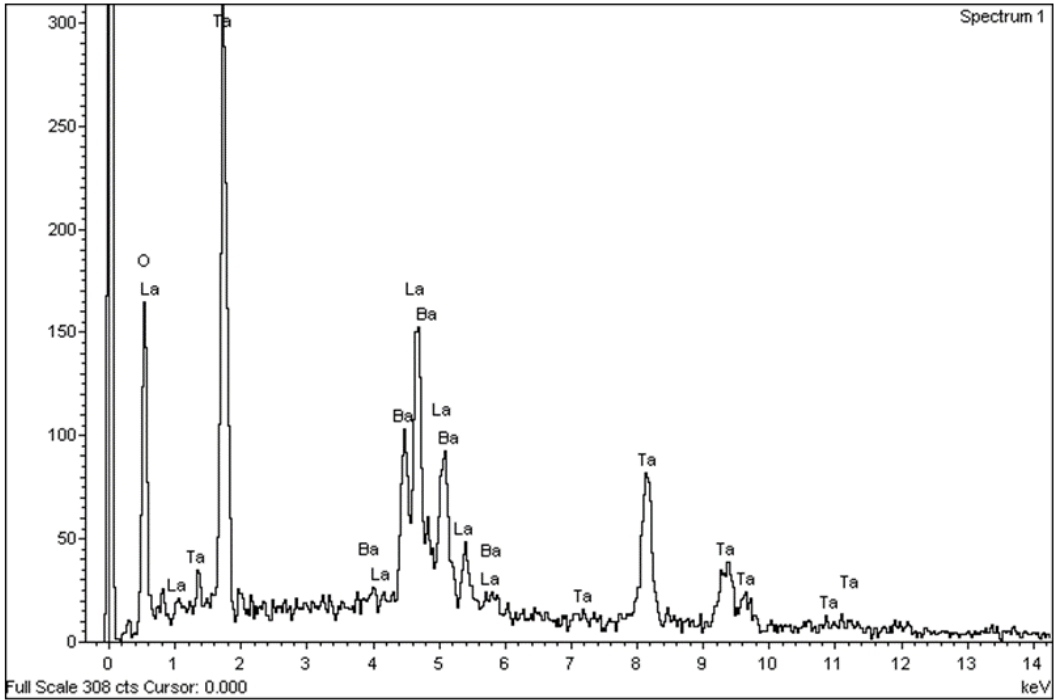


Figure 4.4. EDS spectrum of the synthesized LBLTO ceramic powder at 700 °C for 6h.

Figure 4.4 shows that the synthesized powder did not present noticeable impurities in its formulation (in concentrations above 1% w/w). It can be observed from the spectrum that only La, Ba, Ta, and O were detected. Furthermore, the results were processed with the Oxford INCA software to determine experimental atomic relationships. The experimental and theoretical atomic relationships for each of the metallic elements identified are shown in Table 4.3. Oxygen element was not considered because its low weight tends to cause its over-quantification.

Table 4.3. Experimental and theoretical atomic relationship for each identified metallic element forming the LBLTO electrolyte.

Element	Experimental atomic relationship	Theoretical atomic relationship
Ba	1.0	1.0
La	2.0	2.0
Ta	2.0	2.0

When comparing these values with the theoretical formulation of the ceramic $\text{Li}_6\text{BaLa}_2\text{Ta}_2\text{O}_{12}$, it was observed that all the atomic relationships were equal. Therefore, it was concluded that the synthesized powder presented a correct stoichiometry.

Lithium content in the ceramic powder was quantified using atomic absorption spectrophotometry analysis. A value of 40.4 mg Li/g of ceramic powder was obtained, which represented 4.04% of the total weight. Since the theoretical value is 41.2 mg Li/g (4.12% w/w), it was considered that such a small lithium loss could not significantly affect the electrolyte. Also, a recovery of 96.0% was obtained from a spiked sample, concluding that no matrix effects were altering the quantification.

4.2.1.2. Sintering and Characterization

The synthesized powder was sintered at 900 °C for 24 h in an air atmosphere, as described by V. Thangadurai et al. [149]. Before the thermal process, pellets were covered with a powder of the same mother composition to reduce possible lithium loss due to volatilization [151]. The obtained XRD pattern of the ceramic pellet is shown in Figure 4.5 along with the XRD pattern of the $\text{Li}_6\text{BaLa}_2\text{Ta}_2\text{O}_{12}$ electrolyte obtained from the bibliography [87,149] (Figure 4.5B).

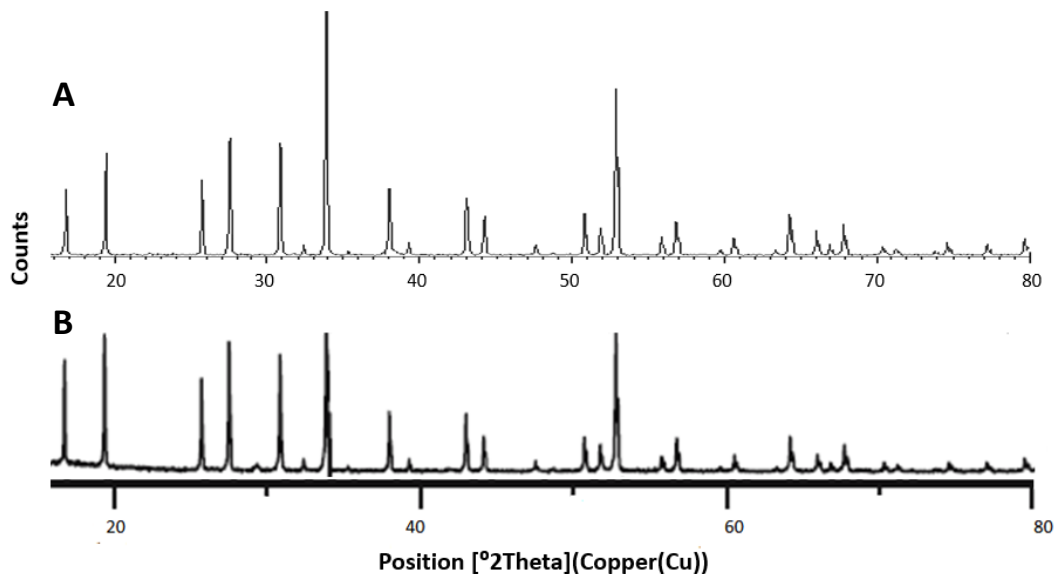


Figure 4.5. XRD patterns corresponding to A) sintered LBLTO pellet at 900 °C for 24h and B) bibliographic data [87,149].

As can be observed in Figure 4.5, the pellet showed a single phase of the garnet-type in good agreement with bibliographic data. It is worth mentioning that the anomalous signal found near the 55° angle originated by the $\text{Li}_2\text{Ba}_3\text{Ta}_2\text{O}_9$ intermediate product (Figure 4.1) had disappeared. This phenomenon was attributed to a lithium re-incorporation by covering the pellet with the electrolyte's powder during the sintering process. Since the XRD analysis from the sintered pellet was satisfactory, the synthesis conditions of the ceramic were not modified.

SEM was used to analyze the surface microstructure of the obtained pellet. The resulting images are shown in Figure 4.6. In the figure, two micrographs are presented, Figure 4.6A was taken at 100x magnification and Figure 4.6B was taken at 2000x magnification.

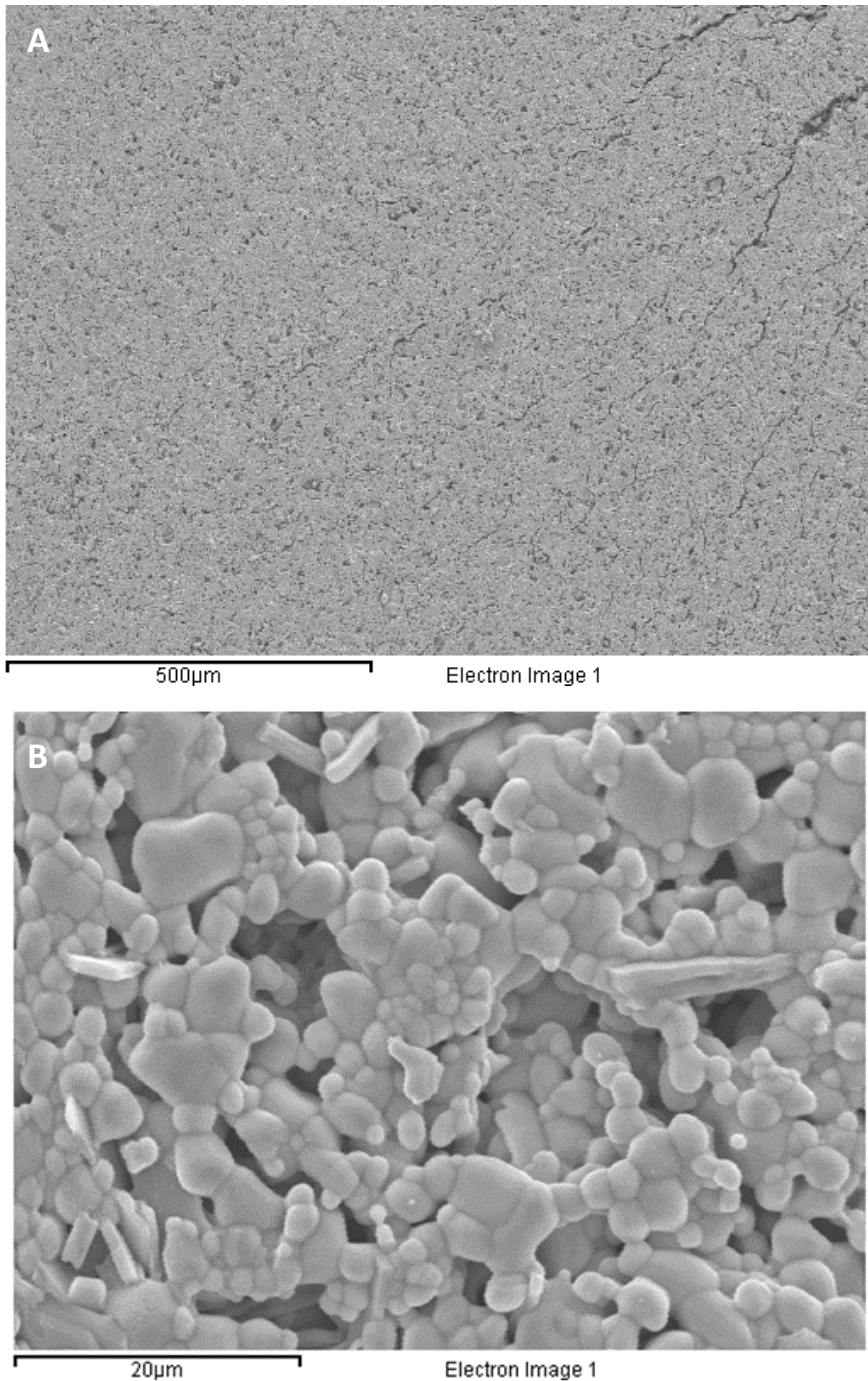


Figure 4.6. SEM micrographs of the LBLTO sintered pellet at 900°C for 24h at different magnifications: A) 100x and B) 2000x.

In the SEM micrograph shown in Figure 4.6A it is observed a compact and homogeneous surface with some cracks on the surface. With higher magnification, it can be observed that the sintering of the ceramic was promising since appropriate densification was attained. A

homogeneous grain distribution was observed with a grain size between 1 to 8 μm approximatively.

A significant porosity was obtained on the surface of the pellet. This parameter was further studied since it is a key parameter that has to be evaluated. First, because a high porosity can lead to permeation through the solid electrolyte, and second because it is strongly related to the ionic conductivity of the solid electrolyte. Pores in the electrolyte's structure act as barriers for ions moving through the ceramic [156].

The porosity was evaluated with the open-source image processing software ImageJ. Pores were identified as the darkest zones on the micrograph. To establish the threshold value between solid and pore, Yen's algorithm was used (included in the software). From the different micrographs taken, a porosity of $15.3\% \pm 3.3\%$ was calculated. An EDS analysis was also performed to check the presence of the elements conforming the ceramic pellet (Figure 4.7).

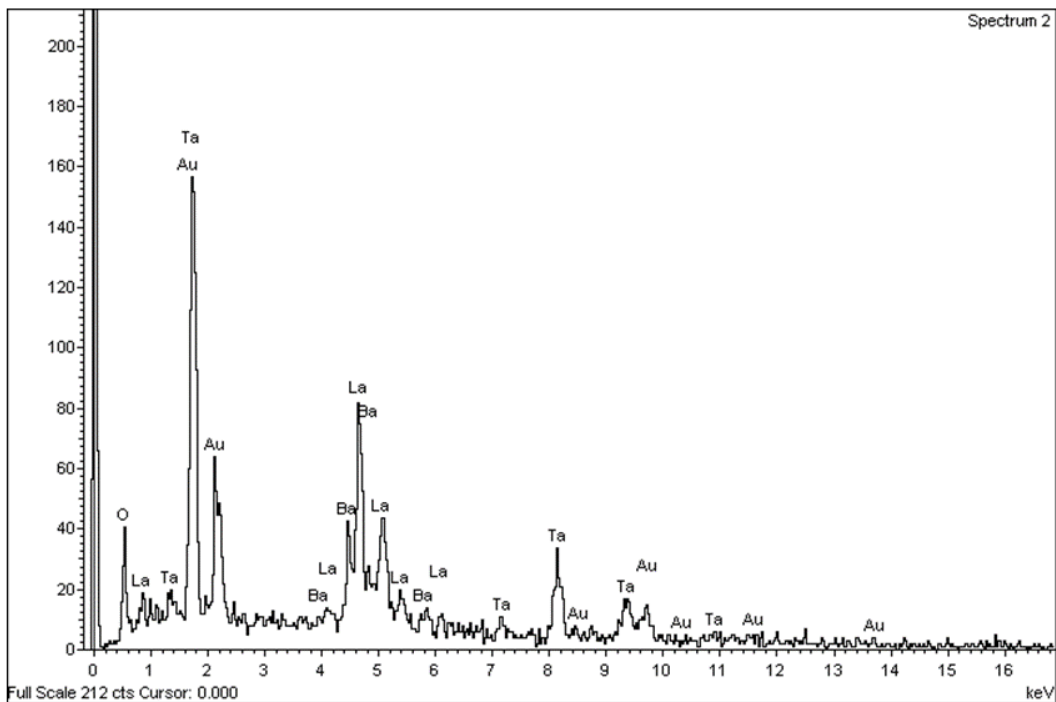


Figure 4.7. EDS spectrum of the LBLTO pellet.

No impurities were found in the EDS analysis, as shown in Figure 4.7. As it can be observed from the spectrum only La, Ba, Ta, and O were detected. The results were processed with the Oxford INCA software to determine experimental atomic relationships. The

experimental and theoretical atomic relationships for each of the metallic elements identified are shown in Table 4.4.

Table 4.4. Experimental and theoretical atomic relationship for each identified metallic element forming the LBLTO electrolyte.

Element	Experimental atomic relationship	Theoretical atomic relationship
Ba	1.0	1.0
La	1.9	2.0
Ta	1.9	2.0

When comparing these values with the theoretical formulation of the ceramic $\text{Li}_6\text{BaLa}_2\text{Ta}_2\text{O}_{12}$, it was observed that the atomic relationship values for each element were very close. Therefore, concluding that the sintered ceramic presented a correct stoichiometry.

The lithium content in the pellet was quantified by AAS-Flame analysis. A resulting value of 38.5 mg Li/g of ceramic was obtained which represents 3.85% of the total weight, being the theoretical value of 41.2 mg Li/g (4.12% w/w). A spiked sample was also performed yielding a recovery of 99.1%, thus no matrix effects were influencing the quantification. The electrolyte's lithium loss was less than 10% (6.55%), which could be considered hardly significant. In addition, no anomalous crystallographic phases were observed on its XRD spectrum (Figure 4.5).

Despite the promising results of the sintering procedure described by V.Thangadurai et al. [149], the electrolyte's superficial porosity had to be diminished. Consequently, the sintering conditions were optimized.

Optimization of the Sintering Conditions

To minimize the porosity of the electrolyte, the sintering conditions were modified by increasing two variables of the process: time and temperature. The first variable chosen to be modified was time, which was increased from 24 hours to 48 hours, thus the first tested sintering program was 900 °C for 48 hours. The surface microstructure and composition of the sintered pellet were characterized with SEM, XRD, and AAS-Flame analysis.

The surface microstructure of the pellet is shown in Figure 4.8A and Figure 4.8B. The figure shows two micrographs with different magnifications: 100x and 2000x. EDS analysis was also performed to determine whether impurities were present in the sample (Figure 4.9).

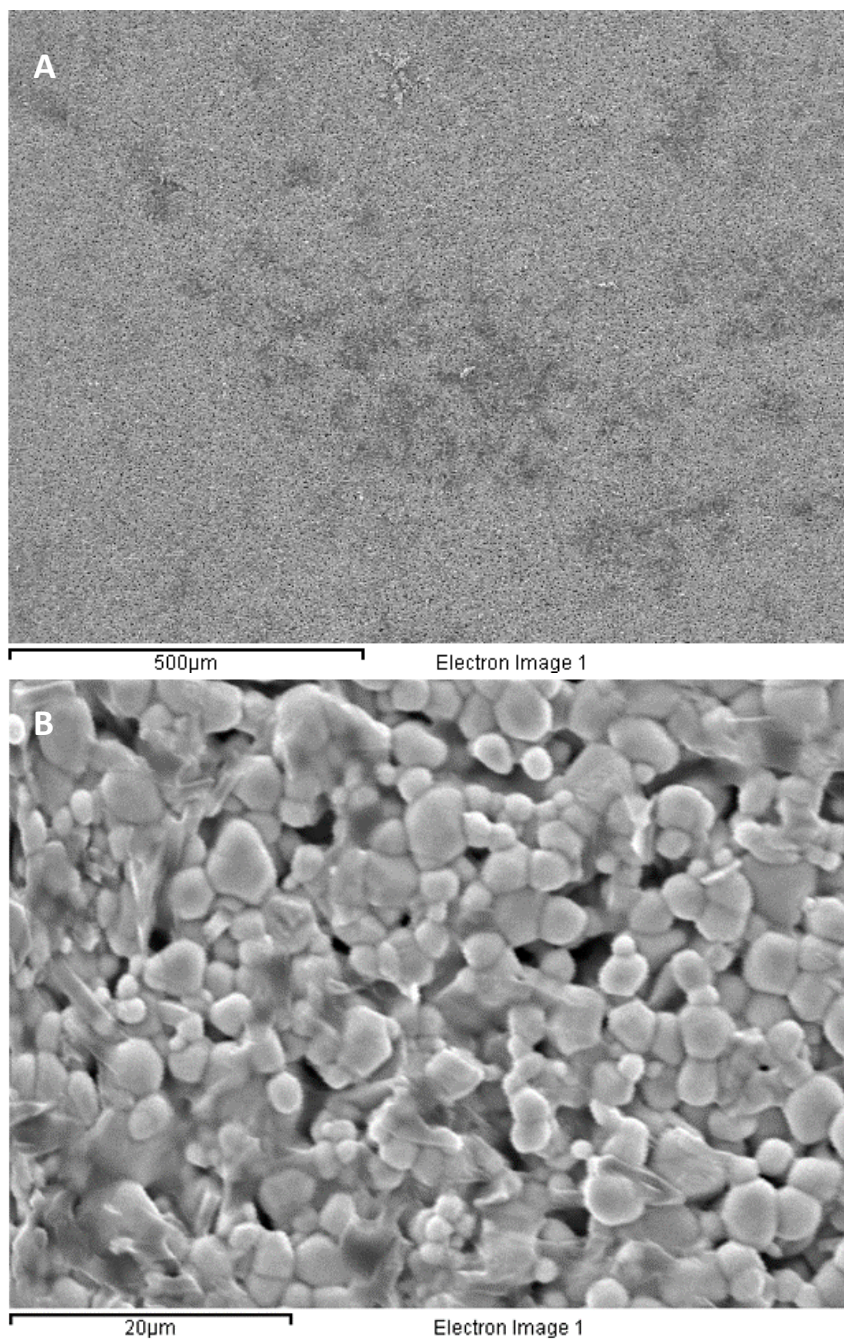


Figure 4.8. SEM micrographs at A) 100x and B) 2000x magnifications of the sintered pellet at 900 °C for 48h.

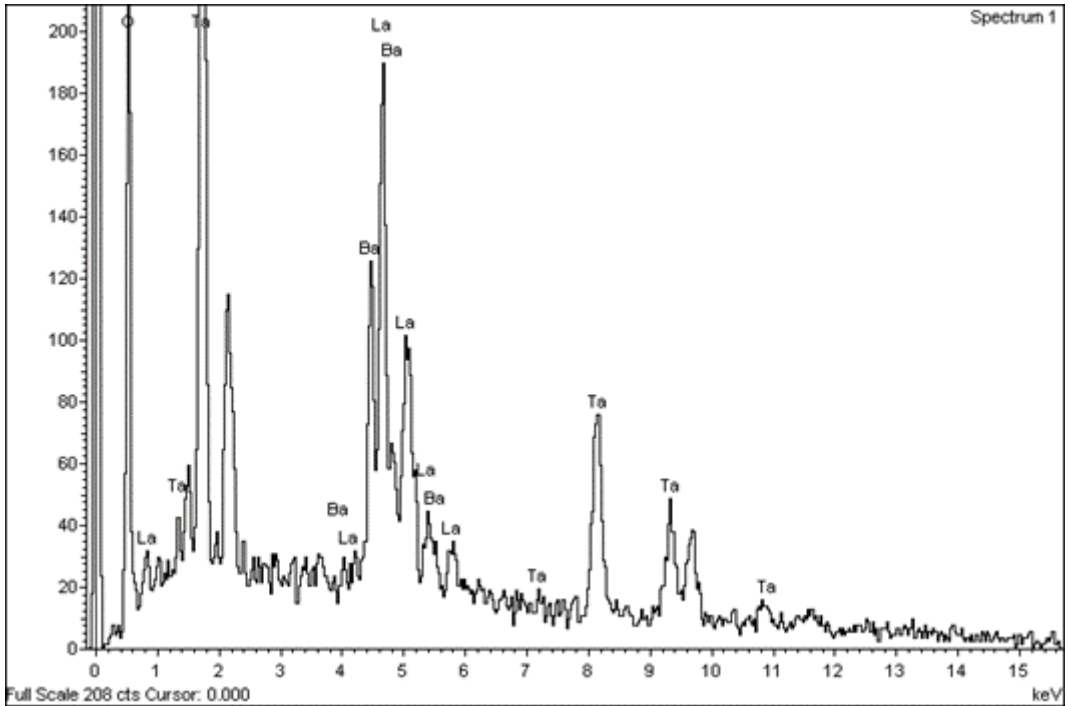


Figure 4.9. EDS analysis of the sintered pellet at 900 °C for 48h.

At 100x magnification, a homogeneous surface was obtained. Compared with the sintering at 900 °C for 24h (Figure 4.6), no cracks were detected on the surface of the pellet. At higher magnification (2000x, Figure 4.8B), it can be observed that grains kept a homogenous size dispersion between 2 and 8 μm approximately. Furthermore, a decrease in the porosity was obtained: $4.5\% \pm 2.4\%$. The EDS analysis, presented in Figure 4.9, revealed that all the elements detected were the ones that belonged to the solid electrolyte.

The XRD analysis of the pellet was also performed to determine if anomalous crystallographic phases were formed. In Figure 4.10 the XRD pattern of the pellet sintered at 900 °C for 48 h is shown along with the XRD pattern of $\text{Li}_6\text{BaLa}_2\text{Ta}_2\text{O}_{12}$ obtained from the bibliography [1,2] (Figure 4.10B).

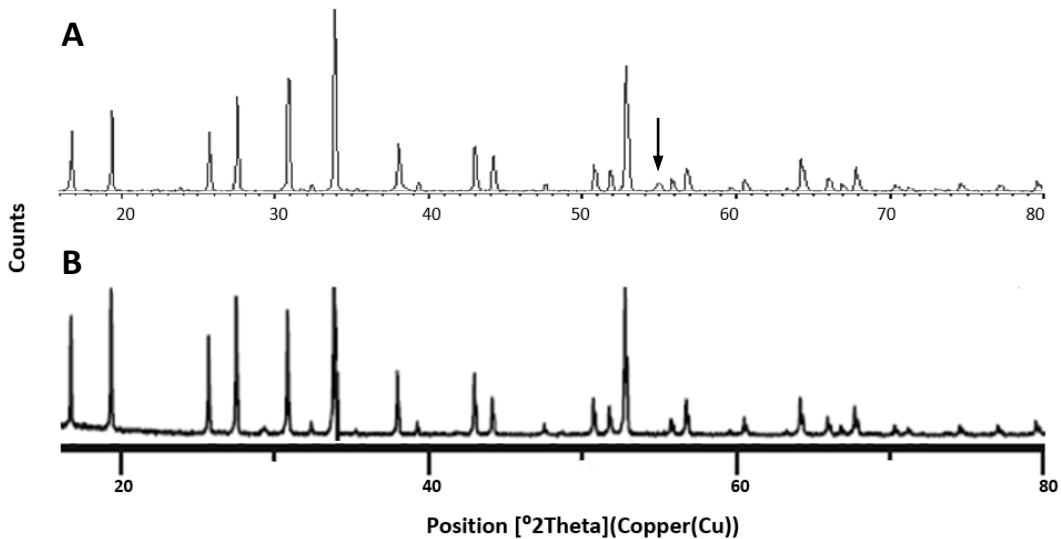


Figure 4.10. XRD patterns corresponding to A) sintered LBLTO pellet at 900 °C for 48h and B) bibliographic data [87,149]. The black arrow designates an unexpected signal.

The sintered disc showed a single phase of the garnet-type and good agreement with the bibliography. However, as marked with an arrow in Figure 4.10A, an unexpected peak was detected between 54° and 56° positions. The same anomalous signal was detected in the synthesized powder. It is possible that due to an increase in the lithium loss, $\text{Li}_2\text{Ba}_3\text{Ta}_2\text{O}_9$ was formed again. Concretely, the lithium content was 3.67% (w/w) which was smaller than the 3.85% obtained at 900 °C for 24h. Although the sintering at 900 °C for 48h presented some interesting features such as increased densification and absence of fissures on the surface of the pellet, there were aspects still to be improved. The apparition of undesired signals on the XRD analysis made this sintering process not to be considered optimal. From the results, it was concluded that longer times than 48 hours should not be used, since the XRD pattern could further deviate from its theoretical.

From this point of view, two experiments increasing the sintering temperature were performed: 950 °C for 24h and 1000 °C for 24h. The new sintered samples were also characterized. SEM micrographs of the sintered pellets at 950 °C for 24h and 1000 °C for 24h are shown in Figure 4.11A and Figure 4.11B respectively.

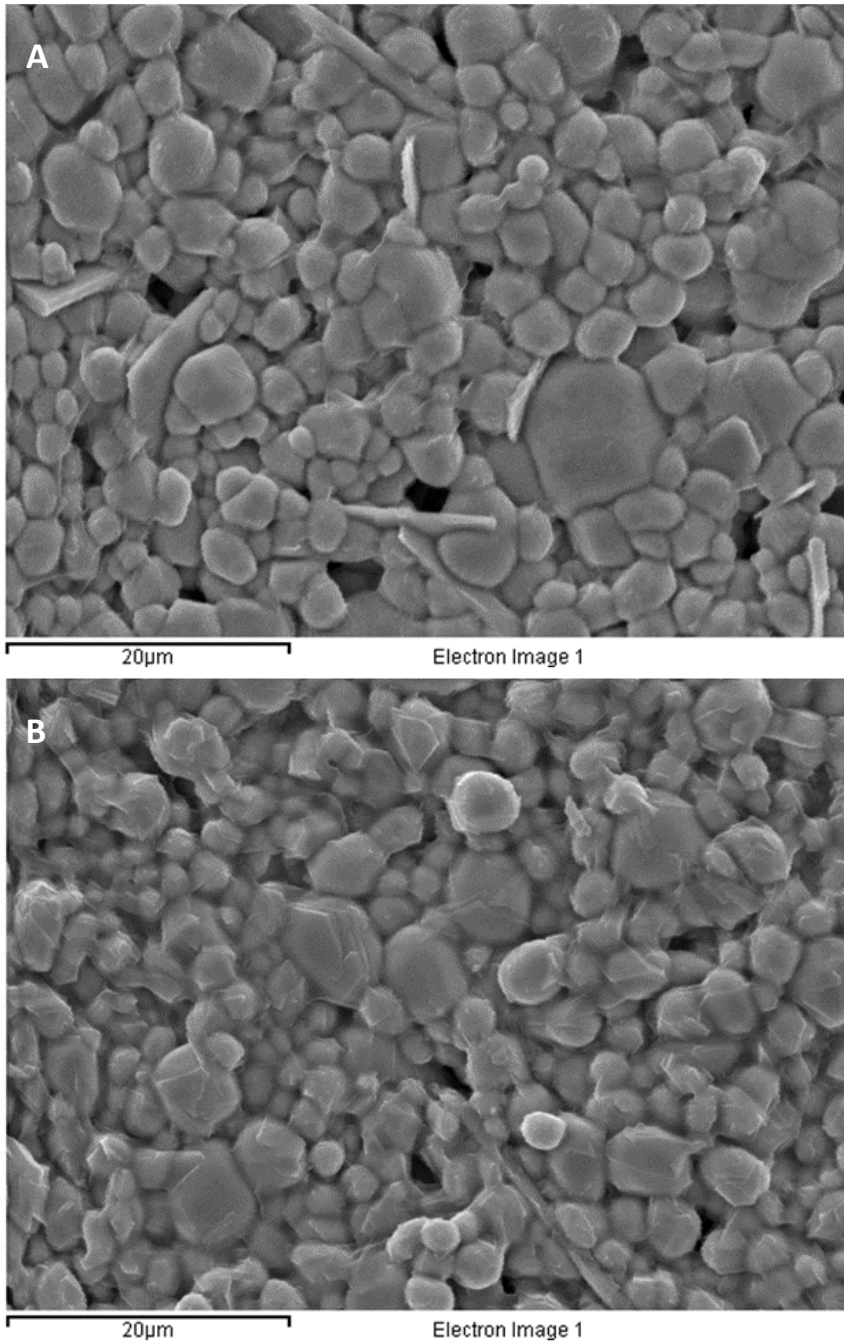


Figure 4.11. SEM micrographs (2000x) of LBLTO sintered pellets at A) 950 °C for 24h and B) 1000 °C for 24h.

Both pellets' micrographs showed a homogeneous grain distribution with a grain size between 2 μm and 10 μm approximatively. Even though defined grain boundaries could be observed, at 1000 °C it can be observed that some grains start to fuse. From Figure 4.11, it is certainly observed densification higher than in previous procedures. An analysis to estimate the porosity was performed for both sintering procedures. At 950 °C for 24h a

porosity of $4.0\% \pm 0.8\%$ was obtained, while at $1000\text{ }^\circ\text{C}$ for 24h it was $1.1\% \pm 0.4\%$. Note that both values exhibited a significant decrease towards the obtained porosity at $900\text{ }^\circ\text{C}$ for 24h ($15.3\% \pm 3.3\%$). In addition, in a higher macroscopically view of the surfaces, no fissures were observed. EDS analysis was also performed on both pellets and is shown in Figure 4.12.

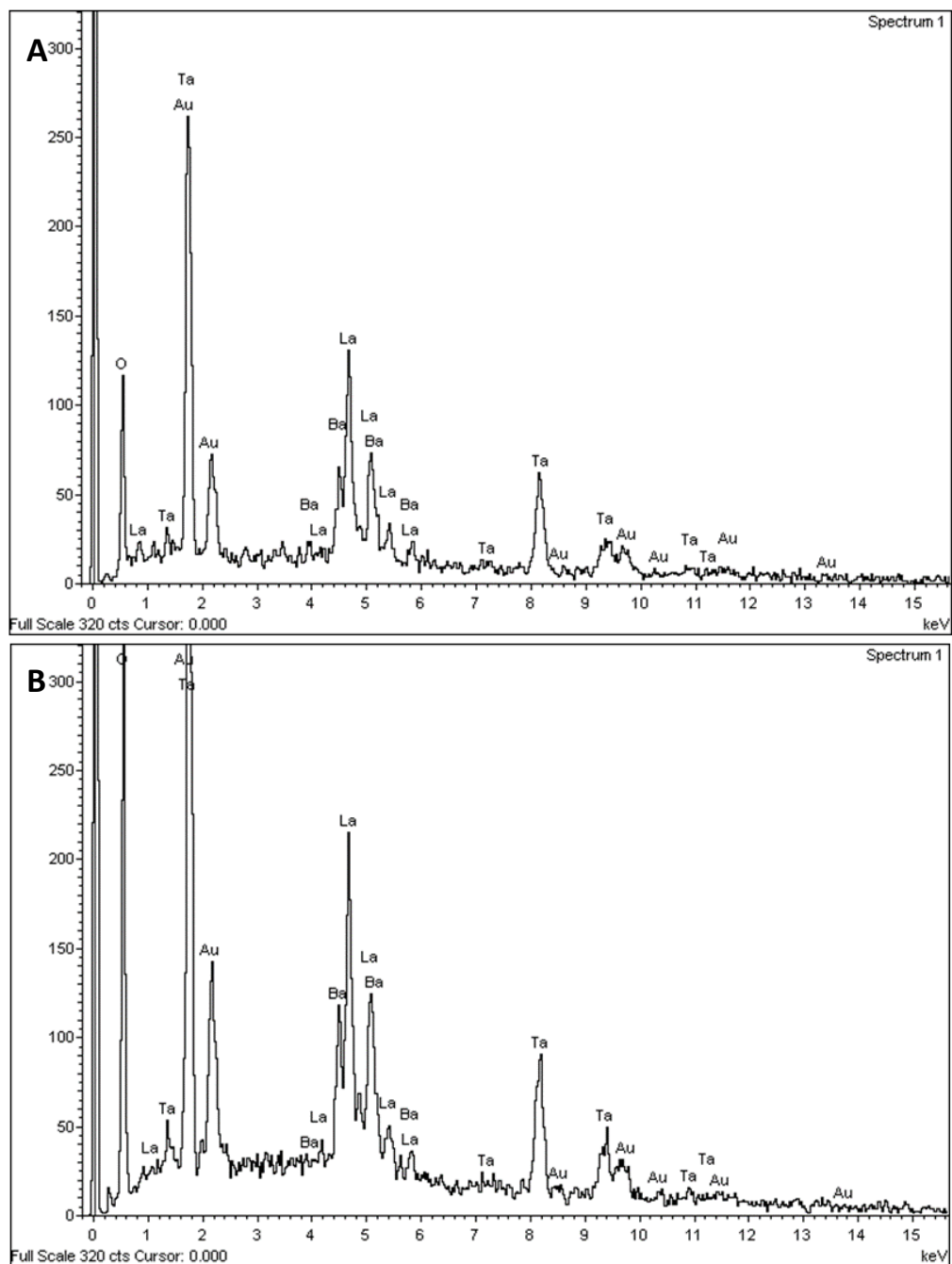


Figure 4.12. EDS spectra of the LBLTO sintered pellets at A) $950\text{ }^\circ\text{C}$ for 24h and B) $1000\text{ }^\circ\text{C}$ for 24h.

In Figure 4.12, the EDS spectra showed all the possible detectable elements belonging to the electrolyte (Ba, La, and Ta) and that no impurities were identified.

XRD analysis was also performed for each of the pellets to determine if anomalous crystallographic phases were formed because of increasing the temperature. In Figure 4.13A and Figure 4.13B the XRD patterns of the pellets sintered at 950 °C for 24h and 1000 °C for 24h are shown respectively.

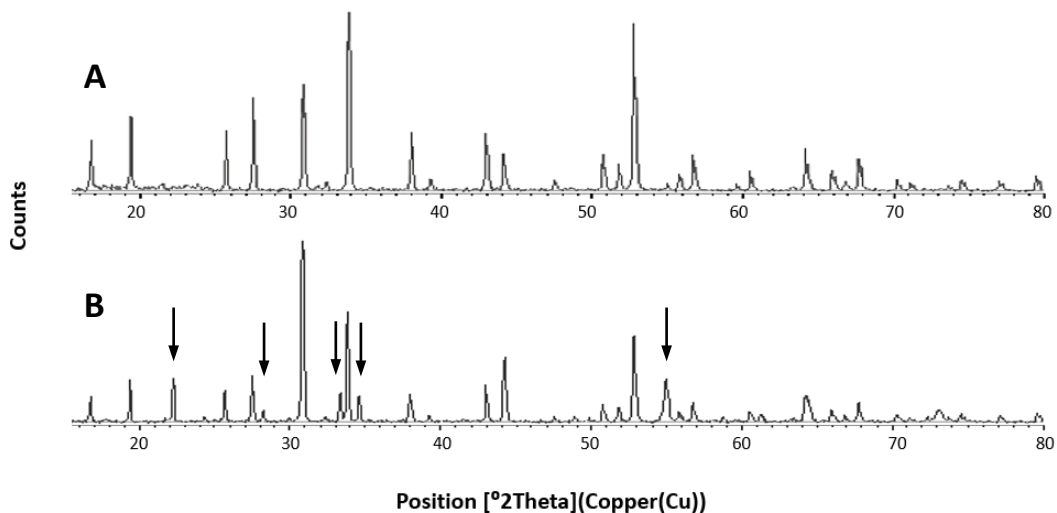


Figure 4.13. XRD patterns corresponding to LBLTO sintered pellets at A) 950 °C for 24h and B) 1000 °C for 24h. Black arrows designate anomalous signals.

The XRD pattern of the sintered pellet at 950 °C for 24h showed a single phase of the garnet-type and good agreement with the bibliography. However, the pattern that resulted from the pellet sintered at 1000 °C presented discrepancies. In its pattern, the presence of undesired peaks, indicated with an arrow in Figure 4.13B, demonstrated the formation of new crystallographic phases.

Finally, the lithium content of both pellets was quantified. A lithium concentration of 4.02% (w/w) was measured in the sintered pellet at 950 °C for 24h, while 3.92% (w/w) was determined in the sintered pellet at 1000 °C for 24h. It was observed that the Li concentration in the pellets decreased as the temperature increased due to its volatilization. Nevertheless, both values were close to the theoretical value of 4.12% (w/w).

To sum up, it was observed from the modified procedures that sintering times superior to 24 hours (900 °C for 48h) produced grain melting and a superior lithium loss. And temperatures higher than 950 °C exhibited the formation of new crystallographic phases that could compromise the ionic conductivity of the electrolyte. Therefore, since the already

obtained results at 950 °C for 24 hours were considered satisfactory, this sintering procedure was considered the optimum.

Finally, the cross-section of the solid electrolyte sintered at 950 °C for 24h was observed by SEM. Despite that the surface porosity was already determined, it is important to check if the inner porosity does not form preferential channels that could connect both sides of the pellet. Otherwise, when incorporating the electrolyte as a component of the Li sensor, the presence of such a pathway would allow the flow of the Li alloys tested, short circuiting the electrodes (see section 4.4 for more information concerning the sensor's configuration). Therefore, to evaluate the inner porosity of the pellet a cross-sectional cut was performed. To this aim, the pellet was encapsulated with an epoxy resin (Epofix Kit, Struers) which was cured overnight. Then, the embedded pellet was cut with a low-speed precision cutter (Buehler Isomet Low Speed Saw). Its cross-section micrograph and its EDS spectrum are shown in Figure 4.14.

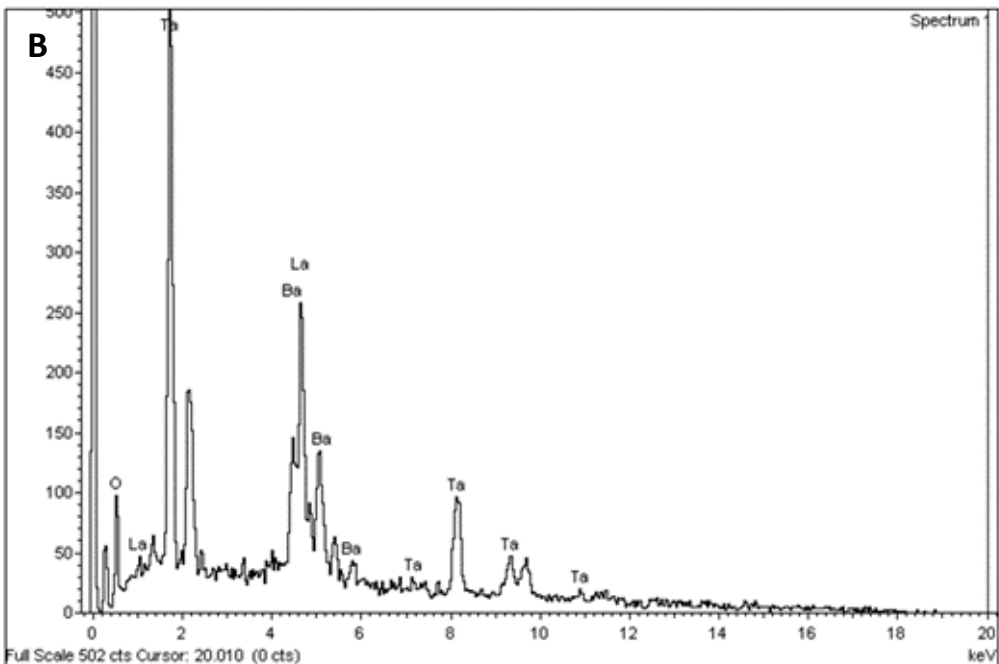
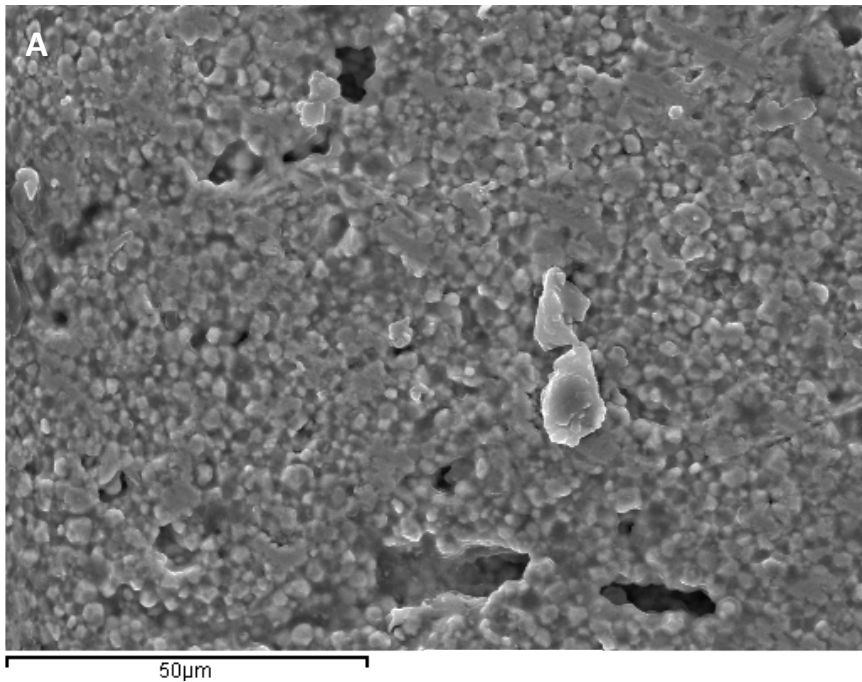


Figure 4.14. A) SEM micrograph (1000x) and B) EDS spectrum of the cross-section of an LBLTO pellet sintered at 950 °C for 24h.

Although some holes were observed in the inner wall of the pellet, no pathways connecting both sides of the pellet were observed. Porosity was measured from different micrographs, yielding a value of $2.6 \pm 0.6\%$. This value was in the same order of magnitude as the one

previously determined for the pellet's surface (4.0%). The performed EDS analysis (Figure 4.14B) showed only signals belonging to the solid electrolyte. Therefore, no impurities were incorporated during the sintering process.

The characterization analysis concluded that the sintered LBLTO pellets at 950 °C for 24 hours exhibited satisfactory physical properties and adequate crystallographic structure. From this thermal process, the ceramic can be shaped into discs suitable for the construction of lithium sensors.

4.2.1.3. Ionic Conductivity

Ionic conductivity is a key parameter of solid electrolytes. Note that, this property directly relates to the adequate performance of the electrolyte when forming part of the lithium sensor. Therefore, its measurement was of great interest.

Although there are reported bibliographic values for the LBLTO electrolyte, both synthesis and sintering procedures will affect its ionic conductivity, making it possible that the obtained conductivity results differ from the reported values.

Electrochemical Impedance Spectroscopy (EIS) was considered the most appropriate technique to determine the ionic conductivity of the electrolytes. However, to be able to perform impedance measurements in a wide range of temperatures, an adequate experimental set-up was required. In this way, the ionic conductivity dependence on the temperature could also be determined. For this purpose, the following set-up was designed and constructed (see Figure 4.15).

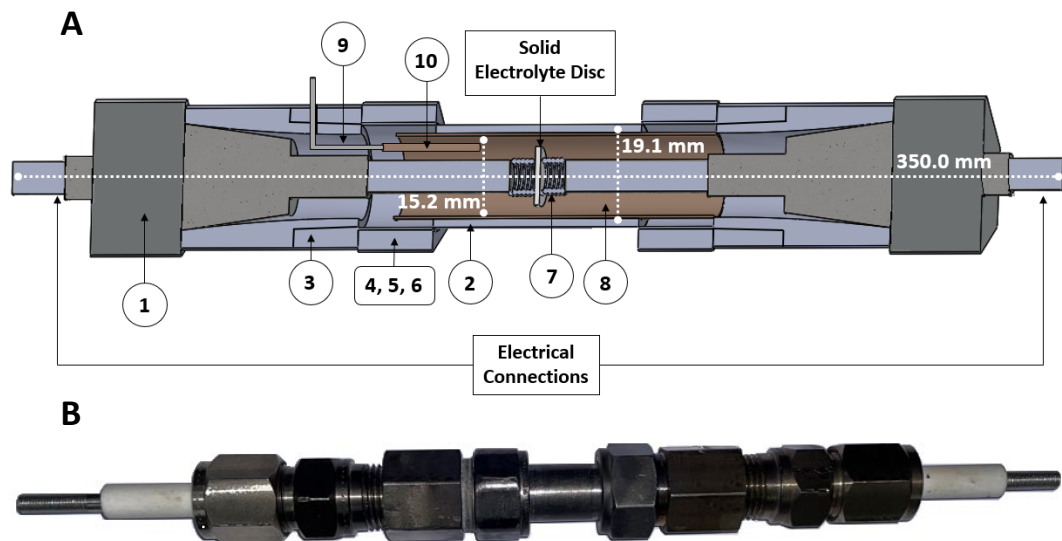


Figure 4.15. A) Scheme and B) Constructed experimental set-up for EIS measurements.

In this set-up, two Conax® feedthroughs (1) were used to insulate the electrical contacts from the metallic housing of the experimental set-up. These feedthroughs were attached to a stainless steel tube (2) with adequate stainless steel tube fittings: female connectors (3), nuts (4), and front and back ferrules (5,6). The electrolyte was placed inside the tube in the middle of the feedthroughs. Two stainless steel springs (7) were placed at the end of the feedthroughs in contact with the ceramic sample. In this way, proper electrical contact was ensured and at the same time, the collapse of the sample due to dilatation at high temperatures could be avoided. To ensure that the electrolyte nor any electrical component was short-circuited with the walls of the stainless-steel tube, an alumina tube (8) was placed in between. Finally, a K-type thermocouple (9) was fitted through a drilled hole on one of the sides of the feedthroughs. To have an accurate temperature measurement, the thermocouple was located as close as possible to the solid electrolyte and it was covered with a thin alumina tube (10) to avoid any electrical contact. The descriptions and references for the different components used are listed in Table 4.5.

Table 4.5. Description, references, and suppliers for the components of the EIS measuring set-up (Figure 4.15).

Number	Component	Reference	Supplier
1	Stainless Steel Feedthroughs	EG-250-A-SS-L	Conax
2	Stainless Steel Tube OD: 3/4 in. x 0.065 mm	SS-T12-S-065-6ME	Swagelok
3	Stainless Steel Female Connector, 3/4 in. x 1/2 female NPT	SS-1210-7-8	Swagelok
4	Stainless Steel Nut, 3/4 in.	SS-1212-1	Swagelok
5	Stainless Steel Front Ferrule, 3/4 in.	SS-1213-1	Swagelok
6	Stainless Steel Back Ferrule, 3/4 in.	SS-1214-1	Swagelok
7	Stainless Steel Springs	M03LE6668	Springmakers
8	Alumina Tube, OD: 15.35 mm	-	Carbosystem
9	Alumina Tube, OD: 4mm	030062.DW	Alfa-Aesar
10	K-type Thermocouple	397-1258	RS Components

The described set-up was placed inside a stainless-steel reactor enclosed by a clamp-type electrical resistance (1200 W) supplied by SANARA S.A. which was regulated via a PID-type temperature controller (Fuji PXR4, K-type thermocouple). An image of the whole assembly is shown in Figure 4.16. The exterior ends of the feedthroughs were connected to a Potentiostat/Galvanostat Autolab PGSTAT302N with an impedance module FRA32M. Due to sample reactivity with moisture and air, the whole assembly was placed in a glovebox (MBraun UNIlab, high purity Ar atmosphere 99.9992%, O₂ and H₂O concentrations < 1 ppm), ensuring a controlled atmosphere during the EIS measurements.

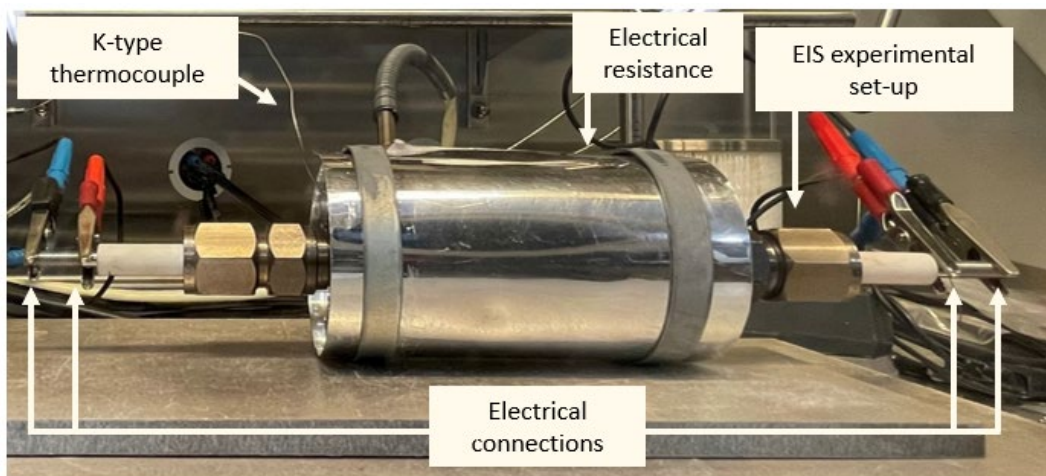


Figure 4.16. Complete assembly for the EIS measurements, composed of the measuring set-up and the heating system.

The EIS assembly was tested and its proper functioning was checked by measuring the ionic conductivities of the electrolytes that will be sintered. Note that the experimental data obtained will be compared to reported ionic conductivity values for similar electrolytes.

Before starting the measurements, the surface of the solid electrolyte discs had to be conditioned. First, pellets were polished to ensure a flat surface, for this purpose, SiC #400, #1200, and #2000 polishing papers were used. Secondly, each side of the pellet was gold-coated through a sputtering process for 3 minutes with a Polaron SC7620 Sputter Coater. During this process, the pellet was placed in a mold which ensured that only a delimited area of one side of the pellet got coated ($\varnothing = 10.3$ mm). The mold also prevented gold-coating the disc sides, if not prevented, it could cause a short-circuit making the measurement invalid.

Once the sample was prepared and the whole assembly was mounted, EIS measurements were ready to start. However, before each measurement, it was necessary to wait for the stabilization of the set temperature. If the electrochemical system under measurement is not stable, the impedance data obtained will most likely be invalid. EIS measurements were performed by applying a voltage amplitude that ranged from 200 mV to 50 mV versus the OCP. This voltage amplitude depended on the temperature, always using the lowest amplitude that could disturb the electrochemical system: as the temperature increased, smaller amplitudes could be applied. The AC measurement was performed from frequencies of 1MHz to 10Hz. Conditions for the impedance measurement are shown in Figure 4.17.

These parameters correspond to NOVA[®] software which is the package designed to control all the Autolab instruments.

The image shows a software interface with two sections: 'Basic' and 'Advanced'. The 'Basic' section includes: 'Maximum integration time' (2 s), 'Minimum number of integration cycles' (5), 'Sample time domain' (checkbox checked), 'Sample frequency domain' (checkbox checked), 'Sample DC' (checkbox checked), and 'Calculate admittance' (checkbox unchecked). The 'Advanced' section includes: 'Transfer function' (dropdown: Re - j Im), 'Lowest bandwidth' (dropdown: High stability), 'Number of cycles to reach steady state' (15), 'Maximum time to reach steady state' (20 s), 'With a minimum fraction of a cycle' (1), 'Automatic amplitude correction' (checkbox checked), 'Iterative' (checkbox checked), 'Amplitude threshold percentage' (5 %), 'Automatic resolution correction' (checkbox unchecked), 'Iterative' (checkbox unchecked), 'Minimum resolution' (32 %), and 'Maximum amount of re-measurements' (15).

Figure 4.17. Basic and Advanced parameters in NOVA[®] software for an EIS measurement.

From the shown parameters, *Maximum integration time* and *Minimum number of integration cycles* determine the time to process the signal. When one of these conditions is reached, the frequency changes to start the subsequent measurement. To process the signal, 2 seconds or 5 cycles were enough to achieve an adequate integration. However, if more time is needed to integrate the signal, both parameters should be modified accordingly. The same criterium was used in *Number of cycles to reach steady state* and *Maximum time to reach steady state*, when one of these parameters reach their value, the system is considered stable and the signal's integration begins. As mentioned before, if more time is required to achieve a stable signal, both parameters should be modified consequently. To start the signal integration, 15 cycles or 20 seconds were enough to ensure a stable state. As a function of the system studied, larger numbers than the ones described

for these parameters could be required. In such situations, the time of the measurement could increase considerably.

One last parameter that is necessary for the correct data acquisition of the EIS measurement is the *Current range*. Before each measurement, NOVA allows the user to set a maximum and minimum value for this parameter. The maximum current range should always be set a bit higher than the highest expected current. If this value is too high or too low, it will cause a loss of accuracy during the measurement that will later translate into noise in the acquired data.

As mentioned previously, when performing the EIS measurements, it is crucial to ensure that the 3 conditions that validate the measurement are satisfied (linearity, causality, and stability). To ensure these 3 conditions, the measurement needs always to comply with a Kramers-Kronig test yielding χ^2 values inferior to 10^{-4} . In addition, these three conditions were double-checked apart. Linearity was also tested by performing the measurement at 3 different voltage amplitudes to verify the proportionality between them. Causality was also tested by measuring the OCP potential at the start and the end of the measure: considering it causal when differences smaller than 1 mV were obtained. Stability was also analyzed when performing the Open Circuit Potential (OCP) measurements, smaller variations than 1 mV/min had to be observed during those measurements.

Once the set temperature was stable, measurements from 1 Mhz to 10 Hz were initialized using the acquisition parameters described in section 3.2. To ensure the validity of the data, Kramers-Kronig tests were performed; only values of χ^2 lower than 10^{-4} were accepted (see section 3.2). Nyquist plots at 30 °C, 100 °C, 175 °C, and 250 °C are shown in Figure 4.18.

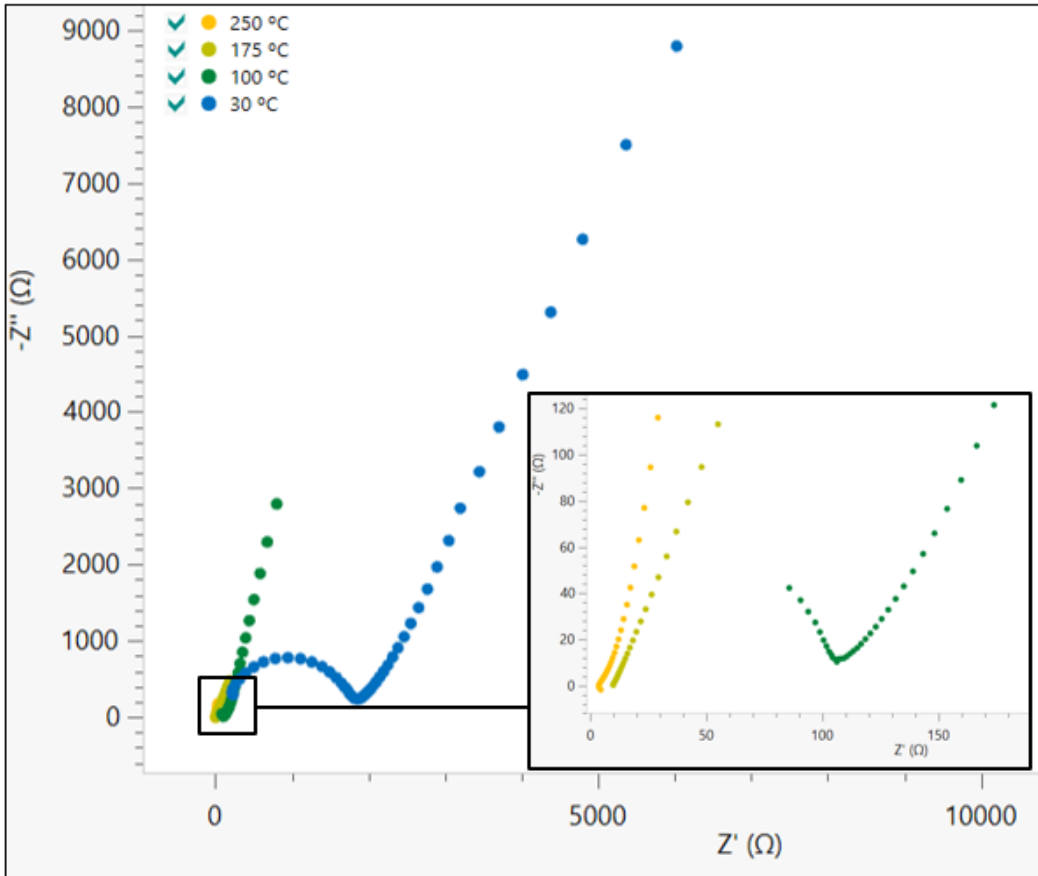


Figure 4.18. Nyquist plots of an LBLTO sintered pellet at 30 °C, 100 °C, 175 °C, and 250 °C.

From Figure 4.18, it can be observed that the real part of the impedance (Z') diminished as the temperature increased. At 30 °C a clear semicircle was obtained in the high-frequencies region. This semi-circle was attributed to the bulk and grain boundary impedances. The capacitive “tail” that appears on the low-frequency side indicated the blocking of mobile Li^+ ions [87].

As the temperature increased, the impedance (Z) diminished and the shape of the Nyquist plot varied. This phenomenon can be appreciated in the zoomed part of the Nyquist plot that is shown at the insert on the right side of Figure 4.18. At temperatures higher than 100 °C, the shape of the remaining fraction of the semicircle got more complex. If the zoomed part of the Nyquist plot is observed (right part of the figure) in the high-frequency region, at 175 °C the imaginary impedance’s component ($-Z''$) started to achieve negative values. All these results were associated with an inductive effect produced by the electrical connections [152–154]. Therefore, an inductor component has to be included in the equivalent circuit. The equivalent circuit that best described all these phenomena is shown in Figure 4.19.

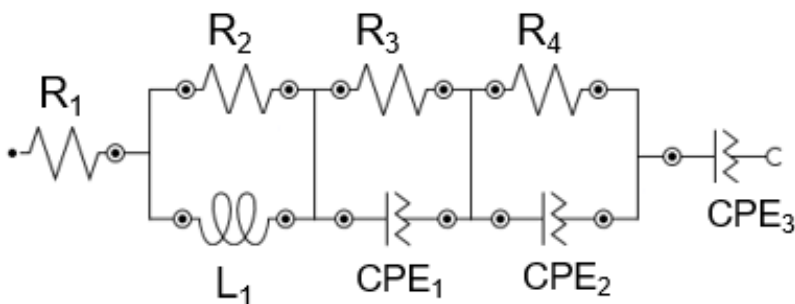


Figure 4.19. Equivalent circuit used to fit EIS data.

The equivalent circuit (EC) shown in Figure 4.19 consisted of $R_1(R_2L_1)(R_3CPE_1)(R_4CPE_2)CPE_3$. In this circuit, R_1 resistance corresponded to the impedance of the measuring set-up, while R_2 and L_1 were correlated to the inductor effect of the electrical connections. R_3 resistance corresponded to the total resistance of the solid electrolyte. This total resistance (R_3) considered the contributions from the bulk and the grain boundary of the electrolyte. As for the other elements of the circuit, CPE_1 was the capacitance effect of the electrolyte, and R_4 , CPE_2 , and CPE_3 corresponded to the impedance contribution of the gold-sputtered lithium-ion blocking electrodes.

In order to consider whether the fitting was adequate, an acceptance value of $\chi^2 < 0.1$ was set [155]. This criterium was less strict than the one previously set for the KK test ($\chi^2 < 10^{-4}$) since in this case, the EC proposed (Figure 4.19) presents the minimum electrical components that can physicochemically describe the system. Conversely, the EC fitted during the KK test is composed of as many RC components as the number of frequencies tested (50 approximatively). It is worth mentioning that the circuit proposed was similar to equivalent circuits found in the bibliography for other lithium-ion electrolytes [103,104,106].

However, at high temperatures, the inductor's influence increased, causing an increase in the complexity to fit an adequate EC. Furthermore, in some cases, the acceptance criterium $\chi^2 < 0.1$ was not fulfilled, or the values for R_3 were not consistent. This phenomenon was observed when the total solid electrolyte impedance was lower than 100 Ω . The effect grew more significant as the total electrolyte resistance decreased when increasing the temperature. To be able to continue studying the ionic conductivity of the electrolyte, strategies to circumvent this inductive effect were evaluated.

Selection of the Optimum Strategy to Circumvent the Inductive Effect

To obtain a proper fitting of the equivalent circuit and thus be able to determine the total resistance of the solid-state electrolyte, three different strategies were proposed. The first one was to remove the two first decades of frequencies. In the measured impedances from 1MHz to 10kHz, the inductor has a high impact. This is because its impedance is directly related to the frequency, as described by [Eq. 4.1] and [Eq. 4.2].

$$Z_{Inductor} = j\omega L \quad [\text{Eq. 4.1}]$$

$$f = 2\pi\omega \quad [\text{Eq. 4.2}]$$

Where Z is the impedance, j is the imaginary unit $\sqrt{-1}$, ω is the angular velocity in $\text{rad}\cdot\text{s}^{-1}$, L is the inductance of the inductor in henrys (H), and f is the frequency in hertz (Hz). Thus, at frequencies higher than 10 kHz, the inductor will have a high impact. For this reason, negative imaginary values are obtained in the left part of the Nyquist plot. When subtracting the mentioned points from the measured impedance, Nyquist plots similar to the one presented in Figure 4.20 were obtained. In Figure 4.20A the Nyquist plot from an LBLTO pellet at 200 °C from 1 MHz to 10 Hz is shown, while in Figure 4.20B the resulting subtracted Nyquist from 10 kHz to 10 Hz.

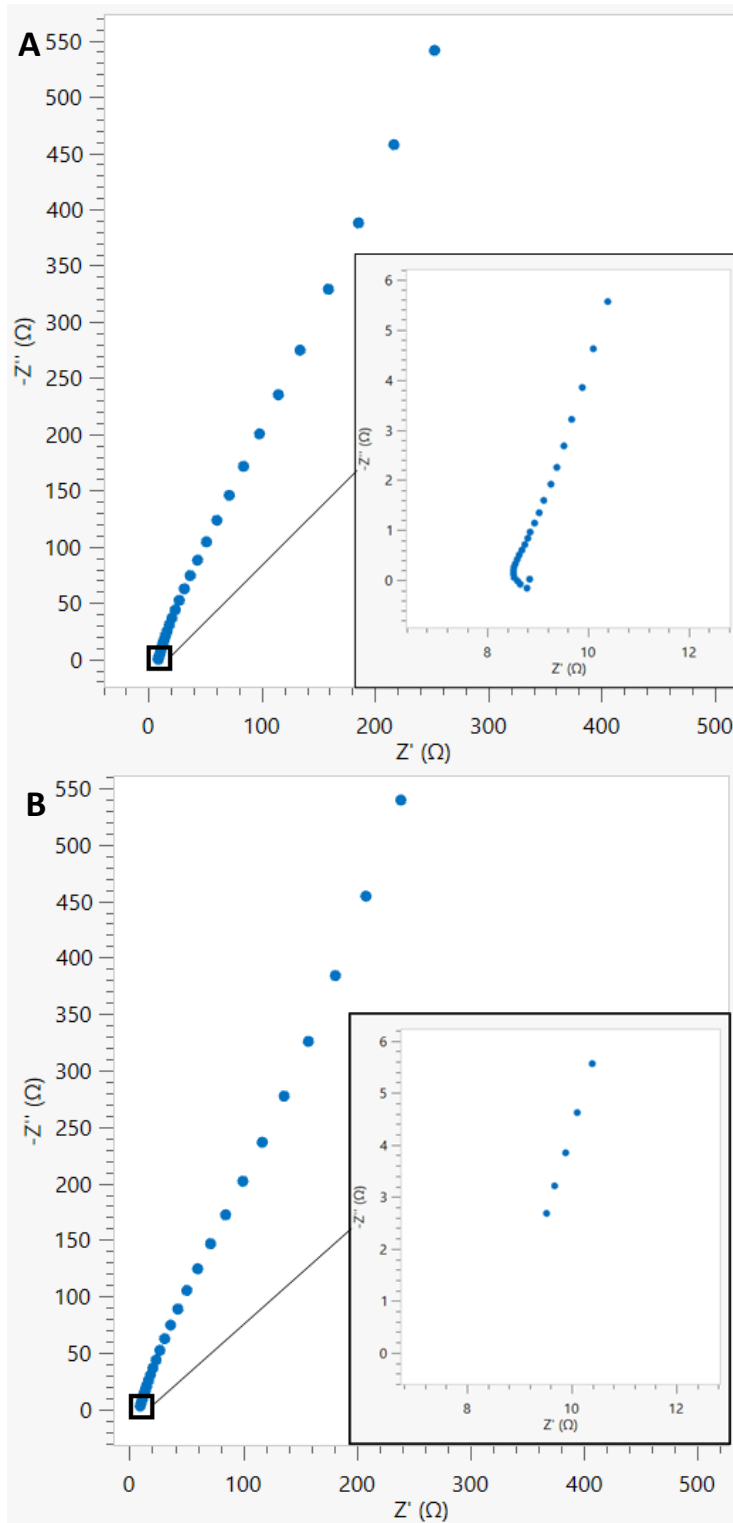


Figure 4.20. Nyquist plot of an LBLTO pellet at 200 °C A) before and B) after removing the impedance data from 1 MHz to 10 kHz.

As can be observed in Figure 4.20, all the impedance values below or near 0Ω ($-Z''$) were eliminated. The equivalent circuit shown in Figure 4.21 was fitted to the resulting data. The inductive component which was included in the previous EC (Figure 4.19) was removed. By removing the highest frequency points almost all its influence was eliminated.

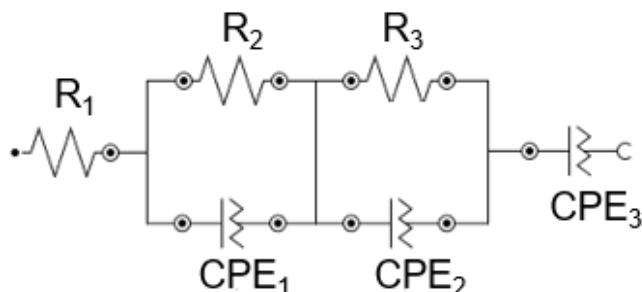


Figure 4.21. Equivalent circuit used to fit the impedance data when values from 1Mhz to 10 kHz had been discarded.

In this circuit, R_1 was the resistance of the measuring set-up, and R_2 was the total resistance of the electrolyte. As for the other elements of the circuit, CPE_1 was the capacitance effect of the electrolyte, and R_3 , CPE_2 , and CPE_3 corresponded to the impedance contribution of the gold-sputtered lithium-ion blocking electrodes. As a result of its simplicity, a fast fitting could be achieved with coherent resistance results and values of $\chi^2 < 0.1$.

The second strategy was based on correcting the effect of the inductor by estimating and withdrawing the inductor impedance. This strategy is reported in a Ph.D. Thesis from A.R. Thompson [156], although other authors have described similar corrections [152,153]. To use this solution, the impedance of the electrical connections has to be measured. For this purpose, an EIS analysis was performed on the measuring set-up (see Figure 4.15) excluding the solid electrolyte. This measurement has to be performed at high frequencies (1 Mhz-10kHz) and at the temperature planned to be corrected. Note that the temperature could affect the impedance of the connections. At 200 °C, the Nyquist plot shown in Figure 4.22A is obtained. From this measurement, the equivalent circuit shown in Figure 4.22B was used to obtain the fitting parameters.

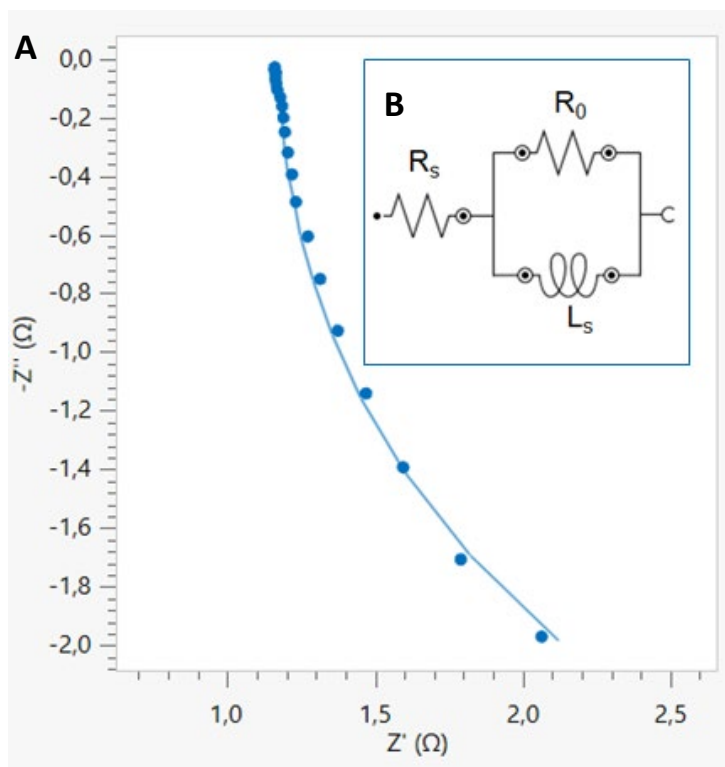


Figure 4.22. A) Nyquist plot of the electrical connections of the measuring set-up at 200 °C, and B) the equivalent circuit used to fit this impedance data.

Good fitting was obtained using the described circuit, where all values for χ^2 were below 0.1. From this equivalent circuit, values for R_0 , and L_s were obtained. The values for each of these components are shown in Table 4.6 as a function of the temperature.

Table 4.6. R_0 and L_s obtained values at each of the studied temperatures.

Temperature / °C	R_0 / Ω	L_s / H
100	7.87	5.36E-07
125	7.45	5.07E-07
150	7.16	4.78E-07
200	7.51	5.02E-07
250	5.09	3.88E-07
275	6.49	4.54E-07
300	6.49	4.54E-07

R_0 and L_s parameters were used in the following mathematical formulas to obtain the corrected impedance. These corrections were implemented for both the imaginary and the real part of the measured impedance of the solid electrolyte. For the real impedance part (Z'), [Eq. 4.3] and [Eq. 4.4] were used.

$$Z'_{corrected} = Z'_{raw} - Z'_{jig-hf} \quad [\text{Eq. 4.3}]$$

$$Z'_{jig-hf} = \frac{R_0(\omega L_s)^2}{R_0^2 + (\omega L_s)^2} \quad [\text{Eq. 4.4}]$$

Where $Z'_{corrected}$ was the real impedance value once corrected from the inductor effect, Z'_{raw} the real impedance value of the solid electrolyte, and Z'_{jig-hf} the calculated real impedance value of the inductor. To calculate Z'_{jig-hf} , the already determined R_0 and L_s parameters were used, as well as ω which is the angular velocity, related to the frequency as described in [Eq. 4.2].

For the correction of the imaginary impedance Z'' , similar equations were used: [Eq. 4.5] and [Eq. 4.6].

$$Z''_{corrected} = Z''_{raw} - Z''_{jig} \quad [\text{Eq. 4.5}]$$

$$Z''_{jig} = \frac{\omega L_s R_0^2}{R_0^2 + (\omega L_s)^2} \quad [\text{Eq. 4.6}]$$

Where $Z''_{corrected}$ was the imaginary impedance value once corrected from the inductor effect, Z''_{raw} the imaginary impedance value of the solid electrolyte measure, and Z''_{jig} the calculated imaginary impedance value of the inductor. To calculate Z''_{jig} , R_0 and L_s parameters were used, as well as ω .

After applying the Z' and Z'' correction to the raw data, the resulting Nyquist plot changed significantly. In Figure 4.23 an example of the data correction is shown. In Figure 4.23A the Nyquist plot of the raw data of an LBLTO pellet at 200 °C is shown, while in Figure 4.23B it is presented the resulting Nyquist of the same sample after the inductance's correction.

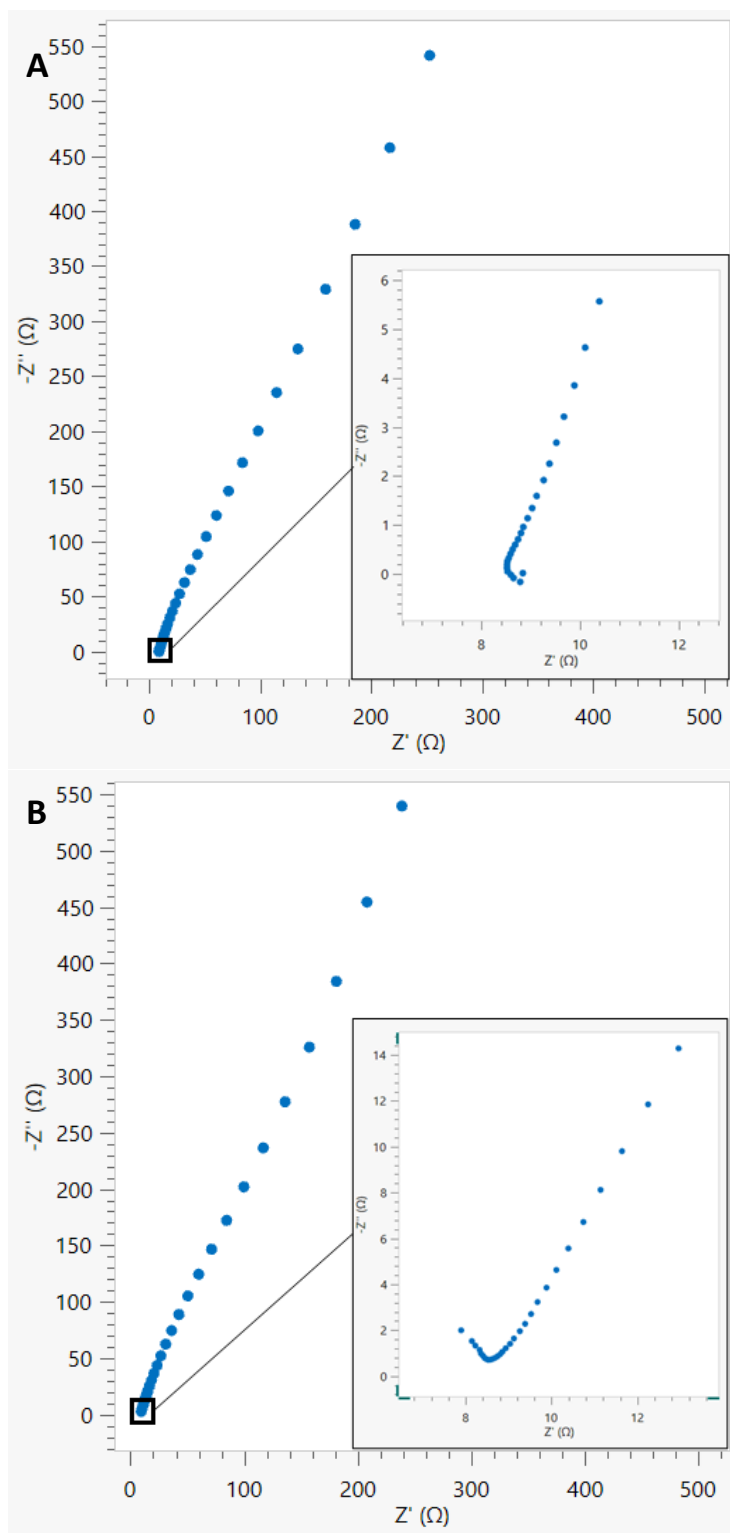


Figure 4.23. Nyquist plots of A) LBLTO pellet at 200 °C and B) of the same LBLTO pellet at 200 °C after the inductance's correction was applied.

As observed in Figure 4.23B, the Nyquist plot acquired a more resembling shape to the one obtained at 100 °C (see Figure 4.18). This result demonstrated that the influence of the inductor had significantly decreased, and its impedance contribution could be eliminated from the EC. Thus, to fit the corrected data, the equivalent circuit from Figure 4.21 was used. Good fitting was obtained using the described circuit, where all values for χ^2 were below 0.1, with coherent resistance results.

The third and last strategy that was evaluated was to directly fit the EIS data with the EC previously presented which is shown in Figure 4.24.

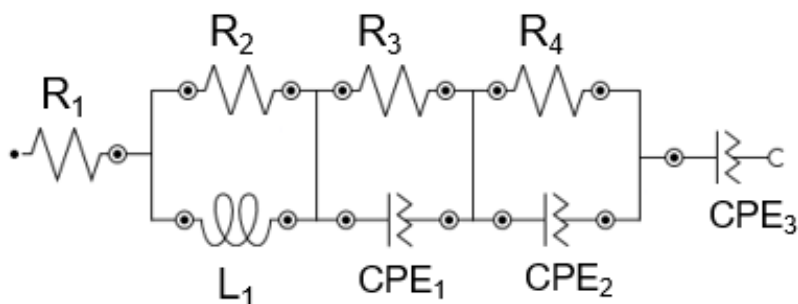


Figure 4.24. Equivalent circuit used to fit EIS data.

In most scenarios, good fitting was obtained using the described circuit, with values for χ^2 below 0.1, and with coherent resistance results. However, the correct fitting of this circuit was time-consuming, since small variations of R_1 or R_2 had a high impact on the value of R_3 (the total resistance of the electrolyte). And due to the high complexity of the circuit with so many variables, many solutions fitted which could yield low values of χ^2 .

When applying each of these 3 strategies to the experimental data, the fitted equivalent circuits yielded coherent results. The resistances and the ionic conductivity values are shown in Table 4.7.

Table 4.7. Determined resistances and ionic conductivities by each of the strategies as a function of the temperature.

Temperature / °C	Strategy 1		Strategy 2		Strategy 3	
	R / Ω	σ / S·cm ⁻¹	R / Ω	σ / S·cm ⁻¹	R / Ω	σ / S·cm ⁻¹
125	50.0	2.45E-03	42.3	2.89E-03	39.8	3.08E-03
150	24.3	5.04E-03	24.5	5.00E-03	24.7	4.96E-03
200	8.35	1.47E-02	8.61	1.42E-02	8.30	1.47E-02
250	3.57	3.43E-02	4.39	2.79E-02	3.29	3.72E-02
275	2.81	4.35E-02	3.36	3.64E-02	2.57	4.76E-02
300	2.36	5.18E-02	2.93	4.18E-02	2.10	5.83E-02

As the temperature increased the total resistance of the electrolyte diminished as expected. At 125 °C, a resistance close to 40 Ω was determined, while at 300 °C, it diminished to values close to 2 Ω. Even though the values followed an adequate trend, there were small differences between the ionic conduction resistances determined by each of the strategies.

To compare these 3 solutions, their total lithium-ion conductivities were calculated (section 3.2, [Eq. 3.2] and [Eq. 3.3]) and were compared to bibliographic data. In Figure 4.25, total lithium-ion conductivities for Li₆BaLa₂Ta₂O₁₂, using the three correction strategies, are shown as a function of temperature. Bibliographic data from V. Thangadurai et al. [87] was also included.

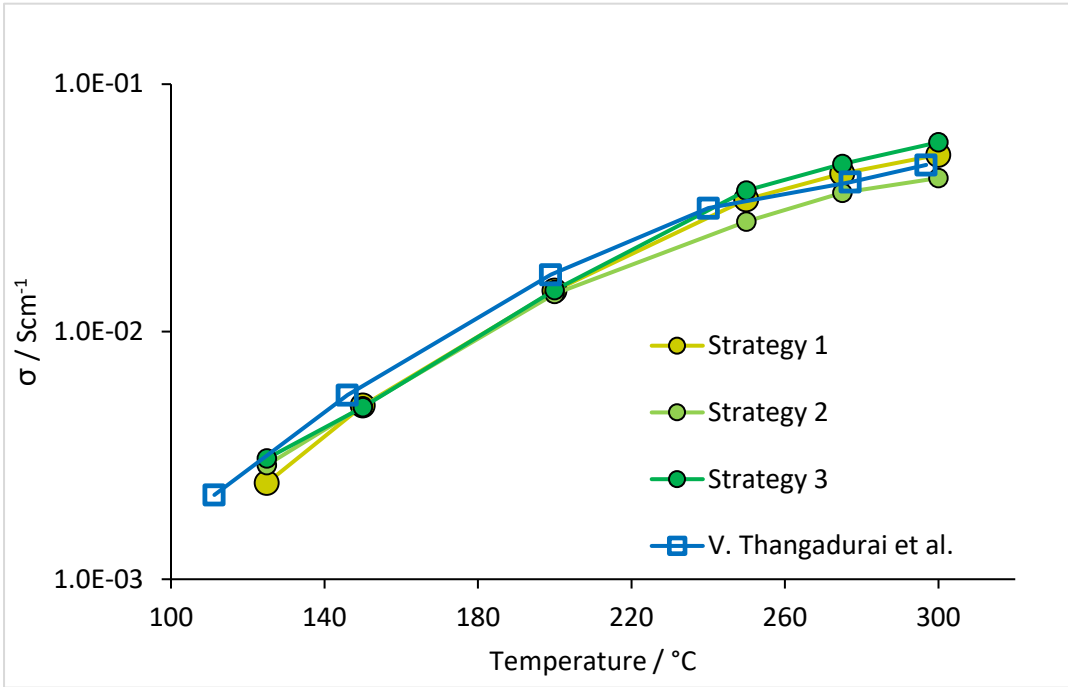


Figure 4.25. Total lithium-ion conductivities as a function of the temperature and strategy for an LBLTO electrolyte. Bibliographic data from V. Thangadurai et al. were also included [87].

All the strategies yielded consistent results which were close to the reported data. Although small deviations were obtained, the overall correlation of the ionic conductivity towards temperature was similar for all the data sets. To further study each of these strategies, the data was linearized using the Arrhenius equation ([Eq. 4.7]), which permitted to correlate the ionic conductivity with temperature.

$$\sigma T = A e^{\frac{-Ea}{kT}} \quad [\text{Eq. 4.7}]$$

Where T is the absolute temperature in kelvin (K), A is the pre-exponential factor, a constant for each chemical reaction, Ea is the activation energy in joule (J), and k is the Boltzmann constant ($1.380649 \times 10^{-23} \text{ J} \cdot \text{K}^{-1}$). Thus, if the natural logarithm is applied to [Eq. 4.7], the following expression is obtained ([Eq. 4.8]), which permits the representation of the data in a linear form.

$$\ln(\sigma T) = \frac{-Ea}{kT} + \ln(A) \quad [\text{Eq. 4.8}]$$

When plotting the natural logarithm of the total lithium-ion conductivities versus the inverse of the temperature, linear correlations were obtained. All correlations for the LBLTO electrolyte are shown in Figure 4.26.

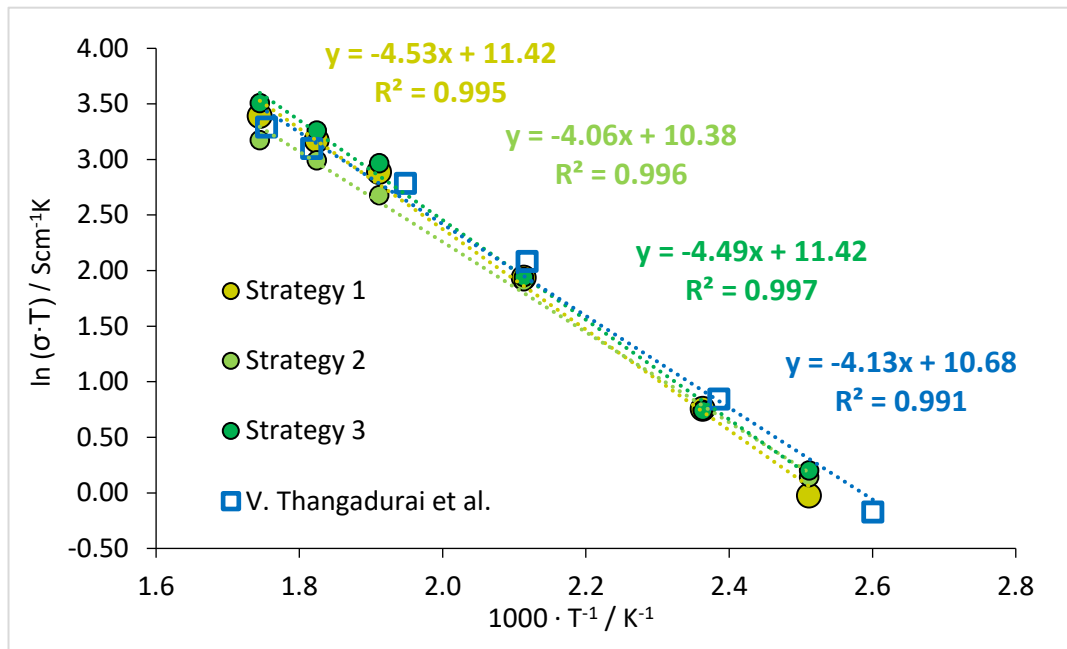


Figure 4.26. Arrhenius plots of the total lithium-ion conductivities obtained from each of the three applied strategies and bibliographic data [87] of the LBLTO electrolyte.

In Figure 4.26, four linear correlations are shown. Each of them was in good agreement with the Arrhenius equation since coefficients of determination (R^2) superior to 0.99 were obtained. The slopes of these linear correlations were directly proportional to the activation energy for the ionic transport and their y-intercept (constant) was the natural logarithm of the pre-exponential term. To determine if significant differences were obtained between each of these strategies and whether these were similar to the bibliographic data, the confidence intervals (95%) of the slope and the constant term of each linear correlation were calculated. The results obtained from the comparison of these intervals are shown in Annex 1 (Figure 7.1). From the study, it was concluded that there were no significant differences between the different strategies and bibliographic data. Furthermore, the results indicated that statistically there was not an optimal strategy since all yielded similar results.

Since the statistical study was not conclusive, among all three strategies, strategy 1 was considered the optimal solution due to the following reasons: First, it was the simplest solution of all three. On the one hand, strategy 2 required the calculation of the inductor effect through different equations to be able to subtract its value from the experimental

data. On the other hand, strategy 3 was time-consuming when fitting an EC, and in some situations, the fitted results were not consistent. Second, since the inductor was considered a parasitic effect, eliminating the high-frequency region was a coherent solution to remove its influence on the measurement. Therefore, strategy 1 was used for all the impedance measurements that showed a certain inductor effect: when the total LBLTO electrolyte resistance was below 100Ω . Once the optimum solution for the inductor effect was established, LBLTO impedance measurements could be properly treated and fitted to calculate their total lithium-ion conductivities.

Impedance measurements were performed for two sintered pellets of the LBLTO electrolyte to test the reproducibility of the measuring system. Measurements were performed in the temperature range of $30 \text{ }^\circ\text{C}$ up to $300 \text{ }^\circ\text{C}$. Higher temperatures could not be studied since the accuracy of the instrument was close to its limits. During the measurements at $300 \text{ }^\circ\text{C}$, total resistances for the electrolyte were near to 1Ω . In Annex 2 (Figure 7.2), the contour map of the instrument is shown. In this plot, the loss of accuracy of the analysis is presented as a function of the frequency and the impedance of the electrochemical system to be measured. The plot indicates that at 1Ω impedances, at frequencies from 1MHz to 10kHz a minimum $\pm 2\%$ error is assumed. Impedances below 1Ω , which would be obtained at higher temperatures, even higher errors would occur.

From the results, using the adequate equivalent circuit fitting (Figure 4.19 and Figure 4.21), and strategy 1, when required, the total resistance of the electrolyte was measured at each temperature. From the resistances, the total lithium-ion conductivities of the electrolyte were calculated. In Figure 4.27, ionic conductivities for the two LBLTO pellets as a function of the temperature are shown. In the same figure, bibliographic data obtained by V. Thangadurai [87] was also included.

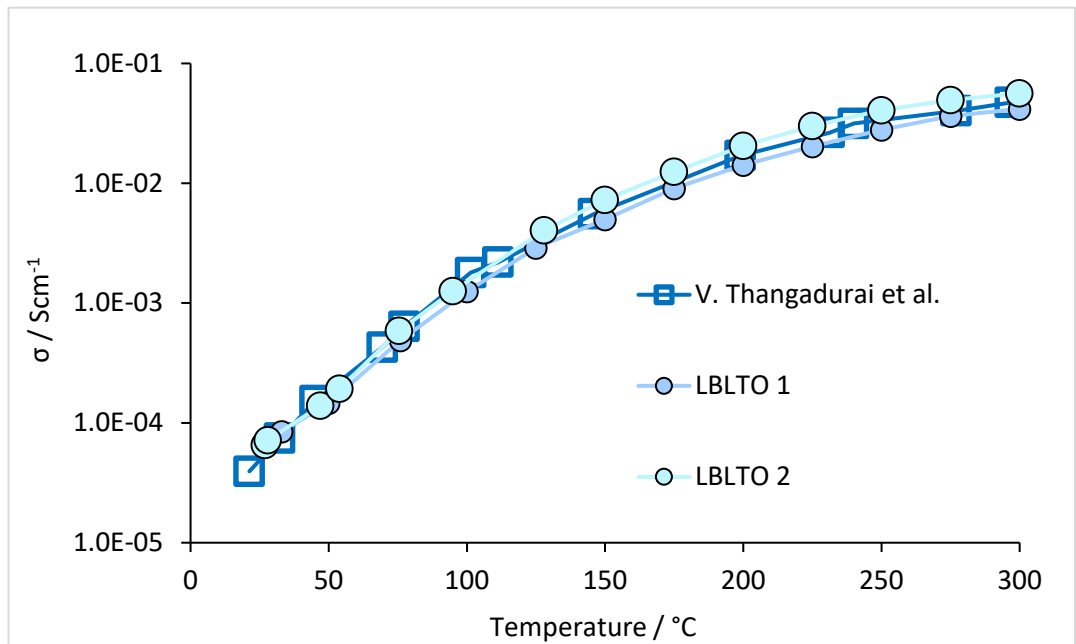


Figure 4.27. Total lithium-ion conductivities against temperature from two LBLTO pellets and bibliographic data [87].

As can be seen from Figure 4.27, both LBLTO pellets followed the tendency of the bibliographic data, which showed a logarithmic evolution. Ionic conductivities of $7.2 \cdot 10^{-5} \text{ S} \cdot \text{cm}^{-1}$ were obtained at 28 °C, increasing up to values of $5.6 \cdot 10^{-2} \text{ S} \cdot \text{cm}^{-1}$ at 300 °C. Although at higher temperatures no results were obtained. If this logarithmic behavior is maintained, a relatively subtle increase in ionic conductivity is expected. To determine whether both LBLTO pellets results were not significantly different from each other and bibliographic data, the results were linearized using the Arrhenius equation ([Eq. 4.7] and [Eq. 4.8]). The resulting Arrhenius plots obtained from each of the pellets are shown in Figure 4.28.

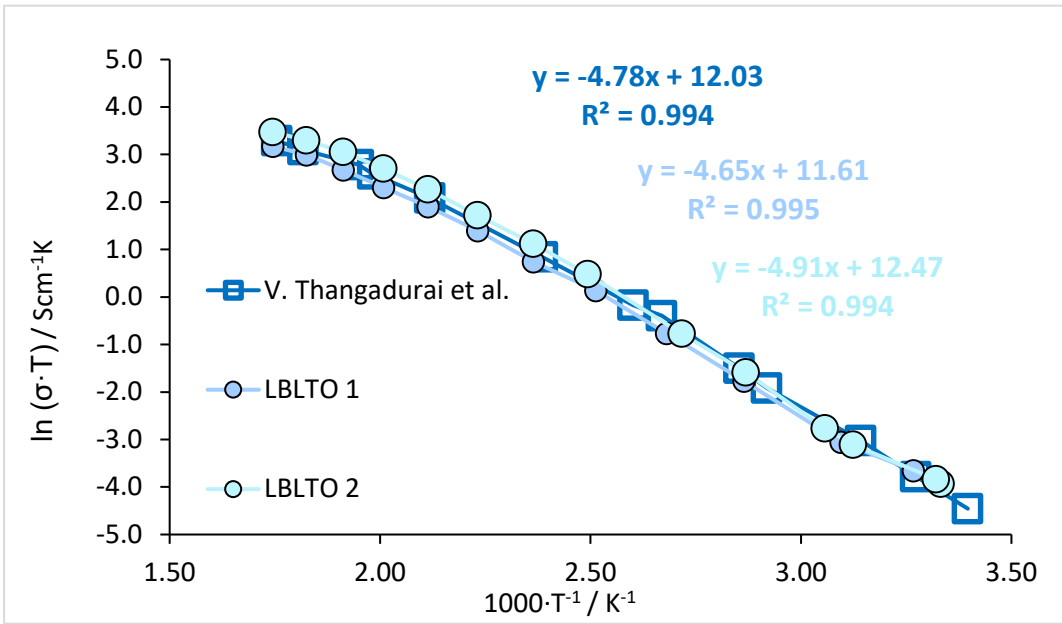


Figure 4.28. Arrhenius plots of the total lithium-ion conductivities from two LBLTO pellets and bibliographic data [87].

The calculated correlations (Figure 4.28) showed a linear relationship since all coefficients of determination were higher than 0.99. This first result demonstrated the quality of the data, as linear relationships are expected from an Arrhenius plot of the ionic conductivity. From these correlations, two evaluations were made: whether both pellets were similar, and whether the results obtained were in accordance with bibliographic data [87].

To first evaluate whether both pellets exhibited similar results, the confidence intervals (95%) of the slopes and constant terms of the correlations were determined. The results obtained from the comparison of these intervals are shown in Annex 3 (Figure 7.3). From the results, it was concluded that there were no significant differences between the pellets since the intervals overlapped.

Furthermore, both correlation's slopes were of the same order of magnitude, -4.65 K and -4.91 K for pellets 1 and 2 respectively, indicating that the measuring set-up built had good reproducibility. The slight variations between pellets' conductivities were assumed to be mainly caused to small differences between their sintering. Slight differences in grain size or densification between samples could have a measurable impact on the resistance of the electrolyte.

The second evaluation considered whether the results obtained were in accordance with bibliographic data. In this case, the confidence intervals (95%) of the correlations for the

pellets and the bibliographic data were compared (Figure 4.28), the resulting graph is shown in Annex 3 (Figure 7.3). From the study, it was concluded that there were no significant differences between the pellets and the bibliographic data since the intervals overlapped.

Moreover, the average value of the pellets' slopes (-4.78 K) was equal to the bibliographic one (-4.78 K), just determining a divergence of 0.1% between both. Such similarity confirmed the proper functioning of the experimental setup constructed. Furthermore, the results indicated the LBLTO electrolytes had similar final sintering to the one achieved by Thangadurai et al. [87].

Overall, the results were satisfactory, concluding that the developed and built experimental set-up could perform EIS measurements in a wide range of temperatures (30 °C – 300 °C). A stable signal was obtained during the measurements, in which no electrical disturbances were observed. Note that all the measurements fully complied with the KK test, further proving the stability of the experimental set-up. In addition, the experimental set-up yielded reproducible measurements since a low divergence was determined between two different LBLTO pellets.

The analysis parameters for EIS, together with the proposed equivalent circuits, have allowed determining satisfactorily the ionic conductivities of the LBLTO electrolyte. This last fact was demonstrated by the proximity of the experimental values to the bibliographic ones. Furthermore, the ionic conductivities values close to $6.0 \cdot 10^{-2} \text{ S} \cdot \text{cm}^{-1}$ obtained at 300 °C, demonstrate that the electrolyte exhibits a high lithium transport through its structure at high temperatures. This conductivity is expected to be enough to allow the connection between both sensor compartments (reference and working electrodes). At even higher temperatures, such as the ones where the sensor will be employed (400-600 °C), this ionic conductivity is expected to keep increasing.

Finally, it was concluded that the LBLTO synthesis and sintering conditions produced satisfactory electrolytes. The proximity observed between experimental and bibliographic ionic conductivities values demonstrated such a result. Note that, although the process conditions were modified with respect to Thangadurai et al. [87], the resulting electrolytes were of similar quality.

4.2.2. $\text{Li}_6\text{La}_3\text{Ta}_{1.5}\text{Y}_{0.5}\text{O}_{12}$

$\text{Li}_6\text{La}_3\text{Ta}_{1.5}\text{Y}_{0.5}\text{O}_{12}$ solid electrolyte was selected due to its promising characteristics (see section 4.1). Before the construction of the sensors, the synthesis and sintering procedure had to be optimized. Further below, both procedures as well as their characterization results are described.

4.2.2.1. Synthesis and Characterization

$\text{Li}_6\text{La}_3\text{Ta}_{1.5}\text{Y}_{0.5}\text{O}_{12}$ (LLTYO) was synthesized as described by S. Narayanan et al. [116]. Stoichiometric amounts of each reagent were weighted in order to obtain the desired composition. To synthesize 15 g of the ceramic powder, 7.59 g of La_2O_3 (Acros Organics, 99.9%), 2.97 g of $\text{Y}(\text{NO}_3)_3 \cdot 6\text{H}_2\text{O}$ (Alfa Aesar, 99.9%), 5.15 g of Ta_2O_5 (Acros Organics, 99.99%), and 7.06 g of LiNO_3 (Acros Organics, +99%) were weighted. LiNO_3 was added in 10 wt.% excess to compensate for lithium losses at elevated temperatures. The reagents were mixed and ground overnight in a rotary ball mill using zirconia balls and 2-propanol. The mixture was heated in air and kept at 700 °C for 6h with a heating ramp and controlled cooling of 350 °C/h, the resulting powder was finely ground with an agate mortar. The structural phases of the solid electrolyte determined by XRD analysis are shown in Figure 4.29A, while in Figure 4.29B the bibliographic pattern is shown [133,157].

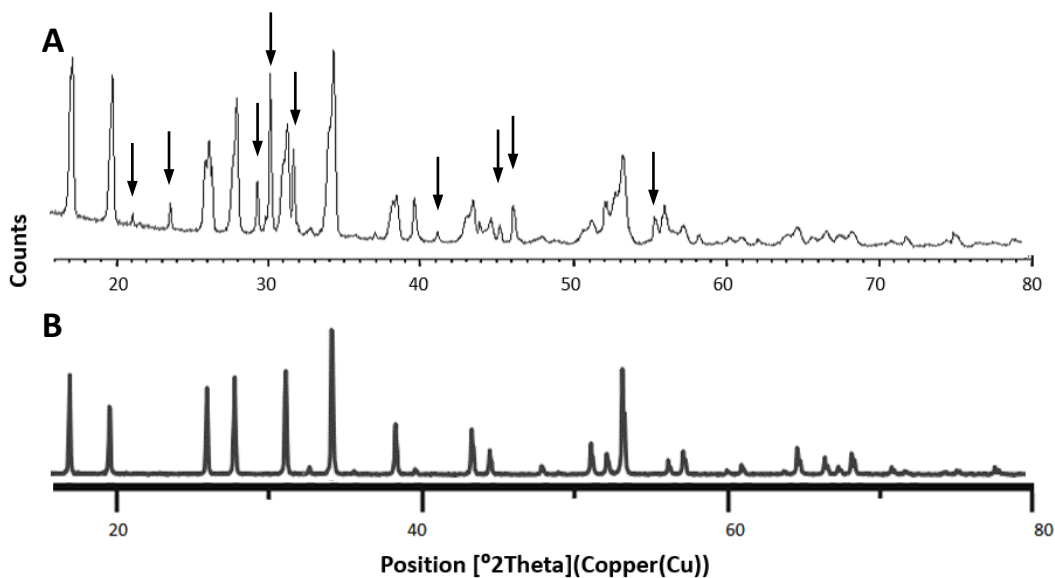


Figure 4.29. XRD patterns corresponding to A) synthesized LLTO electrolyte at 700 °C for 6h [158] and B) bibliographic data [133,157]. The black arrow designates an unexpected signal.

Despite that the synthesized powder showed the characteristic signals of the LLTYO cubic garnet structure [133,157], it also exhibited anomalous signals from some of its precursor reagents (indicated with arrows in Figure 4.29A). The presence of these impurities will have an impact on the electrochemical (ionic conductivity) and physical (hardness) properties of the solid electrolyte, in most situations causing its decrease [159,160]. The peak signals in $\sim 24^\circ$, 30° , 31° , 32° , 40° , 42° , and 48° angles belonged mostly to La_2O_3 and intermediate phases such as $\text{La}_2\text{O}_2\text{CO}_3$, LiTaO_3 , and other stable intermetallic oxides [58]. The peak signal at $\sim 21^\circ$ belonged to Li_2CO_3 which can be explained due to the reactivity of these electrolytes with CO_2 [133,161]. To ensure that no contamination had occurred, an EDS analysis was performed on the powder. As mentioned previously, lithium cannot be detected with this technique. The resulting EDS spectrum is shown in Figure 4.30.

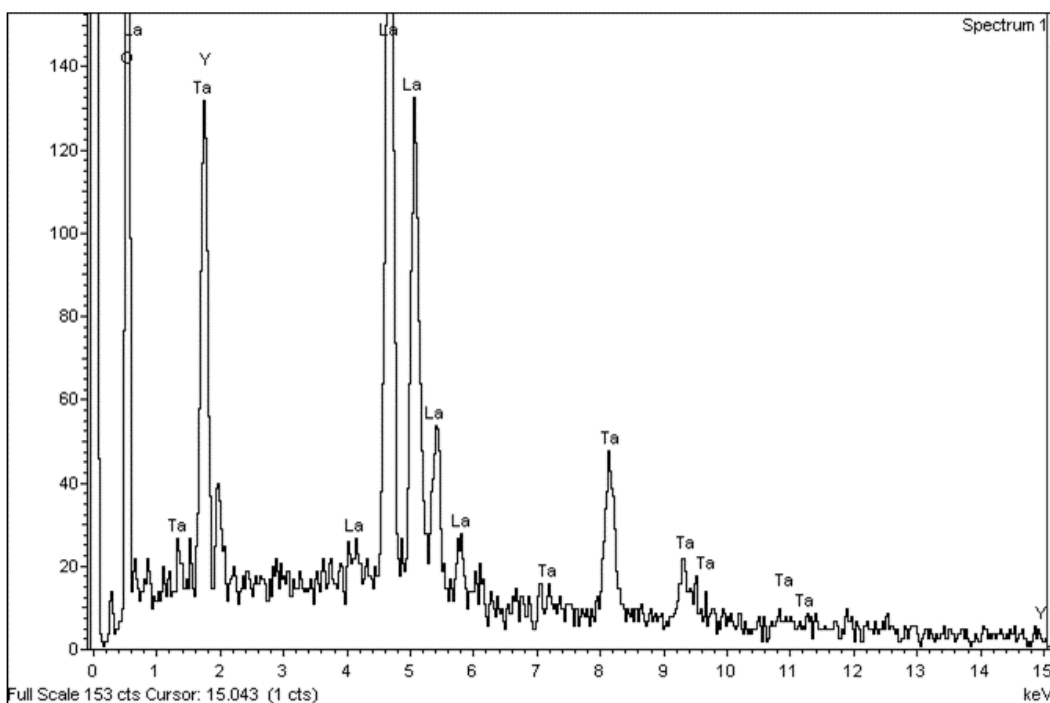


Figure 4.30. EDS of the synthesized LLTYO powder at 700 °C for 6h [158].

From Figure 4.30, only the characteristic elements of the solid electrolyte were identified (O, Y, La, and Ta), thus the hypothesis of a powder's contamination was discarded. However, it was concluded that the synthesis of the ceramic powder was not complete due to the XRD spectra. To achieve a more efficient synthesis, it was considered that a higher temperature than 700 °C could be required. Note that several of the impurities observed in the XRD exhibited melting points higher than 700 °C, such as Li_2CO_3 (720 °C) [58], thus the thermal treatment was modified to eliminate those components: from 700 °C for 6 hours to 700 °C

for 5 hours and 900 °C for 1 hour, with a heating ramp and controlled cooling of 350 °C/h. In Figure 4.31 the LLTYO synthesized powder and the bibliographic XRD patterns are shown [133,157].

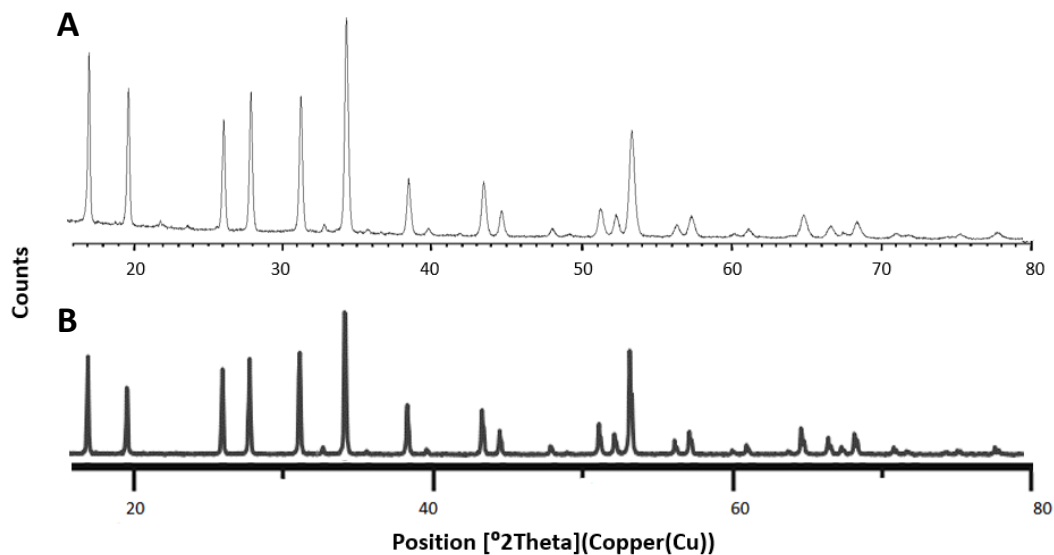


Figure 4.31. XRD patterns corresponding to A) synthesized LLTYO powder at 700°C for 5h and 900 °C for 1h and B) bibliographic data [133,157].

The powder showed a single phase of the garnet-type structure and good agreement with bibliography data. No anomalous peaks were obtained during the analysis, indicating that the synthesis was satisfactory. The particle size distribution was analyzed with SEM. Two micrographs of the synthesized powder are presented in Figure 4.32.

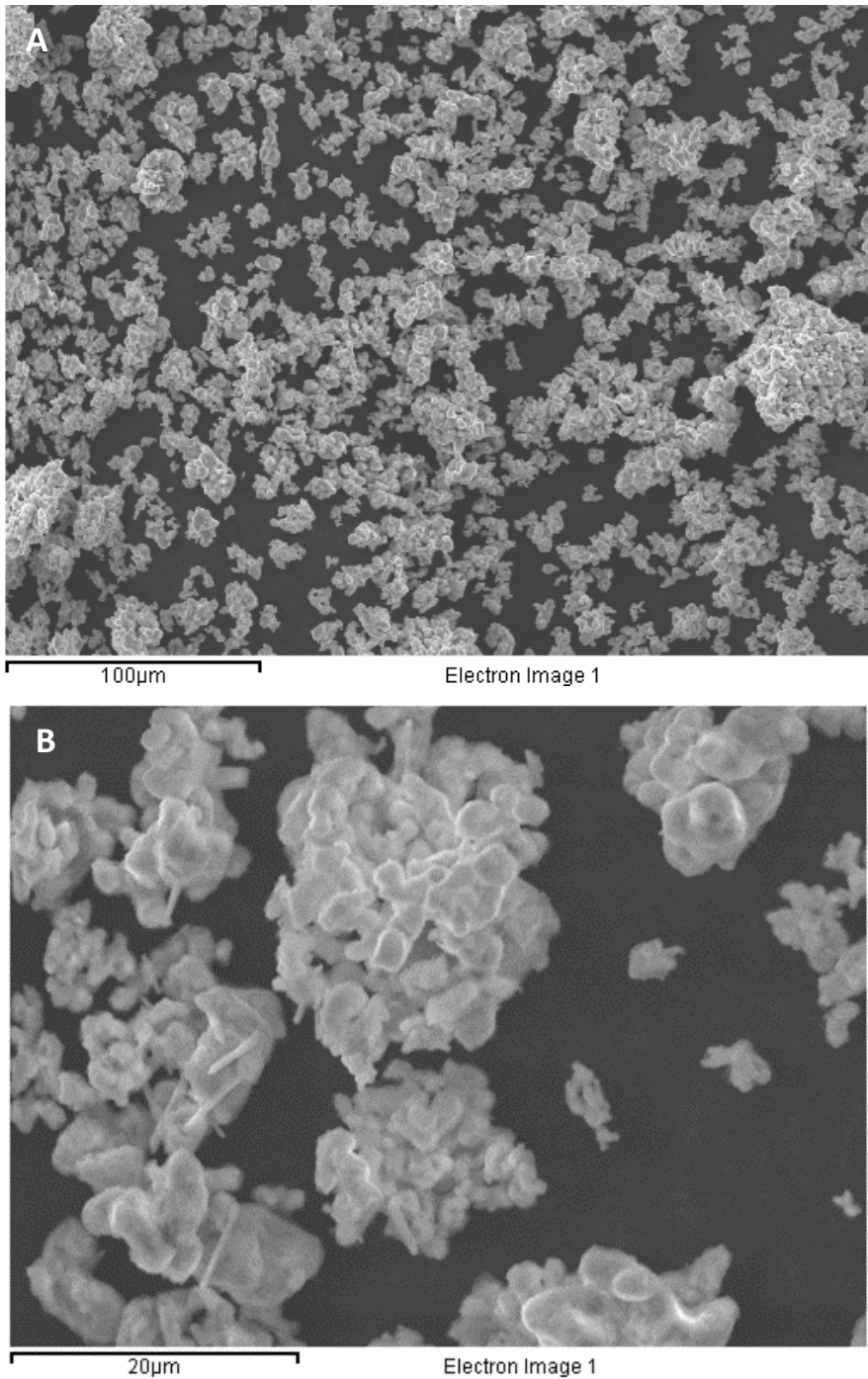


Figure 4.32. SEM micrograph of the synthesized LLTYO powder at 700 °C for 5h and 900 °C for 1h at different magnifications: A) 500x and B) 1500x.

The SEM micrographs showed a particle size distribution between 2 to 10 µm approximately. The heterogeneity observed in Figure 4.32A resulted from particle agglomeration that was present in the powder. EDS analysis was also performed to check

for possible impurities and quantify the elements forming the ceramic. In Figure 4.33 the EDS spectrum of the ceramic powder is shown.

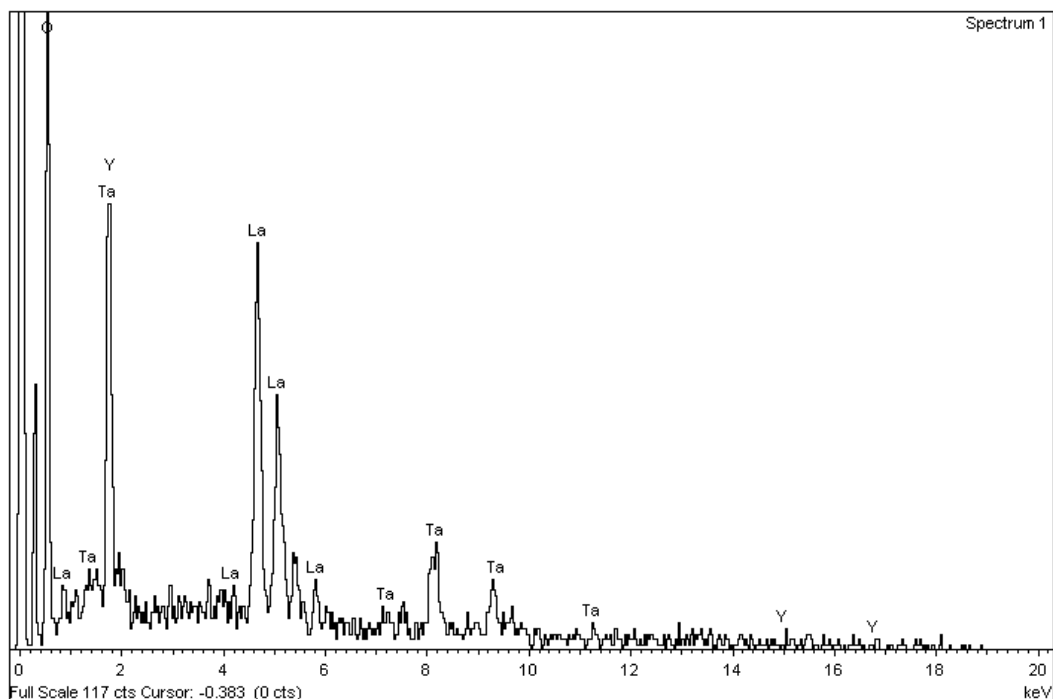


Figure 4.33. EDS spectrum of the synthesized LLTYO ceramic powder at 700 °C for 5h and 900 °C for 1h.

Figure 4.33 showed that the synthesized powder did not present noticeable impurities in its formulation (in concentrations above 1% w/w). As it can be observed from the spectrum, only La, Ta, Y, and O were detected. The results were processed with the Oxford INCA software to determine experimental atomic relationships. Experimental and theoretical atomic relationships for each of the identified metallic elements are shown in Table 4.8.

Table 4.8. Experimental and theoretical atomic relationship for each identified metallic element forming the LLTYO electrolyte.

Element	Experimental atomic relationship	Theoretical atomic relationship
La	3.0	3.0
Ta	1.5	1.5
Y	0.7	0.5

When comparing these values with the theoretical formulation of the ceramic $\text{Li}_6\text{La}_3\text{Ta}_{1.5}\text{Y}_{0.5}\text{O}_{12}$, it was observed that La and Ta showed identical experimental atomic relationships. For the Y element, a small deviation was determined between experimental and theoretical values. Such a result was associated with an increase in the measurement uncertainty due to yttrium small content in the electrolyte. Nevertheless, the deviation was considered not significant, and it was concluded that the synthesized powder presented a correct stoichiometry.

Finally, the lithium content in the ceramic powder was quantified using AAS-Flame analysis. A resulting value of 46.99 mg Li/g of ceramic was obtained which represents 4.70% of the total weight, being the theoretical value of 43.10 mg Li/g (4.31% w/w). From the result, it was considered that both lithium concentration values were of the same order of magnitude, thus the electrolyte's lithium content was in good agreement with its nominal value. A spiked sample was also performed yielding a recovery of 97.0%, thus no matrix effects were influencing the quantification.

4.2.2.2. Sintering and Characterization

Once LLTYO powder was characterized, it was pressed as a pellet. The green body weighed around 0.60 g and measured about 1.5 mm in thickness and 13 mm in diameter. After that, pellets were covered with a powder of the same mother composition (to reduce the lithium loss due to volatilization) [149,157] and were sintered in air at 900 °C for 24 hours. Then, the temperature was increased to 1100 °C and kept constant for 6 hours. It is worth mentioning that to obtain good densification of the pellet, a heating ramp and controlled cooling of 150 °C/h were used [158]. The obtained XRD pattern of the ceramic pellet is shown in Figure 4.34A, while in Figure 4.34B the XRD bibliographic pattern is shown [133,157].

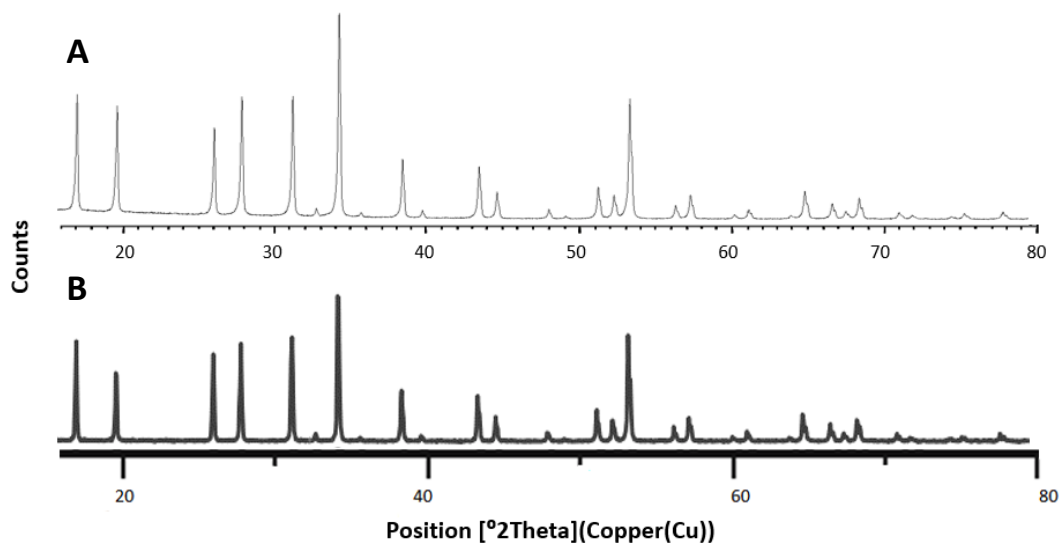


Figure 4.34. Corresponding XRD patterns to A) sintered LLTYO pellet at 900 °C for 24h and 1100 °C for 6h, and B) bibliographic data [133,157].

It can be observed in Figure 4.34 that the powder showed a single phase of the garnet-type structure in good agreement with bibliography data. To analyze the surface microstructure of the pellet, SEM analysis was performed. In Figure 4.35, two resulting micrographs are presented.

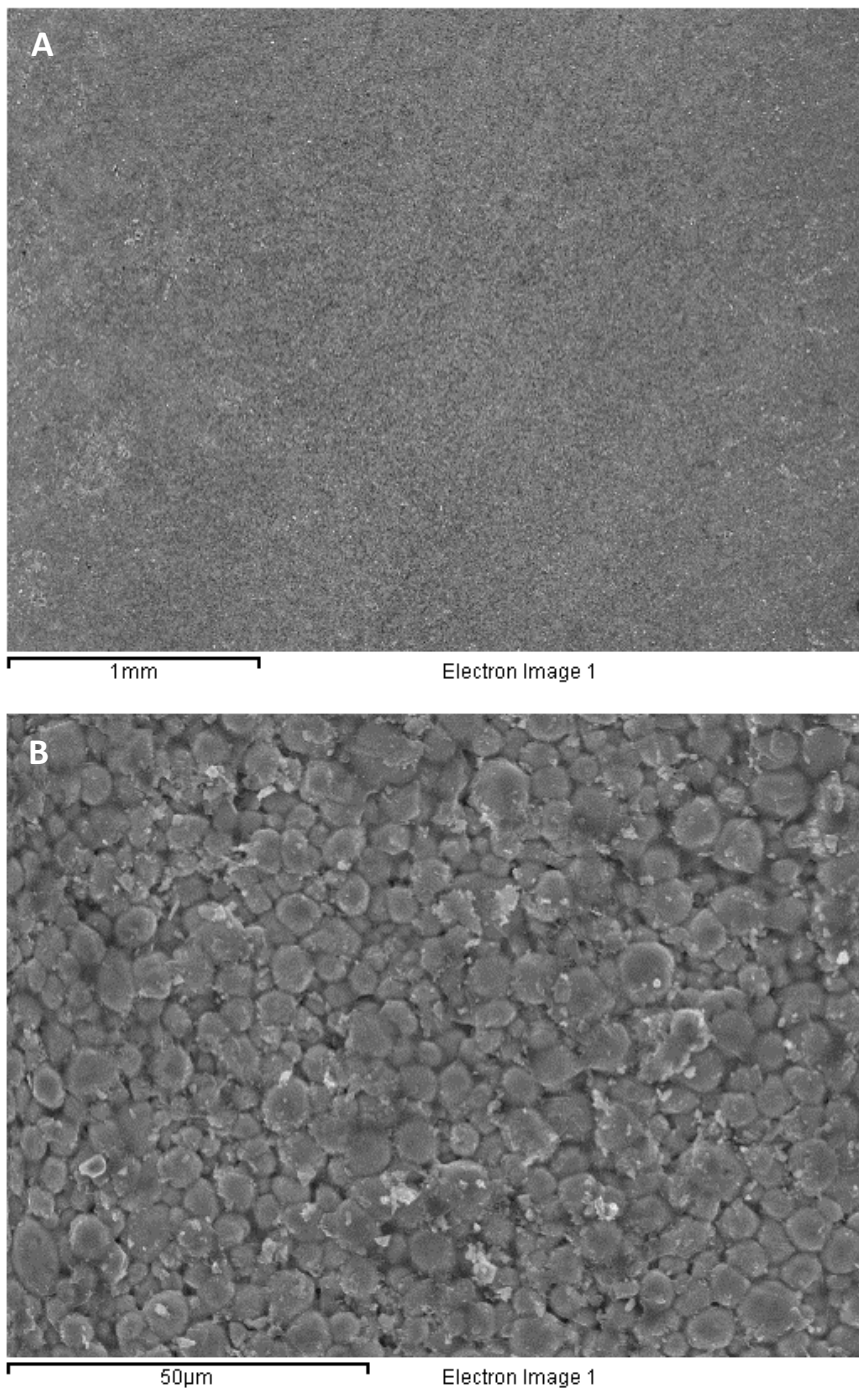


Figure 4.35. SEM micrograph of the LLTYO sintered pellet at 900 °C for 24h and 1100 °C for 6h at different magnifications: A) 50x and B) 750x.

SEM micrographs shown in Figure 4.35A showed a compact and homogeneous surface with no fissures on its surface. With higher magnification, it can be observed that the sintering of the ceramic was suitable since homogeneous grain distribution was obtained with an

approximate grain size distribution between 2 to 10 μm . In addition, low porosity was observed on the surface of the pellet. From the different micrographs, a porosity of $0.7\% \pm 0.1\%$ was measured with the open-source image processing software ImageJ. This value is in good agreement with the one obtained in the bibliography: 0.5% [133]. EDS analysis was also performed to check for possible impurities and quantify the elements conforming the ceramic pellet. In Figure 4.36 it is shown the EDS spectrum of the solid electrolyte.

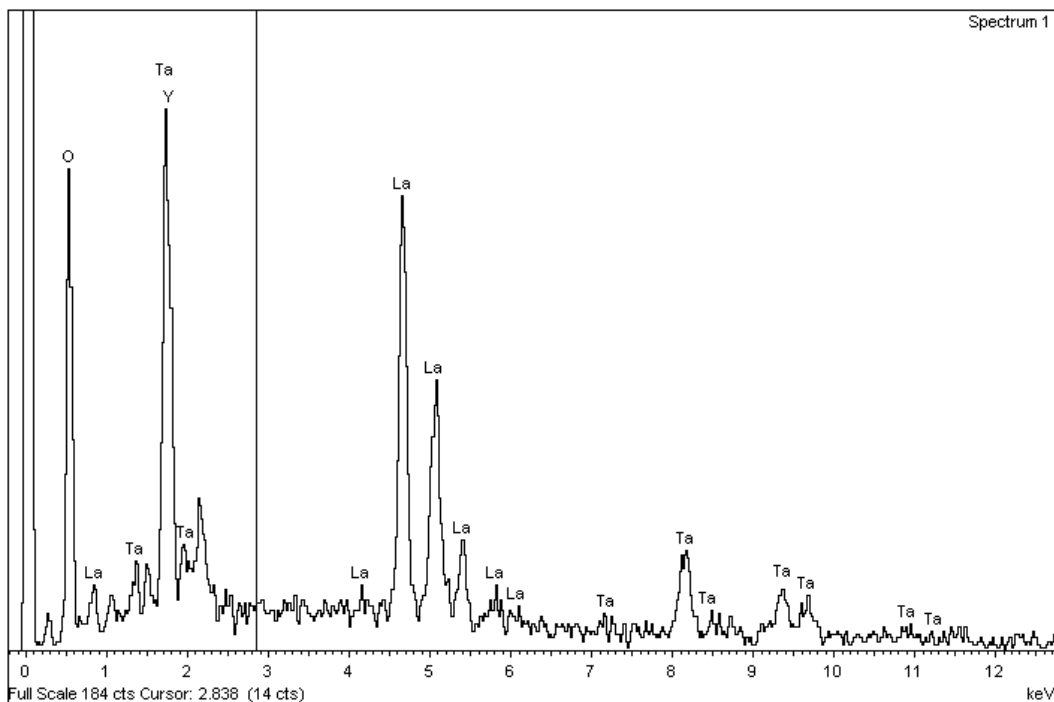


Figure 4.36. EDS spectrum of the LLTYO pellet

Figure 4.36 showed that the synthesized powder did not incorporate impurities and only La, Ta, Y, and O were detected. From the processed results experimental atomic relationships were determined and were compared to theoretical ones (Table 4.9).

Table 4.9. Experimental and theoretical atomic relationship for each identified metallic element forming the LLTYO sintered electrolyte.

Element	Experimental atomic relationship	Theoretical atomic relationship
La	2.6	3.0
Ta	1.5	1.5
Y	0.3	0.5

When comparing these values with the proper formulation of the ceramic $\text{Li}_6\text{La}_3\text{Ta}_{1.5}\text{Y}_{0.5}\text{O}_{12}$, it was observed that both La and Y were below their theoretical atomic relationships. This fact could be explained due to a slight over quantification of the Ta element, and since this element is used as the standard to calculate all the other relations, La and Y were under quantified. Nevertheless, it was considered that theoretical and experimental relationships were all of the same order of magnitude. Therefore it was concluded that the sintered electrolyte exhibited a correct stoichiometry.

The lithium content in the sintered electrolyte was quantified using AAS-Flame analysis. A resulting value of 43.30 mg Li/g of ceramic was obtained which represents 4.33% of the total weight, being the theoretical value of 43.10 mg Li/g (4.31% w/w). It was considered that no significant lithium loss occurred, since both values were of the same order of magnitude. A spiked sample was also performed yielding a recovery of 101.3%, thus no matrix effects were influencing the quantification.

Finally, the cross-section of the solid electrolyte was microscopically examined via SEM. Despite that the surface porosity was already determined, it is important to check if the inner porosity does not form crossing channels that could connect both sides of the pellet. To this aim, the pellet was encapsulated with an epoxy resin (Epofix Kit, Struers) and was cured overnight. Then, the embedded pellet was cut with a low-speed precision cutter (Buehler Isomet Low Speed Saw). Its cross-section micrograph and its EDS analysis are presented in Figure 4.37.

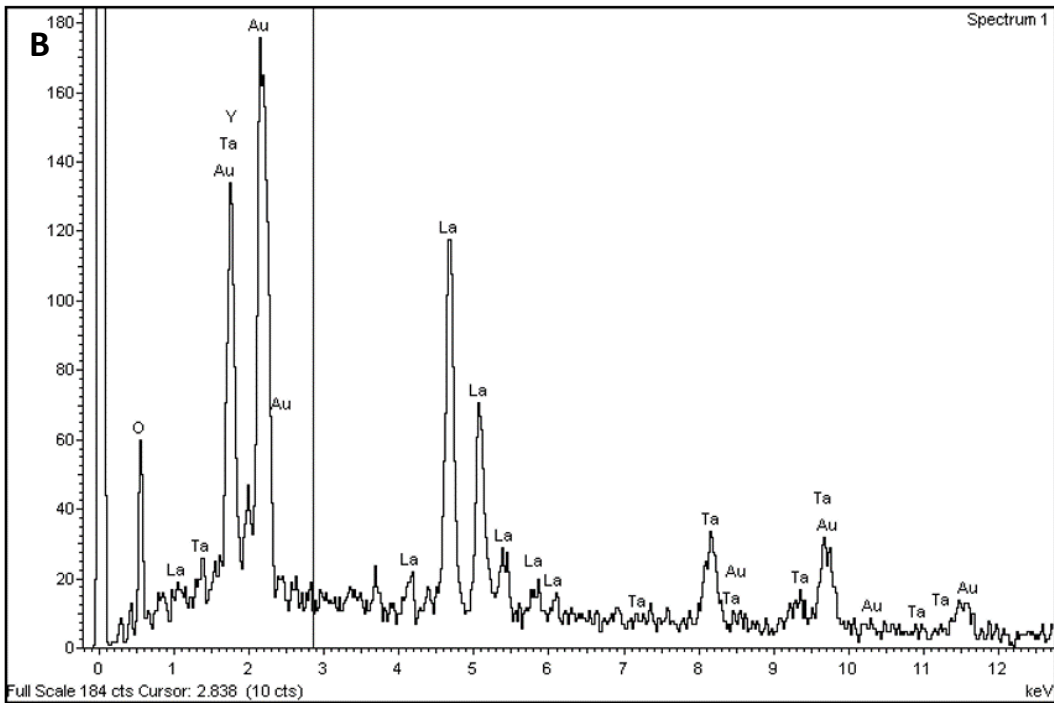
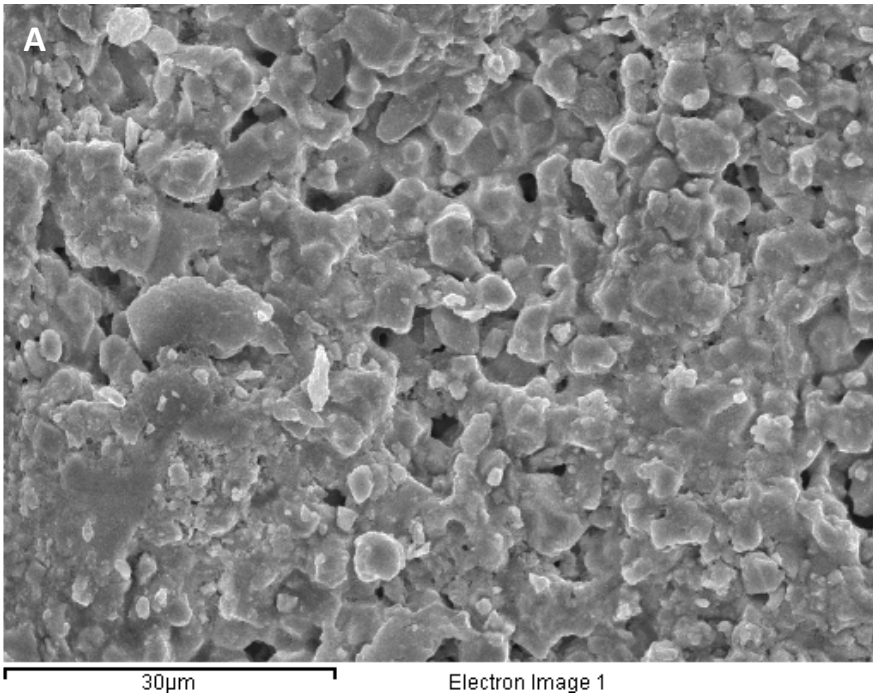


Figure 4.37. A) SEM micrograph of the cross-section and B) EDS spectrum of a sintered LLTYO pellet at 900 °C for 24h and 1100 °C for 6h.

Although some holes can be observed in the inner part of the pellet, which could be caused due to the release of some grains during the cutting process, no pathways connecting both sides of the pellet were detected. Porosity was measured from different micrographs,

yielding a value of $2.3 \pm 0.7\%$. This value was slightly higher than the one previously determined for the pellet's surface (0.7%). Nevertheless, both values were considered of the same order, since both indicated the good densification of the electrolyte. The performed EDS analysis (Figure 4.37B) showed only signals belonging to the solid electrolyte. Therefore, no impurities were incorporated during the sintering process.

The characterization analysis concluded that the sintered LLTYO pellets at 900 °C for 24h and 1100 °C for 6h, with a heating ramp and controlled cooling of 150 °C/h, exhibited suitable sintering and adequate crystallographic structures. From this thermal process, the electrolyte was shaped into discs suitable for the construction of lithium sensors.

4.2.2.3. Ionic Conductivity

Similar to the LBLTO electrolyte, the determination of LLTYO ionic conductivity was of double interest: to evaluate the quality of the synthesized and sintered electrolyte. LLTYO ionic conductivity was measured as described in section 4.2.1.3.

The first step was to determine how the temperature influenced the impedance of the system. In Figure 4.38, Nyquist plots obtained of the solid electrolyte at 30 °C, 75 °C, 125 °C, and 175 °C are shown.

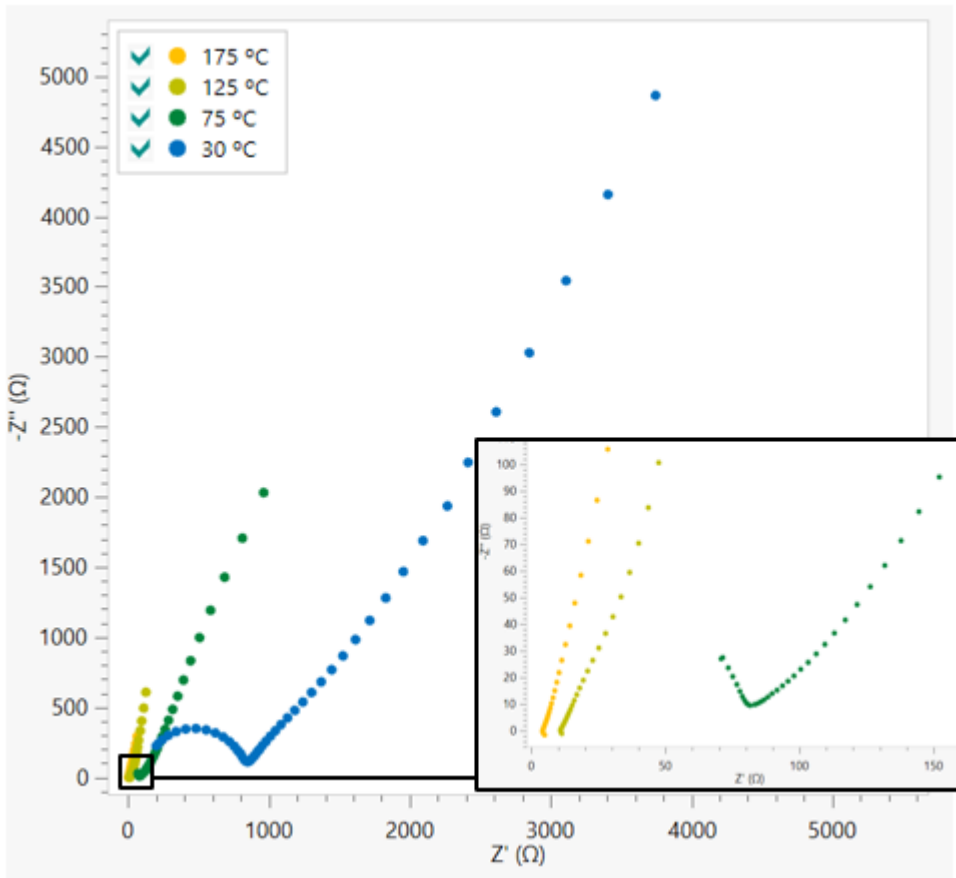


Figure 4.38. Nyquist plots of a LLTYO sintered pellet at 30 °C, 75 °C, 125 °C, and 175 °C.

In Figure 4.38, it can be observed similar Nyquist plots to the ones obtained from the LBLTO electrolyte. In those, the real part of the impedance (Z') diminished as the temperature increased. The semicircle obtained at 30 °C, in the high-frequencies region, was attributed to the bulk and grain boundary impedances. The capacitive “tail” that appears on the low-frequency side indicated the blocking of mobile Li^+ ions [79]. At temperatures higher than 125 °C, upon increasing the ionic conductivity of the electrolyte, it was observed the influence of the electrical connections’ inductive effect. In the insert part of the Nyquist plot of Figure 4.38, it can be observed that at 125 °C and 175 °C the imaginary impedance’s part ($-Z''$) started to achieve negative values. Therefore, in the low-temperature region, impedance data were fitted with the EC described in Figure 4.19 ($R_1(R_2L_1)(R_3CPE_1)(R_4CPE_2)CPE_3$). However, at temperatures equal to or higher than 100 °C, the influence of the inductor made it necessary to test other EC. Thus, in this scenario, the three strategies described in section 4.2.1.3 that accounted for the inductor effect, were also explored. Briefly, the first strategy consisted in discarding the high-frequency data, the

second one corrected the raw impedance data to withdraw the inductor effect, and the third one kept the initial EC.

When applying each of these 3 strategies to the experimental data, the fitted equivalent circuits yielded coherent results. The resistances and the ionic conductivity values are shown in Table 4.10.

Table 4.10. Resistances and ionic conductivities for the LLTYO electrolyte as a function of the temperature from each of the strategies.

Temperature / °C	Strategy 1		Strategy 2		Strategy 3	
	R / Ω	σ / S·cm ⁻¹	R / Ω	σ / S·cm ⁻¹	R / Ω	σ / S·cm ⁻¹
100	31.6	2.62E-03	30.4	2.72E-03	34	2.44E-03
125	10.9	7.60E-03	11.0	7.53E-03	12.8	6.47E-03
150	5.09	1.63E-02	6.44	1.29E-02	6.75	1.23E-02
175	3.1	2.67E-02	3.92	2.11E-02	3.23	2.56E-02
200	1.58	5.24E-02	2.80	2.96E-02	1.67	4.96E-02

As the temperature increased the total resistance of the electrolyte diminished as expected. At 100 °C, a resistance close to 30 Ω was determined, while at 200 °C, it diminished to values close to 2 Ω. Even though the values followed an adequate trend, there were small differences between the ionic conduction resistances determined by each of the strategies.

To compare the 3 solutions, the total lithium-ion conductivities were calculated (section 3.2, [Eq. 3.2] and [Eq. 3.3]) and were compared with bibliographic data. Ionic conductivities were calculated at different temperatures (100 – 200 °C) to be able to obtain a consistent data distribution. In Figure 4.39, it is shown the total lithium-ion conductivities determined for the Li₆La₃Ta_{1.5}Y_{0.5}O₁₂ electrolyte from each of the strategies as a function of the temperature. Bibliographic data from S. Narayanan et al. [157] was also included.

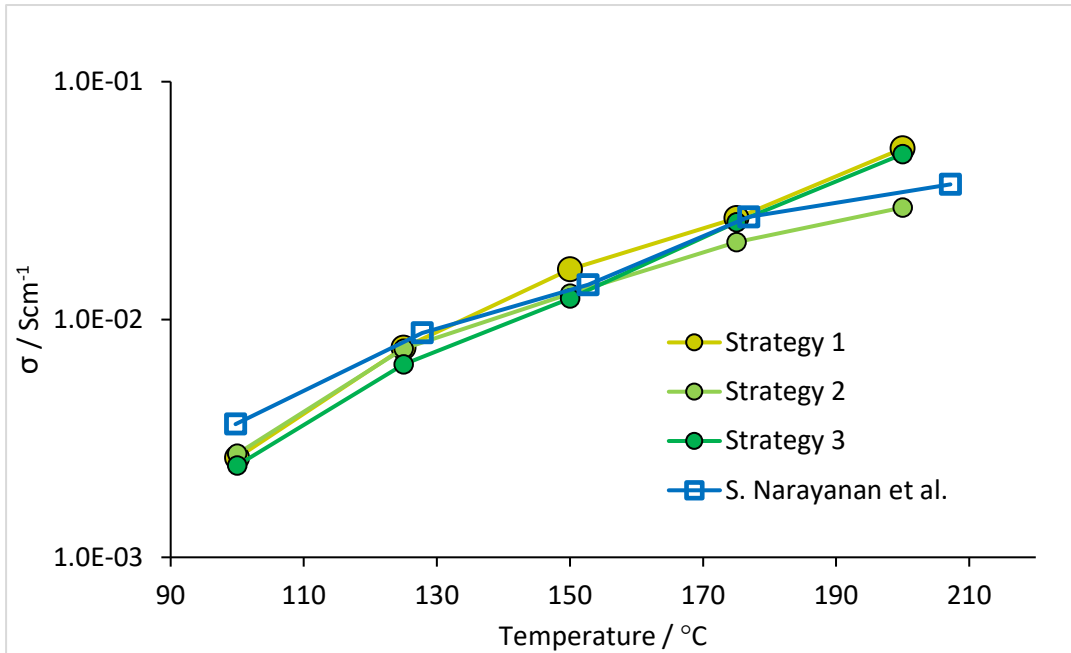


Figure 4.39. Total lithium-ion conductivities as a function of the temperature and strategy for an LLTYO electrolyte. Bibliographic data from S. Narayanan et al. [157] were also included.

All strategies yielded consistent results which were close to the values reported by S. Narayanan. Although small deviations were obtained, the overall tendency of the ionic conductivity towards temperature was similar for all the analyzed data. The small differences when compared to the bibliographic values were not considered any kind of error, since the sintering procedures could show several differences due to their intrinsic craftsmanship. Thus, small deviations were expected since differences in the grain size or densification could affect the total resistance of the electrolyte. To further study each of these strategies, the data was linearized employing the Arrhenius equation ([Eq. 4.7], [Eq. 4.8]). When plotting the natural logarithm of the total lithium-ion conductivities versus the inverse of the temperature, linear relationships were obtained. The correlations for the LLTYO electrolyte are shown in Figure 4.40.

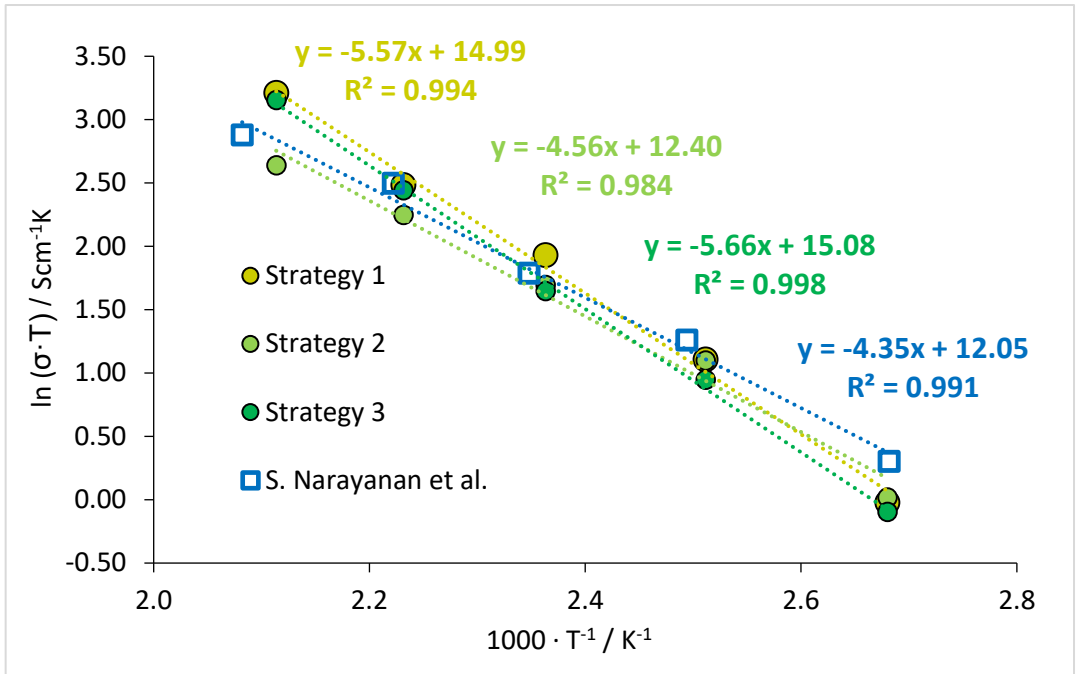


Figure 4.40. Arrhenius plots of the total lithium-ion conductivities of the LLTYO electrolyte from each of the three applied strategies and bibliographic data [157].

From Figure 4.40, four linear correlations are presented. Each of them was in good agreement with the Arrhenius equation since coefficients of determination (R^2) close to or superior to 0.99 were obtained. The slopes of these linear correlations are directly proportional to the activation energy for the ionic transport and their y-intercept (constant) is the natural logarithm of the pre-exponential term. To determine if significant differences were obtained between each of these strategies and whether these were similar to the bibliographic one, the confidence intervals (95%) of the slope and the constant term of each linear correlation were calculated. These intervals were compared and the results obtained are shown in and are as shown in Annex 4 (Figure 7.4). From the study, it was concluded that there were no significant differences between strategies 1, and 2 and bibliographic data. Furthermore, the results indicated that statistically there was not an optimal strategy between 1 and 2.

Since the statistical study was not conclusive, among the two remaining strategies, strategy 1 was considered the optimal solution due to similar reasons as the ones discussed for the LBLTO electrolyte. First, it was the simplest solution of all three. And second, because eliminating the high-frequency region was a coherent solution to remove the inductor's parasitic effect.

Therefore, strategy 1 was used for all the impedance measurements that showed a certain inductor effect: when the total LLTYO electrolyte resistance was below 100 Ω . Once the optimum solution for the inductor effect was determined, LLTYO impedance measurements could be properly treated and fitted to calculate their total lithium-ion conductivities.

To test the reproducibility of the measuring system, impedance measurements were performed on two LLTYO sintered pellets. Measurements were performed in the temperature range of 30 $^{\circ}\text{C}$ up to 200 $^{\circ}\text{C}$. For this electrolyte, at higher temperatures than 200 $^{\circ}\text{C}$, the limit of accuracy of the technique was reached. From EIS results, using the adequate equivalent circuit fitting (Figure 4.19 and Figure 4.21) and strategy 1 when required, the total resistance of the electrolyte and the total lithium-ion conductivity were calculated. In Figure 4.41, ionic conductivities for each pellet as a function of the temperature are shown. In the same figure, bibliographic values reported by S. Narayanan [157] are also included.

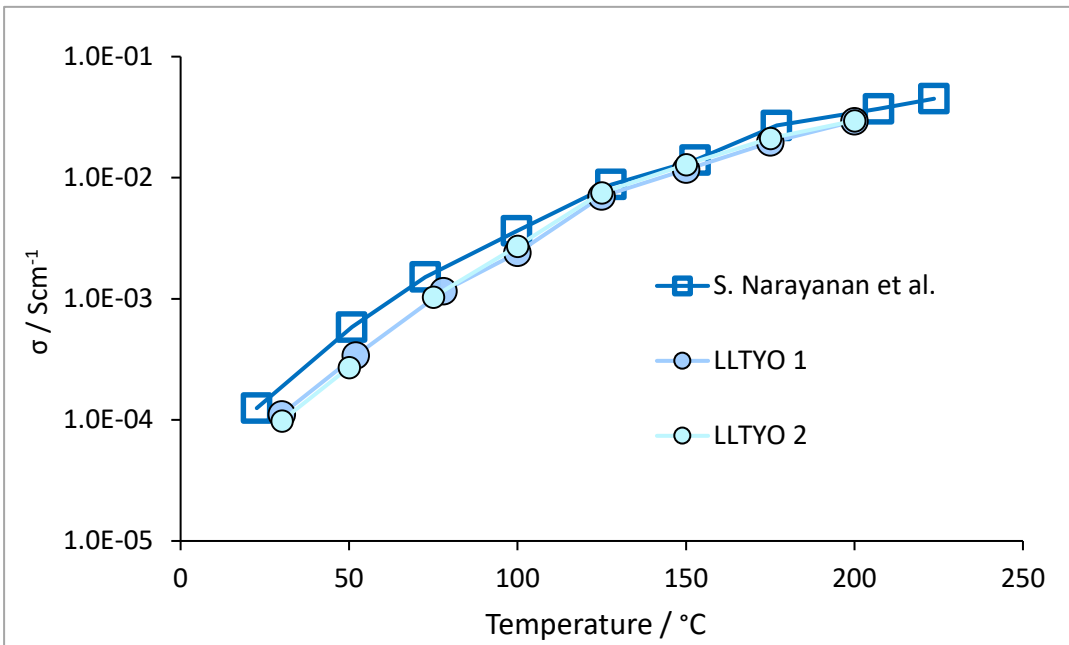


Figure 4.41. Total lithium-ion conductivities against temperature for the LLTYO electrolyte [157].

It can be observed in Figure 4.41, that both LLTYO pellets exhibited similar results and followed the same tendency as the bibliographic data, which exhibited a logarithmic evolution. As observed from the results of LBLTO, strategy 1 also yielded coherent results for the LLTYO electrolyte. Ionic conductivities of $1.1 \cdot 10^{-4} \text{ S}\cdot\text{cm}^{-1}$ were obtained at 30 $^{\circ}\text{C}$, increasing up to values of $3.0 \cdot 10^{-2} \text{ S}\cdot\text{cm}^{-1}$ at 200 $^{\circ}\text{C}$. To determine whether both LLTYO pellets'

results were not significantly different from each other and bibliographic data, the results were linearized using the Arrhenius equation ([Eq. 4.7] and [Eq. 4.8]). The resulting Arrhenius plots obtained from each of the pellets are shown in Figure 4.42.

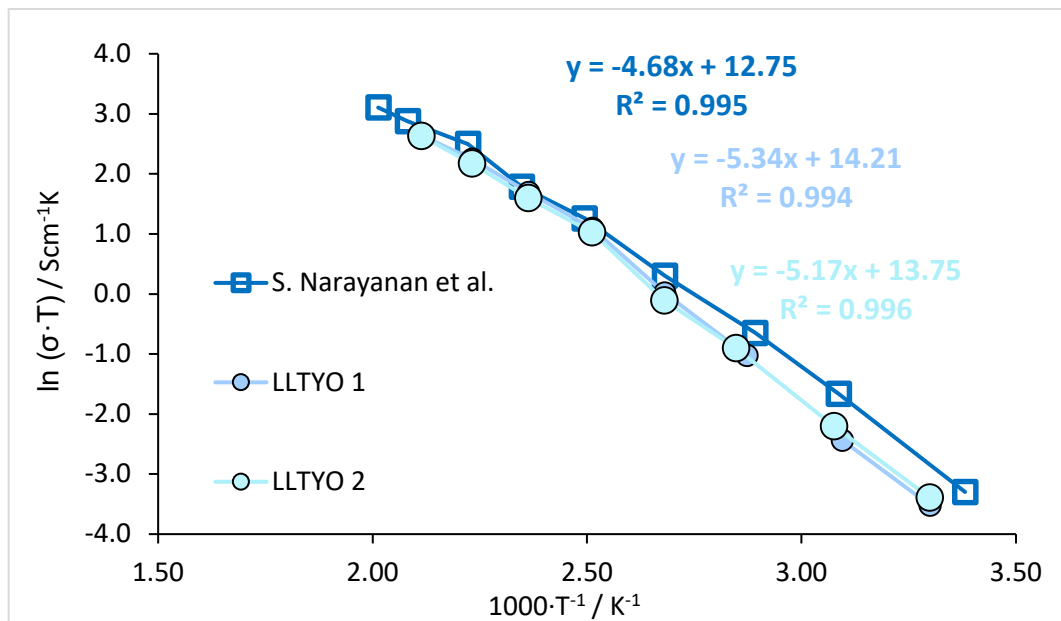


Figure 4.42. Arrhenius plots of the total lithium-ion conductivities from two LLTYO pellets and bibliographic data [157].

The calculated correlations (Figure 4.42) showed a linear relationship since all coefficients of determination were higher than 0.99. This first result demonstrated the quality of the data, as linear relationships are expected from an Arrhenius plot of the ionic conductivity. From these correlations, two evaluations were made: whether both pellets were similar, and whether the results obtained were in accordance with bibliographic data [157].

To first evaluate whether both pellets exhibited similar results, the confidence intervals (95%) of the slopes and constant terms of the correlations were determined. The results obtained from the comparison of these intervals are shown in Annex 5 (Figure 7.5). From the results, it was concluded that there were no significant differences between the pellets since the intervals overlapped.

Furthermore, both correlation's slopes were of the same order of magnitude, -5.34 K and -5.17 K for pellets 1 and 2 respectively, indicating that the measuring setup constructed had good reproducibility. The slight variations between pellets' conductivities were assumed to be mainly caused to small differences between their sintering.

The second evaluation considered whether the results obtained were in accordance with bibliographic data. To do so, the confidence intervals (95%) of the correlations for the pellets and the bibliographic data were compared (Figure 4.42), the resulting graph is shown in Annex 3 (Figure 7.3). From the study, it was concluded that there were no significant differences between the pellets and the bibliographic data since the intervals overlapped.

Moreover, the average value of the pellets' slopes (-5.26 K) was similar to the bibliographic one (-4.68 K), determining a divergence of 12.3% between both. Note that, the largest dissimilarities between the experimental and bibliographic ionic conductivities are observed in the low-temperature region (25-100 °C). As the temperature increases, these differences are minimized and both values stay close. Therefore, the ionic conductivities at larger temperatures are expected to keep a similar trend as the one reported by S. Narayanan et al. [157]. The results indicated the LLTYO electrolytes had similar final sintering to the one achieved by S. Narayanan et al. [157], and it was confirmed once more the adequate functioning of the experimental setup constructed.

From the results, it was also concluded that the LLTYO synthesis and sintering conditions produced satisfactory electrolytes. The proximity observed between experimental and bibliographic ionic conductivities values demonstrated such a result. Note that, although the synthesis conditions were modified with respect to Narayanan et al. [157], the resulting electrolytes were of similar quality.

Overall, it could be concluded that the EIS experimentation was satisfactory. One on hand, the experimental set-up designed and constructed yielded ionic conductivity results that were in accordance with bibliographic values. This also supported the adequate EIS test parameters and the posterior signal treatment. On the other hand, these results were reproducible, consolidating the proper functioning of the set-up, while demonstrating the reproducibility of the pellets' sintering procedure. Consequently, it was assumed that the constructed measuring set-up and the posterior signal treatment provided adequate know-how to be able to perform ionic conductivity measurements on solid electrolytes.

4.2.3. Comparison and Discussion of the Solid Electrolytes

$\text{Li}_6\text{BaLa}_2\text{Ta}_2\text{O}_{12}$ and $\text{Li}_6\text{La}_3\text{Ta}_{1.5}\text{Y}_{0.5}\text{O}_{12}$ were selected as solid electrolytes candidates to be used in the construction of electrochemical sensors due to their interesting properties:

- Thermal stability up to 600 °C.
- Low reactivity towards molten lithium.
- Low reactivity towards moisture and air.
- Higher lithium-ion conductivity than $10^{-5} \text{ S}\cdot\text{cm}^{-1}$ at 25 °C.

It is worth mentioning that, because the electrolytes were not commercially available, these had to be synthesized and sintered in the laboratory. Although their synthesis and sintering procedures are reported, during those processes, several variables can influence the quality of the final product: temperature, time, the grain size distribution of the precursors, etc. For these reasons, these procedures had to be optimized.

To facilitate the comparison and discussion of the results for LBLTO and LLTYO electrolytes, these were divided into three parts: their synthesis, sintering, and ionic conductivity.

Concerning the electrolytes synthesis, LBLTO final conditions were kept as the ones described by V. Thangadurai et al. [87]: 700 °C for 6h. Conversely, the LLTYO electrolyte synthesis conditions described by Narayanan et al. [157] were modified. From its XRD spectra, it was observed that using its original thermal conditions its synthesis was incomplete. To achieve a complete synthesis, a two-step temperature program of 700 °C for 5 hours and 900 °C for 1 hour was used. Although no differences were made when compared to S. Narayanan's publication, it could be assumed that this difference in the final synthesis conditions could be related to the size of the reagents. Small particle size is related to an increase in reactivity [162], which explains why 700 °C could have been enough to achieve a complete synthesis. Therefore, smaller particle sizes due to reagents from distinct suppliers or a finer-grain powder resulting from the subsequent milling procedure before the synthesis could be a possible explanation.

After their synthesis, both electrolytes showed homogeneous particle sizes when observed from SEM analysis. Their approximate size distributions were similar: 1 to 5 μm and 2 to 10 μm for LBLTO and LLTYO respectively. LLTYO's larger particle size could be related to the 900 °C for 1 h thermal step that was added to its synthesis conditions. As a result, the electrolyte particles could have grown larger [163].

From the synthesized powders no noticeable impurities were observed from the EDS analysis. Furthermore, the determined elements belonging to each of the electrolytes presented a correct stoichiometry: Ba: 1.0, La: 2.0, and Ta: 2.0 for $\text{Li}_6\text{BaLa}_2\text{Ta}_2\text{O}_{12}$ electrolyte and La: 3.0, Ta: 1.5, and Y: 0.7 for $\text{Li}_6\text{La}_3\text{Ta}_{1.5}\text{Y}_{0.5}\text{O}_{12}$. Thus, demonstrating that no contaminations occurred during all the different steps of the synthesis procedures.

Both electrolyte powders were also in good agreement with their respective bibliographic garnet-phase pattern. Despite that, an anomalous peak was identified in the XRD analysis of the LBLTO powder. This peak was found near the 55° angle and was associated with an intermediate product ($\text{Li}_2\text{Ba}_3\text{Ta}_2\text{O}_9$). In this case, since it was considered a minor impurity, the synthesis conditions were not modified.

Lithium concentration was also in its correct order of magnitude for both electrolytes. LBLTO exhibited only a 1.9% (w/w) lithium loss, while LLTYO only consumed a 1.0% (w/w) of the 10% (w/w) lithium excess added to account for its volatilization [157]. Although a major lithium loss would be expected in the LLTYO sintered pellet since a higher temperature than LBLTO was used, it has to be noted that different lithium reagents were used. LBLTO lithium source was $\text{LiOH}\cdot\text{H}_2\text{O}$, while LiNO_3 was used during LLTYO synthesis. A significant melting temperature difference is observed between both of them: 680°C [164] and 253°C [165] respectively. Such property could imply that LiNO_3 starts reacting at lower temperatures than $\text{LiOH}\cdot\text{H}_2\text{O}$, forming intermediate lithium compounds that hinder lithium volatilization. These more stable compounds could be the ones observed in the XRD spectra when synthesizing the LLTYO ceramic (Figure 4.29): LiTaO_3 and Li_2CO_3 , which present 1650°C [166] and 726°C [167] melting temperatures respectively.

Concerning the electrolytes sintering, LLTYO final conditions were kept as the ones described by S. Narayanan et al. [157]: 900°C for 24 hours and 1100°C for 6 hours respectively. A heating ramp and a controlled cooling of $150^\circ\text{C}/\text{h}$ were used. Conversely, the LBLTO electrolyte synthesis conditions described by Thangadurai et al. [87] were modified. Maintaining the 24 hours duration specified in the initial conditions, the sintering temperature was increased from 900°C to 950°C to achieve higher densification.

As a result of optimizing LBLTO sintering conditions, the surface porosity of the pellet significantly diminished from $15.3\% \pm 3.3\%$ to $4.0\% \pm 0.8\%$, with an inner wall porosity of $2.6\% \pm 0.6\%$. Lower surface porosities were achieved on the LLTYO pellet ($0.7\% \pm 0.1\%$) and in its inner wall ($2.3\% \pm 0.7\%$). This slightly lower porosity was principally associated with the higher temperature used during LLTYO sintering, which enhance the densification rate [168]. For instance, lower porosity values were also achieved when LBLTO was sintered at 1000°C

for 24h ($1.1\% \pm 0.4\%$). However, anomalous crystallographic phases formed, which made to discard these sintering conditions despite the interesting results. Nevertheless, both final sintering procedures produced sintered pellets with satisfactory high densification, surface homogeneity, and homogeneous grain sizes (between 2 to 10 μm approximately).

Furthermore, LBLTO and LLTYO sintered electrolytes did not present any noticeable impurities from their EDS analysis, and a correct stoichiometry was determined from the signals of the elements belonging to each of the electrolytes: Ba: 1.0, La: 1.9, and Ta: 1.9 for LBLTO electrolyte and La: 2.6, Ta: 1.5, and Y: 0.3 for LLTYO. Thus, demonstrating that no contaminations occurred during all the different steps of the sintering procedures. The slightly higher deviations observed for the LLTYO were mainly related to the larger composition discrepancy between its elements, which could increase the inaccuracy of the measurement.

Both electrolyte powders were also in good agreement with their bibliographic garnet-phase pattern. It is worth mentioning that the peak found near the 55° angle associated with an intermediate product ($\text{Li}_2\text{Ba}_3\text{Ta}_2\text{O}_9$) disappeared. Such a phenomenon was associated with a lithium re-incorporation by covering the pellet with the electrolyte's powder during the sintering process.

Moreover, small or insignificant lithium losses were quantified for each of the electrolyte pellets. These lithium losses increased when compared to the ones of the synthesized powders since higher temperatures and times were used. The LBLTO electrolytes exhibited a final 2.4% (w/w) lithium loss, while LLTYO still kept 0.5% (w/w) of the 10% (w/w) of the Li excess added.

The last parameter evaluated was the ionic conductivity of the solid electrolytes sintered. For this purpose, two main challenges were faced. On the one hand, an adequate experimental set-up was required to obtain EIS accurate data at different temperatures. The assembly was designed and constructed to be able to withstand high temperatures and minimize electrical noise. On the other hand, suitable equivalent circuits were required to describe and fit the measured impedance.

Furthermore, during EIS measurements, an inductive effect was obtained for both electrolytes. To minimize or circumvent its influence at the highest temperatures, three strategies were tested. From both electrolytes' results, it was concluded that the best strategy consisted in eliminating the high-frequency points (1 MHz-10 kHz), which eliminated the inductor parasitic effect. Using this strategy and the proposed EC, the ionic

conductivities calculated from the fitted resistances values were close to their bibliographic values.

LBLTO EIS measurements were performed from 30 °C to 300 °C. At 30 °C, resistances close to 2000 Ω were fitted, calculating an average ionic conductivity value of $7.2 \cdot 10^{-5} \text{ S} \cdot \text{cm}^{-1}$. This resistance decreased near to 2 Ω at 300 °C, determining an average conductivity of $5.6 \cdot 10^{-2} \text{ S} \cdot \text{cm}^{-1}$.

Linearized data with the Arrhenius equation demonstrated that the correlation's slopes for both LBLTO pellets were of the same order of magnitude: -4.65 K and -4.91 K, indicating the good reproducibility of the measuring set-up built. Additionally, the average value of these pellets' slopes (-4.78 K) was equivalent to the bibliographic one (-4.78 K). Only a divergence of 0.1% was determined between both, confirming the proper functioning of the constructed experimental setup and the satisfactory quality of the sintered electrolytes.

Concerning the LLTYO electrolyte, EIS measurements were performed from 30 °C to 200 °C. At 30 °C, resistances close to 650 Ω were fitted, calculating an average ionic conductivity value of $1.1 \cdot 10^{-4} \text{ S} \cdot \text{cm}^{-1}$. This resistance decreased near to 2 Ω at 200 °C, determining an average conductivity of $3.0 \cdot 10^{-2} \text{ S} \cdot \text{cm}^{-1}$.

Good reproducibility was also observed when linearizing LLTYO ionic conductivity data with the Arrhenius equation. Both LLTYO pellets showed correlation slopes of the same order of magnitude: -5.34 K and -5.17 K. Moreover, it was concluded that the synthesis and sintering conditions produced satisfactory electrolytes since the measured ionic conductivities showed good agreement with bibliographic data [157]. The average value of the pellets' slopes (-5.26 K) was similar to the bibliographic one (-4.68 K), determining a divergence of 12.3% between both.

When comparing both electrolytes, LLTYO electrolyte exhibited higher ionic conductivity than LBLTO, *e.g.*: at 200 °C, $2.94 \cdot 10^{-2} \text{ S} \cdot \text{cm}^{-1}$ (LLTYO) and $1.7 \cdot 10^{-2} \text{ S} \cdot \text{cm}^{-1}$ (LBLTO). The higher ionic conductivity of the LLTYO electrolyte could be explained due to Y partial doping at the La sites. This improves the Li-ion mobility in its structure [133] since the unit cell dimension is increased because of the larger ionic radius of Y^{3+} (0.90 Å) compared to that of Ta^{5+} (0.64 Å) [169].

Nevertheless, both results indicated that the electrolytes would exhibit a high ionic conductivity at the working temperature of the sensor (400-600 °C). In the end, even though the LLTYO seemed a slightly better candidate due to its lower porosity and higher

conductivity values than the LBLTO electrolyte, both were considered suitable to be used in the construction of lithium sensors.

4.3. Pb-Li Synthesis and Characterization

To electrochemically test the sensors, Pb-Li alloys were required. The adequate preparation of each alloy is important since variations in their lithium concentration significantly modify their melting point (Figure 4.43).

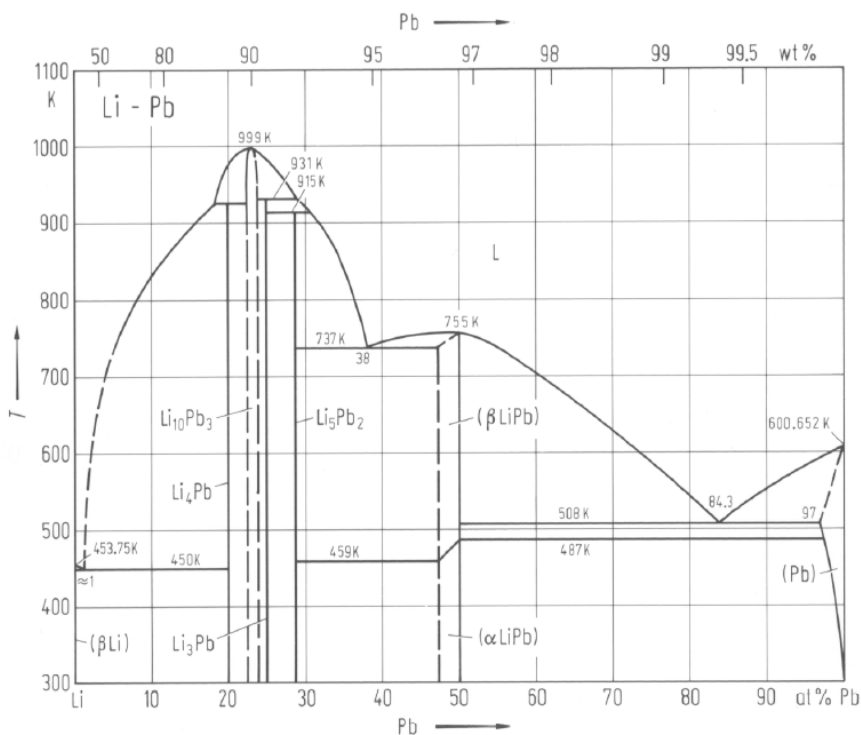


Figure 4.43. Pb-Li phase diagram [37].

As presented in Figure 4.43, if the mixture of both metallic components is not homogeneous, lithium-rich phases such as Li₃Pb, Li₄Pb, Li₁₀Pb₃, etc., can be formed with high melting points (~730 °C). These phases would not melt at the expected working temperatures of the sensor, causing the lithium concentration on the alloy measured with the sensor to be below its nominal value.

Pb-Li alloys were prepared in a glovebox (MBraun UNILab) weighing the required quantities of Li (granular, Sigma Aldrich, 99%) and Pb (chunks, Goodfellow, 99.95%). Both metals were molten and mixed with an alumina rod for several minutes until a homogeneous liquid was

obtained. Then, the liquid was carefully poured into an alumina tube with one end closed. The tube was 4 cm long and had an inner diameter of 10 mm. A few seconds later of its pouring, the alloy solidified and an ingot of the desired Li at% was obtained.

To evaluate whether stratification occurred, three different sections were cut for each ingot: upper, middle, and bottom. To obtain samples of adequate size for the analysis, the ingots were cut meticulously to obtain a small piece of the ingots' interior, as shown in Figure 4.44.

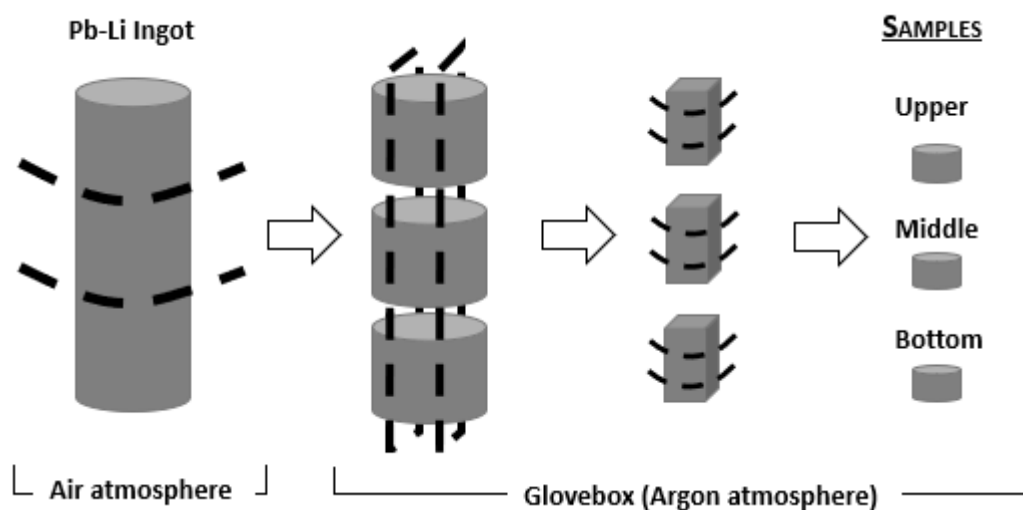


Figure 4.44. Pb-Li ingot sample preparation procedure.

It is worth mentioning, that only the interior part of the ingot was of interest since the initial cutting process had to be done outside the glovebox. Due to the sample's size, an initial hand-sawed process was required. Once this initial cut was performed, as shown in Figure 4.44, the sample was returned inside the glovebox. Since air could have affected the sample's surface during its preparation outside the inert atmosphere, once inside the glovebox, its outer layer was removed to eliminate the oxidized surface following the procedure described in Figure 4.44.

4.3.1. Flame-Atomic Absorption Spectrophotometry (AAS)

Flame-Atomic Absorption Spectrophotometry (FAAS) analysis was performed with a PerkinElmer AAnalyst 200 atomic absorption spectrometer. This process served to ensure that the synthesized alloys' concentrations matched the ones expected from the weighed Li

and Pb quantities. Moreover, during the characterization, it was also checked the ingot's homogeneity. With this aim, 6 Pb-Li ingots with different Li concentrations were prepared: 3.1%, 5.7%, 9.5%, 15.0%, 23.2% and 35.0%at Li.

From each ingot, following the procedure described in Figure 4.44, three samples were obtained (upper, middle, and bottom). Each of these samples weighed around 200 mg and was digested in 10% nitric acid on a hot plate. When the alloy was completely dissolved, pertinent dilutions were performed, and the final solution was analyzed by AAS-Flame. Calibration curves were obtained by using the following Li standards: 0.10 mg·L⁻¹, 0.25 mg·L⁻¹, 0.50 mg·L⁻¹, and 1.00 mg·L⁻¹ Li. One of the calibration curves obtained during the analysis is shown in Annex 6 (Figure 7.6). Each sample was measured three times and its absorbance's average value was interpolated into the calibration curve.

In Table 4.11, the Li at% quantified for each of the alloys is shown. Deviations in % towards the weighted Li at% were calculated and are also shown in the table in parentheses. An average value from the three different ingot parts was also calculated and is included in the last column of Table 4.11.

Table 4.11. AAS-Flame characterization results of Pb-Li ingots with different Li concentrations.

Nominal Pb-Li at%	AAS - Li at% (Deviation (%))			
	Upper	Middle	Bottom	Average
3.1%	3.0 (-2.2)	3.1 (0.5)	3.1 (0.0)	3.1 (-0.6)
5.7%	5.8 (0.7)	5.9 (3.6)	5.8 (1.6)	5.8 (2.0)
9.5%	9.3 (-2.6)	9.5 (-0.2)	9.4 (-1.4)	9.4 (-1.4)
15.0%	14.8 (-1.7)	14.5 (-3.7)	14.8 (-1.8)	14.7 (-2.4)
23.2%	22.9 (-1.6)	23.4 (0.6)	23.6 (1.7)	23.3 (0.2)
35.0%	34.9 (-0.4)	35.1 (0.1)	34.2 (-2.3)	34.7 (-0.9)

From the results, it was of interest to answer two questions. First, whether there were significant differences between the different ingot parts: upper, middle, and bottom. Note that, it was important to ensure that no stratification was occurring along the ingot. And

second, whether the average value obtained from each ingot quantification differed significantly from the nominal concentration of the prepared alloys.

To study the ingots' stratification, a statistical study that checked for significant differences between each of the parts was performed. The whole test is presented in Annex 7, but briefly, all the final P-values (Table 7.1) were above the significance level ($\alpha = 0.05$), indicating that no significant differences were obtained. Moreover, the different ingots showed standard deviations below 0.5at% Li and average CV(%) below 2.0%. These low differences calculated among the different ingots' parts also demonstrated that no stratification was occurring.

After that, it was important to determine whether there were no significant differences between the quantified and the nominal concentrations of each ingot. The statistical study is shown in Annex 7. From the obtained P-values (Table 7.2), it was demonstrated that it could not be concluded to be significant differences. Furthermore, all the calculated deviations shown in Table 4.11 were below 4.0%, indicating small differences between nominal and quantified concentrations.

From such results, it was concluded that Pb-Li alloys could be properly synthesized in the 3.1at% to 35.0at% Li concentration range. It had been demonstrated that the synthesis procedure would produce homogeneous alloys with no stratification. Furthermore, the prepared alloys will have Li concentrations in accordance with their nominal concentration values.

4.3.2. DSC - Characterization

The Pb-Li alloy eutectic composition was established by Hubberstey et al. as 15.72at% Li [170]. However, in his investigation, it was not considered necessary to adjust the composition of the eutectic from the previously established 17at% Li [170]. For this reason, different authors have considered the eutectic composition to be comprised between 15.7at% and 16.98at% Li [171–174]. Thus, in this work, this was acknowledged as the adequate concentration range to synthesize eutectic Pb-Li. Note that, the eutectic melting point is considered in the range of 233.85 °C- 236.85 °C [171,173,175,176]. DSC analyses were performed to determine the alloy's melting point and to evaluate the quality of the synthesized eutectic Pb-Li.

Measurements were performed with a STARE SYSTEM DSC Mettler Toledo in aluminum capsules. The scanning was performed from 150 °C to 400 °C with a heating rate of 10 °C/min and a cooling rate of 5 °C/min. A batch of a Pb-Li alloy with eutectic composition was prepared (15.9at% Li) and an ingot of the alloy was produced. From the ingot, samples were obtained employing a similar procedure as described for the AAS-Flame analysis. The melting temperature of the upper, middle, and bottom parts of the ingot was compared to the reported melting temperature of the eutectic alloy (233.85 °C - 236.85 °C) [171,173,175,176]. In Figure 4.45, one of the DSC curves of the 15.9at% Li alloy is presented. The determination of the melting point was performed as the intersection of a linear fit to the downward-sloping linear section of the melting peak and the extrapolation of the baseline, also known as onset temperature [177,178].

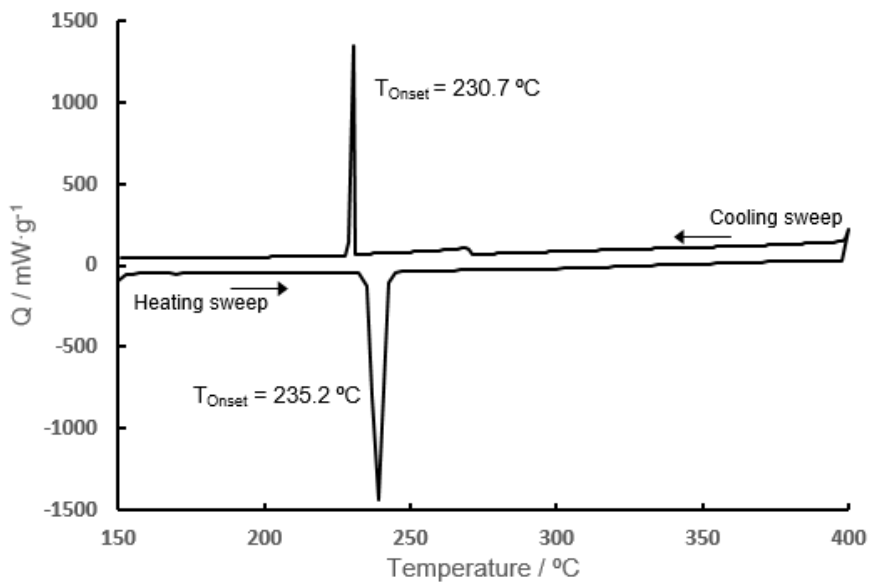


Figure 4.45. DSC curve of a 15.9at% Li Pb-Li alloy.

As shown in Figure 4.45, from the DSC analysis, two temperature peaks were obtained, one from the fusion process (heating sweep, 235.2 °C) and one from the solidification of the alloy (cooling sweep, 230.7 °C). This last temperature was below the reference range of the eutectic Pb-Li alloy (233.85 °C - 236.85 °C). This phenomenon is attributed to the fact that the solidification process requires initial nucleation to take place [179,180]. Nucleation usually occurs on foreign crystals, such as ceramic grains of the crucible, oxide on the melt surface, or fine particles dispersed throughout the melt. Nucleation temperatures can vary up to 100 or more degrees below the liquidus temperature, depending on the alloy system and other factors [178]. For these reasons, the temperature determined during the cooling

process cannot be considered the melting point of the alloy. The melting point is the temperature determined from the heating sweep ($T_{\text{onset}} = 235.2 \text{ }^{\circ}\text{C}$), which was inside the acceptance range ($233.85 \text{ }^{\circ}\text{C} - 236.85 \text{ }^{\circ}\text{C}$).

In Table 4.12, the results obtained from the Pb-15.9Li ingot are presented. The results are divided into the positions where the samples were prepared (upper, middle, and bottom) from the ingot. Three replicates were performed from each of these parts. The average value, as well as the standard deviation (SD) from each of the ingot's parts, are also shown in the last two rows of the table.

Table 4.12. Determined melting points for a Pb-15.9Li ingot. The upper, middle, and bottom parts of the ingot were evaluated separately.

	Melting point / $^{\circ}\text{C}$		
	Upper	Middle	Bottom
Replicate 1	234.7	235.5	236.8
Replicate 2	234.5	235.7	235.2
Replicate 3	234.9	235.5	234.9
Mean	234.7	235.6	235.7
SD / $^{\circ}\text{C}$	0.2	0.1	1.0

From the results, it was observed that all melting points were inside the acceptance range of the eutectic Pb-Li alloy ($233.85 \text{ }^{\circ}\text{C} - 236.85 \text{ }^{\circ}\text{C}$). Furthermore, as observed in Table 4.12, the standard deviation (SD) values were less than or equal to $\pm 1.0 \text{ }^{\circ}\text{C}$. If these SDs are considered, all the ingots' parts fulfilled the quality criteria ($233.85 \text{ }^{\circ}\text{C} - 236.85 \text{ }^{\circ}\text{C}$): $234.7 \text{ }^{\circ}\text{C} \pm 0.2 \text{ }^{\circ}\text{C}$ for the upper part, $235.6 \text{ }^{\circ}\text{C} \pm 0.1 \text{ }^{\circ}\text{C}$ for the middle part, and $235.7 \text{ }^{\circ}\text{C} \pm 1.0 \text{ }^{\circ}\text{C}$ for the lower part. From the results, the alloy was assumed to be satisfactorily synthesized and in the eutectic composition. Moreover, during the heating and cooling process (Figure 4.45) only two peaks were determined which indicated that the alloy behaved as a pure compound.

From the AAS-Flame and DSC analysis, it was assumed that the fabrication procedure yielded homogeneous Pb-Li ingots and that their Li at% concentrations were in accordance with the weighted quantities of each of its elements.

4.4. Electrochemical Lithium Sensors

The design of the lithium sensor consisted of a sintered disc of the solid electrolyte bonded to an alumina tube (Alfa Aesar, \varnothing_{int} = 10mm, \varnothing_{ext} = 13mm, and L= 30mm). Alumina was selected due to its low reactivity towards lithium alloys [176] and because tubes of different sizes are commercially available. These sensors were designed as potentiometric sensors, that have a reference and a working electrode. The reference electrode (RE) was a Pb-Li alloy placed in the inner compartment. In the working electrode (WE), molten Pb-Li alloys with different Li concentrations were used. Both electrodes were connected to a high impedance voltmeter using molybdenum wires (Alfa Aesar, 99.95%). Molybdenum was used due to its low reactivity toward metallic lithium [87]. In Figure 4.46, a scheme of the sensor design is shown.

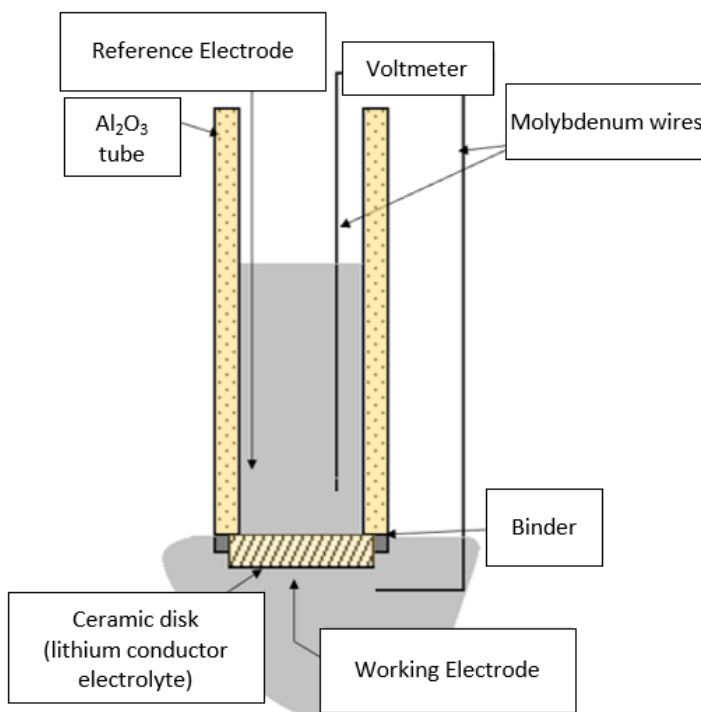


Figure 4.46. Scheme of the Li sensor.

In this sensor design, an adequate binder is needed to attach the pellet to the alumina tube. This binder had to fulfill a series of criteria for the correct operability of the sensor: low reactivity towards lithium, temperature resistance up to 600 °C, binding temperature not superior to 950 °C (electrolytes crystallographic structures could be affected at higher temperatures, as it will be later mentioned in section 4.2.1.2) and completely hermetic seal.

The binder was composed of a solid and a liquid component. As the solid part, sealants based on ceramic components and silicate glasses were proposed and tested in the Master's Thesis of Santiago Moreno at the Electrochemical Methods Laboratory in IQS [181]. These proposed materials, which were mainly composed of SiO_2 , could resist high temperatures and achieve a hermetic seal since these exhibit glass transition temperatures from 230 °C-930 °C [182,183]. In addition, it is expected to be able to withstand the chemical reactivity of the lithium alloys melts, since it is stable to eutectic Pb-Li [176].

Concerning the liquid component, it was required that this compound had a negligible amount of water since it could react with the solid electrolytes in the sealing process [184]. Therefore, different organic solvents with minimal water content were tested: cyclohexane, heptane, and 1-octanol. Among them, the only satisfactory compound was 1-octanol. The vapor pressure of the other solvents was too high and caused the mixture of the solid to dry too quickly.

Once an adequate solvent was found, three different solids were tested: a ceramic binder developed in the Electrochemical Methods Laboratory [185], a commercial cement (Zircon Potting Cement R13, Glassbond), and conventional glass. Note that, the first binder tested was developed to seal proton-conducting electrolytes which exhibit a different reactivity, and was composed of 35% alumina, 22.5% Pyrex®, 22.5% SiO_2 , and 20% NaAl_2O in weight.

To attain adequate sealing, the following thermal process was described in previous work: 1200 °C for 30 minutes [185]. Independently of this, three different temperatures were tested to qualitatively evaluate this binder: 1200 °C, 1300 °C, and 1400 °C. An image of the binding results is shown in Figure 4.47.

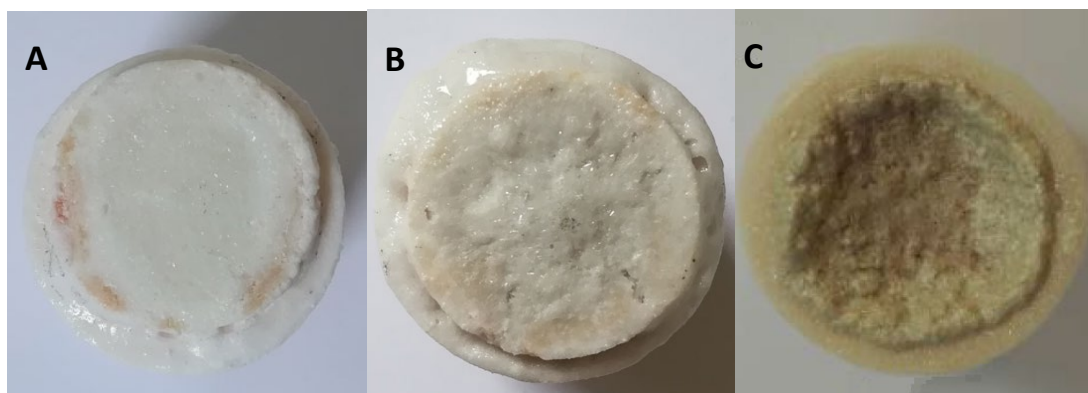


Figure 4.47. Developed ceramic binder treated for 30 minutes at A) 1200 °C, B) 1300 °C, and C) 1400 °C [181].

All the binding results showed a well-sealed surface, where the electrolyte's disc was firmly attached to the alumina tube. However, part of the binder was covering the surface of the pellets, modifying notably the electrolyte's active area. Furthermore, it could be observed that the color and shape of the electrolyte had changed. Such a phenomenon became more evident as the temperature increased. Due to all these reasons, the developed binder was downselected.

As an alternative, commercial Zircon Potting Cement R13 and conventional glass were mixed in different proportions: 4:1, 1:1, 1:4, and 0:1 and evaluated. These mixtures were heat-treated at 950 °C for 1 hour. The temperature was lowered compared to the previous binder since the new binder's components did not require such high temperatures to melt. The final binding results are observed in Figure 4.48.

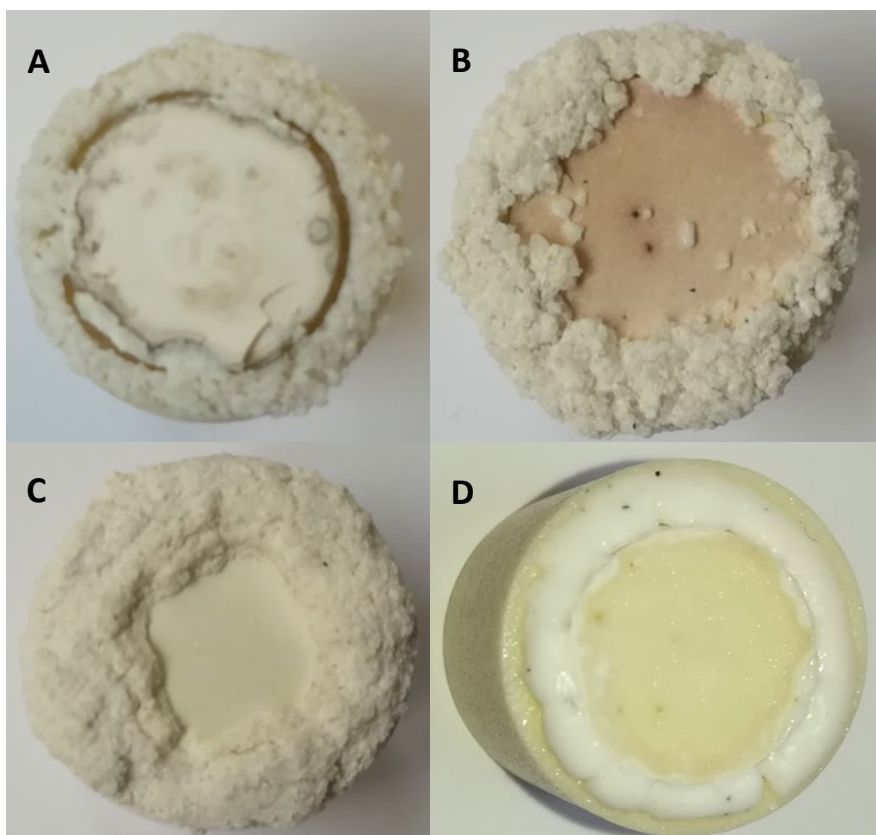


Figure 4.48. Mixtures of ceramic cement and conventional glass A) 4:1, B) 1:1, C) 1:4, and D) 0:1 respectively, treated at 950 °C for 1 hour [181].

From Figure 4.48, it can be observed that all mixtures with ceramic cement showed a granular appearance. In these cases, the binder component did not completely melt, which resulted in an uncompacted solid that shredded easily on contact. By contrast, the

conventional glass binder showed excellent results, since a firm union was observed with no detrimental effects on the electrolyte's disc. From the excellent results of the conventional glass binder, two more heat-treatment were tested to determine the optimal conditions and if possible, minimize the thermal impact on the electrolyte: 900 °C for 1 hour and 1050 °C for 30 minutes. Images of the binding results are presented in Figure 4.49.

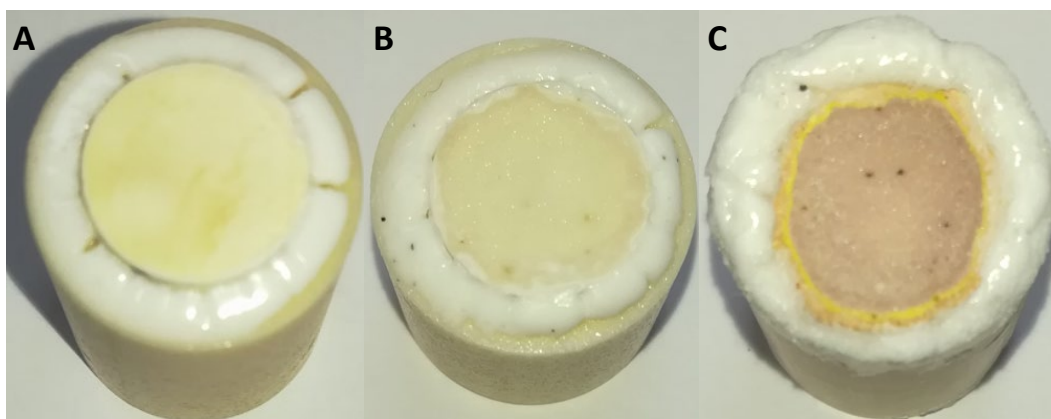


Figure 4.49. Conventional glass binder treated at A) 900 °C for 1 hour, B) 950 °C for 1 hour, and C) 1050 °C for 30 minutes [181].

All thermal treatments tested exhibited good binding results, where the electrolyte's disc was well attached to the surface of the alumina tube. However, it was observed that at 1050 °C it had affected the electrolytes since a color change was visible (Figure 4.49C). Assuming that, at higher temperatures, a larger modification of the electrolyte structure would occur, the optimal heat treatment was concluded to be 900 °C for 1 hour (Figure 4.49A). However, some of the bonded pellets exhibited fractures and/or fissures on their surface after the thermal process. The main reason assumed to be causing the fracture of the pellets was the difference in expansion coefficients between the pellet and the binder. Therefore, relatively slow heating ramps and controlled cooling were included in the thermal treatment to minimize the expansion and shrinkage rate of the pellet and binder during the process. In addition, several temperature stabilization steps were included in the thermal process to relieve some of the internal stresses that could have been accumulated during the heating step [186] (Figure 4.50).

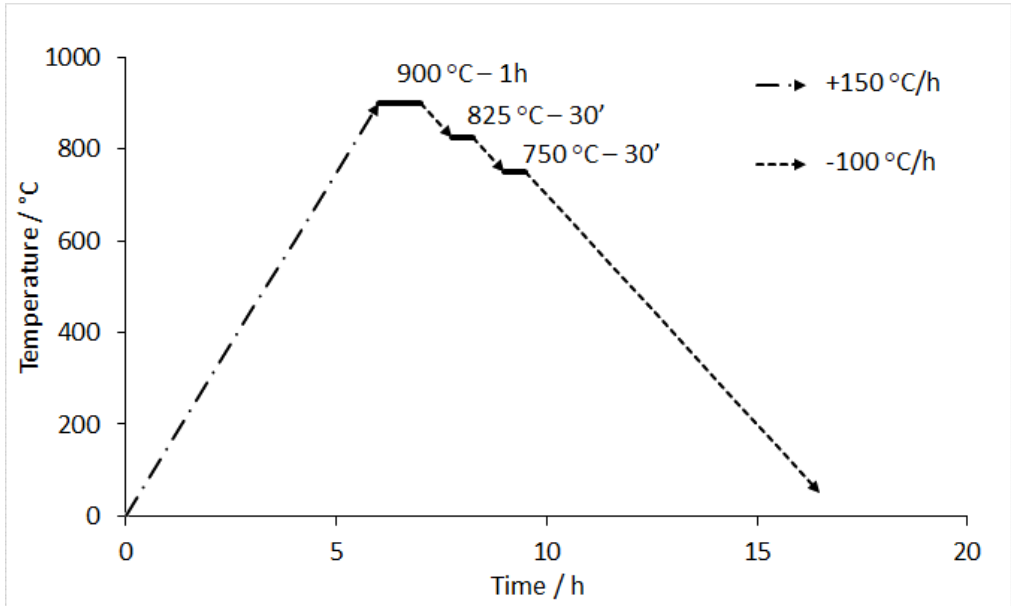


Figure 4.50. Binding thermal process.

The thermal process consisted of a first heating ramp of 150 °C/h until 900 °C, then the temperature was kept for 1 hour. Next, a -100 °C/h controlled cooling was programmed until 825 °C, this temperature was maintained for 30 minutes. Then another controlled cooling step was programmed until 750 °C and 30 more minutes were waited. Finally, a last controlled cooling was applied to room temperature. An image of the final result is shown in Figure 4.51.



Figure 4.51. Binding result after the final thermal process (Figure 4.50).

As observed from Figure 4.51, the pellet was properly bonded to the alumina tube, where no cracks nor fissures could be observed with the naked eye on the surface of the electrolyte. Nevertheless, some cracks could be observed on the sealant part, thus a more rigorous analysis of the interface between binder, electrolyte, and tube was performed. To this aim, a cross-sectional cut of a sensor was performed, which was previously encapsulated with an epoxy resin (Epofix Kit, Struers) and cured overnight. Then, the embedded specimen was cut with a low-speed precision cutter (Buehler Isomet Low Speed Saw). The sample was metalized with a Polaron SC7620 Sputter Coater and was analyzed with a JEOL JSM-5310 scanning electron microscope (SEM), a micrograph resultant from this analysis is shown in Figure 4.52.

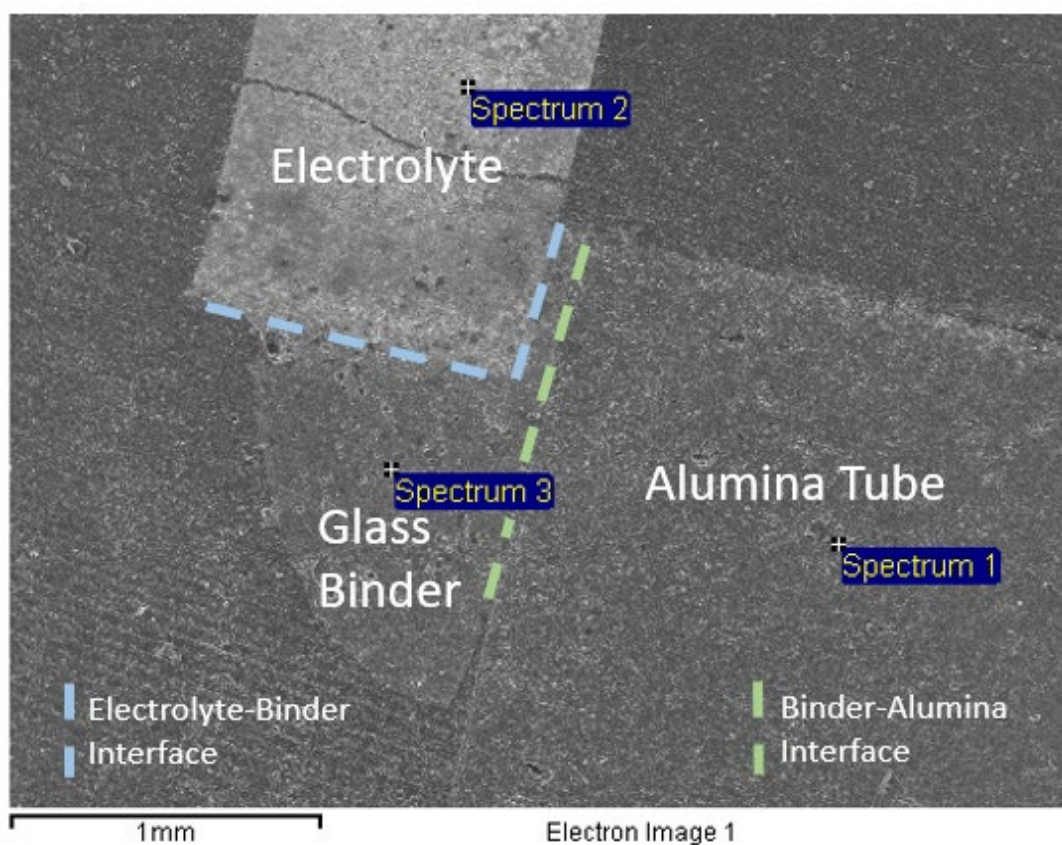


Figure 4.52. SEM micrograph of a cross-sectional cut showing the union interface of a solid electrolyte's pellet to an alumina tube merged with the glass binder. The electrolyte and binder interface is pointed with a blue dashed line and the binder and alumina interface is pointed with a green dashed line.

As shown in Figure 4.52, three regions could be distinguished: the alumina tube (Spectrum 1), the electrolyte (Spectrum 2), and the glass binder (Spectrum 3). EDS analyses were

performed in each of these parts to ensure the identification of the zones, the resulting spectra can be observed in Figure 4.53, Figure 4.54, and Figure 4.55.

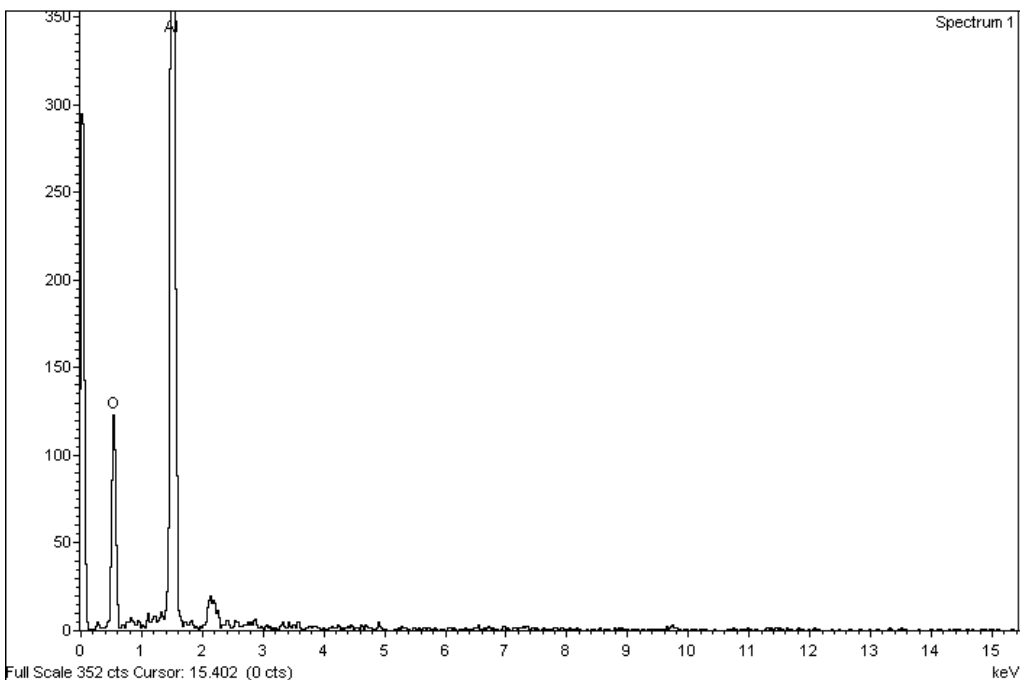


Figure 4.53. EDS spectrum of the alumina tube (Spectrum 1)

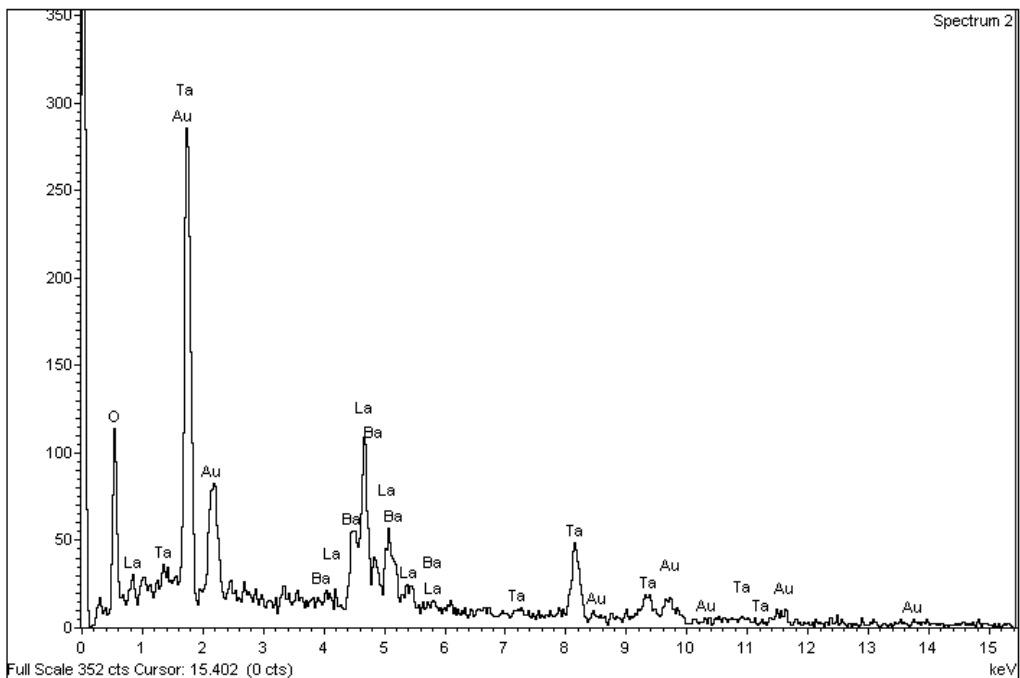


Figure 4.54. EDS spectrum of the LBLTO electrolyte (Spectrum 2)

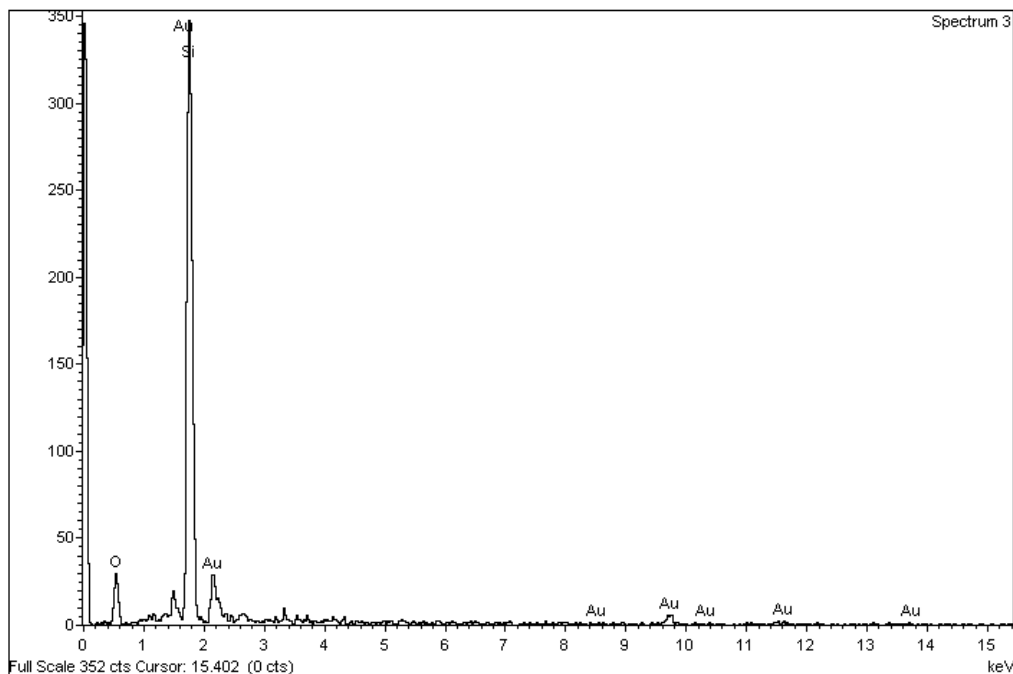


Figure 4.55. EDS spectrum of the glass binder (Spectrum 3).

From Figure 4.53, Figure 4.54, and Figure 4.55, it could be observed that only the principal elements forming the alumina tube, the LBLTO electrolyte, and the glass binder were on the spectra. Thus, each of the zones had been adequately identified. From the EDS spectrum 1 (Figure 4.53) which corresponded to the alumina tube, only Al and O were detected. In spectrum 2 (Figure 4.54), which belonged to the LBLTO electrolyte, its characteristic elements were detected: Ba, La, Ta, and O. Lastly, in spectrum 3 (Figure 4.55), the main components of the glass binder were detected: Si and O. Note that, the presence of Au element in spectrum 2 and 3, corresponds to the gold that had been sputtered to coat the sample.

Although a fracture can be observed in the electrolyte, which could have been done during the cutting process, the main purpose of the analysis was to observe the interface between the binder and the merged elements. From Figure 4.52, it was observed a satisfactory binding, since it was difficult to distinguish each region in their interfaces (blue and green dashed lines) and no fissures nor imperfections were observed. In addition, it could be seen how the pellet rested on the glass and not on the tube, which resulted in a tighter seal.

Although the observed micrographs showed adequate sealing, a final permeation test was performed. It was indispensable to ensure that no permeation of a molten alloy would occur during the experimentation with the sensors since it would cause a short circuit of both electrodes. To perform this test, an electrolyte's pellet bound to an alumina tube was placed

inside a porcelain crucible upside down, then lead was placed inside the tube. A schematic representation of the described composite is presented in Figure 4.56.

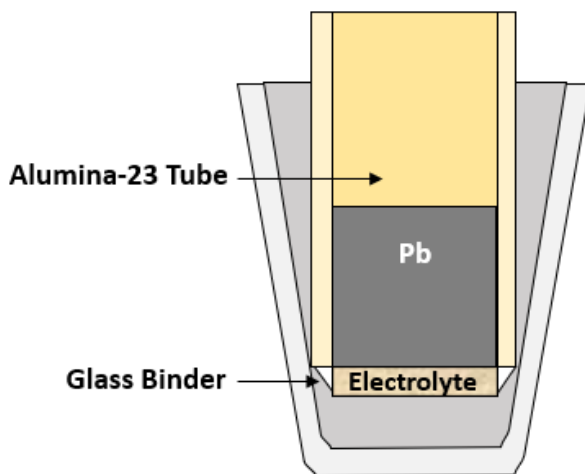


Figure 4.56. Schematic illustration of the assembly for permeation testing.

The assembly was introduced in a reactor, which was heated with a clamp-type electrical resistance (1500 W) at 450 °C to melt the metal. The temperature was controlled with a PID-type temperature controller (Fuji PXR4, K-type thermocouple) and was maintained for 7 days under an Argon atmosphere with 10% hydrogen gas to avoid lead oxidation. After this period, no leaks of lead were found at the bottom of the crucible, which meant that molten lead did not permeate through the binder. Therefore, lithium sensors could be constructed following the sensor's assembly shown in Figure 4.46.

These Li-probes were constructed by binding the sintered pellets (LLTYO or LBLTO) to an Al-23 tube (Alfa Aesar, $\varnothing_{\text{int}}= 10\text{mm}$, $\varnothing_{\text{ext}}= 13\text{mm}$, and $L= 40\text{mm}$) with a glass binder. The tube and the pellet were heated as described in Figure 4.50. Once the sensor was completely constructed, it was placed in an experimental set-up similar to the one schematically represented in Figure 4.57.

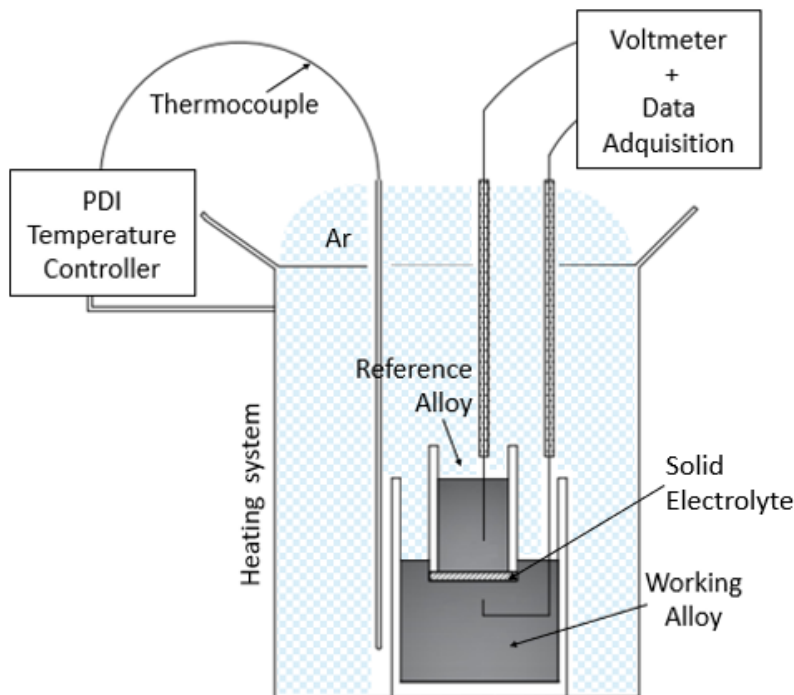


Figure 4.57. Experimental set-up for sensors testing.

In the experimental set-up, the sensor's reference electrode (RE) was a Li alloy that was placed in the inner compartment of the sensor. This alloy had a constant and known concentration throughout the entire experiment. The working electrode (WE) was the Li alloy where the sensor was submerged. In this alloy, lithium concentration was varied after performing the potentiometric measurement. Both electrodes were connected to a high impedance voltmeter using molybdenum wires (Alfa Aesar, 99.95%).

To perform the potentiometric measurements, the constructed Li-probes were introduced in a stainless-steel reactor which was placed in a glovebox (MBraun UNIlab, high purity Ar atmosphere 99.9992%, O_2 and H_2O concentrations < 1 ppm). The reactor was heated with a clamp-type electrical resistance (1500 W) and a PID-type temperature controller (Fuji PXR4, K-type thermocouple).

4.4.1. Characterization of the $\text{Li}_6\text{BaLa}_2\text{Ta}_2\text{O}_{12}$ Sensor

Electrochemical measurements in Pb-Li alloys were performed using a Solartron 1286 Electrochemical Interface or a Potentiostat/Galvanostat Autolab PGSTAT302N. The sensors built with the solid electrolyte LBLTO were used in a potentiometric configuration. As previously mentioned in section 4.3, the sensor required a reference and working electrodes (Figure 4.58).

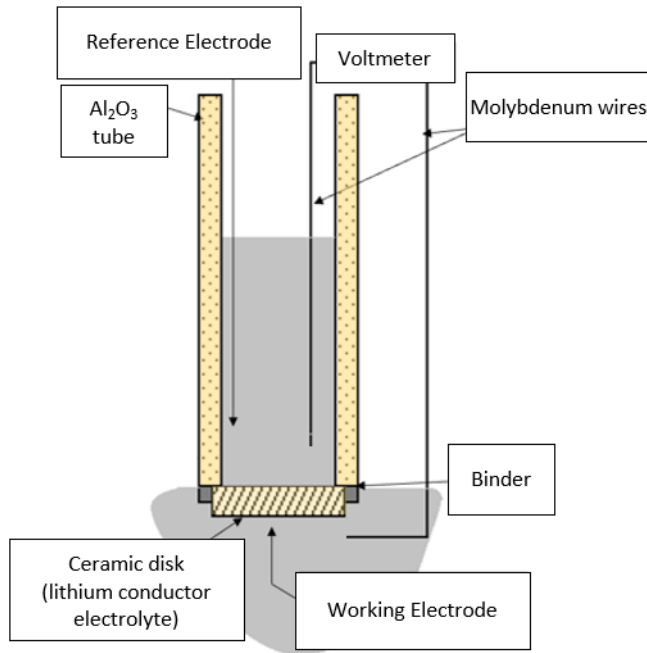


Figure 4.58. Schematic representation of the Li sensor.

In this work, three temperatures were studied: 400 °C, 500 °C, and 600 °C. This temperature range was selected since it is within the expected operational temperature range of future breeding modules [186]. Upon temperature stabilization, the sensor assembly was then submerged in the Pb-Li WE alloy of interest, as shown in Figure 4.58. Then, the Open Circuit Potential (OCP) was measured for 30-40 minutes. After that, this process was repeated with a different Pb-Li WE alloy or setting a different temperature. Measured OCPs were compared to theoretical ones calculated using the Nernst equation ([Eq. 4.9]):

$$\Delta E = \frac{RT}{nF} \ln\left(\frac{a_{\text{Li(WE)}}}{a_{\text{Li(RE)}}}\right) \quad [\text{Eq. 4.9}]$$

where $a_{Li(WE)}$ is the lithium activity in the working alloy, $a_{Li(RE)}$ is the lithium activity in the reference system, R is the gas constant ($8.314 \text{ J}\cdot\text{K}^{-1}\cdot\text{mol}^{-1}$), F is the Faraday constant ($96485.34 \text{ C}\cdot\text{mol}^{-1}$), n is the number of electrons involved in the electrochemical reaction (1), and T is the working temperature in kelvin. Lithium activities in Pb-Li were calculated using Hubberstey correlations [187]. These correlations established linear relationships, in the range $0.01 < \text{lithium molar fraction } (x_{Li}) < 0.17$, which permitted the calculation of lithium activities at temperatures of 400 °C, 500 °C, and 600 °C. These correlations are described in [Eq. 4.10], [Eq. 4.11], and [Eq. 4.12] respectively.

$$400 \text{ °C} \rightarrow \ln(a_{Li}) = - 8.127 + 1.03\ln(x_{Li}) \quad [\text{Eq. 4.10}]$$

$$500 \text{ °C} \rightarrow \ln(a_{Li}) = - 7.085 + 1.08\ln(x_{Li}) \quad [\text{Eq. 4.11}]$$

$$600 \text{ °C} \rightarrow \ln(a_{Li}) = - 6.047 + 1.13\ln(x_{Li}) \quad [\text{Eq. 4.12}]$$

4.4.1.1. Alloy synthesis procedure's effect on the OCP

When initially planning OCP measurements, two different procedures could be used to synthesize the Pb-Li alloys in the WE. On the one hand, the alloys to be tested could be prepared as an ingot and replaced after the OCP measurement. This type of procedure would produce homogenous alloys that will meet their expected nominal Li concentrations (see section 4.3). On the other hand, a simpler synthesis procedure was considered. This consisted of sequentially adding lithium to an initial Pb-Li alloy to increase its lithium concentration after the OCP measurement. To compare both synthesis procedures, potentiometric measurements were performed.

In the first place, OCP measurements with freshly prepared Pb-Li alloys were performed, starting with a 3.1at% Li alloy in the working electrode. In the reference electrode, Pb-Li with a 16.1at% Li was used. Then, the assembly was heated at 400 °C and the sensor was submerged in the molten alloy. Upon temperature stabilization, the Open Circuit Potential (OCP) was measured. Similar measurements were performed at 500 °C and 600 °C. Figure 4.59 shows the OCP for the 3.1at% Pb-Li (WE) vs 16.1at% Pb-Li (RE) as a function of time at each working temperature.

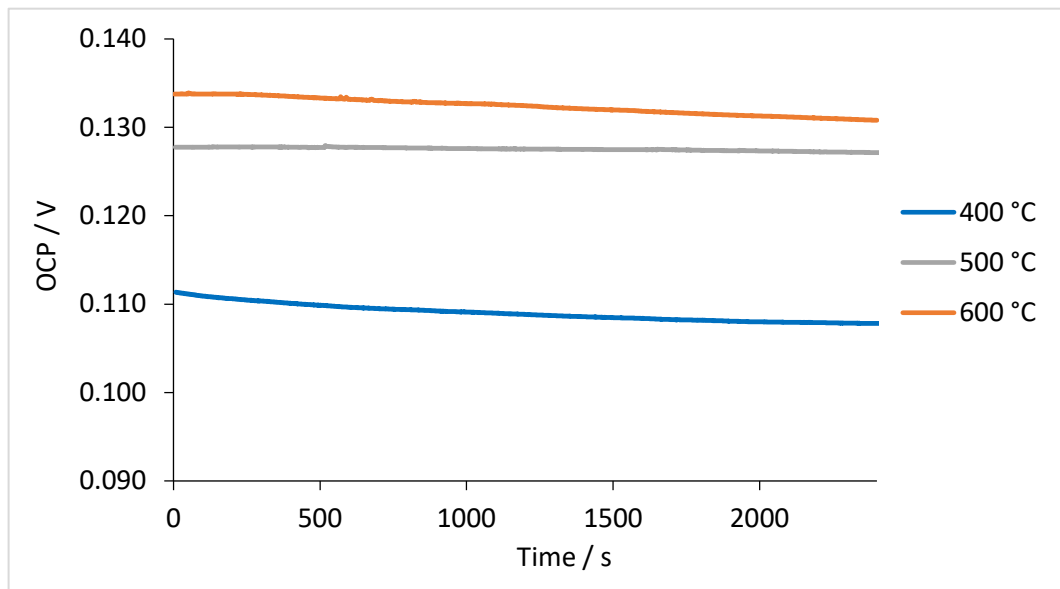


Figure 4.59. OCP measurements in Pb-Li 3.1at% alloy at 400 °C, 500 °C, and 600 °C. Pb-16.1Li was used in the reference electrode.

It can be observed in Figure 4.59 that by increasing the temperature, the OCP also increased as described by the Nernst equation ([Eq. 4.9]). The theoretical OCP values calculated using the Nernst equation were 98 mV at 400 °C, 118 mV at 500 °C, and 140 mV at 600 °C. Deviations in the order of mV were determined between theoretical and experimental OCP values at the end of the measurements. At 400 °C the measured OCP was 107 mV and presented a deviation of 8 mV. At 500 °C and 600 °C, the measured OCP were 127 mV and 131 mV respectively, and both experimental OCP exhibited a deviation of 9 mV. It can be also seen from Figure 4.59, that the OCP showed good stability throughout the entire measurement: the average OCP difference between the initial and the final value was below 2 mV, and standard deviations (SD) below ± 1 mV were obtained at each temperature.

The same procedure was used in Pb-Li alloys prepared with concentrations of 10.1at%, and 16.1at% Li. OCP values measured at each working temperature are shown in Table 4.13, along with calculated cell potentials using the Nernst equation. Lithium activities at each concentration and temperature were calculated using Hubberstey's correlations [187]. In the last column of Table 4.13, the deviations between the experimental OCP compared to the calculated ones are also shown. This value was calculated as the modulus of the difference between the two potentials and is expressed in mV.

Table 4.13. Experimental and calculated potentials in Pb-Li with 3.1at%, 10.14at%, and 16.10at% Li, at 400 °C, 500 °C, and 600 °C. Pb-16.1Li was used in the reference electrode.

Temperature (°C)	WE at% Li	$\Delta E_{\text{Experimental}}$ (OCP, V)	$\Delta E_{\text{Calculated}}$ (V)	Deviation / mV
400	3.1	0.107	0.098	8
	10.1	0.027	0.028	1
	16.1	0.000	0.000	0
500	3.1	0.127	0.118	9
	10.1	0.038	0.033	4
	16.1	0.000	0.000	0
600	3.1	0.131	0.140	9
	10.1	0.040	0.039	1
	16.1	0.000	0.000	0

It can be observed in Table 4.13 that OCP values were close to the calculated ones. The largest deviations were obtained when using Pb-Li with a 3.1at% Li: 8 mV, 9 mV, and 9 mV at 400 °C, 500 °C, and 600 °C respectively. These deviations were related to the analytical balance's uncertainty associated with lithium weighting. Note that, only a few milligrams of Li were required to prepare the alloy, thus probably carrying a significant uncertainty. When increasing the Li concentration, deviations diminished as can be observed in the measurements performed at 10.1at% Li and 16.1at% Li.

The 8 mV and 9 mV deviations resulted in discrepancies below 14% between the experimental concentration determined with the sensor (3.5 at%Li at 400 °C and 500 °C and 3.4 at%Li at 600 °C) and the nominal lithium concentration (3.1 at% Li). The experimental lithium concentrations were determined from the potential measured. First, the Nernst equation ([Eq. 4.9]) was used to obtain the lithium activity in the working electrode, and ultimately Hubberstey's correlations were used to obtain its lithium concentration. It is worth mentioning that, such divergences were inferior to the acceptance criteria (15%) suggested by the Association of Analytical Communities (AOAC) [188]. Therefore, the OCP measurement demonstrated adequate accuracy.

To further verify whether the results followed the Nernst equation, the sensor's calibration curves were represented. In these curves, experimental OCPs were plotted as a function of the logarithm of the lithium activity in the working electrode. The fitted curves at 400 °C, 500 °C, and 600 °C are shown in Figure 4.60.

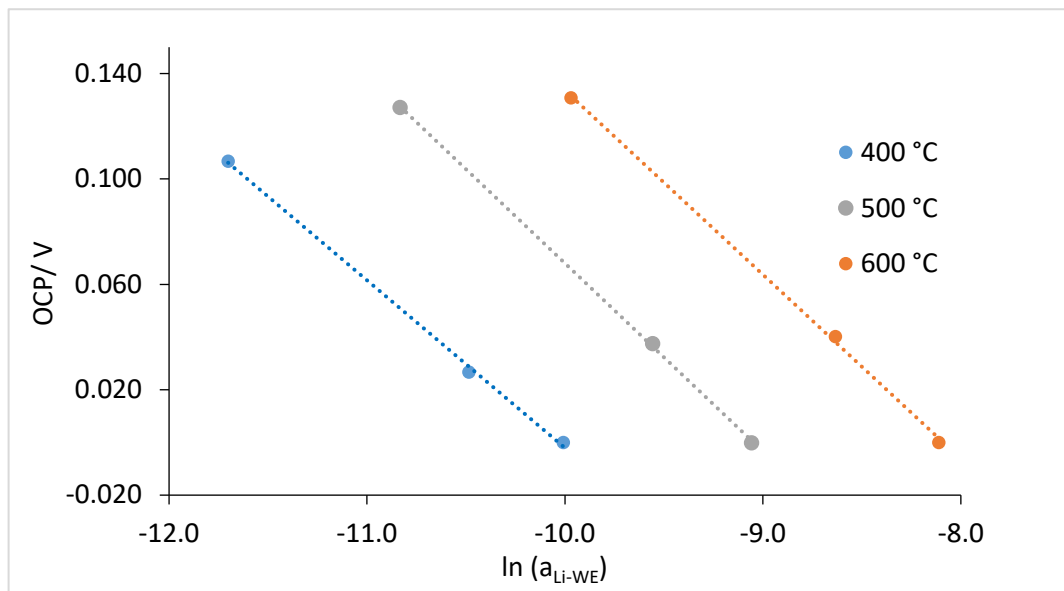


Figure 4.60. Plotted OCPs versus the logarithm of the lithium activity in the working electrode at 400 °C, 500 °C, and 600 °C. Pb-16.1Li was used in the reference electrode.

Correlations obtained in Figure 4.60 are shown below:

$$400\text{ }^{\circ}\text{C} \rightarrow \Delta E(V) = -0.064 \ln(a_{Li}) - 0.638; R^2 = 0.9989 \quad [\text{Eq. 4.13}]$$

$$500\text{ }^{\circ}\text{C} \rightarrow \Delta E(V) = -0.071 \ln(a_{Li}) - 0.646; R^2 = 0.9997 \quad [\text{Eq. 4.14}]$$

$$600\text{ }^{\circ}\text{C} \rightarrow \Delta E(V) = -0.070 \ln(a_{Li}) - 0.565; R^2 = 0.9992 \quad [\text{Eq. 4.15}]$$

Theoretical slopes calculated with the Nernst equation ($-RT/nF$) are -0.058 at 400 °C, -0.067 at 500 °C, and -0.075 at 600 °C. When comparing these values with those experimentally obtained, divergences below 10% were obtained in all cases: 9.6%, 7.1%, and 7.1% respectively. These results were considered satisfactory since the slopes of the correlations showed good agreement with the Nernst equation, and determination coefficients superior to 0.99 were obtained.

When studying the synthesis procedure by sequential lithium addition, a Pb-Li alloy with an initial concentration of 3.3at% Li was prepared in the working electrode. In the reference

electrode, Pb-Li with a 15.9at% Li concentration was used. Then, the assembly was heated at 400 °C and the sensor was submerged in the molten alloy. Upon temperature stabilization, the Open Circuit Potential (OCP) was measured. Similar measurements were performed at 500 °C and 600 °C. Figure 4.61 shows the OCP for the 3.3at% Pb-Li (WE) vs 15.9at% Pb-Li (RE) alloy as a function of time at each working temperature.

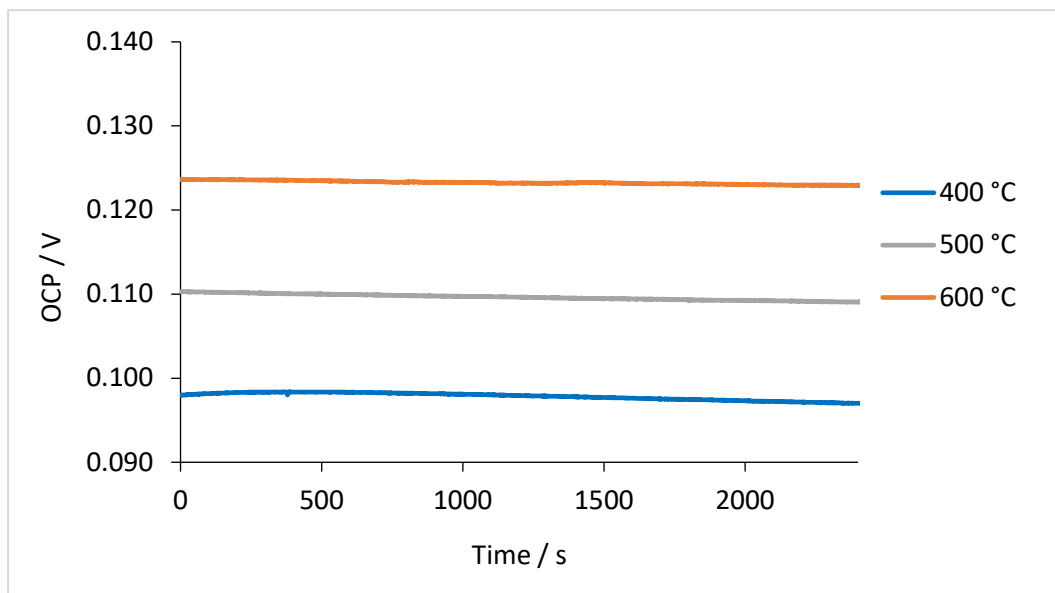


Figure 4.61. OCP measurements in Pb-Li 3.3at% alloy at 400 °C, 500 °C, and 600 °C. Pb-15.9Li was used in the reference electrode.

It can be seen in Figure 4.61 that by increasing the temperature, the potential also increased as described by the Nernst equation ([Eq. 4.9]). The theoretical OCP values of the 3.3at% Li alloy calculated using the Nernst equation were 94 mV at 400 °C, 114 mV at 500 °C, and 134 mV at 600 °C. Deviations in the order of mV were determined between the theoretical and the experimental OCP values at the end of the measurements. At 400 °C, 500 °C, and 600 °C the experimental OCP were 97 mV, 110 mV, and 123 mV respectively, and presented deviations of 2 mV, 4mV, and 11 mV. It can be also seen from Figure 4.61, that the OCP showed good stability throughout the entire measurement: the average potential difference between the initial and the final value was below 1 mV, and SD < ±0.4 mV was obtained at each temperature.

After OCP measurements in the Pb-Li alloy with a 3.3 at% Li, more lithium was added with continuous stirring, to this alloy to increase its lithium content. Then, the OCP of this alloy was measured at the three temperatures of interest. Measurements with Pb-Li alloys of 5.8at%, 10.0at%, and 15.9at% Li were performed following the described procedure. OCP

values measured at each working temperature are shown in Table 4.14, along with calculated cell potentials. Lithium activities at each concentration and temperature were calculated using Hubberstey's correlations [187]. In the last column of the table, the deviations between experimental and calculated OCP are shown.

Table 4.14. Experimental and calculated potentials in Pb-Li with 3.27at%, 5.83at%, 10.00at%, and 15.90at% Li, at 400 °C, 500 °C, and 600 °C. Pb-15.9Li was used in the reference electrode.

Temperature (°C)	WE at% Li	$\Delta E_{\text{Experimental}}$ (OCP, V)	$\Delta E_{\text{Calculated}}$ (V)	Deviation / mV
400	3.3	0.097	0.094	2
	5.8	0.062	0.060	2
	10.0	0.029	0.028	2
	15.9	0.000	0.000	0
500	3.3	0.110	0.114	4
	5.8	0.069	0.072	3
	10.0	0.033	0.033	0
	15.9	0.000	0.000	0
600	3.3	0.123	0.134	11
	5.8	0.079	0.085	6
	10.0	0.037	0.039	2
	15.9	0.000	0.000	0

It can be observed in Table 4.14 that OCP values were close to the calculated ones. The maximum deviations were obtained at 600 °C, with values of 11 mV and 6 mV at lithium concentrations of 3.3at% Li and 5.8at% Li respectively. Despite that, the divergences between their nominal and experimental lithium concentrations were less than 14%. Therefore, the OCP measurement demonstrated adequate accuracy.

To further verify whether the results followed the Nernst equation, the sensor's calibration curves were represented. In these curves, experimental OCPs were plotted versus the logarithm of the lithium activity in the working electrode. The fitted curves at 400 °C, 500 °C, and 600 °C are shown in Figure 4.62.

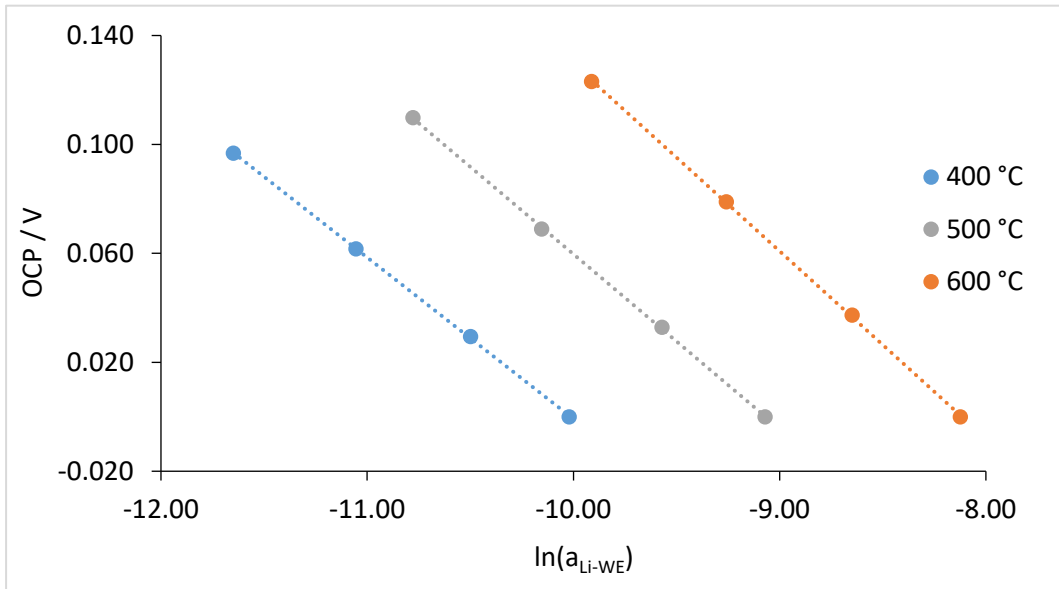


Figure 4.62. Plotted OCPs versus the logarithm of the lithium activity in the working electrode at 400 °C, 500 °C, and 600 °C. Pb-15.9Li was used in the reference electrode.

Correlations obtained in Figure 4.62 are shown below:

$$400\text{ °C} \rightarrow \Delta E(V) = -0.059 \ln(a_{Li}) - 0.594; R^2 = 0.9999 \quad [\text{Eq. 4.16}]$$

$$500\text{ °C} \rightarrow \Delta E(V) = -0.064 \ln(a_{Li}) - 0.581; R^2 = 0.9999 \quad [\text{Eq. 4.17}]$$

$$600\text{ °C} \rightarrow \Delta E(V) = -0.069 \ln(a_{Li}) - 0.558; R^2 = 0.9999 \quad [\text{Eq. 4.18}]$$

When comparing the calculated values with the Nernst equation with those experimentally obtained, divergences below 10% were obtained in all cases: 2.2%, 3.8%, and 8.6% respectively. These results were considered satisfactory since the slopes of the correlations showed good agreement with the Nernst equation, and determination coefficients superior to 0.99 were obtained.

To compare both Pb-Li synthesis procedures, a statistical study was performed to determine whether there were significant differences between both preparation procedures (separately and by addition). To do so, the confidence intervals (95%) of their linear correlations' slopes ([Eq. 4.13]-[Eq. 4.18]) were calculated and compared at each temperature as shown in Annex 8 (Figure 7.8). From the study, it could be concluded that there were no significant differences between both preparation methods independently of the temperature since all confidence intervals overlapped.

Furthermore, the sensor exhibited satisfactory results independently of the Pb-Li synthesis procedure. On the one hand, all OCP measurements had a stable signal with a final experimental OCP close to its theoretical value. On the other hand, the sensor calibration curves have shown low discrepancies towards the Nernst theoretical slope values, demonstrating good agreement with the Nernst equation.

For all these reasons, it was considered that both synthesis procedures yielded similar results. Nevertheless, due to the mentioned advantages of the preparation method by Li addition, this procedure was used for the synthesis of all the Pb-Li alloys required in the following experiments.

4.4.1.2. Reference System

The reference system is a key component of the overall sensor performance. Note that, the already used reference electrode consisted of eutectic Pb-Li. This composition is not advised when monitoring a Pb-Li alloy with a similar concentration since, in this scenario, OCP values close to 0V would be measured. Such ΔE values will be difficult to distinguish from a short-circuit situation. Since the target of application of the sensor is the monitoring of a Pb-Li alloy, alternative reference systems were explored to avoid the situation described.

Pb-Li Reference System

After the satisfactory results with a eutectic Pb-Li alloy as a reference, it was important to test if Pb-Li alloys with different Li concentrations could be used. To perform such analysis, a Pb-Li alloy with Li concentrations close to 3.0at% was tested in the RE. This concentration was chosen after considering the range of application of Hubberstey's correlations: a 3.0at% Li would represent the lowest part of this range and the already tested eutectic Pb-Li the highest part.

To study the effect of the Pb-Li reference system near the 3.0at% Li concentration, an alloy with a concentration of 3.1at% Li was prepared. This alloy was used in the reference electrode and as the initial Pb-Li alloy in the working electrode. Once the assembly was heated at 400 °C, the sensor was submerged in the molten alloy. Upon temperature stabilization, the OCP was measured. The same procedure was used to perform three more OCP measurements with Pb-Li alloys in the WE with 5.3, 9.3, and 15.4at% Li concentrations at 400 °C. Note that, these Pb-Li alloys were prepared by subsequent Li addition after each

OCP measurement. In Figure 4.63 there are shown the OCP measurements for the mentioned alloys at 400 °C.

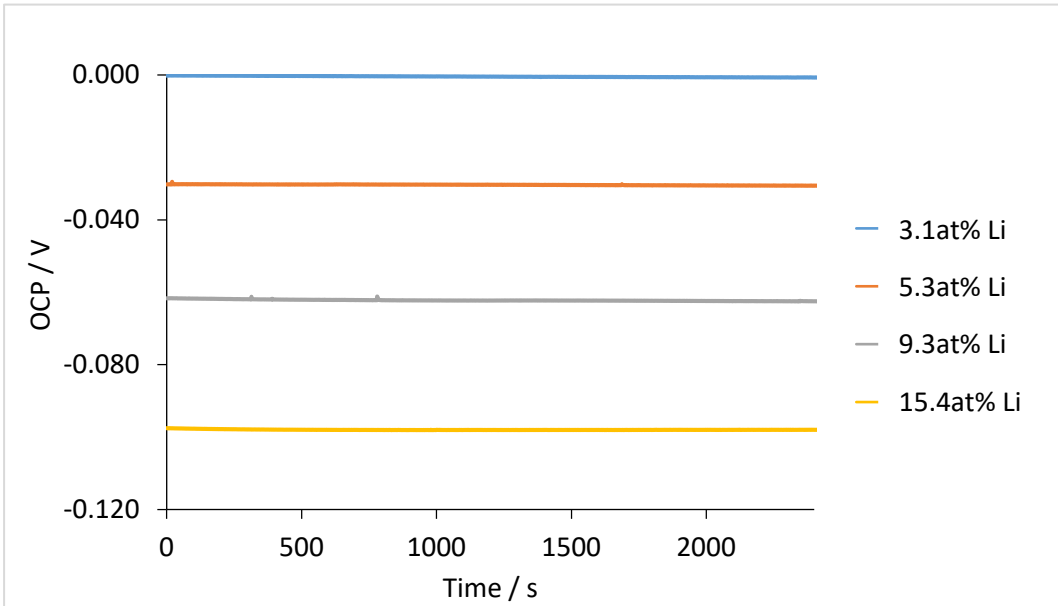


Figure 4.63. OCP measurements in Pb-Li alloys with Li concentrations of 3.3at%, 5.3at%, 9.3at% and 15.4at% at 400 °C. Pb-3.1Li was used in the reference electrode.

It can be observed in Figure 4.63 that by increasing the Li concentration in the WE, the potential decreased as described by the Nernst equation ([Eq. 4.9]). At 400 °C, the theoretical OCP values calculated using the Nernst equation were: 0 mV, -33 mV, -66 mV, and -96 mV for the Pb-Li alloys with 3.3at%, 5.3at%, 9.3at% and 15.4at% Li. Deviations in the order of mV were determined between the theoretical and the experimental OCP values at the end of the measurements. From low to high Li concentration alloys, experimental OCP were -1 mV, -31 mV, -62 mV, and -98 mV respectively, and 1 mV, 2 mV, 4mV, and 2 mV deviations. It can be also seen from Figure 4.63, that the OCP showed good stability throughout the entire measurement: the potential difference between the initial and the final OCP values were below 1 mV with SDs $\leq \pm 0.2$ mV.

Similar measurements were performed at 500 °C and 600 °C in Pb-Li alloys with 3.2at%, 5.9at%, 9.5at%, and 15.1at% Li concentrations versus a reference alloy of 3.2at% Li. All OCP values determined at each working temperature are included in Table 4.15, along with calculated cell potentials using the Nernst equation. Lithium activities at each concentration and temperature were calculated using Hubberstey's correlations [187]. In the last column of Table 4.15, the deviations between experimental and calculated OCP are shown.

Table 4.15. Experimental and calculated potentials in Pb-Li alloys with different Li concentrations (WE) at 400 °C, 500 °C, and 600 °C. Pb-3.2Li was used in the reference electrode.

Temperature (°C)	WE at% Li	$\Delta E_{\text{Experimental}}$ (OCP, V)	$\Delta E_{\text{Calculated}}$ (V)	Deviation / mV
400	3.1	-0.001	0.000	1
	5.3	-0.031	-0.033	2
	9.3	-0.062	-0.066	4
	15.4	-0.098	-0.096	2
500	3.2	-0.001	0.000	1
	5.9	-0.042	-0.044	2
	9.5	-0.077	-0.078	1
	15.1	-0.113	-0.111	2
600	3.2	0.001	0.000	1
	5.9	-0.049	-0.052	3
	9.5	-0.090	-0.092	2
	15.1	-0.131	-0.132	1

It can be observed in Table 4.15 that the OCP experimental values were close to the calculated ones. An average value of deviations below 2 mV was obtained, with a maximum deviation of 4 mV. Such results indicated good measurement accuracy since the maximum deviation represented a divergence of 7% between its nominal and experimental lithium concentration.

To further verify whether the results followed the Nernst equation, the sensor's calibration curves were represented. In these curves, experimental OCPs were plotted versus the logarithm of the lithium activity in the working electrode. The fitted curves at 400 °C, 500 °C, and 600 °C are shown in Figure 4.64.

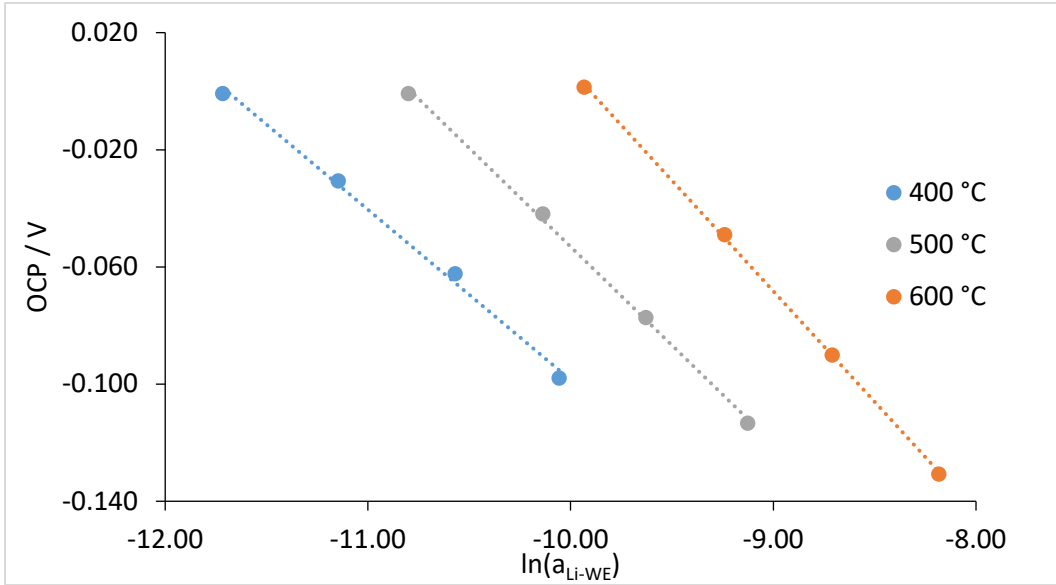


Figure 4.64. Plotted OCPs versus the logarithm of the lithium activity in the working electrode at 400 °C, 500 °C, and 600 °C. Pb-3.2Li was used in the reference electrode.

Correlations obtained in Figure 4.64 are shown below:

$$400\text{ °C} \rightarrow \Delta E(V) = -0.058 \ln(a_{Li}) - 0.680; R^2 = 0.9957 \quad [\text{Eq. 4.19}]$$

$$500\text{ °C} \rightarrow \Delta E(V) = -0.067 \ln(a_{Li}) - 0.726; R^2 = 0.9987 \quad [\text{Eq. 4.20}]$$

$$600\text{ °C} \rightarrow \Delta E(V) = -0.076 \ln(a_{Li}) - 0.748; R^2 = 0.9997 \quad [\text{Eq. 4.21}]$$

When comparing Nernst values (-0.058, -0.067, -0.075) with those experimentally obtained, relative errors equal to or below 1% were obtained in all cases: 0.2%, 1.0%, and 0.4% respectively. Therefore, the results were considered satisfactory since the slopes of the correlations were in good agreement with the Nernst equation, and determination coefficients superior to 0.99 were obtained.

To compare the eutectic Pb-Li (see results in section 4.4.1.1) and the 3at% Li reference systems, a statistical study was performed. In the study, the confidence intervals (95%) of their calibration curves' slopes ([Eq. 4.16]-[Eq. 4.21]) were calculated to determine whether there were significant differences between both reference systems. These confidence intervals were compared at each temperature. The results are presented in Annex 9 (Figure 7.9). From the study, it was observed that all the confidence intervals overlapped. Thus, it

was concluded that there were no significant differences between both reference systems independently of the temperature.

Moreover, both reference systems exhibited satisfactory results: high stability, accuracy, and good agreement with the Nernst equation. Therefore, both lithium concentrations could be used as reference systems. However, in the case of monitoring a eutectic Pb-Li alloy, the 3at% Li reference system will be the best option to distinguish a short-circuit situation.

Sn-Li Reference System

As mentioned before, an adequate reference system is important for the correct performance of the sensor. In previous sensors' configurations reported in the bibliography, different Li reference systems have been used such as Li-Bi mixtures [42,49,134] or pure lithium [189,190]. Thus, exploring other Li alloys as reference systems can be of great interest. When considering similar Li alloys as Pb-Li, Sn resulted in an interesting alloying element due to its similarities with lead: both are in the same group in the periodic table and exhibit a low melting point. This last fact permitted synthesizing Sn-Li alloys with a low lithium concentration, hence minimizing their lithium activity. In this way, the reactivity of the alloy could be diminished. The phase diagram of the lithium-tin system can be observed in Figure 4.65.

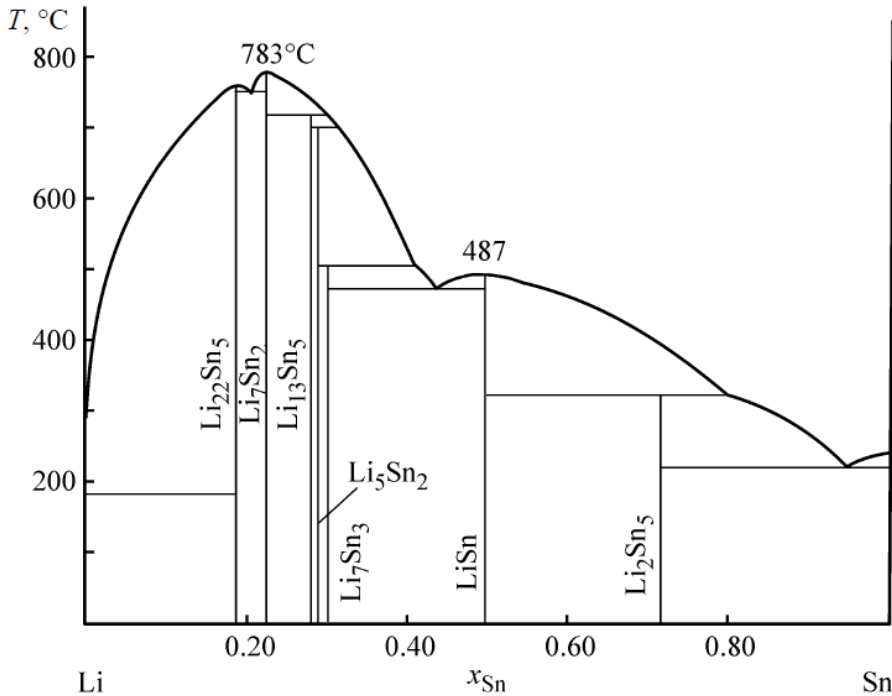


Figure 4.65. Phase diagram of the lithium-tin system [191].

In the right part of the diagram, the low lithium phases are observed, exhibiting melting points lower than 400 °C at $x_{\text{Li}} < 0.25$. At a lithium concentration of 5at% Li, a eutectic mixture is formed (214 °C) [192]. Close to this eutectic composition, a ~3at% Li concentration was chosen as the reference system. This concentration was also decided since it was similar to the previously tested Pb-3Li reference alloy.

Sn-Li compounds were prepared analogously to Pb-Li, inside a glovebox (MBraun UNILab, high purity Ar atmosphere 99.9992% with O₂ and H₂O concentration under 1 ppm values) weighting the adequate quantities of each of the metals: Li granular (Sigma Aldrich, 99%) and Sn granulated (Scharlau, extra pure). For each alloy, the metals were melted and mixed with an alumina rod for several minutes until a homogeneous liquid was obtained. It is worth mentioning that no characterization procedure was performed such as the one described for Pb-Li (section 4.3). It was considered that the results and conclusions extracted for the first lithium alloy could be made extensive for the Sn-Li alloys prepared.

The Sn-Li reference system was tested in four Pb-Li alloys (3.0at%, 5.4at%, 9.4at%, and 15.53at% Li) versus Sn-3.0Li RE. Similar to previous experiments, the Open Circuit Potential (OCP) was measured at 400 °C, 500 °C, and 600 °C sequentially. In Figure 4.66 there are shown the OCP measurements for the mentioned alloys at 400 °C.

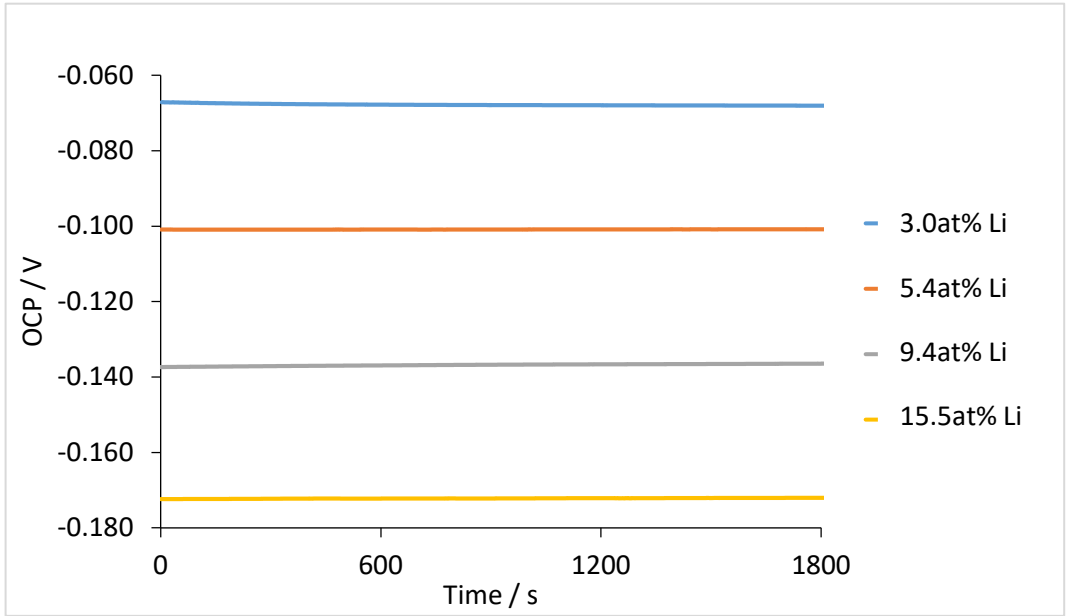


Figure 4.66. OCP measurements in Pb-Li alloys with Li concentrations of 3.0at%, 5.4at%, 9.4at% and 15.5at% at 400 °C. Sn-3.0Li was used in the reference electrode.

It can be observed in Figure 4.66 that the OCP showed good stability throughout the entire measurement: the potential difference between the initial and the final OCP value was below 1 mV with SDs $\leq \pm 0.3$ mV. Note that, in this case, to calculate theoretical OCP values the lithium activity of the reference Sn-3.0Li had to be determined. However, no correlations were found in the bibliography that could be used to calculate the lithium activity of the reference system. Only values of lithium activity coefficients (γ_{Li}) have been reported in bibliography restricted to specific Li concentrations and temperatures. It is worth mentioning that lithium activity coefficients correlate to lithium activities as described in [Eq. 4.22].

$$a_{Li} = \gamma_{Li} * x_{Li} \quad [\text{Eq. 4.22}]$$

Furthermore, none of the reported coefficients were at the same temperature and concentration under study. Therefore, to obtain a rough estimation of the lithium activity, a linear interpolation from the two closest values was made. At 400 °C, the γ_{Li} in Sn-Li was calculated from the activity coefficients $3.30 \cdot 10^{-5}$ at 381 °C [193] and $5.46 \cdot 10^{-5}$ at 421 °C [193], determining a value of $4.33 \cdot 10^{-5}$.

Using the 400 °C Hubberstey's correlation ([Eq. 4.10]) [187] to calculate Li activities in Pb and the $4.33 \cdot 10^{-5}$ Li activity coefficient in Sn, theoretical OCPs were calculated. For the 3.0at%,

5.4at%, 9.4at%, and 15.5at% Li alloys, these OCP values were: -106 mV, -140 mV, -173 mV, and -203 mV. Deviations near 30 to 40 mV were determined between the theoretical and the experimental OCP values at the end of the measurements. From low to high Li concentration alloys, the experimental OCP measured at the end of the measurements were -68 mV, -101 mV, -136 mV, and -172 mV with 38 mV, 39 mV, 37 mV, and 31 mV deviations respectively. These high deviations were assumed to be a consequence of the estimated lithium activity coefficients.

Similar OCP measurements were performed at 500 °C and 600 °C. Activity coefficients at these temperatures were also estimated from near values since no data in the studied conditions was reported in the bibliography. At 500 °C, an γ_{Li} of $2.73 \cdot 10^{-4}$ was calculated from the activity coefficients $5.46 \cdot 10^{-5}$ at 421 °C [193] and $5.46 \cdot 10^{-5}$ at 550 °C [193]. Lastly, at 600 °C, the determined γ_{Li} was $6.04 \cdot 10^{-4}$ and was calculated from the activity coefficients $4.70 \cdot 10^{-4}$ at 589 °C [194] and $1.53 \cdot 10^{-3}$ at 676 °C [193]. From these activity coefficients, theoretical OCPs were calculated and are shown in Table 4.16 along with their deviations towards the experimental values.

Table 4.16. Experimental and calculated potentials in Pb-Li with 3.0at%, 5.4at%, 9.4 at%, and 15.5at% Li, at 400 °C, 500 °C, and 600 °C. Sn-3.0Li was used in the reference electrode.

Temperature (°C)	WE at% Li	$\Delta E_{\text{Experimental}}$ (OCP, V)	$\Delta E_{\text{Calculated}}$ (V)	Deviation / mV
400	3.0	-0.068	-0.106	38
	5.4	-0.101	-0.140	39
	9.4	-0.136	-0.173	37
	15.5	-0.172	-0.203	31
500	3.0	-0.059	-0.056	2
	5.4	-0.103	-0.097	5
	9.4	-0.145	-0.137	7
	15.5	-0.185	-0.173	12
600	3.0	-0.060	-0.069	9
	5.4	-0.104	-0.117	14
	9.4	-0.152	-0.165	13
	15.5	-0.198	-0.207	9

It can be observed in Table 4.16 that a notable difference was obtained between the experimental OCP and the calculated values. The highest deviations were observed at 400 °C, determining deviations that exceeded 30 mV. The deviations were far superior to the ones observed from previous potentiometric measurements in Pb-Li. These deviations signified, in some cases, divergences higher than 60% between the nominal and the experimental lithium concentrations. These large unconformities were associated with the lithium activity coefficients used for their determination. It is worth mentioning, that significant discrepancies have been observed between activity coefficients reported in different bibliographic sources [193–195].

Despite the later results, the sensor’s calibration curves were represented. In these curves, experimental OCPs were plotted versus the logarithm of the lithium activity in the working electrode. The fitted curves at 400 °C, 500 °C, and 600 °C are shown in Figure 4.67.

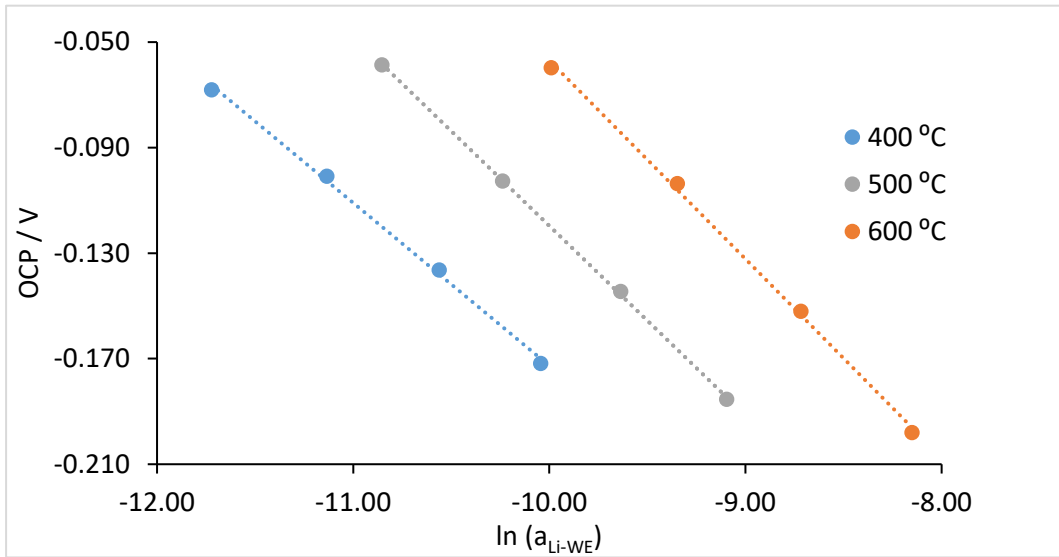


Figure 4.67. Plotted OCPs versus the logarithm of the lithium activity in the working electrode at 400 °C, 500 °C, and 600 °C. Sn-3.04Li was used in the reference electrode.

Correlations obtained in Figure 4.67 are shown below:

$$400\text{ °C} \rightarrow \Delta E(V) = -0.062 \ln(a_{Li}) - 0.790; R^2 = 0.9979 \quad [\text{Eq. 4.23}]$$

$$500\text{ °C} \rightarrow \Delta E(V) = -0.072 \ln(a_{Li}) - 0.838; R^2 = 0.9998 \quad [\text{Eq. 4.24}]$$

$$600\text{ °C} \rightarrow \Delta E(V) = -0.075 \ln(a_{Li}) - 0.809; R^2 = 0.9985 \quad [\text{Eq. 4.25}]$$

Theoretical slopes calculated with the Nernst equation ($-RT/nF$) are -0.058 at 400 °C, -0.067 at 500 °C, and -0.075 at 600 °C. When comparing these values with those experimentally obtained, relative errors below 10% were obtained: 6.5%, 7.8%, and 0.1% respectively. The results were considered satisfactory since the slopes of the calibration curves showed good agreement with the Nernst equation, and determination coefficients superior to 0.99 were obtained. Furthermore, the results were similar to those obtained from Pb-Li measurements, discussed in previous sections. Since the reference system was kept constant, its lithium activity did not affect the slope of the linear correlation, and only the independent term of the equation was influenced.

From the results, Sn-Li appeared as a viable reference system. Despite that, further investigation was required due to the lack of information and poor consensus concerning lithium coefficients and activities in Sn-Li alloys. As observed in Table 4.16, not knowing

these activities compromise the estimation of the reference system's contribution, determining high deviations between calculated and experimental values.

To obtain a more accurate value of the lithium activity coefficients, the previous experimental OCPs were used for its estimation (Table 4.16). Note that, although the lithium activity of the reference electrode was unknown, it was kept constant during the experiments. Since the lithium activity from each of the tested Pb-Li alloys in the working electrode is known from Hubberstey's correlations, the activity coefficients for a Sn-3.0Li system could be calculated using the following [Eq. 4.26] and [Eq. 4.22]:

$$\ln(a_{Li(RE)}) = \frac{-\Delta E \cdot nF}{RT} + \ln(a_{Li(WE)}) \quad [\text{Eq. 4.26}]$$

From the equations and the experimental OCP values at the three temperatures studied, activity coefficients were determined. At each temperature, four activity coefficients were calculated, the average value and its variation were the following: at 400 °C, $8.06 \cdot 10^{-5}$ with a CV(%) of 5.7%, $2.47 \cdot 10^{-4}$ at 500 °C with a CV(%) of 6.0%, and $7.01 \cdot 10^{-4}$ with a CV(%) of 3.1% at 600 °C. Note that, all CVs(%) were below 10%, indicating a low variation between the calculated coefficients at each temperature.

From the results, Sn-3.0Li was considered a viable reference system. During its testing, the sensor exhibited excellent stability and good agreement with the Nernst equation, as in previous experiments with Pb-Li alloys. Nevertheless, further experiments should be performed to test the determined activity coefficients to validate the accuracy of the measured OCP.

From this outcome, the sensor's flexibility was expanded, expecting that even more Li alloys could be explored as reference electrodes. Moreover, the satisfactory results also indicated the possibility that the sensor could be used for Li measurements in molten Sn-Li alloys.

4.4.1.3. Lithium activity in Pb-Li alloys

Lithium activity in Pb-Li alloys is a subject that generates many interests. To study its relationship with lithium concentration, potentiometric experiments have been performed by different authors [196–198]. From the results, Hubberstey et al. proposed a series of relationships that predicted the lithium activity evolution with the temperature or its concentration [187]. Among these, the described correlations in [Eq. 4.10], [Eq. 4.11], [Eq. 4.12] were established, permitting to relate the lithium activity with the Li concentration at

400 °C, 500 °C, and 600 °C. However, these correlations were specific for a concentration range of $0.01 < x_{\text{Li}} < 0.17$. At larger lithium concentrations than the eutectic, Hubberstey recommended not to use these correlations since, in that situation ($x_{\text{Li}} > 0.17$), the calculated lithium activities were anticipated to exhibit a significant deviation [187].

To be able to further study the lithium activity in Pb-Li ($x_{\text{Li}} > 0.17$), it is of interest to evaluate the sensor's range and revalidate the sensor agreement with the proposed Hubberstey's correlations [187]. From this evaluation, it is possible to determine the suitability of the sensor to be used as a tool for the thermodynamic study of this binary system. Gaining insight into the lithium chemistry at compositions larger than $x_{\text{Li}} > 0.17$ opens the possibility to formulate new correlations that can describe the lithium activity dependence on its concentration at different temperatures.

Evaluation of the Sensor's Range

To evaluate the sensor's range, potentiometric measurements were performed in the following concentration range: $3\text{at}\% \leq x_{\text{Li}} \leq 35\text{at}\%$. At 400 °C, 25at% Li was the maximum lithium concentration measured since at a higher Li at% the melting point of the alloy would exceed 400 °C. In those experiments, the RE was set at a lithium concentration close to 3at% Li. In Figure 4.68 the OCP measurements at 400 °C of the Pb-Li alloys with at% Li concentrations of 3.1, 5.3, 9.3, 15.4, and 25.0 are shown. The OCP of these alloys (WE) were measured against a Pb-Li alloy of 3.2at% Li as the reference electrode.

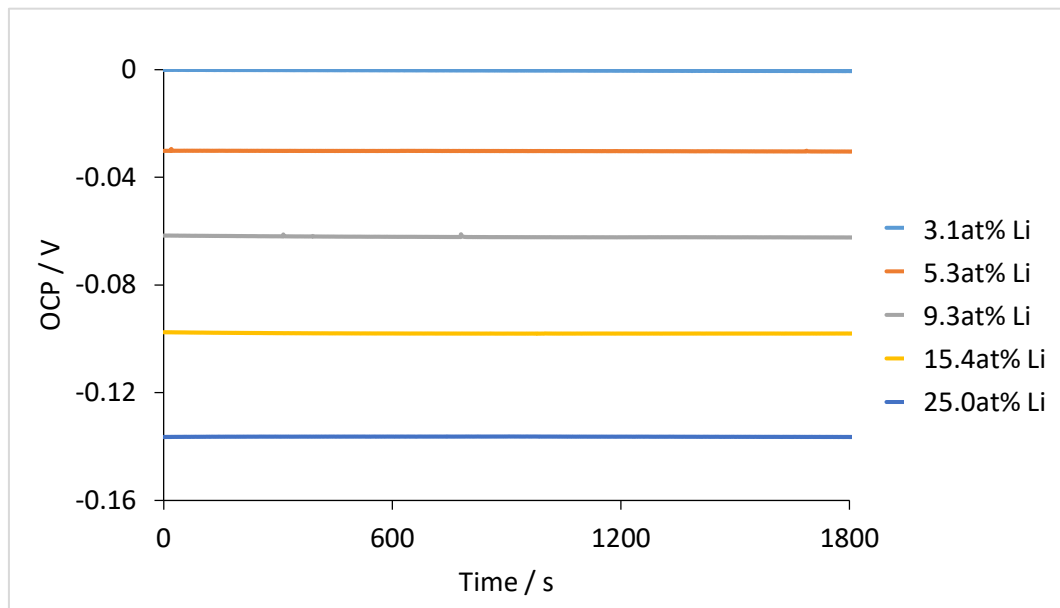


Figure 4.68. OCP measurements in Pb-Li alloys with Li concentrations of 3.1at%, 5.3at%, 9.3at%, 15.4at%, and 25.0at% Li at 400 °C. Pb-3.2Li was used in the reference electrode.

From Figure 4.68, it was noticed that OCP measurements showed good stability throughout the entire measurement: the potential differences between the initial and the final OCP values were below 1 mV with SDs $\leq \pm 0.1$ mV. From the measured Pb-Li alloys with 3.3at%, 5.3at%, 9.3at%, 15.4at%, and 25.0at% Li the calculated OCPs using the Nernst equation were: 0 mV, -33 mV, -66 mV, -96 mV, and -125 mV respectively. To calculate the OCPs, the theoretical Li activities were calculated using Hubbestey's correlations independently of the Li concentration of the alloy. Low deviations in the order of a few mV were obtained between the calculated and the experimental OCP values for the Pb-Li alloys with Li concentrations equal to or below 15.4at%. From low to high Li concentration, experimental OCP were -1 mV, -31 mV, -62 mV, -98 mV, with deviations of 1 mV, 2 mV, 4mV, and 2 mV, respectively. For the 25.0at% Li alloy, the final OCP was -136 mV, with a deviation of 11 mV. This large deviation was associated with the fact that the lithium activity was calculated extrapolating Hubberstey's correlations.

Similar measurements were performed at 500 °C and 600 °C. All OCP values at each working temperature are shown in Table 4.17, along with the calculated cell potentials. In the last column of the table, the deviations between experimental and calculated potentials are shown in mV.

Table 4.17. Experimental and calculated potentials in Pb-Li alloys with different Li concentrations (WE) at 400 °C, 500 °C, and 600 °C. Pb-3Li was used in the reference electrode.

Temperature (°C)	WE at% Li	$\Delta E_{\text{Experimental}}$ (OCP, V)	$\Delta E_{\text{Calculated}}$ (V)	Deviation / mV
400	3.1	-0.001	0.000	1
	5.3	-0.031	-0.033	2
	9.3	-0.062	-0.066	4
	15.4	-0.098	-0.096	2
	25.0	-0.136	-0.125	11
500	3.2	-0.001	0.000	1
	5.9	-0.042	-0.044	2
	9.5	-0.077	-0.078	1
	15.1	-0.113	-0.111	2
	23.6	-0.150	-0.144	6
	35.2	-0.200	-0.172	28
600	3.2	0.001	0.000	1
	5.9	-0.049	-0.052	3
	9.5	-0.090	-0.092	2
	15.1	-0.131	-0.132	1
	23.6	-0.175	-0.170	6
	35.2	-0.226	-0.204	22

It can be observed in Table 4.17 that OCPs were close to the calculated ones for Pb-Li alloys with concentrations lower than 17at% Li. In those experiments, average deviations of 2 mV \pm 1 mV were obtained. At larger concentrations than 17at% Li, the deviations increased. The largest deviation was obtained for the measurement in the Pb-Li alloy with a 35.2at% Li, which showed a deviation larger than 20 mV at 500 °C and 600 °C. These resulted in a significant deviation between their nominal and experimental lithium concentrations since

divergences larger than 15% were estimated, thus, validating that Hubberstey's linear correlations cannot be used outside the $0.01 < x_{Li} < 0.17$ range.

To study the agreement between the experimental results in the 3at% to 15at% Li range and Hubberstey's correlations ([Eq. 4.10], [Eq. 4.11], [Eq. 4.12]), lithium activity for each of the measured alloys was determined using equation ([Eq. 4.27]). It is worth noting that to calculate the lithium activities in the WE ($a_{Li(WE)}$), the lithium activity in the RE ($a_{Li(RE)}$) was calculated using Hubberstey's relationships.

$$\ln(a_{Li(WE)}) = \frac{\Delta E \cdot nF}{RT} + \ln(a_{Li(RE)}) \quad [\text{Eq. 4.27}]$$

Then, the natural logarithm of these $a_{Li(WE)}$ was plotted against the natural logarithm of the lithium atomic fraction (x_{Li}). The obtained relationships at the three studied temperatures are shown in Figure 4.69.

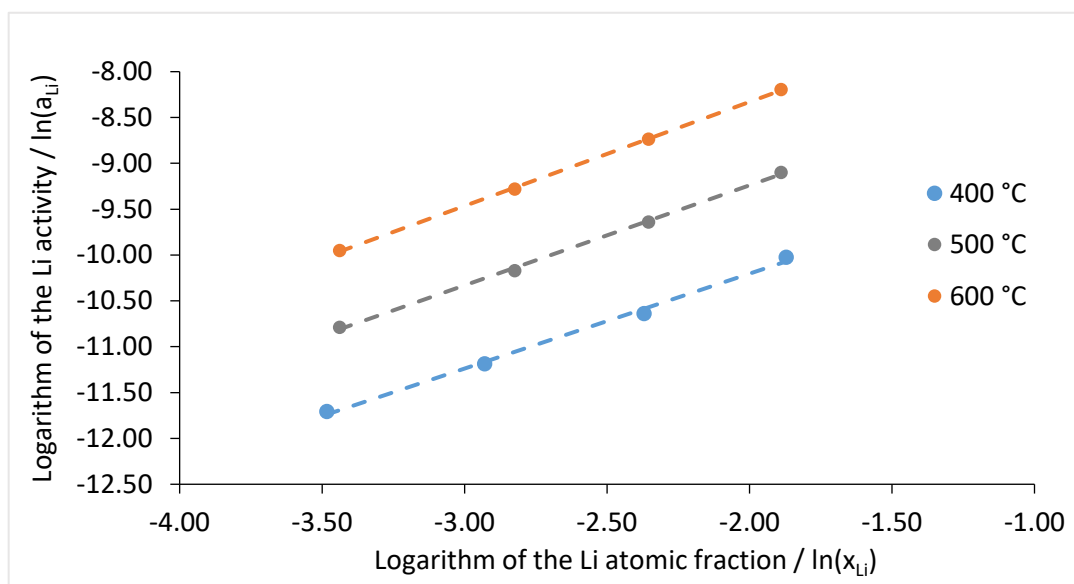


Figure 4.69. The logarithm of the lithium activity against the logarithm of lithium atomic fraction in Pb-Li alloys at 400 °C, 500 °C, and 600 °C.

The equations for the correlations in the $0.03 < x_{Li} < 0.15$ concentration range at each temperature were the following:

$$400 \text{ °C} \rightarrow \ln(a_{Li}) = 1.035 \cdot x_{Li} - 8.133; R^2 = 0.996 \quad [\text{Eq. 4.28}]$$

$$500 \text{ °C} \rightarrow \ln(a_{Li}) = 1.091 \cdot x_{Li} - 7.057; R^2 = 0.999 \quad [\text{Eq. 4.29}]$$

$$600\text{ }^{\circ}\text{C} \rightarrow \ln(a_{\text{Li}}) = 1.134 \cdot x_{\text{Li}} - 6.061; R^2 = 0.999 \quad [\text{Eq. 4.30}]$$

The correlations showed a linear relationship toward lithium atomic fraction since coefficients of determination of $R^2 > 0.99$ were obtained. Furthermore, their slopes and y-intercepts were close to Hubberstey's published values [187]. Divergences between experimental and theoretical values were calculated at each of the studied temperatures (Table 4.18).

Table 4.18. Slope and y-intercept divergences between experimental and Hubberstey's correlations at 400 °C, 500 °C, and 600 °C.

Temperature / °C	Slope Divergence (%)	Y-intercept Divergence (%)
400	0.5	0.1
500	1.0	0.4
600	0.4	0.2

From Table 4.18, it can be seen that divergences equal to or below 1% were obtained when comparing their slopes and y-intercepts, demonstrating that the sensors' OCP experimental data was in good agreement with Hubberstey's linear correlations.

From these results, it could be concluded two facts. First, that the sensor showed linearity in the $0.03 < x_{\text{Li}} < 0.17$ range at 400 °C, 500 °C, and 600 °C. And second, the correlations obtained when studying its linearity ([Eq. 4.28]-[Eq. 4.30]) are in good agreement with those previously published in Hubberstey's work [187]. These results further proved the proper performance of the constructed electrochemical sensors demonstrating that the sensor can be used for the simple and quick determination of the lithium activity in a Pb-Li alloy.

Experiments that served Hubberstey to establish its correlations relied on OCP versus Li concentration values reported by other authors [196–198]. In those experiments, concentration cells were used to measure the potential of a Pb-Li alloy versus the potential of pure lithium. Moreover, as electrolytes, they used a mixture of lithium and potassium liquid salts. Compared to this previous work, the developed electrochemical sensors present some major advantages: I) Such a reactive material as pure lithium is not required to be used as a reference electrode. Pb-Li alloys prepared with a known concentration can be used since their activities can be easily determined. II) A solid electrolyte will exhibit a lower interaction with the system measured. Note that, the liquid electrolyte has a higher probability to contaminate or cause side reactions when in contact with the alloys under measurement.

Lithium activity correlations in the $x_{Li} \geq 0.17$ Li range

From the previously obtained results (see Table 4.17), it was observed that significant deviations were determined between experimental and calculated OCP for Li concentrations higher than 17at% Li. Consequently, it was concluded that Hubberstey's linear correlations could not be used to extrapolate lithium activities ($x_{Li} > 0.17$). Thus, to be able to use the sensor at larger Li concentrations, the lithium activity relationship towards lithium atomic fraction was further studied.

To this aim, from the experimental OCP of the alloys with Li concentration higher than 17at% (see Table 4.17), lithium activities in the WE were calculated using the equation [Eq. 4.27] and are shown in Table 4.19. Due to the small number of data points from the previous experiment, the OCP of Pb-Li alloys with Li at% of 17.0 and 20.0 was measured using as a reference electrode a eutectic Pb-Li alloy. Their Li activities were also calculated and included in Table 4.19.

Table 4.19. Experimental potentials and calculated lithium activities' logarithm in Pb-Li alloys with different Li concentrations (WE) at 400 °C, 500 °C, and 600 °C.

Temperature (°C)	WE at% Li	$\Delta E_{\text{Experimental}}$ (OCP, V)	Logarithm of the Li activity ($\ln(a_{Li})$)
400	17.0	0.000	-9.95
	20.0	-0.015	-9.75
	25.0	-0.136	-9.37
500	17.0	0.000	-8.99
	20.0	-0.017	-8.80
	23.6	-0.150	-8.55
	35.2	-0.200	-7.80
600	17.0	0.000	-8.04
	20.0	-0.025	-7.78
	23.6	-0.175	-7.60
	35.2	-0.226	-6.93

Then, the natural logarithm of these $a_{Li}(WE)$ was plotted against the natural logarithm of the lithium atomic fraction (x_{Li}). The obtained relationships at the three studied temperatures are shown in Figure 4.70.

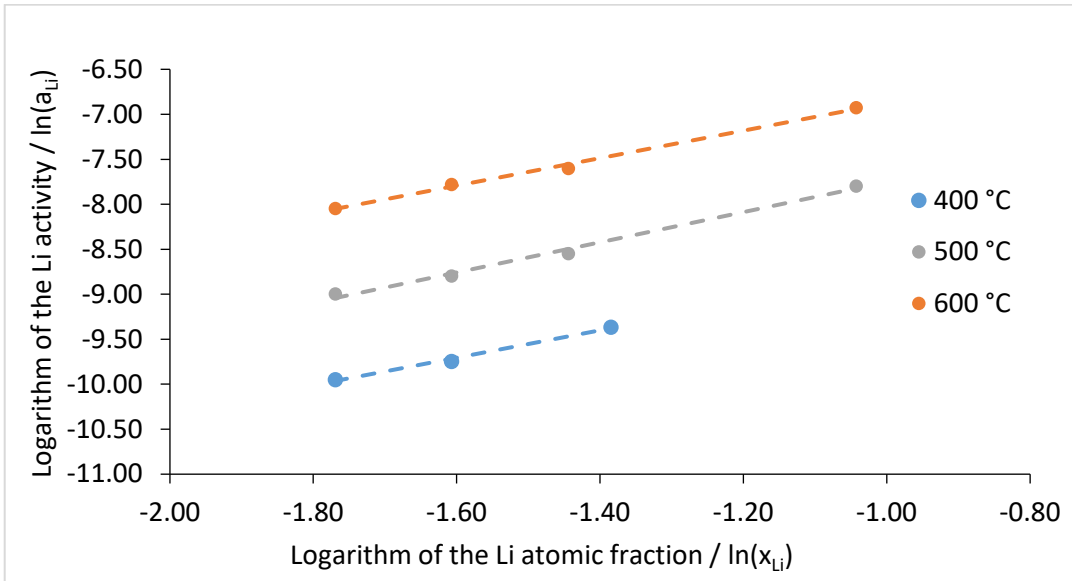


Figure 4.70. The logarithm of the lithium activity plotted against the logarithm of lithium atomic fraction in Pb-Li alloys with $x_{Li} \geq 0.17$ at 400 °C, 500 °C, and 600 °C.

The equations for the correlations in the $x_{Li} \geq 0.17$ concentration range at each temperature were the following:

$$400 \text{ °C} \rightarrow \ln(a_{Li}) = 1.524 \cdot x_{Li} - 7.268; R^2 = 0.993 \quad [\text{Eq. 4.31}]$$

$$500 \text{ °C} \rightarrow \ln(a_{Li}) = 1.677 \cdot x_{Li} - 6.074; R^2 = 0.992 \quad [\text{Eq. 4.32}]$$

$$600 \text{ °C} \rightarrow \ln(a_{Li}) = 1.527 \cdot x_{Li} - 5.349; R^2 = 0.996 \quad [\text{Eq. 4.33}]$$

The correlations demonstrated a linear relationship toward lithium atomic fraction since coefficients of determination of $R^2 > 0.99$ were obtained. These $x_{Li} \geq 0.17$ linear range correlations were established from 17at% Li up to 25at% Li at 400 °C, and from 17at% Li up to 35at% at 500 °C and 600 °C. When comparing the slopes and y-intercepts of these new correlations to those from Hubberstey's ([Eq. 4.10], [Eq. 4.11], [Eq. 4.12]), significant differences were observed. These were superior to 30% evidencing that Hubberstey's correlation could not be used to extrapolate. Note that a similar approach as Hubberstey's correlations has to be considered with these $x_{Li} \geq 0.17$ linear range correlations:

extrapolating the activities outside the specified ranges should not be performed due to the unclear relationship between the a_{Li} and the x_{Li} [199].

To have a first approach to how these $x_{\text{Li}} \geq 0.17$ linear range equations would perform in a real-case scenario, four Pb-Li alloy samples were synthesized with concentrations of 15.8at%, 18.2at%, 21.1at%, and 25.0at% Li. Then OCPs were measured versus a Pb-15.8Li reference electrode at 400 °C. In this measurement, the RE exhibited a eutectic concentration since it is advised to keep similar lithium activities in both electrodes [48]. Furthermore, since only the first Pb-Li alloy sample concentration was in the eutectic range, a short-circuit situation would be easily distinguished from the subsequent OCP measurements. In Figure 4.71 there are shown the OCP measurements for the mentioned alloy samples.

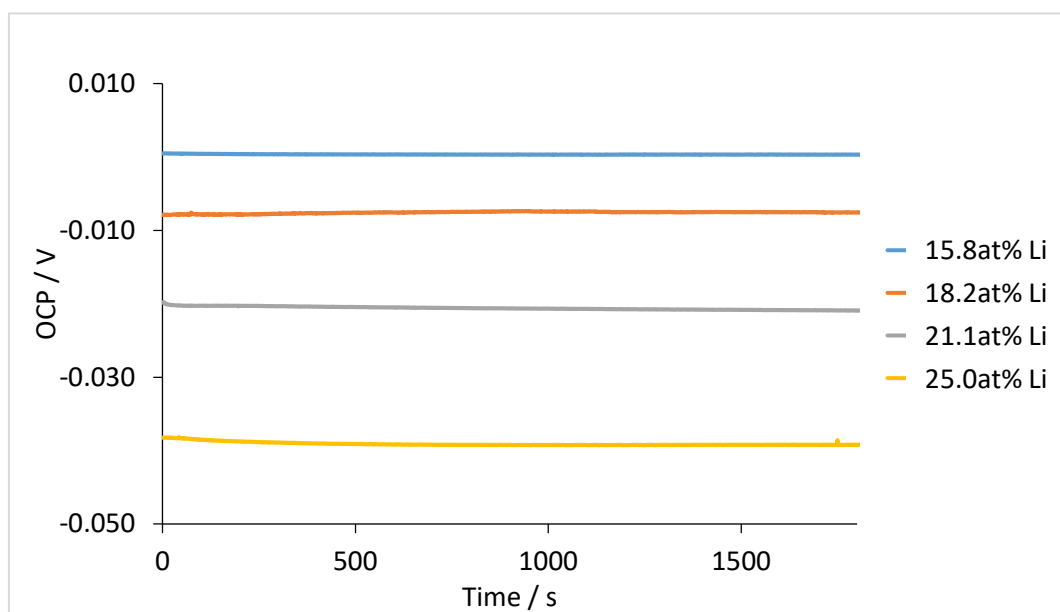


Figure 4.71. OCP measurements in Pb-Li alloys samples with Li concentrations of 15.8at%, 18.2at%, 21.1at%, and 25.0at% Li at 400 °C. Pb-15.8Li was used in the reference electrode.

From Figure 4.71, OCP measurements showed good stability throughout the entire measurement: the potential difference between the initial and the final OCP values were below 1 mV with SDs $\leq \pm 0.2$ mV. The experimental OCP potentials measured at the end of the measurements are shown in Table 4.20. From the measured potentials, lithium activities at the WE were calculated using the Nernst equation (see [Eq. 4.27]). Finally, using the calculated lithium activities and the adequate linear range correlations the lithium atomic concentration (at% Li) was quantified for each alloy sample: [Eq. 4.10] was used for samples with at% Li lower than 17% and [Eq. 4.31] was used for samples with higher concentrations

than 17at% Li. The quantification results are presented in Table 4.20, relative errors were also included in the last column of the table.

Table 4.20. Lithium quantification results for the Pb-Li samples with concentrations: 15.8at%, 18.2at%, 21.1at%, and 25.0at% Li. The OCP measurements were performed at 400 °C.

WE at% Li	$\Delta E_{\text{Experimental}}$ (OCP, V)	$\ln(a_{\text{Li}})_{\text{Calculated}}$	Quantified at% Li	Relative Err. (%)
15.8	0.000	-10.0	15.7	-0.5
18.2	-0.008	-9.9	17.8	-2.0
21.1	-0.020	-9.7	20.6	-2.3
25.0	-0.039	-9.4	25.4	1.6

From the quantification results, deviations equal to or below 0.5%at Li were determined when compared to the nominal concentrations of the Pb-Li samples. Furthermore, relative errors below 3.0% were obtained. From the obtained results it was concluded that both the sensor and the linear correlations worked satisfactorily in the concentration range studied. With these $x_{\text{Li}} \geq 0.17$ linear range correlations, Li probes appeared as an interesting analytical tool for Li determination in molten Pb-Li alloys in a wide range of concentrations ($0.03 \leq x_{\text{Li}} \leq 0.25$ at 400 °C, and $0.03 \leq x_{\text{Li}} \leq 0.35$ at 500 °C and 600 °C).

Being able to quantify the Li concentration at a larger atomic percentage than 17at% can be helpful to monitor a lithium overdose in the TBMs. Note that, when trying to resupply lithium to these modules, this kind of situation can occur. As previously mentioned, the optimal breeding performance is achieved by keeping the PbLi alloys in the TBMs in their eutectic composition. A change in the Li concentration will affect the physicochemical properties of the alloy and may detrimentally affect the performance of the reactor. Therefore, by using the developed electrochemical sensors it would be able to rapidly detect and respond to these situations to minimize the impact of any possible adverse outcome.

Furthermore, the study of the lithium chemistry and thermodynamics of the Pb-Li binary system is a subject that generates much interest due to its application in fusion technology. Moreover, the capability and easiness that the developed sensor has demonstrated when thermodynamically studying the Pb-Li system suggest that the sensor could be used to explore other lithium binary systems such as Sn-Li, Zn-Li, Bi-Li, etc.

4.4.1.4. Evaluation of the Sensor's Precision

To study the precision of the sensor, two tests were performed. On one hand, the reproducibility, repeatability, and intermediate precision of the measurement device were evaluated. To this end, it could be determined the extent to which the OCP could vary as a function of different variables. For the tests, a Pb-Li alloy with a concentration of 16.0 at% Li was used in the WE versus a Pb-3.0Li reference electrode. On the second hand, the resolution of the sensor was evaluated, trying to quantify different alloys with concentrations close to the eutectic. In this way, it was possible to determine if the sensor allowed to monitor small concentration variations.

Repeatability, Intermediate Precision, and Reproducibility

The first parameter evaluated was the repeatability of the sensor, which determines the sensor's precision under the following conditions: the same method on identical test items, in the same laboratory, by the same operator using the same equipment, and within short intervals of time [188]. For this purpose, the alloy measured in the WE was divided into three similar aliquots, and the OCP of each was measured with the same sensor at 500 °C. Each of the OCP measurements lasted 30 minutes. Note that, the OCP measuring time was decreased from 40 to 30 minutes due to the good signal stability that was obtained in previous experiments. In Figure 4.72, the OCP measurement from each of the three replicates is shown.

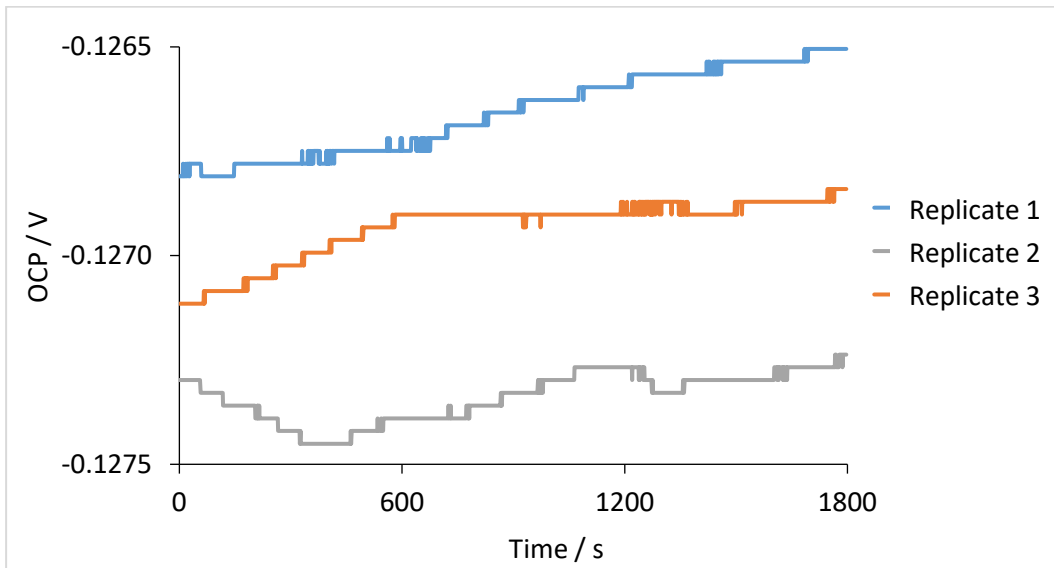


Figure 4.72. OCP measurement of three replicates in a Pb-Li alloy with Li concentration of 16.0at% at 500 °C. Pb-3.0Li was used in the reference electrode.

As observed in Figure 4.72, OCP values showed good stability throughout the entire measurement: the potential differences between the initial and the final OCP values were below 0.5 mV, with SDs $< \pm 0.2$ mV. The experimental OCP potentials measured at the end of the measurements were -126.5 mV, -127.2 mV, and -126.8 mV for Replicates 1, 2, and 3 respectively. These results yielded an average value of -126.8 mV with a standard deviation of ± 0.4 mV and a coefficient of variation (CV) of 0.3%. The CV(%) of 0.3%, indicated good repeatability since it is inferior to the maximum reference value (2.7%) suggested by the Association of Analytical Communities (AOAC) [188].

The second parameter to be studied was the intermediate precision of the sensor. To evaluate this parameter, one single sensor was used to measure the OCP of the same Pb-Li alloy on three different days. A 30 minutes OCP measurement was performed at 500 °C on three different days. In Figure 4.73, the OCP measurements are shown.

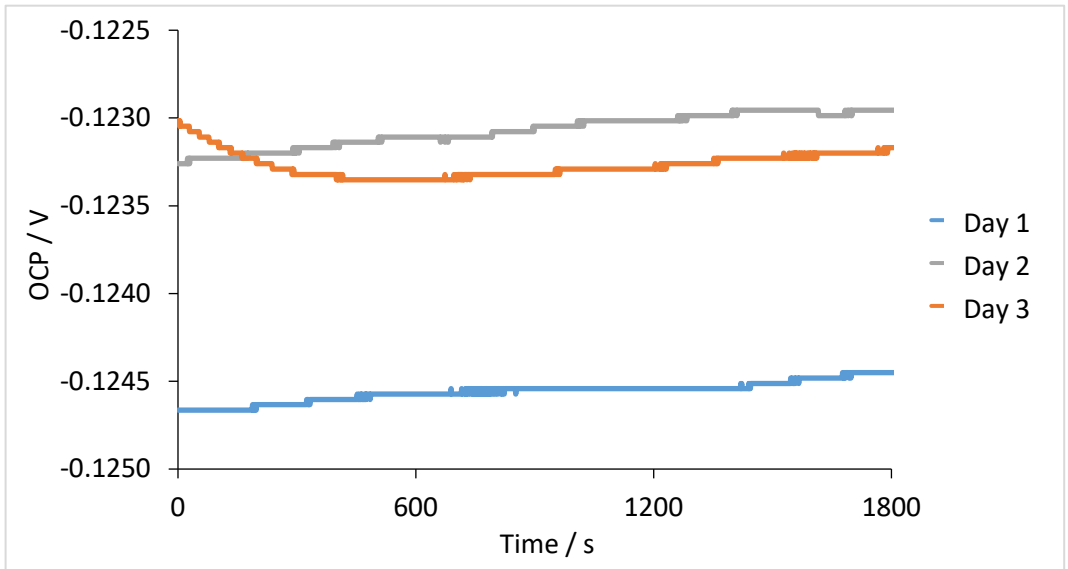


Figure 4.73. OCP measurement on three different days in the same Pb-Li alloy with a Li concentration of 16.0at% at 500 °C. Pb-3.0Li was used in the reference electrode.

As shown in Figure 4.73, OCP values showed good stability throughout the entire measurement: the potential difference between the initial and the final OCP value was below 0.3 mV, with SDs $\leq \pm 0.1$ mV. The experimental OCP measured at the end of the measurements were -124.4 mV, -122.9 mV, and -123.1 mV for days 1, 2, and 3 respectively. These results yielded an average potential value of -123.6 mV with a standard deviation of ± 0.8 mV and a coefficient of variation of 0.7%. It indicated good intermediate precision since it is inferior to the maximum reference value (4.0%) suggested by AOAC [188].

The last parameter studied was the reproducibility of the sensor. To evaluate this parameter, three lithium sensors were used to measure the OCP of the same Pb-Li alloy in the WE. In Figure 4.74, the OCP measurement performed with each of the three sensors is shown.

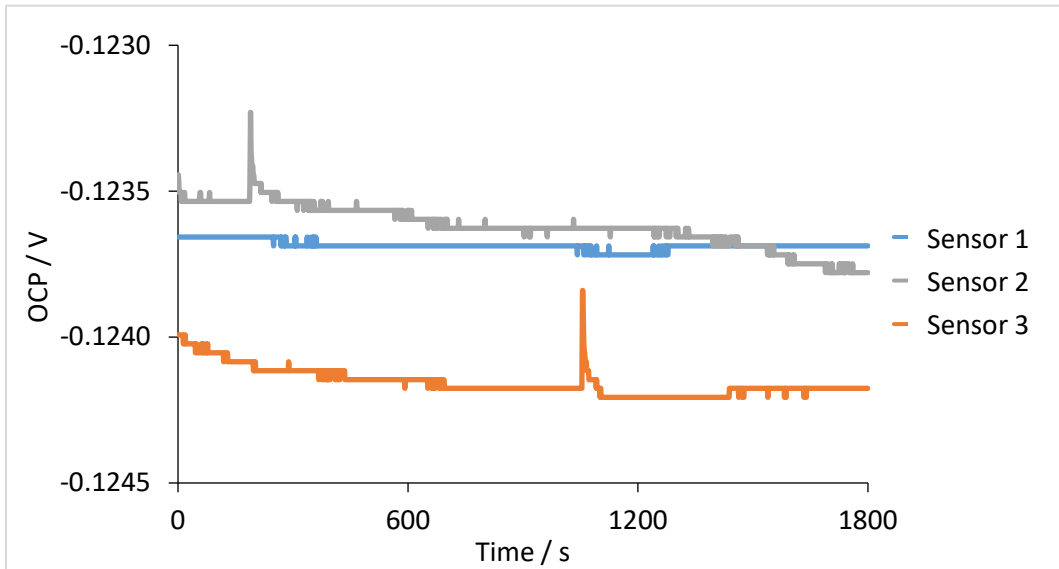


Figure 4.74. OCP measurement with three different lithium sensors in the same 16.0at% Li Pb-Li alloy at 500 °C. Pb-3.0Li was used in the reference electrode.

As shown in Figure 4.74, OCP values showed good stability throughout the entire measurement: the potential difference between the initial and the final OCP value was below 0.3 mV, with SDs $< \pm 0.4$ mV. The experimental OCP potentials measured at the end of the measurements were -123.7 mV, -123.8 mV, and -124.2 mV for sensors 1, 2, and 3 respectively. These results yielded an average potential value of -123.9 mV with a standard deviation of ± 0.3 mV and a coefficient of variation of 0.2%. It indicated good reproducibility since it is inferior to the maximum reference value (4.0%) suggested by AOAC [188].

Overall, the sensor exhibited excellent repeatability, intermediate precision, and reproducibility. All the coefficients of variations obtained from the evaluations were under the maximum reference values suggested by the AOAC. From the results, it was concluded that the constructed Li sensor yielded consistent results in Pb-Li alloys.

Sensor Precision Near the Pb-Li Eutectic

All the previous evaluations were performed with eutectic Pb-Li, and it was still necessary to test the sensor's precision in its final target application: lithium monitoring of eutectic Pb-Li. With this aim, OCP measurements were performed at 500 °C on the following Pb-Li alloy samples: 13.1at%, 14.5at%, 16.0at%, and 17.5at%. These samples were prepared with variations of ~ 1.5 at% Li to test whether the sensor could satisfactorily quantify these small

Li concentration differences near the eutectic. Since the alloy samples concentrations were close to the eutectic, to be able to distinguish a short-circuit situation, a 3.0at% Li alloy was used in the RE. In Figure 4.75 it is shown the OCP measurements of the mentioned Pb-Li sample alloys at 500 °C.

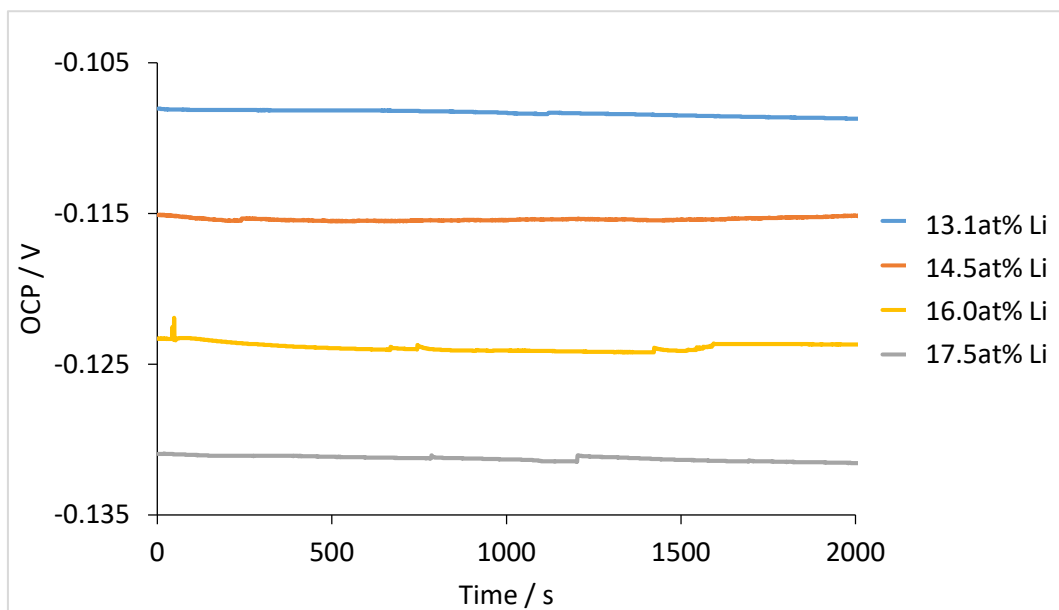


Figure 4.75. OCP measurements of five Pb-Li sample alloys with Li concentrations of 13.1at%, 14.5at%, 16.0at%, and 17.5at% Li at 500 °C. Pb-3.0Li was used in the reference electrode.

It can be seen in Figure 4.75 that OCP measurements showed good stability throughout the entire measurement: the potential difference between the initial and the final OCP values were below 1 mV with SDs < ± 0.4 mV. OCP values measured at the end of the measurements are shown in Table 4.21. From the measured potentials and using the known lithium activity of the reference electrode, lithium activities at the WE were calculated through the Nernst equation ([Eq. 4.27]). Then, the determined lithium activities were used to calculate the lithium atomic fraction (x_{Li}) in the WE. To do so, Hubberstey correlation (13.1at% Li- 16.0at% Li, [Eq. 4.11]) or the $x_{Li} \geq 0.17$ linear range correlation discussed in section 4.4.1.3 (17.5 at% Li, [Eq. 4.32]) were used based on the nominal concentration of the samples. Ultimately, from the atomic fractions, the lithium atomic concentrations (at% Li) were quantified. The quantification results are presented in Table 4.21, as well as relative errors which were also included in the last column of the table.

Table 4.21. Lithium quantification results for the Pb-Li samples with concentrations: 13.1at%, 14.5at%, 16.0at%, and 17.5at%. The OCP measurements were performed at 500 °C.

WE at% Li	$\Delta E_{\text{Experimental}}$ (OCP, V)	$\ln(a_{\text{Li}})_{\text{Calculated}}$	Quantified at% Li	Relative Err. (%)
13.1	-0.108	-9.25	13.5	2.9
14.5	-0.115	-9.14	14.9	2.5
16.0	-0.124	-9.02	16.6	3.7
17.5	-0.131	-8.91	18.5	5.7

From the quantification results, low discrepancies were obtained when compared to the nominal concentration of the Pb-Li samples. The relative errors determined were below 6.0%. However, upon observing the deviations from the quantified results, a systematic error could be occurring. Note that, from high to low nominal concentrations, deviations were: 0.4at% Li, 0.4at% Li, 0.6at% Li, and 1.0at% Li. Such results indicate the possibility that as Li concentration increased the same happened to the deviation. This phenomenon could be explained if it is considered that the reference alloy could have been prepared with a concentration slightly lower than 3.0at% Li. Note that, if the lithium concentration of the reference electrode was decreased in the order of 0.1at% Li, these deviations would be below 0.5at% Li and would be more arbitrary: -0.1at% Li, -0.2at% Li, 0.0at% Li, and 0.5at% Li. Nevertheless, an average deviation of 0.6at% Li was obtained from the quantification results, which was below the 1.5at% Li tested in the experiment. Therefore, it was confirmed that the sensor showed enough precision to be able to quantify small Li concentration variations (~1.5 at% Li) in a Pb-Li alloy.

To further test the Li probe, a similar approach was performed but, in this situation, the lithium concentration in a Pb-Li alloy sample was monitored in real-time. In this experiment, a continuous OCP measurement was performed while the Li concentration in the WE alloy was decreased as the potential stabilized by adding Pb to the melt. Since the measurements were performed from high to low concentrations, it had to be considered that the sensor could be affected by memory effect.

Experiments started with the highest Li concentration in the WE: 17.5at% Li. Then, the assembly was heated at 500 °C and the sensor was submerged in the molten alloy. Upon temperature stabilization, the OCP measurement was initiated. Once the potential was considered stable, to decrease the Li concentration in the WE alloy, weighted Pb chunks

were added and mixed with an alumina rod. During the experiment, three consecutive Pb additions were performed, while the OCP was continuously monitored. A Pb-Li reference system of 3.0at% Li was used. OCP measurement is shown in Figure 4.76.

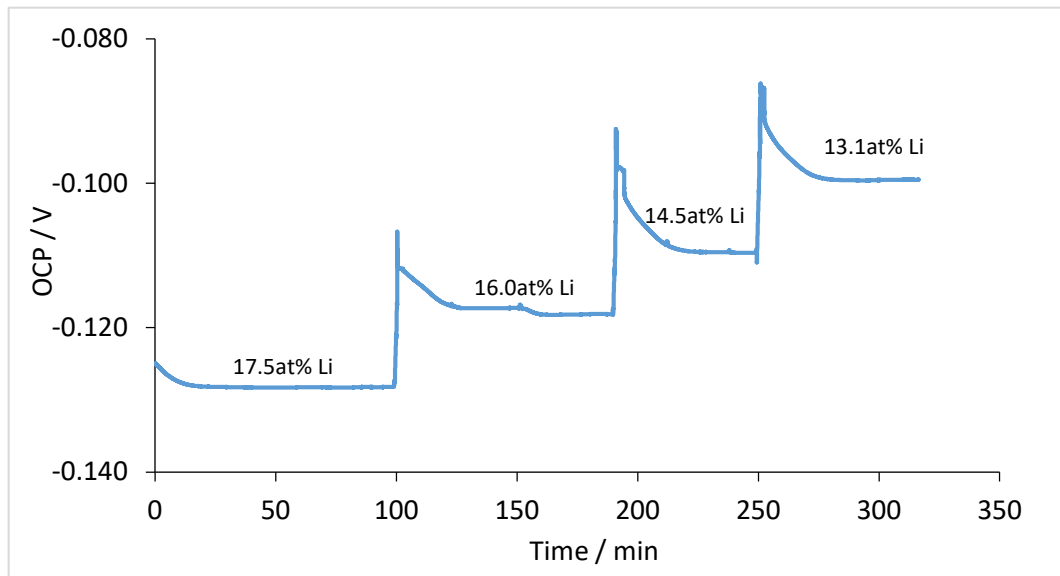


Figure 4.76. OCP measurements in a Pb-Li alloy with a varying Li concentration of 17.5at%, 16.0at%, 14.5at%, and 13.1at% Li at 500 °C. Pb-3.0Li was used in the reference electrode.

Before each Pb addition, a period of 60-120 minutes was waited to ensure the stabilization of the signal of the sensor. The signal's stabilization was associated with two main factors, the homogenization of the Li composition in the alloy and the rebalance of the temperature. It has to be noted that when performing the Pb additions, the cover of the experimental set-up had to be temporarily removed causing heat dissipation. The response time of the sensor, which was considered the time needed to reach 95% of the equilibrium value [44], was achieved under 10 minutes for each of the Pb additions. Once the potential reached its equilibrium value, the OCP showed good stability with SDs $< \pm 0.5$ mV.

From the OCP potentials measured at the plateaus, the lithium activities and the lithium atomic fraction (x_{Li}) in the WE were calculated. To do so, the Hubberstey correlation (13.1at% Li- 16.0at% Li, [Eq. 4.11]) or the $x_{Li} \geq 0.17$ linear range correlation discussed in section 4.5.3 (17.5 at% Li, [Eq. 4.33]) were used based on the nominal concentration of the samples. Ultimately, from the atomic fractions, the lithium atomic concentrations (at% Li) were determined. The quantification results are presented in Table 4.22 along with the relative errors calculated.

Table 4.22. Lithium quantification results for the Pb-Li samples with concentrations: 17.5at%, 16.0at%, 14.5at%, and 13.0at% Li. The OCP measurements were performed at 500 °C, with Pb-3.0Li as the reference electrode.

WE at% Li	$\Delta E_{\text{Experimental}}$ (OCP, V)	$\ln(a_{\text{Li}})_{\text{Calculated}}$	Quantified at% Li	Relative Err. (%)
17.5	-0.128	-8.96	17.9	2.2
16.0	-0.118	-9.11	15.3	4.6
14.5	-0.110	-9.24	13.6	6.4
13.0	-0.100	-9.39	11.8	9.2

From the quantification results, relative errors below 10.0% were determined. Furthermore, from these values, a systematic error could be observed, since the relative error kept increasing after each addition. Furthermore, the deviations from the quantified also demonstrated this kind of error: 0.4at% Li, -0.7at% Li, -0.9at% Li, and -1.2at% Li, from high to low nominal concentrations respectively. These relatively high deviations could not be uniquely attributed to the reference electrode, since the difference between the deviations of the 17.5at% Li and 16.0at% Li alloys was particularly large (1.1at% Li). For this reason, this phenomenon was also attributed to a possible concentration inhomogeneity in the starting Pb-Li alloys, growing after each Pb addition. This phenomenon should be further studied to clarify and minimize the error. Nevertheless, this effect seemed to discard a possible memory effect, since over-quantification would be expected, a contrary result that the one observed.

Although a few experimental aspects should be improved, on balance, the results were considered satisfactory. These indicated that the sensor worked properly and demonstrated that measurements in real-time could be performed to monitor the Li concentration of a Pb-Li alloy.

4.4.2. $\text{Li}_6\text{La}_3\text{Ta}_{1.5}\text{Y}_{0.5}\text{O}_{12}$ Sensor

As discussed in section 4.2, two different lithium conducting solid electrolytes were adequately synthesized and sintered in this work: $\text{Li}_6\text{BaLa}_2\text{Ta}_2\text{O}_{12}$ and $\text{Li}_6\text{La}_3\text{Ta}_{1.5}\text{Y}_{0.5}\text{O}_{12}$. The first potentiometric experiments were performed with the LBLTO, but once synthesized, the LLTYO electrolyte was also potentiometrically tested in Pb-Li alloys.

To this aim, potentiometric experiments with this electrolyte were performed in the concentration range: from a 3at% to 17at% Li. OCP measurements were performed in four Pb-Li alloys (WE) with concentrations of 2.9at%, 5.3at%, 9.8at%, and 17.1at% Li. Since the majority of the measured alloys were not close to the eutectic composition, a Pb-17.0Li reference electrode was used. As in previous tests, the OCP was measured at 400 °C, 500 °C, and 600 °C sequentially. Figure 4.77 shows the OCP for the 2.9at% Pb-Li (WE) versus the 17.0at% Pb-Li (RE) alloy as a function of time at each working temperature.

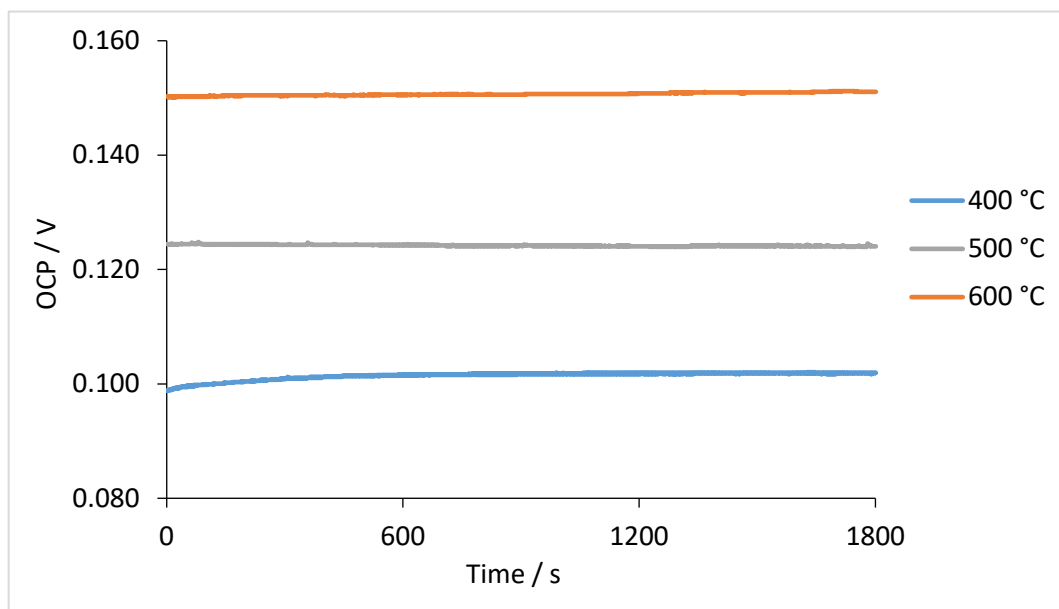


Figure 4.77. OCP measurements in Pb-Li 2.9at% alloy at 400 °C, 500 °C, and 600 °C. Pb-17.0Li was used in the reference electrode.

It can be observed in Figure 4.77 that by increasing the temperature, the OCP also increased as described by the Nernst equation ([Eq. 4.9]). The theoretical OCP values calculated using the Nernst equation were 106 mV at 400 °C, 128 mV at 500 °C, and 151 mV at 600 °C. Deviations in the order of mV were determined between theoretical and experimental OCP values at the end of the measurements. At 400 °C and 500 °C, the measured OCP were 102 mV and 128 mV respectively, and both presented a deviation of 4 mV. At 600 °C, the

measured OCP was 151 mV and exhibited a deviation of 1 mV. It can be also seen from Figure 4.77, that the OCP showed good stability throughout the entire measurement: the average potential difference between the initial and the final value was below 2 mV, and SDs below ± 0.4 mV were determined at each temperature.

After OCP determinations in a Pb-Li alloy with a 2.9at% Li (WE), lithium was added to this alloy to increase its lithium concentration. Then, OCP was measured at the three temperatures of interest. Measurements with the Pb-Li alloys composed of 5.3at%, 9.8at%, and 17.1at% Li were performed following the described procedure. OCP values measured at each working temperature are shown in Table 4.23, along with calculated cell potentials. Lithium activities at each concentration and temperature were calculated using Hubberstey's correlations [187]. In the last column of the table, the deviations of the experimental potentials compared to the calculated ones are shown.

Table 4.23. Experimental and calculated potentials in Pb-Li with 2.87at%, 5.33at%, 9.85at%, and 17.16at% Li, at 400 °C, 500 °C, and 600 °C. Pb-17.02Li was used in the reference electrode.

Temperature (°C)	WE at% Li	$\Delta E_{\text{Experimental}}$ (OCP, V)	$\Delta E_{\text{Calculated}}$ (V)	Deviation / mV
400	2.9	0.102	0.106	4
	5.3	0.070	0.069	0
	9.8	0.032	0.033	0
	17.1	0.000	-0.001	1
500	2.9	0.124	0.128	4
	5.3	0.085	0.084	2
	9.8	0.040	0.039	1
	17.1	0.000	-0.001	1
600	2.9	0.151	0.151	1
	5.3	0.100	0.099	1
	9.8	0.048	0.046	2
	17.1	0.000	-0.001	1

It can be observed in Table 4.23 that OCP values were close to the calculated ones. The maximum deviations were observed at 400 °C and 500 °C, where deviations of 4 mV were obtained from the 2.9at% Li alloy. Nevertheless, such deviation signified less than a 10.0% divergence between their nominal and experimental lithium concentrations. Therefore, the OCP measurement demonstrated satisfactory accuracy.

To further verify whether the results followed the Nernst equation, the sensor’s calibration curves were represented. In these curves, experimental OCP potentials were plotted as a function of the logarithm of the lithium activity in the working electrode. The fitted curves at 400 °C, 500 °C, and 600 °C are shown in Figure 4.78.

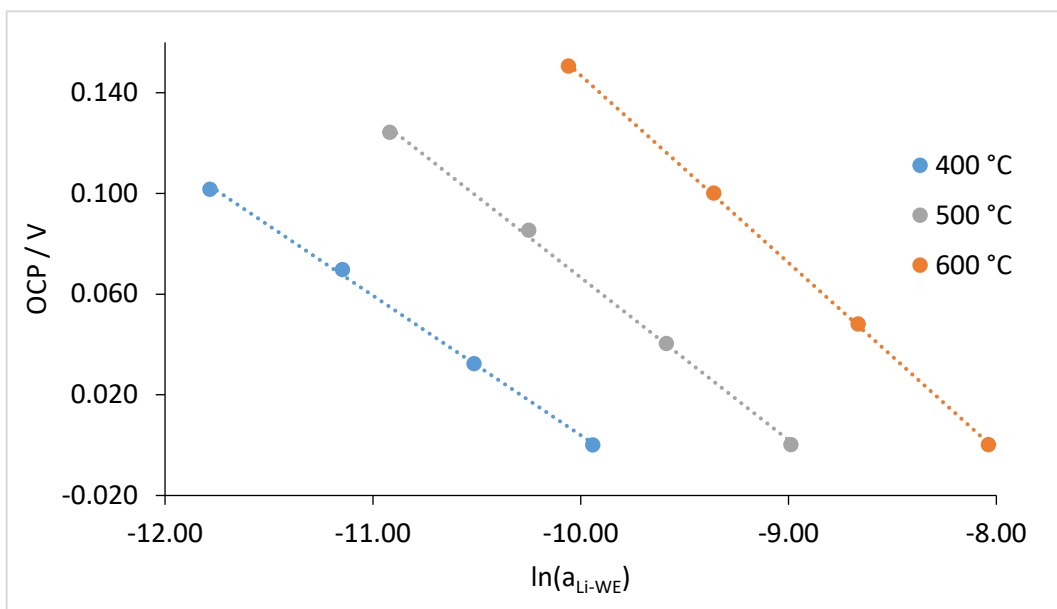


Figure 4.78. OCP potentials plotted versus the logarithm of the lithium activity in the working electrode at 400 °C, 500 °C, and 600 °C. Pb-17.0Li was used in the reference electrode.

Correlations obtained in Figure 4.78 are shown below:

$$400\text{ °C} \rightarrow \Delta E(V) = -0.055 \ln(a_{Li}) - 0.551; R^2 = 0.9988 \quad [\text{Eq. 4.34}]$$

$$500\text{ °C} \rightarrow \Delta E(V) = -0.065 \ln(a_{Li}) - 0.579; R^2 = 0.9987 \quad [\text{Eq. 4.35}]$$

$$600\text{ °C} \rightarrow \Delta E(V) = -0.074 \ln(a_{Li}) - 0.598; R^2 = 0.9998 \quad [\text{Eq. 4.36}]$$

Theoretical slopes calculated with the Nernst equation ($-RT/nF$) are -0.058 at 400 °C, -0.067 at 500 °C, and -0.075 at 600 °C. When comparing these values with those experimentally

obtained, deviations below 5% were obtained: 4.3%, 3.0%, and 1.0% respectively. On balance, satisfactory results were obtained since the slopes of the correlations were in good agreement with the Nernst equation. Furthermore, determination coefficients superior to 0.99 demonstrated the linearity of the calibration curves.

Overall, the LLTYO sensor performance was similar to the previously discussed LBLTO sensor (section 4.2.1). Both electrolytes conformed sensors that showed high stability, accuracy, and good agreement with the Nernst equation at the studied temperatures. Consequently, it was concluded that the LLTYO sensor could also have the capacity to become a Li sensing analytical tool in molten Pb-Li alloys.

4.4.3. Discussion of the Lithium Sensors Results in Pb-Li

Electrochemical Li sensors based on LBLTO and LLTYO electrolytes were developed and tested in molten Pb-Li alloys. These sensors operated in potentiometric configuration similarly to concentration cells, measuring the OCP between the WE and the RE. From their potentiometric experiments performed with Pb-Li alloys in the 3at% to 17at% Li range, LBLTO and LLTYO sensors exhibited excellent characteristics. Among these, two interesting characteristics to compare are the signal stability and the accuracy of the sensors.

As previously discussed, both sensors' OCP measurements showed excellent signal stability. This stability was evaluated in two forms: 1) the standard deviation obtained from all the data in each OCP measurement, and 2) the difference between the OCP at the start and end of the experiments (Δ OCP). From all the OCP measurements performed at 400 °C, 500 °C, and 600 °C the average values for these two parameters (SDs and Δ OCP) are calculated and shown in Table 4.24 according to the used electrolyte in the sensor.

Table 4.24. Signal stability results at 400 °C, 500 °C, and 600 °C of the LBLTO and LLTYO sensors.

Temperature / °C	LBLTO		LLTYO	
	SDs / mV	Δ OCP / mV	SDs / mV	Δ OCP / mV
400	0.2	0.5	0.2	0.4
500	0.1	0.3	0.1	0.3
600	0.2	0.4	0.2	0.4

From Table 4.24, all the OCP measurements showed standard deviations of the same order of magnitude. SDs equal to or below ± 0.2 mV were obtained independently of the temperature or the sensors' electrolyte. Such a result was also observed for OCP differences between initial and final potential. An average value of ≤ 0.4 mV was obtained from all experiments performed with a maximum value of 0.5 mV that was determined for the LBLTO sensor at 400 °C. Only differences of 0.1 mV were measured between the Δ OCP of LBLTO and LLTYO sensors. These results were considered satisfactory due to the high signal stability that the sensors demonstrated. Note that a 0.4 mV difference would impact only 0.7% of the quantified Li atomic composition, which corresponds to a 0.02-0.11at% Li variation from 3at% to 17at% Li respectively. From the results, the physicochemical stability of both LBLTO and LLTYO electrolytes in molten Pb-Li was proved. Note that these electrolytes were selected, among other reasons, due to their low reactivity towards metallic lithium and thermal stability up to 600 °C (see section 4.1).

Another characteristic of the developed LBLTO and LLTYO lithium sensors is their excellent accuracy. This was evaluated as the divergence (%) between the nominal concentrations of the alloys tested alloys and the calculated concentrations from OCP experimental data. Note that the lithium activity was determined through the Nernst equation, which was later transformed to lithium concentration using Hubberstey's correlations. From all the OCP measurements performed at 400 °C, 500 °C, and 600 °C the average divergence values are calculated and shown in Table 4.25.

Table 4.25. Average accuracy results at 400 °C, 500 °C, and 600 °C.

	LBLTO	LLTYO
Temperature / °C	Divergence	Divergence
400	4%	3%
500	4%	3%
600	4%	2%

From Table 4.25, all the divergences' values were of the same order of magnitude. These divergences were all equal to or below 4%, independently of the temperature or the sensors' electrolyte. Furthermore, the average divergence value obtained from the measurements performed with the LBLTO sensor (4%) completely agreed with the value obtained for the LLTYO sensor (3%). It is worth noting that a 4% divergence in the 3.0-17.0at% Li range studied would imply a 0.1-0.7at% Li difference between the nominal and the quantified Li

concentration of the alloy. These results were considered satisfactory, demonstrating that the sensor had excellent accuracy.

From all that has been discussed, the constructed sensors were considered a satisfactory analytical tool for lithium analysis in molten Pb-Li alloys. All things considered, these tools showed excellent features which could compare to or even surpass other Li monitoring devices that have been described in the bibliography. Although little information is found about these Li sensing devices, which include electrochemical sensors and an electrical resistivity meter, there are still a few characteristics that are worth comparing.

The first interesting characteristic to compare to other electrochemical Li sensors is the reference system. For instance, the most commonly used reference electrode in the bibliography was pure lithium or Li-Bi mixtures [42,44,45,48]. On one hand, using pure lithium should not be used due to two main reasons. At first, it is a highly chemically reactive material, which may cause compatibility problems with the solid electrolyte or any other component of the sensor in contact. Second, because its activity ($a_{\text{Li}}=1$) is much higher than that of Pb-17Li ($a_{\text{Li}(\text{Pb}_{17}\text{Li})}\sim 10^{-4}$ at 750 K) and it is reported that higher sensitivities can be obtained when the lithium activity of the reference system is comparable with that of the Pb-Li liquid alloy under measure [48]. On the other hand, using Li-Bi mixtures requires calibration, since they consist of solid Li_3Bi and a liquid solution of Bi and Li. However, phase transformation of the original reference mixture is possible, thus the potential measured with the sensor is also dependent on these temperature-dependent phase transformations that alter the lithium activity of the RE [42,48]. Conversely, the constructed sensors demonstrated their operability with different Pb-Li reference electrodes. These reference systems exhibit an easier preparation and do not require calibration since their Li activities are known and stable throughout the OCP measurements. Furthermore, having proved the suitability of different Pb-Li alloys as reference electrodes allow the selection of the most suitable alloy for the measurement. For instance, when monitoring a eutectic Pb-Li alloy, using a Pb-3Li reference permits distinguishing short-circuit situations.

Another interesting factor about the constructed sensors is that they have demonstrated their excellent operability as Li measuring tools in Pb-Li at different temperatures and lithium concentrations. Compared to other authors, being able to use a series of correlations to relate the measured potential with the lithium activity is of great advantage. In other publications, the developed sensors only showed correlations that linked the OCP of the cell to a unique composition as a function of the temperature. For instance, F. de Schutter [44] established three different linear fitting correlations for the sensors' OCP values concerning

pure Li with the Li/L₃Bi, LiBi/Li₃Bi, and Li/LiBi reference systems from 573K to 773K. Another example is Wu et al. [45] who reported calibration curves for two of its reference systems: Sn-0.635Li and Sn-1.62Li ([Eq. 1.8], [Eq. 1.9]). These reference electrodes were calibrated against pure Li versus temperature between 340 and 680 °C. Although these correlations may become useful in some situations, these do not exhibit much utility for Li monitoring in Pb-Li matrices. Conversely, the constructed sensors show good agreement with the proposed Hubberstey's correlations ([Eq. 4.10]-[Eq. 4.12]) which relate lithium activity with its concentration in a PbLi alloy. Moreover, since these tools permit to study the lithium activity towards the lithium composition, $x_{\text{Li}} \geq 0.17$ linear range correlations have been proposed in this work ([Eq. 4.31]-[Eq. 4.33]).

The response time of the sensor was also evaluated when performing a continuous potentiometric measurement by adding Pb to the measured Pb-Li alloy. This response time stayed below 10 minutes and included the time to reequilibrate the system (see section 4.4.1.4). Similar response times were observed when compared to other sensors. F. De Schutter et al. [44], tested their sensors by consecutively exposing them to different PbLi alloys. They reported an equilibration time of 5 minutes after the reintroduction of the sensor. However, the first 15 minutes were not considered in this determination. Another example is F. Barbier's electrochemical sensor, which showed a stable signal after 10 minutes after some small lead additions [48]. Therefore, the sensor's response time is in the same order of magnitude as the other reported sensors. Despite that, it is worth noting that since some of the reported sensors were based on sodium β -alumina, these electrolytes required a prior period of conditioning to replace Na ions for Li [43]. On the contrary, since the constructed sensors were based on Li-ion electrolytes these did not require this aging period to start their measurements.

Finally, when comparing the designed electrochemical sensors with the resistivity monitor it can be observed that each has its strengths. On one hand, the resistivity monitor can be considered a more mature technique since it has been tested in dynamic conditions using the Anapurna loop (see section 1.2.2). This technique exhibits a high sensitivity to Li concentration change, showing a minimum unambiguously detectable limit of $\pm 0.15\text{at}\%$ Li. Furthermore, after the additions of Pb-Li to the alloy of the Anapurna loop, it was observed that its response time was only limited by the mixing rate in the loop: showing a stabilization of the signal between 10 and 20 minutes [48]. On the other hand, one of the main advantages of the developed sensors is their simpler design. Although the resistivity meter is easy to handle, its replacement in the loop could be more complicated than the electrochemical sensor, and will always require calibration before insertion [48].

Furthermore, the sensors are more selective tools for lithium, since the resistivity monitor is sensitive to any solute [41]. Thus, even though both analytical tools could be used for lithium monitoring, lithium electrochemical sensors appear as a very attractive option owing to their simpler design and lower cost without significantly compromising their analytical characteristics.

4.5. General Discussion

This thesis's final goal was the development and characterization of lithium sensors to be used in molten alloys. During the achievement of this goal, some general concepts could be drawn that highlight the most important breakthroughs throughout this thesis's research.

First, when obtaining the lithium-ion conducting electrolytes (LBLTO and LLTYO), the most impactful variables on the final product were temperature, time, and the starting reagents' particle size. Specifically, during the synthesis, these variables had a major impact on the crystallographic phases of the ceramics obtained. Note that, the obtention of the characteristic structure of the electrolyte is essential to ensure lithium-ion conductivity. This property is one that defines whether these electrolytes would be able to be used in the construction of the lithium sensors. From these three variables, time and temperature were the ones that could be more easily modified. Although the reagents were zirconia ball-milled for more than 12 hours to ensure good mixing and low particle size, from this process their particle size could not be more finely ground. It was considered that for this reason, in some cases, following the processes described by their respective authors, resulted in an inadequate final product. For instance, during the synthesis of the LLTYO electrolyte, its thermal treatment was modified by adding a second thermal step with a higher temperature to achieve its desired garnet structure. Thus, temperature and time were the two final decisive variables that had to be suitably selected to obtain satisfactory lithium-ion conducting crystallographic structures.

During sintering, temperature and time played again a key role in obtaining a highly densified disc electrolyte that would maintain its initial crystallographic structure. Maximum densification was pursued since it directly relates to the ionic conductivity of the electrolyte. In this process, it was observed that at higher temperatures and times, lower porosity was always achieved. However, this also increased the lithium loss in the ceramic while growing the chances of altering its crystallographic phases. In the end, a situation of compromise had to be reached between the porosity and the structure of the electrolyte: the heat treatments

that lead to the lowest porosities without compromising its crystallographic phases were selected. Similar to what has been mentioned previously, some of the sintering conditions had to be modified when compared to its bibliographic sources. This fact was also related to the particle size of the starting electrolyte, which has a high impact on the sintering result. A clear example is the LBLTO electrolyte, whose sintering temperature was increased from 900 °C to 950 °C, decreasing its surface porosity more than three-fold.

Once the electrolytes were optimally sintered with low porosities and adequate crystallographic structures, its electrochemical characterization needed to be performed. This characterization was essential to verify that the electrolytes exhibited sufficiently high ionic conductivity in order to be used in the construction of lithium electrochemical sensors. For this, an impedance measurement system was designed and built. With the constructed system, the ionic conductivities of the electrolytes were measured up to 200-300 °C. From the values obtained it was demonstrated that both electrolytes showed at the tested temperatures, sufficiently high ionic conductivities [148]. Knowing that they were going to be used at even higher temperatures (400-600 °C), it was certain that both LBLTO and LLTYO would perform satisfactorily when forming part of the sensors. In addition, the ionic conductivity values obtained were in good agreement with those obtained in the bibliography [87,157]. The latter was also good evidence that, despite having modified their synthesis and sintering conditions, the LBLTO and LLTYO electrolytes presented a similar quality to the ones from V. Thangadurai [87] and S. Narayanan [157] respectively.

Another very critical part that took place during the thesis was the validation of the Pb-Li alloys' synthesis process: verifying the procedure while at the same time evaluating the quality of the Li and Pb elements. This step was important because it had to be possible to ensure the quality of the alloys used for the electrochemical characterization of the sensors. From the different analyses, it was demonstrated that the synthesis process produced alloys matching their nominal concentration. Furthermore, these alloys were homogeneous throughout the whole piece, showing no stratification. In addition, it was found that the synthesized eutectic alloys satisfied one of the nuclear quality criteria for Pb-Li, a melting temperature within the range of (233.85 °C- 236.85 °C) [171]. From these results, it was concluded that manually mixing with an alumina rod the adequate amounts of each element in an alumina crucible produced Pb-Li ingots with sufficient quality to electrochemically characterize the Li sensors.

Having demonstrated the correct synthesis of the alloys, the electrochemical characterization of the constructed LBLTO and LLTYO sensors at 400 °C, 500 °C, and 600 °C

was performed. From this characterization, the main conclusion drawn was that both sensors allow the determination of the nominal concentration of a Pb-Li alloy by measuring its OCP. This quantification can be made by using the Nernst equation and the appropriate activity-composition correlations for lithium in Pb-Li. These correlations depend on the temperature and the Li concentration in the sample. In the $0.03 < x_{\text{Li}} < 0.17$ range, Hubbestey's correlations should be used according to the temperature of the system ([Eq. 4.10]-[Eq. 4.12]). For higher lithium concentrations, the correlations proposed in this work should be used ([Eq. 4.31]-[Eq. 4.33]). These correlations covered the $0.17 < x_{\text{Li}} < 0.25$ range at 400 °C, and the $0.17 < x_{\text{Li}} < 0.35$ range at 500 °C and 600 °C.

Moreover, it is worth mentioning that the developed sensors not only can be used as analysis tools but also offer the opportunity to determine the lithium activity correlations of different electrochemical systems at different temperatures. To measure these activities, an approach similar to that used by Hubberstey et al. has been followed in this work. In fact, Hubberstey relied on OCP versus Li concentration values reported by other authors [196–198]. These also used concentration cells and measured the potential of a Pb-Li alloy versus the potential of pure lithium. In addition, they used a mixture of lithium and potassium salts as liquid electrolytes. However, compared to this previous work, the developed sensors present two major advantages. First, metallic lithium is not required to be used as a reference electrode. Pb-Li alloys with a known concentration work perfectly since their activities can be easily determined. And second, using a solid electrolyte ensures no contamination or side reactions that could originate between the liquid electrolytes and the system measured.

Overall, it should be noted that the developed sensors when compared with other Li monitoring instruments have shown similar or superior analysis capacity. Note that they have demonstrated superior simplicity, especially since they do not require calibration due to their good agreement with the Nernst equation. These instruments also exhibit low response times (< 10 minutes) and a very stable signal along with high measurement accuracy. All these characteristics have demonstrated the viability of the developed sensors as Li monitoring tools for molten Pb-Li alloys.

5. CONCLUSIONS

5. CONCLUSIONS

The following conclusions have been obtained from this thesis:

1. To synthesize the LBLTO electrolyte a heat-treatment of 700 °C for 6 hours is required, while LLTYO synthesis requires a two-step temperature program of 700 °C for 5 hours and 900 °C for 1 hour. This allowed the obtention of garnet-type crystallographic phases from the XRD characterization of the synthesized $\text{Li}_6\text{BaLa}_2\text{Ta}_2\text{O}_{12}$ (LBLTO) and $\text{Li}_6\text{La}_3\text{Ta}_{1.5}\text{Y}_{0.5}\text{O}_{12}$ (LLTYO) electrolytes.
2. Sintering the LBLTO electrolyte discs at 950 °C for 24 hours results in pellets exhibiting a surface porosity of 4.0% \pm 0.8% that maintains their garnet-type structure. Sintering the LLTYO electrolyte discs using a two-step temperature program of 900 °C for 24 hours and 1100 °C for 6 hours results in pellets with a surface porosity of 0.7% \pm 0.1% that keep their initial crystallographic structure.
3. Both LBLTO and LLTYO electrolytes exhibit high enough ionic conductivities to be considered suitable to develop electrochemical lithium sensors. Furthermore, despite modifying their synthesis and sintering conditions from the bibliographic ones, their ionic conductivities determined are in the same order of magnitude as their reported values. From the results, the LLTYO electrolyte shows a slightly higher ionic conductivity than the LBLTO electrolyte, proving that LLTYO has a higher capacity than the LBLTO electrolyte to conduct Li-ions.
4. The developed lithium sensors consist of an LBLTO or LLTYO sintered disc joined to an alumina tube using a glass binder. The sensors were designed as electrochemical concentration cells. These operate in a potentiometric configuration and have a working and a reference electrodes. Sensors are submerged in the WE alloy, while in the inner part of the tube, the RE is placed, which can consist of Pb-17Li, Pb-3Li, or Sn-3Li. Both electrodes are connected through molybdenum wires to the measuring system.
5. Eutectic Pb-Li, Pb-3Li, or Sn-3Li can be selected as reference electrodes according to the sensor's target application. The LBLTO sensors' calibration curves were in good agreement with the Nernst equation independently of the reference system used. Differences below 10% were obtained between the calibration curves' slopes and Nernst's theoretical values when using eutectic Pb-Li, Pb-3Li, or Sn-3Li as reference electrodes.

6. LBLTO sensor showed a CV(%) of 0.3%, 0.7%, and 0.2% when evaluating its repeatability, intermediate precision, and reproducibility respectively. All these results were under the maximum AOAC reference values: 2.7% for repeatability and 4.0% for intermediate precision and reproducibility. Therefore, the LBLTO sensor can be considered a precise tool for Li analysis since its repeatability, intermediate precision, and reproducibility results fulfill the acceptance criteria suggested by the AOAC.
7. The sensors showed linearity in the $0.03 < x_{\text{Li}} < 0.17$ range at 400 °C, 500 °C, and 600 °C. The obtained correlations presented $R^2 > 0.99$ and were in good agreement with those previously published by Hubbestey.
8. $x_{\text{Li}} \geq 0.17$ linear range correlations have been formulated, allowing the determination of lithium activities beyond the range established by Hubberstay. The correlations' range covers from 17at% Li to 25at% Li at 400 °C, while at 500 °C and 600 °C it reaches up to 35at% Li. Due to these correlations, it was demonstrated that the LBLTO sensor could quantify higher lithium concentrations than 17at% Li in molten Pb-Li samples.
9. Pb-Li samples prepared with Li concentrations of 13.1at%, 14.5at%, 16.0at%, and 17.5at% Li have been quantified using the LBLTO sensor at 500 °C. Relative errors lower than 6.0% were obtained when comparing the quantification results to the nominal compositions of the alloys. Therefore, the sensor is able to detect and differentiate concentration variations of 1.5at% Li.
10. Potentiometric sensors based on LBLTO and LLTYO exhibit excellent stability and high accuracy independently of the temperature or the linear range under study. Sensors' stability has been demonstrated since an average standard deviation of ± 0.2 mV is obtained from all the OCP recorded data. The sensor accuracy has been proven since average deviations equal to or below 3% were determined between nominal and experimental concentrations. The high accuracy has been related to the sensor's good agreement with the Nernst equation. Differences below 4.0% were obtained when comparing their calibration curves' slopes to the Nernst theoretical values. According to all these results, the constructed sensors can be considered valid tools for Li monitoring in molten Pb-Li alloys.

6. REFERENCES

6. REFERENCES

- [1] A. Razmjoo, L. Gakenia Kaigutha, M.A. Vaziri Rad, M. Marzband, A. Davarpanah, M. Denai, A Technical analysis investigating energy sustainability utilizing reliable renewable energy sources to reduce CO₂ emissions in a high potential area, *Renew. Energy*. 164 (2021) 46–57. <https://doi.org/10.1016/j.renene.2020.09.042>.
- [2] BP plc, *Statistical Review of World Energy 2021*, 2021.
- [3] What is ITER?, (2021). <https://www.iter.org/proj/inafewlines> (accessed November 8, 2021).
- [4] J.K. Shultis, R.E. Faw, *Fundamentals of Nuclear Science and Engineering*, CRC Press, 2002. <https://doi.org/10.1201/9780203910351>.
- [5] T. Tanabe, *Tritium: Fuel of Fusion Reactors*, Springer Japan, Tokyo, 2017. <https://doi.org/10.1007/978-4-431-56460-7>.
- [6] F. Eyrolle, L. Ducros, S. Le Dizès, K. Beaugelin-Seiller, S. Charmasson, P. Boyer, C. Cossonnet, An updated review on tritium in the environment, *J. Environ. Radioact.* 181 (2018) 128–137. <https://doi.org/10.1016/j.jenvrad.2017.11.001>.
- [7] Broader Approach agreement, (n.d.). <https://www.iter.org/sci/iterandbeyond> (accessed February 14, 2022).
- [8] G. Aiello, J. Aubert, L. Forest, J.-C. Jaboulay, A. Li Puma, L.V. Boccaccini, Design of the helium cooled lithium lead breeding blanket in CEA: from TBM to DEMO, *Nucl. Fusion*. 57 (2017) 046022. <https://doi.org/10.1088/1741-4326/aa5f65>.
- [9] M. Abdou, N.B. Morley, S. Smolentsev, A. Ying, S. Malang, A. Rowcliffe, M. Ulrickson, Blanket/first wall challenges and required R&D on the pathway to DEMO, *Fusion Eng. Des.* 100 (2015) 2–43. <https://doi.org/10.1016/j.fusengdes.2015.07.021>.
- [10] A.M. Bradshaw, T. Hamacher, U. Fischer, Is nuclear fusion a sustainable energy form?, *Fusion Eng. Des.* 86 (2011) 2770–2773. <https://doi.org/10.1016/j.fusengdes.2010.11.040>.
- [11] D.P. Jackson, R.A. Verrall, P.M. Garvey, W.N. Selander, R.L. Tapping, W.J. Holtslander, B.M. Townes, J.S. Geiger, I.J. Hastings, T.C. Leung, O.S. Tatone, A.D. Lane, J.N. Miller, E.C. Carlick, A Review of Fusion Breeder Blanket Technology Part 1 / Review and Findings CFFTP Report Number Cross Reference Report, 1985.
- [12] U. Schumacher, H. Herold, Nuclear Technology, 4. Nuclear Fusion, in: *Ullmann's Encycl. Ind. Chem.*, Wiley-VCH Verlag GmbH & Co. KGaA, Weinheim, Germany, 2011. https://doi.org/10.1002/14356007.o17_o07.
- [13] D. Martelli, A. Venturini, M. Utili, Literature review of lead-lithium thermophysical properties, *Fusion Eng. Des.* 138 (2019) 183–195. <https://doi.org/10.1016/j.fusengdes.2018.11.028>.
- [14] W. Krauss, S.-E. Wulf, J. Konys, Long-term corrosion behavior of ODS-Eurofer in

flowing Pb-15.7Li at 550 °C, Nucl. Mater. Energy. 9 (2016) 512–518. <https://doi.org/10.1016/j.nme.2016.04.011>.

- [15] A. Aiello, A. Ciampichetti, M. Utili, G. Benamati, TRIEX facility: An experimental loop to test tritium extraction systems from lead lithium, Fusion Eng. Des. 82 (2007) 2294–2302. <https://doi.org/10.1016/j.fusengdes.2007.07.037>.
- [16] M. Utili, C. Alberghi, L. Candido, F. Papa, M. Tarantino, A. Venturini, TRIEX-II: an experimental facility for the characterization of the tritium extraction unit of the WCLL blanket of ITER and DEMO fusion reactors, Nucl. Fusion. 62 (2022) 066036. <https://doi.org/10.1088/1741-4326/ac5c74>.
- [17] B. Garcinuño, D. Rapisarda, I. Fernández-Berceruelo, E. Carella, J. Sanz, The CIEMAT LiPb Loop Permeation Experiment, Fusion Eng. Des. 146 (2019) 1228–1232. <https://doi.org/10.1016/j.fusengdes.2019.02.045>.
- [18] D.-K. Sze, M. Tillack, L. El-Guebaly, Blanket system selection for the ARIES-ST, Fusion Eng. Des. 48 (2000) 371–378. [https://doi.org/10.1016/S0920-3796\(00\)00146-0](https://doi.org/10.1016/S0920-3796(00)00146-0).
- [19] S. Fukada, Y. Edao, Unsolved issues on tritium mass transfer in Li-Pb liquid blankets, J. Nucl. Mater. 417 (2011) 727–730. <https://doi.org/10.1016/j.jnucmat.2010.12.127>.
- [20] E. Platacis, A. Ziks, A. Poznjak, F. Muktepavela, A. Shisko, S. Sarada, P. Chakraborty, K. Sanjay, M. Vrushank, R. Fotedar, E.K. Rajendra, A.K. Suri, Investigation of the Li-Pb flow corrosion attack on the surface of P91 steel in the presence of magnetic field, Magnetohydrodynamics. 48 (2012) 343–350. <https://doi.org/10.22364/mhd.48.2.12>.
- [21] S. Fukada, T. Terai, S. Konishi, K. Katayama, T. Chikada, Y. Edao, T. Muroga, M. Shimada, B. Merrill, D.K. Sze, Clarification of tritium behavior in pbli blanket system, Mater. Trans. 54 (2013) 425–429. <https://doi.org/10.2320/matertrans.MG201203>.
- [22] F.A. Hernández, P. Pereslavtsev, First principles review of options for tritium breeder and neutron multiplier materials for breeding blankets in fusion reactors, Fusion Eng. Des. 137 (2018) 243–256. <https://doi.org/10.1016/j.fusengdes.2018.09.014>.
- [23] Y. Wu, S. Şahin, 3.13 Fusion Energy Production, in: Compr. Energy Syst., Elsevier, 2018: pp. 538–589. <https://doi.org/10.1016/B978-0-12-809597-3.00330-8>.
- [24] J. Aubert, G. Aiello, D. Alonso, T. Batal, R. Boullon, S. Burles, B. Cantone, F. Cismondi, A. Del Nevo, L. Maqueda, A. Morin, E. Rodríguez, F. Rueda, M. Soldaini, J. Vallory, Design and preliminary analyses of the new Water Cooled Lithium Lead TBM for ITER, Fusion Eng. Des. 160 (2020) 111921. <https://doi.org/10.1016/j.fusengdes.2020.111921>.
- [25] G. Aiello, G. de Dinechin, L. Forest, F. Gabriel, A.L. Puma, G. Rampal, E. Rigal, J.F. Salavy, H. Simon, HCLL TBM design status and development, Fusion Eng. Des. 86 (2011) 2129–2134. <https://doi.org/10.1016/j.fusengdes.2011.04.017>.
- [26] M. Abdou, D. Sze, C. Wong, M. Sawan, A. Ying, N.B. Morley, S. Malang, U.S. plans and strategy for ITER blanket testing, in: Fusion Sci. Technol., 2005: pp. 475–487.

<https://doi.org/10.13182/FST05-A732>.

- [27] C.P.C. Wong, V. Chernov, A. Kimura, Y. Katoh, N. Morley, T. Muroga, K.W. Song, Y.C. Wu, M. Zmitko, ITER-Test blanket module functional materials, *J. Nucl. Mater.* 367–370 (2007) 1287–1292. <https://doi.org/10.1016/j.jnucmat.2007.03.241>.
- [28] I. Palermo, D. Rapisarda, I. Fernández-Bercheruelo, A. Ibarra, Optimization process for the design of the DCLL blanket for the European DEMONstration fusion reactor according to its nuclear performances, *Nucl. Fusion.* 57 (2017) 076011. <https://doi.org/10.1088/1741-4326/AA6C14>.
- [29] D. Rapisarda, I. Fernandez, I. Palermo, F.R. Urgan, L. Maqueda, D. Alonso, T. Melichar, O. Frýbort, L. Vála, M. Gonzalez, P. Norajitra, H. Neuberger, A. Ibarra, Status of the engineering activities carried out on the European DCLL, *Fusion Eng. Des.* 124 (2017) 876–881. <https://doi.org/10.1016/J.FUSENGDES.2017.02.022>.
- [30] D. Rapisarda, I. Palermo, M. Gonzalez, F. Martin-Fuertes, C. Moreno, A. Ibarra, I. Fernandez, E.M. De Les Valls, Overview of DCLL research activities in the EU/Spain, *Proc. - Symp. Fusion Eng.* 2016-May (2016). <https://doi.org/10.1109/SOFE.2015.7482358>.
- [31] J. Aubert, G. Aiello, P. Arena, T. Barrett, L.V. Boccaccini, G. Bongiovì, R. Bouillon, F. Cismondi, I. Critescu, P.K. Domalapally, L. Forest, J.C. Jaboulay, B. Kiss, A. Morin, J. Peyraud, G. Porempovics, M. Utili, L. Vála, Status of the EU DEMO HCLL breeding blanket design development, *Fusion Eng. Des.* 136 (2018) 1428–1432. <https://doi.org/10.1016/j.fusengdes.2018.04.133>.
- [32] P. Arena, A. Del Nevo, F. Moro, S. Noce, R. Mozzillo, V. Imbriani, F. Giannetti, F. Edemetti, A. Froio, L. Savoldi, S. Siriano, A. Tassone, F. Roca Urgan, P.A. Di Maio, I. Catanzaro, G. Bongiovì, The DEMO Water-Cooled Lead–Lithium Breeding Blanket: Design Status at the End of the Pre-Conceptual Design Phase, *Appl. Sci.* 11 (2021) 11592. <https://doi.org/10.3390/app112411592>.
- [33] J. Aubert, G. Aiello, N. Jonquères, A. Li Puma, A. Morin, G. Rampal, Development of the water cooled lithium lead blanket for DEMO, *Fusion Eng. Des.* 89 (2014) 1386–1391. <https://doi.org/10.1016/j.fusengdes.2014.01.061>.
- [34] J. Konys, W. Krauss, H. Steiner, J. Novotny, A. Skrypnik, Flow rate dependent corrosion behavior of Eurofer steel in Pb–15.7Li, *J. Nucl. Mater.* 417 (2011) 1191–1194. <https://doi.org/10.1016/j.jnucmat.2010.12.277>.
- [35] S.J. Zinkle, N.M. Ghoniem, Prospects for accelerated development of high performance structural materials, *J. Nucl. Mater.* 417 (2011) 2–8. <https://doi.org/10.1016/j.jnucmat.2011.05.021>.
- [36] D. Rapisarda, I. Fernández-Bercheruelo, A. García, J.M. García, B. Garcinuño, M. González, C. Moreno, I. Palermo, F.R. Urgan, A. Ibarra, The European Dual Coolant Lithium Lead breeding blanket for DEMO: status and perspectives, *Nucl. Fusion.* 61 (2021) 115001. <https://doi.org/10.1088/1741-4326/ac26a1>.
- [37] B. Predel, Li-Pb (Lithium-Lead), in: O. Madelung (Ed.), *Li-Mg – Nd-Zr*, Springer-Verlag,

Berlin/Heidelberg, 1997: pp. 1–4. https://doi.org/10.1007/10522884_1915.

- [38] M. Kamenica, R. Kothur, A. Willows, B. Patel, P. Cragg, Lithium Ion Sensors, *Sensors*. 17 (2017) 2430. <https://doi.org/10.3390/s17102430>.
- [39] J.A. Wheat, Isotopic Analysis of Lithium by Atomic Absorption Spectrophotometry, *Appl. Spectrosc.* 25 (1971) 328–330. <https://doi.org/10.1366/000370271779949069>.
- [40] P. Hubberstey, T. Sample, M.G. Barker, Continuous monitoring of the composition of liquid Pb-17Li eutectic using electrical resistivity methods, *J. Nucl. Mater.* 179–181 (1991) 886–890. [https://doi.org/10.1016/0022-3115\(91\)90231-U](https://doi.org/10.1016/0022-3115(91)90231-U).
- [41] P. Hubberstey, M.G. Barker, T. Sample, An electrical resistivity monitor for the detection of composition changes in Pb17Li, *Fusion Eng. Des.* 14 (1991) 227–233. [https://doi.org/10.1016/0920-3796\(91\)90006-C](https://doi.org/10.1016/0920-3796(91)90006-C).
- [42] F. De Schutter, J. Dekeyser, J. Luyten, H. Tas, Electrochemical sensors for oxygen and lithium detection in Pb-17Li, *Fusion Eng. Des.* 14 (1991) 241–248. [https://doi.org/10.1016/0920-3796\(91\)90008-E](https://doi.org/10.1016/0920-3796(91)90008-E).
- [43] R.J. and H.T. F. DE SCHUTTER, JA. DEKEYSER, R. DEKNOCK, Surface conditioning of a sodium B-alumina based lithium sensor for lithium-lead blends, *Solid State Ionics*. 40/41 (1990) 754–757.
- [44] F. de Schutter, J. Dekeyser, J. Luyten, H. Tas, Monitoring system for chemical characterization of liquid breeder alloys, *Sensors Actuators B. Chem.* 1 (1990) 446–450. [https://doi.org/10.1016/0925-4005\(90\)80247-W](https://doi.org/10.1016/0925-4005(90)80247-W).
- [45] J. Wu, L. Yamarte, A. Petric, Fabrication of a Lithium Sensor Based on LiYO₂ by Liquid Phase Processing, *J. Electroceramics*. 9 (2002) 57–66. <https://doi.org/10.1023/A:1021694102959>.
- [46] C.C. Addison, G.K. Creffield, P. Hubberstey, R.J. Pulham, Electrical resistivity of solutions of barium in liquid sodium, *J. Chem. Soc. A Inorganic, Phys. Theor.* (1971) 1393. <https://doi.org/10.1039/j19710001393>.
- [47] F. Barbier, Continuous monitoring and adjustment of the lithium content in liquid Pb-Li alloys: assessment of an electrical resistivity meter in a loop system, *Fusion Eng. Des.* 36 (1997) 299–308. [https://doi.org/10.1016/S0920-3796\(96\)00697-7](https://doi.org/10.1016/S0920-3796(96)00697-7).
- [48] F. Barbier, Continuous monitoring of lithium in dynamic Pb–17Li systems, *Fusion Eng. Des.* 46 (1999) 77–88. [https://doi.org/10.1016/S0920-3796\(99\)00076-9](https://doi.org/10.1016/S0920-3796(99)00076-9).
- [49] M. Saboungi, J. Marr, M. Blander, Thermodynamic properties of a quasi-ionic alloy from electromotive force measurements: The Li–Pb system, *J. Chem. Phys.* 68 (1978) 1375–1384. <https://doi.org/10.1063/1.435957>.
- [50] G.C. Farrington, W.L. Roth, Li+–Na+ beta alumina—A novel Li+ solid electrolyte, *Electrochim. Acta.* 22 (1977) 767–772. [https://doi.org/10.1016/0013-4686\(77\)80033-9](https://doi.org/10.1016/0013-4686(77)80033-9).
- [51] W. Gasior, Z. Moser, Thermodynamic properties of binary lithium-zinc system, *J.*

- Chim. Phys. 90 (1993) 387–397. <https://doi.org/10.1051/jcp/1993900387>.
- [52] F. Barbier, Continuous monitoring of lithium in dynamic Pb–17Li systems, *Fusion Eng. Des.* 46 (1999) 77–88. [https://doi.org/10.1016/S0920-3796\(99\)00076-9](https://doi.org/10.1016/S0920-3796(99)00076-9).
- [53] S. Ferrari, M. Loveridge, S.D. Beattie, M. Jahn, R.J. Dashwood, R. Bhagat, Latest advances in the manufacturing of 3D rechargeable lithium microbatteries, *J. Power Sources.* 286 (2015) 25–46. <https://doi.org/10.1016/j.jpowsour.2015.03.133>.
- [54] N.Q. Minh, Ceramic Fuel Cells, *J. Am. Ceram. Soc.* 76 (1993) 563–588. <https://doi.org/10.1111/j.1151-2916.1993.tb03645.x>.
- [55] J.-M. Tarascon, M. Armand, Issues and challenges facing rechargeable lithium batteries, *Nature.* 414 (2001) 359–367. <https://doi.org/10.1038/35104644>.
- [56] N. Yamazoe, N. Miura, Environmental gas sensing, *Sensors Actuators B Chem.* 20 (1994) 95–102. [https://doi.org/10.1016/0925-4005\(93\)01183-5](https://doi.org/10.1016/0925-4005(93)01183-5).
- [57] E. Traversa, Ceramic sensors for humidity detection: the state-of-the-art and future developments, *Sensors Actuators B Chem.* 23 (1995) 135–156. [https://doi.org/10.1016/0925-4005\(94\)01268-M](https://doi.org/10.1016/0925-4005(94)01268-M).
- [58] Suresh Mulmi and Venkataraman Thangadurai, Solid-State Electrolytes: Structural Approach, in: R. Murugan, W. Weppner (Eds.), *Solid Electrolytes Adv. Appl.*, Springer International Publishing, 2019: pp. 3–24. <https://doi.org/10.1007/978-3-030-31581-8>.
- [59] E.D. Tsagarakis, W. Weppner, Electrode kinetic phenomena of solid state ionic devices, *Ionics (Kiel).* 11 (2005) 240–247. <https://doi.org/10.1007/BF02430383>.
- [60] H.-P. Hong, Crystal structure and ionic conductivity of $\text{Li}_{14}\text{Zn}(\text{GeO}_4)_4$ and other new Li^+ superionic conductors, *Mater. Res. Bull.* 13 (1978) 117–124. [https://doi.org/10.1016/0025-5408\(78\)90075-2](https://doi.org/10.1016/0025-5408(78)90075-2).
- [61] Y. -W. Hu, I.D. Raistrick, R.A. Huggins, Ionic Conductivity of Lithium Orthosilicate—Lithium Phosphate Solid Solutions, *J. Electrochem. Soc.* 124 (1977) 1240–1242. <https://doi.org/10.1149/1.2133537>.
- [62] R.D. Shannon, B.E. Taylor, A.D. English, T. Berzins, New Li solid electrolytes, *Electrochim. Acta.* 22 (1977) 783–796. [https://doi.org/10.1016/0013-4686\(77\)80035-2](https://doi.org/10.1016/0013-4686(77)80035-2).
- [63] M. Murayama, Synthesis of New Lithium Ionic Conductor Thio-LISICON—Lithium Silicon Sulfides System, *J. Solid State Chem.* 168 (2002) 140–148. <https://doi.org/10.1006/jssc.2002.9701>.
- [64] P. Zhou, J. Wang, F. Cheng, F. Li, J. Chen, A solid lithium superionic conductor $\text{Li}_{11}\text{AIP}_2\text{S}_{12}$ with a thio-LISICON analogous structure, *Chem. Commun.* 52 (2016) 6091–6094. <https://doi.org/10.1039/C6CC02131J>.
- [65] Y. Mo, S.P. Ong, G. Ceder, First Principles Study of the $\text{Li}_{10}\text{GeP}_2\text{S}_{12}$ Lithium Super Ionic Conductor Material, *Chem. Mater.* 24 (2012) 15–17.

<https://doi.org/10.1021/cm203303y>.

- [66] S.P. Ong, Y. Mo, W.D. Richards, L. Miara, H.S. Lee, G. Ceder, Phase stability, electrochemical stability and ionic conductivity of the $\text{Li}_{10\pm 1}\text{M}_2\text{X}_{12}$ ($\text{M} = \text{Ge}, \text{Si}, \text{Sn}, \text{Al}$ or P , and $\text{X} = \text{O}, \text{S}$ or Se) family of superionic conductors, *Energy Environ. Sci.* 6 (2013) 148–156. <https://doi.org/10.1039/C2EE23355J>.
- [67] J.C. Bachman, S. Muy, A. Grimaud, H.-H. Chang, N. Pour, S.F. Lux, O. Paschos, F. Maglia, S. Lupart, P. Lamp, L. Giordano, Y. Shao-Horn, Inorganic Solid-State Electrolytes for Lithium Batteries: Mechanisms and Properties Governing Ion Conduction, *Chem. Rev.* 116 (2016) 140–162. <https://doi.org/10.1021/acs.chemrev.5b00563>.
- [68] O. BOHNKE, The fast lithium-ion conducting oxides $\text{Li}_3\text{xLa}_{2/3-\text{x}}\text{TiO}_3$ from fundamentals to application, *Solid State Ionics.* 179 (2008) 9–15. <https://doi.org/10.1016/j.ssi.2007.12.022>.
- [69] J. Wu, L. Chen, T. Song, Z. Zou, J. Gao, W. Zhang, S. Shi, A review on structural characteristics, lithium ion diffusion behavior and temperature dependence of conductivity in perovskite-type solid electrolyte $\text{Li}_3\text{xLa}_{2/3-\text{x}}\text{TiO}_3$, *Funct. Mater. Lett.* 10 (2017) 1–10. <https://doi.org/10.1142/S179360471730002X>.
- [70] T. Teranishi, M. Yamamoto, H. Hayashi, A. Kishimoto, Lithium ion conductivity of Nd-doped (Li, La) TiO_3 ceramics, *Solid State Ionics.* 243 (2013) 18–21. <https://doi.org/10.1016/j.ssi.2013.04.014>.
- [71] X. Gao, C.A.J. Fisher, T. Kimura, Y.H. Ikuhara, H. Moriwake, A. Kuwabara, H. Oki, T. Tojigamori, R. Huang, Y. Ikuhara, Lithium Atom and A-Site Vacancy Distributions in Lanthanum Lithium Titanate, *Chem. Mater.* 25 (2013) 1607–1614. <https://doi.org/10.1021/cm3041357>.
- [72] Y. Inaguma, C. Lique, M. Itoh, T. Nakamura, T. Uchida, H. Ikuta, M. Wakihara, High ionic conductivity in lithium lanthanum titanate, *Solid State Commun.* 86 (1993) 689–693. [https://doi.org/10.1016/0038-1098\(93\)90841-A](https://doi.org/10.1016/0038-1098(93)90841-A).
- [73] C. Chen, Ionic conductivity, lithium insertion and extraction of lanthanum lithium titanate, *Solid State Ionics.* 144 (2001) 51–57. [https://doi.org/10.1016/S0167-2738\(01\)00884-0](https://doi.org/10.1016/S0167-2738(01)00884-0).
- [74] V. Thangadurai, A.K. Shukla, J. Gopalakrishnan, $\text{LiSr}_{1-x}\text{Ba}_x\text{Ti}_2\text{O}_9$ ($\text{B} = \text{Ti}, \text{Zr}$; $\text{B}' = \text{Nb}, \text{Ta}$): New Lithium Ion Conductors Based on the Perovskite Structure, *Chem. Mater.* 11 (1999) 835–839. <https://doi.org/10.1021/cm9810382>.
- [75] H. Aono, E. Sugimoto, Y. Sadaoka, N. Imanaka, G. Adachi, The Electrical Properties of Ceramic Electrolytes for $\text{LiM}_x\text{Ti}_{2-x}(\text{PO}_4)_3 + y\text{Li}_2\text{O}$, $\text{M} = \text{Ge}, \text{Sn}, \text{Hf}$, and Zr Systems, *J. Electrochem. Soc.* 140 (1993) 1827–1833. <https://doi.org/10.1149/1.2220723>.
- [76] G.F. Ortiz, M.C. López, P. Lavela, C. Vidal-Abarca, J.L. Tirado, Improved lithium-ion transport in NASICON-type lithium titanium phosphate by calcium and iron doping, *Solid State Ionics.* 262 (2014) 573–577. <https://doi.org/10.1016/j.ssi.2013.09.012>.

- [77] Y. Ren, K. Chen, R. Chen, T. Liu, Y. Zhang, C.-W. Nan, Oxide Electrolytes for Lithium Batteries, *J. Am. Ceram. Soc.* 98 (2015) 3603–3623. <https://doi.org/10.1111/jace.13844>.
- [78] K. Takada, SECONDARY BATTERIES – LITHIUM RECHARGEABLE SYSTEMS – LITHIUM-ION | Electrolytes: Solid Oxide, in: *Encycl. Electrochem. Power Sources*, Elsevier, 2009: pp. 328–336. <https://doi.org/10.1016/B978-044452745-5.00211-2>.
- [79] C. Cao, Z.-B. Li, X.-L. Wang, X.-B. Zhao, W.-Q. Han, Recent Advances in Inorganic Solid Electrolytes for Lithium Batteries, *Front. Energy Res.* 2 (2014) 1–10. <https://doi.org/10.3389/fenrg.2014.00025>.
- [80] P. Knauth, Inorganic solid Li ion conductors: An overview, *Solid State Ionics.* 180 (2009) 911–916. <https://doi.org/10.1016/j.ssi.2009.03.022>.
- [81] P. Hartmann, T. Leichtweiss, M.R. Busche, M. Schneider, M. Reich, J. Sann, P. Adelhelm, J. Janek, Degradation of NASICON-Type Materials in Contact with Lithium Metal: Formation of Mixed Conducting Interphases (MCI) on Solid Electrolytes, *J. Phys. Chem. C.* 117 (2013) 21064–21074. <https://doi.org/10.1021/jp4051275>.
- [82] J.C. Bachman, S. Muy, A. Grimaud, H.-H. Chang, N. Pour, S.F. Lux, O. Paschos, F. Maglia, S. Lupart, P. Lamp, L. Giordano, Y. Shao-Horn, Inorganic Solid-State Electrolytes for Lithium Batteries: Mechanisms and Properties Governing Ion Conduction, *Chem. Rev.* 116 (2016) 140–162. <https://doi.org/10.1021/acs.chemrev.5b00563>.
- [83] W. Zhao, J. Yi, P. He, H. Zhou, Solid-State Electrolytes for Lithium-Ion Batteries: Fundamentals, Challenges and Perspectives, *Electrochem. Energy Rev.* 2 (2019) 574–605. <https://doi.org/10.1007/s41918-019-00048-0>.
- [84] E.J. Cussen, T.W.S. Yip, G. O’Neill, M.P. O’Callaghan, A comparison of the transport properties of lithium-stuffed garnets and the conventional phases $\text{Li}_3\text{Ln}_3\text{Te}_2\text{O}_{12}$, *J. Solid State Chem.* 184 (2011) 470–475. <https://doi.org/10.1016/j.jssc.2010.12.021>.
- [85] M.P. O’Callaghan, D.R. Lynham, E.J. Cussen, G.Z. Chen, Structure and Ionic-Transport Properties of Lithium-Containing Garnets $\text{Li}_3\text{Ln}_3\text{Te}_2\text{O}_{12}$ (Ln = Y, Pr, Nd, Sm–Lu), *Chem. Mater.* 18 (2006) 4681–4689. <https://doi.org/10.1021/cm060992t>.
- [86] V. Thangadurai, S. Narayanan, D. Pinzaru, Garnet-type solid-state fast Li ion conductors for Li batteries: critical review, *Chem. Soc. Rev.* 43 (2014) 4714. <https://doi.org/10.1039/c4cs00020j>.
- [87] V. Thangadurai, W. Weppner, $\text{Li}_6\text{AAl}_2\text{Ta}_2\text{O}_{12}$ (A = Sr, Ba): Novel Garnet-Like Oxides for Fast Lithium Ion Conduction, *Adv. Funct. Mater.* 15 (2005) 107–112. <https://doi.org/10.1002/adfm.200400044>.
- [88] A. Ramzy, V. Thangadurai, Tailor-Made Development of Fast Li Ion Conducting Garnet-Like Solid Electrolytes, *ACS Appl. Mater. Interfaces.* 2 (2010) 385–390. <https://doi.org/10.1021/am900643t>.
- [89] H. El Shinawi, J. Janek, Stabilization of cubic lithium-stuffed garnets of the type

“Li₇La₃Zr₂O₁₂” by addition of gallium, *J. Power Sources*. 225 (2013) 13–19. <https://doi.org/10.1016/j.jpowsour.2012.09.111>.

- [90] S. Kumazaki, Y. Iriyama, K.-H. Kim, R. Murugan, K. Tanabe, K. Yamamoto, T. Hirayama, Z. Ogumi, High lithium ion conductive Li₇La₃Zr₂O₁₂ by inclusion of both Al and Si, *Electrochem. Commun.* 13 (2011) 509–512. <https://doi.org/10.1016/j.elecom.2011.02.035>.
- [91] R. Murugan, V. Thangadurai, W. Weppner, Fast Lithium Ion Conduction in Garnet-Type Li₇La₃Zr₂O₁₂, *Angew. Chemie Int. Ed.* 46 (2007) 7778–7781. <https://doi.org/10.1002/anie.200701144>.
- [92] A. Sree Rama Murthy, T. Gnanasekaran, V. Jayaraman, Preparation and characterization of some lithium – Ion conductors, *Solid State Ionics*. 303 (2017) 138–143. <https://doi.org/10.1016/j.ssi.2017.03.006>.
- [93] European Pharmacopoeia, European Pharmacopoeia Commission, Council of Europe, European Department for the Quality of Medicines, Published by Strasbourg: Council of Europe, 2005.
- [94] Z. Yu, S.L. Shang, J.H. Seo, D. Wang, X. Luo, Q. Huang, S. Chen, J. Lu, X. Li, Z.K. Liu, D. Wang, Exceptionally High Ionic Conductivity in Na₃P_{0.62}As_{0.38}S₄ with Improved Moisture Stability for Solid-State Sodium-Ion Batteries, *Adv. Mater.* 29 (2017) 1–7. <https://doi.org/10.1002/adma.201605561>.
- [95] S. Song, J. Lu, F. Zheng, H.M. Duong, L. Lu, A facile strategy to achieve high conduction and excellent chemical stability of lithium solid electrolytes, *RSC Adv.* 5 (2015) 6588–6594. <https://doi.org/10.1039/C4RA11287C>.
- [96] DIETER K. SCHRODER, SEMICONDUCTOR MATERIAL AND DEVICE CHARACTERIZATION, 2nd ed, 1998. <https://doi.org/10.1002/0471749095.fmatter>.
- [97] J. Pütz, S. Heusing, M.A. Aegerter, Characterization of Electrical Properties, in: *Handb. Sol-Gel Sci. Technol.*, Springer International Publishing, Cham, 2016: pp. 1–30. https://doi.org/10.1007/978-3-319-19454-7_52-1.
- [98] L. Valdes, Resistivity Measurements on Germanium for Transistors, *Proc. IRE.* 42 (1954) 420–427. <https://doi.org/10.1109/JRPROC.1954.274680>.
- [99] F.M. Smits, Measurement of Sheet Resistivities with the Four-Point Probe, *Bell Syst. Tech. J.* 37 (1958) 711–718. <https://doi.org/10.1002/j.1538-7305.1958.tb03883.x>.
- [100] A. Uhlir, The Potentials of Infinite Systems of Sources and Numerical Solutions of Problems in Semiconductor Engineering, *Bell Syst. Tech. J.* 34 (1955) 105–128. <https://doi.org/10.1002/j.1538-7305.1955.tb03765.x>.
- [101] J.-M. Winand, J. Depireux, Measurement of Ionic Conductivity in Solid Electrolytes, *Europhys. Lett.* 8 (1989) 447–452. <https://doi.org/10.1209/0295-5075/8/5/009>.
- [102] S. Xuefu, H. Nemori, S. Mitsuoka, P. Xu, M. Matsui, Y. Takeda, O. Yamamoto, N. Imanishi, High Lithium-Ion-Conducting NASICON-Type Li_{1+x}Al_xGeyTi_{2-x-y}(PO₄)₃ Solid Electrolyte, *Front. Energy Res.* 4 (2016) 2–10.

<https://doi.org/10.3389/fenrg.2016.00012>.

- [103] A. Sharafi, C.G. Haslam, R.D. Kerns, J. Wolfenstine, J. Sakamoto, Controlling and correlating the effect of grain size with the mechanical and electrochemical properties of Li₇La₃Zr₂O₁₂ solid-state electrolyte, *J. Mater. Chem. A*. 5 (2017) 21491–21504. <https://doi.org/10.1039/C7TA06790A>.
- [104] P. Braun, C. Uhlmann, A. Weber, H. Störmer, D. Gerthsen, E. Ivers-Tiffée, Separation of the bulk and grain boundary contributions to the total conductivity of solid lithium-ion conducting electrolytes, *J. Electroceramics*. 38 (2017) 157–167. <https://doi.org/10.1007/s10832-016-0061-y>.
- [105] Y. Wang, W. Lai, Phase transition in lithium garnet oxide ionic conductors Li₇La₃Zr₂O₁₂: The role of Ta substitution and H₂O/CO₂ exposure, *J. Power Sources*. 275 (2015) 612–620. <https://doi.org/10.1016/j.jpowsour.2014.11.062>.
- [106] A. Sharafi, H.M. Meyer, J. Nanda, J. Wolfenstine, J. Sakamoto, Characterizing the Li–Li₇La₃Zr₂O₁₂ interface stability and kinetics as a function of temperature and current density, *J. Power Sources*. 302 (2016) 135–139. <https://doi.org/10.1016/j.jpowsour.2015.10.053>.
- [107] X. Zhang, T.-S. Oh, J.W. Fergus, Densification of Ta-Doped Garnet-Type Li_{6.75}La₃Zr_{1.75}Ta_{0.25}O₁₂ Solid Electrolyte Materials by Sintering in a Lithium-Rich Air Atmosphere, *J. Electrochem. Soc.* 166 (2019) A3753–A3759. <https://doi.org/10.1149/2.1031915jes>.
- [108] L. Zhang, L. Cheng, J. Cabana, G. Chen, M.M. Doeff, T.J. Richardson, Effect of lithium borate addition on the physical and electrochemical properties of the lithium ion conductor Li_{3.4}Si_{0.4}P_{0.6}O₄, *Solid State Ionics*. 231 (2013) 109–115. <https://doi.org/10.1016/j.ssi.2012.09.002>.
- [109] E. Barsoukov, J.R. Macdonald, eds., *Impedance Spectroscopy*, John Wiley & Sons, Inc., Hoboken, NJ, USA, 2018. <https://doi.org/10.1002/9781119381860>.
- [110] A. Lasia, *Electrochemical impedance spectroscopy and its applications*, 2014. <https://doi.org/10.1007/978-1-4614-8933-7>.
- [111] J. MACDONALD, L. POTTERJR, A flexible procedure for analyzing impedance spectroscopy results: Description and illustrations, *Solid State Ionics*. 24 (1987) 61–79. [https://doi.org/10.1016/0167-2738\(87\)90068-3](https://doi.org/10.1016/0167-2738(87)90068-3).
- [112] B. BOUKAMP, A package for impedance/admittance data analysis, *Solid State Ionics*. 18–19 (1986) 136–140. [https://doi.org/10.1016/0167-2738\(86\)90100-1](https://doi.org/10.1016/0167-2738(86)90100-1).
- [113] B. BOUKAMP, A Nonlinear Least Squares Fit procedure for analysis of immittance data of electrochemical systems, *Solid State Ionics*. 20 (1986) 31–44. [https://doi.org/10.1016/0167-2738\(86\)90031-7](https://doi.org/10.1016/0167-2738(86)90031-7).
- [114] V.F. Lvovich, *Impedance Spectroscopy: Applications to Electrochemical and Dielectric Phenomena*, 2012.
- [115] Y. Hoshi, S. Kawakita, I. Shitanda, M. Itagaki, Diffusion Impedance Analyzed by

Equivalent Circuit Involving CPE Using Microelectrode, *ECS Trans.* 50 (2013) 9–13. <https://doi.org/10.1149/05035.0009ecst>.

- [116] S. Narayanan, G.T. Hitz, E.D. Wachsman, V. Thangadurai, Effect of Excess Li on the Structural and Electrical Properties of Garnet-Type $\text{Li}_6\text{La}_3\text{Ta}_{1.5}\text{Y}_{0.5}\text{O}_{12}$, *J. Electrochem. Soc.* 162 (2015) A1772–A1777. <https://doi.org/10.1149/2.0321509jes>.
- [117] D.D. Macdonald, Reflections on the history of electrochemical impedance spectroscopy, *Electrochim. Acta.* 51 (2006) 1376–1388. <https://doi.org/10.1016/j.electacta.2005.02.107>.
- [118] D.D. Macdonald, M. Urquidi-Macdonald, Application of Kramers-Kronig Transforms in the Analysis of Electrochemical Systems: I. Polarization Resistance, *J. Electrochem. Soc.* 132 (1985) 2316–2319. <https://doi.org/10.1149/1.2113570>.
- [119] D.D. Macdonald, M. Urquidi-Macdonald, Kramers-Kronig Transformation of Constant Phase Impedances, *J. Electrochem. Soc.* 137 (1990) 515–517. <https://doi.org/10.1149/1.2086490>.
- [120] M. Urquidi-Macdonald, S. Real, D.D. Macdonald, Application of Kramers-Kronig Transforms in the Analysis of Electrochemical Impedance Data: II. Transformations in the Complex Plane, *J. Electrochem. Soc.* 133 (1986) 2018–2024. <https://doi.org/10.1149/1.2108332>.
- [121] J.M. Esteban, M.E. Orazem, On the Application of the Kramers-Kronig Relations to Evaluate the Consistency of Electrochemical Impedance Data, *J. Electrochem. Soc.* 138 (1991) 67–76. <https://doi.org/10.1149/1.2085580>.
- [122] Metrohm Autolab, Kronig-Kramers test, in: *Nov. Impedance Spectrosc. Tutor.*, n.d.: pp. 101–106.
- [123] G. Sahu, Z. Lin, J. Li, Z. Liu, N. Dudney, C. Liang, Air-stable, high-conduction solid electrolytes of arsenic-substituted Li_4SnS_4 , *Energy Environ. Sci.* 7 (2014) 1053–1058. <https://doi.org/10.1039/c3ee43357a>.
- [124] D. Petit, P. Colomban, G. Collin, J.P. Boilot, Fast ion transport in $\text{LiZr}_2(\text{PO}_4)_3$: Structure and conductivity, *Mater. Res. Bull.* 21 (1986) 365–371. [https://doi.org/10.1016/0025-5408\(86\)90194-7](https://doi.org/10.1016/0025-5408(86)90194-7).
- [125] R. Kanno, M. Murayama, Lithium Ionic Conductor Thio-LISICON: The $\text{LiS-GeS}_2\text{-P}_2\text{S}_5$ System, *J. Electrochem. Soc.* 148 (2001) A742. <https://doi.org/10.1149/1.1379028>.
- [126] N. Anantharamulu, K. Koteswara Rao, G. Rambabu, B. Vijaya Kumar, V. Radha, M. Vithal, A wide-ranging review on Nasicon type materials, *J. Mater. Sci.* 46 (2011) 2821–2837. <https://doi.org/10.1007/s10853-011-5302-5>.
- [127] V. Thangadurai, A.K. Shukla, J. Gopalakrishnan, New lithium-ion conductors based on the NASICON structure, *J. Mater. Chem.* 9 (1999) 739–741. <https://doi.org/10.1039/a807007e>.
- [128] A.D. Robertson, A.R. West, A.G. Ritchie, Review of crystalline lithium-ion conductors suitable for high temperature battery applications, *Solid State Ionics.* 104 (1997) 1–

11. [https://doi.org/10.1016/s0167-2738\(97\)00429-3](https://doi.org/10.1016/s0167-2738(97)00429-3).
- [129] A.-M. Welsch, H. Behrens, S. Ross, D. Murawski, Structural control of ionic conductivity in $\text{LiAlSi}_2\text{O}_6$ and $\text{LiAlSi}_4\text{O}_{10}$ glasses and single crystals, *Zeitschrift Für Phys. Chemie.* 226 (2012) 491–511. <https://doi.org/10.1524/zpch.2012.0230>.
- [130] C. Zhong, X. Su, G. Hou, F. Yu, S. Bi, Z. Liu, H. Li, Effect of different treatment methods on the electrochemical properties of LiV_3O_8 at elevated temperatures, *Ceram. Int.* 43 (2017) 414–419. <https://doi.org/10.1016/j.ceramint.2016.09.174>.
- [131] S. Konishi, H. Ohno, T. Hayashi, K. Okuno, T. Matsuo, Investigation of Lithium Diffusion in Octalithium Plumbate by Conductivity and NMR Measurements, *J. Am. Ceram. Soc.* 73 (1990) 1710–1713. <https://doi.org/10.1111/j.1151-2916.1990.tb09817.x>.
- [132] H. Ohno, S. Konishi, T. Nagasaki, T. Kurasawa, H. Katsuta, H. Watanabe, T. Matsuo, Electrical conductivity of a sintered pellet of octalithium zirconate, *J. Nucl. Mater.* 132 (1985) 222–230. [https://doi.org/10.1016/0022-3115\(85\)90367-8](https://doi.org/10.1016/0022-3115(85)90367-8).
- [133] S. Narayanan, F. Ramezanipour, V. Thangadurai, Dopant Concentration-Porosity-Li-Ion Conductivity Relationship in Garnet-Type $\text{Li}_{5+2x}\text{La}_3\text{Ta}_2-x\text{Y}_x\text{O}_{12}$ ($0.05 \leq x \leq 0.75$) and Their Stability in Water and 1 M LiCl , *Inorg. Chem.* 54 (2015) 6968–6977. <https://doi.org/10.1021/acs.inorgchem.5b00972>.
- [134] Y. Shimonishi, A. Toda, T. Zhang, A. Hirano, N. Imanishi, O. Yamamoto, Y. Takeda, Synthesis of garnet-type $\text{Li}_7-x\text{La}_3\text{Zr}_2\text{O}_{12}$ - $1/2x$ and its stability in aqueous solutions, *Solid State Ionics.* 183 (2011) 48–53. <https://doi.org/10.1016/j.ssi.2010.12.010>.
- [135] C.H. Chen, S. Xie, E. Sperling, A.S. Yang, G. Henriksen, K. Amine, Stable lithium-ion conducting perovskite lithium-strontium-tantalum- zirconium-oxide system, *Solid State Ionics.* 167 (2004) 263–272. <https://doi.org/10.1016/j.ssi.2004.01.008>.
- [136] C. Bernuy-Lopez, W. Manalastas, J.M. Lopez del Amo, A. Aguadero, F. Aguesse, J.A. Kilner, Atmosphere Controlled Processing of Ga-Substituted Garnets for High Li-Ion Conductivity Ceramics, *Chem. Mater.* 26 (2014) 3610–3617. <https://doi.org/10.1021/cm5008069>.
- [137] C. Yada, Y. Iriyama, T. Abe, K. Kikuchi, Z. Ogumi, Amorphous Li-V-Si-O Thin Films as High-Voltage Negative Electrode Materials for Thin-Film Rechargeable Lithium-Ion Batteries, *J. Electrochem. Soc.* 153 (2006) A1148–A1153. <https://doi.org/10.1149/1.2192730>.
- [138] A. Khorassani, A.R. West, Li^+ ion conductivity in the system $\text{Li}_4\text{SiO}_4\text{-Li}_3\text{VO}_4$, *J. Solid State Chem.* 53 (1984) 369–375. [https://doi.org/10.1016/0022-4596\(84\)90114-2](https://doi.org/10.1016/0022-4596(84)90114-2).
- [139] H. Ohtsuka, J.I. Yamaki, Preparation and electrical conductivity of $\text{Li}_2\text{O-V}_2\text{O}_5\text{-SiO}_2$ thin films, *Jpn. J. Appl. Phys.* 28 (1989) 2264–2267. <https://doi.org/10.1143/JJAP.28.2264>.
- [140] M. BOSE, A. BASU, D. MAZUMDAR, D. BOSE, Solid solutions of $\text{Li}_3\text{VO}_4\text{-Li}_4\text{GeO}_4$ as solid electrolytes: NMR and related studies, *Solid State Ionics.* 15 (1985) 101–107.

[https://doi.org/10.1016/0167-2738\(85\)90087-6](https://doi.org/10.1016/0167-2738(85)90087-6).

- [141] G.I. and A.R.W. A. Khorassani, THE SOLID ELECTROLYTE SYSTEM, $\text{Li}_3\text{PO}_4\text{-Li}_4\text{SiO}_4$, Mater. Res. Bull. 16 (1981) 1561–1567. <http://dx.doi.org/10.1016/j.cedpsych.2017.09.002>.
- [142] J. Auvergniot, A. Cassel, D. Foix, V. Viallet, V. Seznec, R. Dedryvère, Redox activity of argyrodite $\text{Li}_6\text{PS}_5\text{Cl}$ electrolyte in all-solid-state Li-ion battery: An XPS study, Solid State Ionics. 300 (2017) 78–85. <https://doi.org/10.1016/j.ssi.2016.11.029>.
- [143] H.M. Chen, C. Maohua, S. Adams, Stability and ionic mobility in argyrodite-related lithium-ion solid electrolytes, Phys. Chem. Chem. Phys. 17 (2015) 16494–16506. <https://doi.org/10.1039/C5CP01841B>.
- [144] V. Ramar, S. Kumar, S.R. Sivakkumar, P. Balaya, NASICON-type La^{3+} -substituted $\text{LiZr}_2(\text{PO}_4)_3$ with improved ionic conductivity as solid electrolyte, Electrochim. Acta. 271 (2018) 120–126. <https://doi.org/10.1016/j.electacta.2018.03.115>.
- [145] W.-G. Wang, X.-P. Wang, Y.-X. Gao, J.-F. Yang, Q.-F. Fang, Investigation on the stability of $\text{Li}_5\text{La}_3\text{Ta}_2\text{O}_{12}$ lithium ionic conductors in humid environment, Front. Mater. Sci. China. 4 (2010) 189–192. <https://doi.org/10.1007/s11706-010-0017-0>.
- [146] G. EICHINGER, Decomposition mechanisms of some lithium ionic conductors, Solid State Ionics. 2 (1981) 289–295. [https://doi.org/10.1016/0167-2738\(81\)90029-1](https://doi.org/10.1016/0167-2738(81)90029-1).
- [147] W. Xia, B. Xu, H. Duan, X. Tang, Y. Guo, H. Kang, H. Li, H. Liu, Reaction mechanisms of lithium garnet pellets in ambient air: The effect of humidity and CO_2 , J. Am. Ceram. Soc. 100 (2017) 2832–2839. <https://doi.org/10.1111/jace.14865>.
- [148] V. Thangadurai, W. Weppner, Recent progress in solid oxide and lithium ion conducting electrolytes research, Ionics (Kiel). 12 (2006) 81–92. <https://doi.org/10.1007/s11581-006-0013-7>.
- [149] V. Thangadurai, W. Weppner, Investigations on electrical conductivity and chemical compatibility between fast lithium ion conducting garnet-like $\text{Li}_6\text{BaLa}_2\text{Ta}_2\text{O}_{12}$ and lithium battery cathodes, J. Power Sources. 142 (2005) 339–344. <https://doi.org/10.1016/j.jpowsour.2004.11.001>.
- [150] X. Kuang, G. Carotenuto, L. Nicolais, Review of ceramic sintering and suggestions on reducing sintering temperatures, Adv. Perform. Mater. 4 (1997) 257–274. <https://doi.org/10.1023/A:1008621020555>.
- [151] R. Murugan, V. Thangadurai, W. Weppner, Lithium ion conductivity of $\text{Li}_{5+x}\text{Ba}_x\text{La}_{3-x}\text{Ta}_2\text{O}_{12}$ ($x \in [0, 2]$) with garnet-related structure in dependence of the barium content, Ionics (Kiel). 13 (2007) 195–203. <https://doi.org/10.1007/s11581-007-0097-8>.
- [152] G. Raikova, P. Carpanese, Z. Stoyanov, D. Viadikova, M. Viviani, A. Barbucci, Inductance correction in impedance studies of solid oxide fuel cells, Bulg. Chem. Commun. 41 (2009) 199–206.
- [153] N. Bonanos, P. Pissis, J.R. Macdonald, Impedance Spectroscopy of Dielectrics and

Electronic Conductors, in: *Charact. Mater.*, John Wiley & Sons, Inc., Hoboken, NJ, USA, 2012: pp. 1–14. <https://doi.org/10.1002/0471266965.com121>.

- [154] H. Brandstätter, I. Hanzu, M. Wilkening, Myth and Reality about the Origin of Inductive Loops in Impedance Spectra of Lithium-Ion Electrodes - A Critical Experimental Approach, *Electrochim. Acta.* 207 (2016) 218–223. <https://doi.org/10.1016/j.electacta.2016.03.126>.
- [155] M.H.S. McLaughlin, A.C. Pakpour-Tabrizi, R.B. Jackman, A detailed EIS study of boron doped diamond electrodes decorated with gold nanoparticles for high sensitivity mercury detection, *Sci. Rep.* 11 (2021) 9505. <https://doi.org/10.1038/s41598-021-89045-2>.
- [156] A.R. Thompson, Chapter 3: Impedance spectroscopy of solid oxide cells: Experimental investigation, in: *Impedance Spectrosc. Solid Oxide Cells YSZ Electrolytes Methodol. Characterisation*, 2019: pp. 43–48.
- [157] S. Narayanan, G.T. Hitz, E.D. Wachsman, V. Thangadurai, Effect of Excess Li on the Structural and Electrical Properties of Garnet-Type $\text{Li}_6\text{La}_3\text{Ta}_{1.5}\text{Y}_{0.5}\text{O}_{12}$, *J. Electrochem. Soc.* 162 (2015) A1772–A1777. <https://doi.org/10.1149/2.0321509jes>.
- [158] Ò.F. March, Sensor electroquímico de litio para medidas potenciométricas en metales fundidos, 2020.
- [159] M. Matsuka, I.E. Agranovski, R.D. Braddock, Preparation of asymmetric perovskite-type membranes by a settlement method, *Ceram. Int.* 36 (2010) 643–651. <https://doi.org/10.1016/j.ceramint.2009.10.007>.
- [160] Z. Li, R. Liu, Y. Xie, S. Feng, J. Wang, A novel method for preparation of doped $\text{Ba}_3(\text{Ca}_{1.18}\text{Nb}_{1.82})\text{O}_9-\delta$: Application to ammonia synthesis at atmospheric pressure☆, *Solid State Ionics.* 176 (2005) 1063–1066. <https://doi.org/10.1016/j.ssi.2005.01.009>.
- [161] L. Huaiyu, Q. Yanping, C. Lei, The development and prospect of lithium carbon dioxide battery, *IOP Conf. Ser. Earth Environ. Sci.* 218 (2019). <https://doi.org/10.1088/1755-1315/218/1/012156>.
- [162] X. Wang, L. Zhang, Y. Ji, J. Chu, P. Pan, S. Pan, H. Wang, L. Wang, M. Zhang, $\text{Gd}_2\text{Zr}_2\text{O}_7$ ceramics synthesized by solid-state reactive sintering: Effects of starting powders with different-scale particle sizes, *Ceram. Int.* 48 (2022) 16839–16844. <https://doi.org/10.1016/j.ceramint.2022.02.238>.
- [163] F. Rubio-Marcos, J.J. Romero, J.F. Fernandez, Effect of the temperature on the synthesis of (K,Na)NbO₃-modified nanoparticles by a solid state reaction route, *J. Nanoparticle Res.* 12 (2010) 2495–2502. <https://doi.org/10.1007/s11051-009-9817-5>.
- [164] D.L. Perry, *Handbook of Inorganic Compounds*, 2nd ed., Taylor & Francis Group, 2011.
- [165] D.L. Perry, *Handbook of Inorganic Compounds*, 2nd ed., Taylor & Francis Group, 2011.
- [166] A.W. Warner, A.A. Ballman, Low temperature coefficient of frequency in a lithium

tantalate resonator, Proc. IEEE. 55 (1967) 450–450.
<https://doi.org/10.1109/PROC.1967.5537>.

- [167] D.L. Perry, Handbook of Inorganic Compounds, 2nd ed., Taylor & Francis Group, 2011.
- [168] M.N. Rahaman, Ceramic Fabrication Processes, in: Ceram. Process. Sinter., 2nd ed., CRC Press, 2003: pp. 1–48.
- [169] R.D. Shannon, Revised effective ionic radii and systematic studies of interatomic distances in halides and chalcogenides, Acta Crystallogr. Sect. A. 32 (1976) 751–767.
<https://doi.org/10.1107/S0567739476001551>.
- [170] P. Hubberstey, T. Sample, M.G. Barker, Is Pb-17Li really the eutectic alloy? A redetermination of the lead-rich section of the Pb-Li phase diagram ($0.0 < x_{\text{Li}}(\text{at}\%) < 22.1$), J. Nucl. Mater. 191–194 (1992) 283–287. [https://doi.org/10.1016/S0022-3115\(09\)80051-2](https://doi.org/10.1016/S0022-3115(09)80051-2).
- [171] E. Mas de les Valls, L.A. Sedano, L. Batet, I. Ricapito, A. Aiello, O. Gastaldi, F. Gabriel, Lead–lithium eutectic material database for nuclear fusion technology, J. Nucl. Mater. 376 (2008) 353–357. <https://doi.org/10.1016/j.jnucmat.2008.02.016>.
- [172] M.G. Barker, T. Sample, The solubilities of nickel, manganese and chromium in Pb-17Li, Fusion Eng. Des. 14 (1991) 219–226. [https://doi.org/10.1016/0920-3796\(91\)90005-B](https://doi.org/10.1016/0920-3796(91)90005-B).
- [173] C.J. Ford, J. Heighway, E.F.W. Seymour, Magnetic properties of lead alloys in the solid and liquid states (NMR), J. Phys. F Met. Phys. 2 (1972) 373–385.
<https://doi.org/10.1088/0305-4608/2/2/027>.
- [174] H. Feuerstein, L. Hörner, S. Horn, Self-adjustment of Li in Pb–17Li systems, J. Nucl. Mater. 258–263 (1998) 505–507. [https://doi.org/10.1016/S0022-3115\(98\)00273-6](https://doi.org/10.1016/S0022-3115(98)00273-6).
- [175] R.E. Buxbaum, A chemical theory analysis of the solution thermodynamics of oxygen, nitrogen and hydrogen in lead-rich Li-Pb mixtures, J. Less Common Met. 97 (1984) 27–38. [https://doi.org/10.1016/0022-5088\(84\)90005-5](https://doi.org/10.1016/0022-5088(84)90005-5).
- [176] P. Hubberstey, Pb-17Li and lithium: A thermodynamic rationalisation of their radically different chemistry, J. Nucl. Mater. 247 (1997) 208–214.
[https://doi.org/10.1016/S0022-3115\(97\)00071-8](https://doi.org/10.1016/S0022-3115(97)00071-8).
- [177] M. Saunders, Thermal Analysis of Pharmaceuticals, in: P. Gabbott (Ed.), Princ. Appl. Therm. Anal., 2008: pp. 287–327. <https://doi.org/10.1002/9780470697702>.
- [178] K. and J.H.P. Hildal, Metals and Alloys, in: S.N.K. and C.S. Vyazovkin; (Ed.), Handb. Therm. Anal. Calorim., Second Edi, 2018: pp. 781–816.
- [179] R.I. Wu, J.H. Perepezko, Liquidus temperature determination in multicomponent alloys by thermal analysis, Metall. Mater. Trans. A Phys. Metall. Mater. Sci. 31 (2000) 497–501. <https://doi.org/10.1007/s11661-000-0285-x>.
- [180] W.J. Boettinger, U.R. Kattner, K.-W. Moon, J.H. Perepezko, R.C. Cresanti, W. Jeffrey, DTA and Heat-flux DSC Measurements of Alloy Melting and Freezing, Natl. Inst. Stand.

Technol. (2006).

- [181] S.S. Moreno, Síntesi i conformació de ceràmiques conductores de liti, 2018.
- [182] M.K. Mahapatra, K. Lu, Glass-based seals for solid oxide fuel and electrolyzer cells – A review, *Mater. Sci. Eng. R Reports.* 67 (2010) 65–85. <https://doi.org/10.1016/j.mser.2009.12.002>.
- [183] I. Avramov, T. Vassilev, I. Penkov, The glass transition temperature of silicate and borate glasses, *J. Non. Cryst. Solids.* 351 (2005) 472–476. <https://doi.org/10.1016/j.jnoncrysol.2005.01.044>.
- [184] W. Xia, B. Xu, H. Duan, X. Tang, Y. Guo, H. Kang, H. Li, H. Liu, Reaction mechanisms of lithium garnet pellets in ambient air: The effect of humidity and CO₂, *J. Am. Ceram. Soc.* 100 (2017) 2832–2839. <https://doi.org/10.1111/jace.14865>.
- [185] A.R. Diez, Sistemas electroquímicos para la separación de gases. Diseño básico de un sistema para la separación selectiva de hidrógeno, 2017.
- [186] M.B. Uday, M.N. Ahmad-Fauzi, A.M. Noor, S. Rajoo, Current Issues and Problems in the Joining of Ceramic to Metal, in: *Join. Technol.*, 2016. <https://doi.org/10.5772/64524>.
- [187] P. Hubberstey, T. Sample, Pb-17Li-water interactions: a thermodynamic and experimental characterisation, *J. Nucl. Mater.* 199 (1993) 149–158. [https://doi.org/10.1016/0022-3115\(93\)90291-6](https://doi.org/10.1016/0022-3115(93)90291-6).
- [188] AOAC, Appendix F: Guidelines for Standard Method Performance Requirements, in: *AOAC Off. Methods Anal.*, 2016: pp. 1–18.
- [189] M. Saboungi, M. Blander, Electromotive Force Measurements in Molten Lithium-Magnesium Alloys, *J. Electrochem. Soc.* 122 (1975) 1631–1634. <https://doi.org/10.1149/1.2134082>.
- [190] J. Wu, L. Yamarte, A. Petric, Fabrication of a lithium sensor based on LiYO₂ by liquid phase processing, *J. Electroceramics.* 9 (2002) 57–66. <https://doi.org/10.1023/A:1021694102959>.
- [191] J. Sangster, C.W. Bale, The Li-Sn (Lithium-Tin) System, *J. Phase Equilibria.* 19 (1998) 70–75. <https://doi.org/10.1361/105497198770342788>.
- [192] A.G. Morachevskii, Thermodynamic properties and electrochemical studies of lithium-tin alloys, *Russ. J. Appl. Chem.* 88 (2015) 1087–1105. <https://doi.org/10.1134/S1070427215070010>.
- [193] A.G. Morachevskii, Thermodynamic properties and electrochemical studies of lithium-tin alloys, *Russ. J. Appl. Chem.* 88 (2015) 1087–1105. <https://doi.org/10.1134/S1070427215070010>.
- [194] C.J. Wen, R.A. Huggins, Thermodynamic Study of the Lithium-Tin System, *J. Electrochem. Soc.* 128 (1981) 1181–1187. <https://doi.org/10.1149/1.2127590>.

- [195] M.S. Foster, C.E. Crouthamel, S.E. Wood, Thermodynamics of Binary Alloys. II. The Lithium—Tin System 1, *J. Phys. Chem.* 70 (1966) 3042–3045. <https://doi.org/10.1021/j100882a004>.
- [196] W. Becker, G. Schwitzgebel, H. Ruppertsberg, Thermodynamic Investigations of Liquid Li-Pb and Li-Ag-Alloys — A Comparative Study, *Int. J. Mater. Res.* 72 (1981) 186–190. <https://doi.org/10.1515/ijmr-1981-720306>.
- [197] A. Neubert, Thermodynamic study of solid and liquid lithium + lead alloys using Knudsen-effusion mass spectrometry, *J. Chem. Thermodyn.* 11 (1979) 971–977. [https://doi.org/10.1016/0021-9614\(79\)90046-6](https://doi.org/10.1016/0021-9614(79)90046-6).
- [198] M. Saboungi, J. Marr, M. Blander, Thermodynamic properties of a quasi-ionic alloy from electromotive force measurements: The Li–Pb system, *J. Chem. Phys.* 68 (1978) 1375–1384. <https://doi.org/10.1063/1.435957>.
- [199] A. Neubert, Thermodynamic study of solid and liquid lithium + lead alloys using Knudsen-effusion mass spectrometry, *J. Chem. Thermodyn.* 11 (1979) 971–977. [https://doi.org/10.1016/0021-9614\(79\)90046-6](https://doi.org/10.1016/0021-9614(79)90046-6).

7. ANNEXES

7. ANNEXES

ANNEX 1: Statistical Study of the Three Different Strategies on LBLTO Ionic Conductivity Results

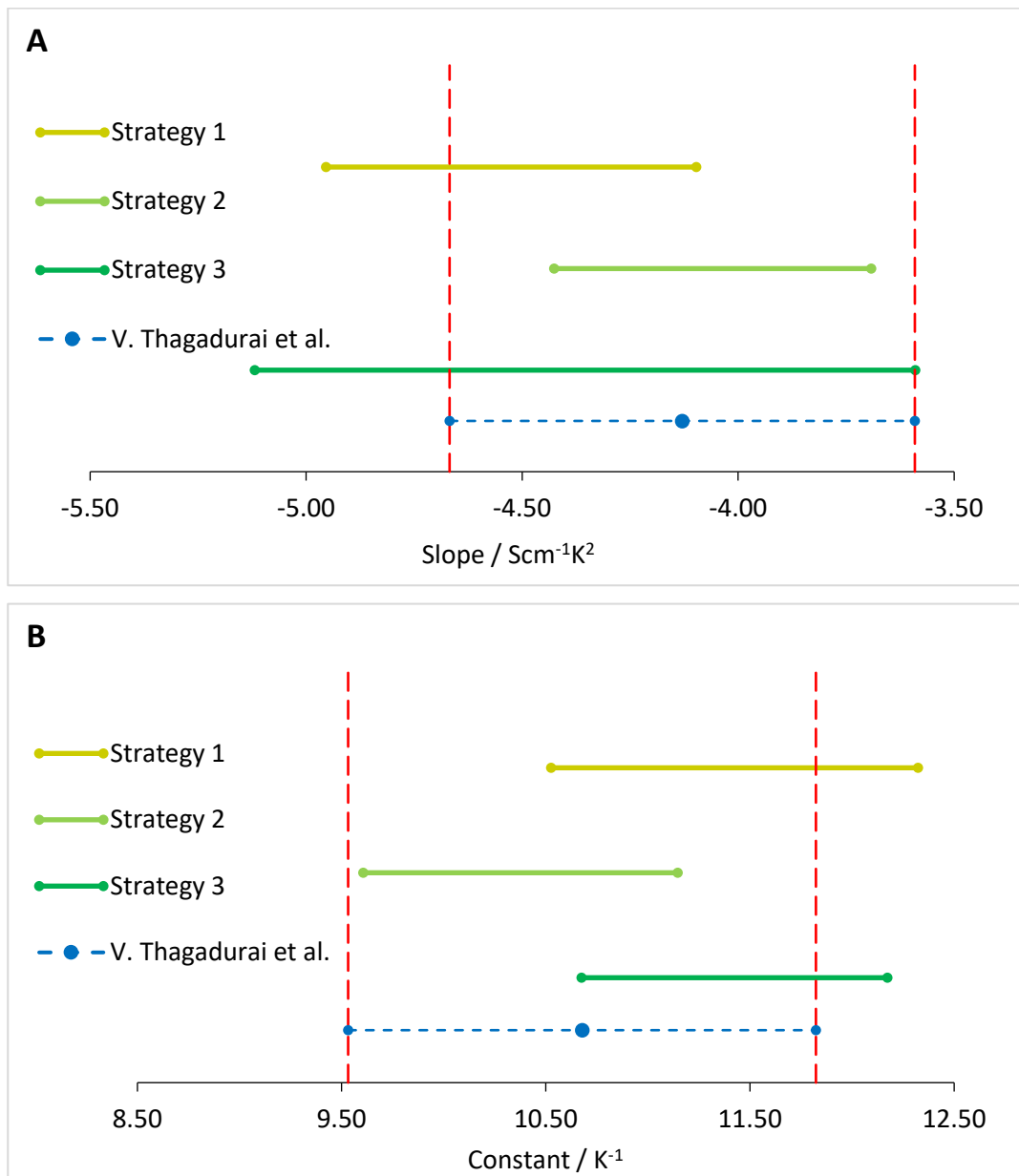


Figure 7.1. Confidence intervals of the A) slope and B) constant term of each obtained linear correlation from the different strategies and bibliographic data [87].

ANNEX 2: PGSTAT302N/FRA2 Contour Map

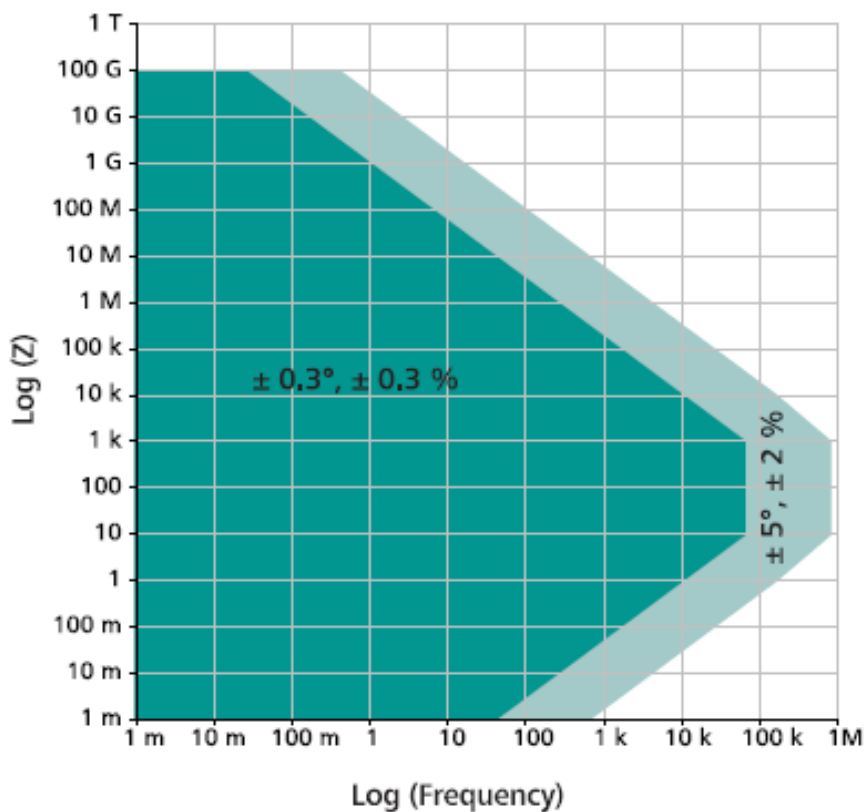


Figure 7.2. Contour map of the PGSTAT302N/FRA2 combination.

ANNEX 3: Statistical Study of the Two LBLTO Replicates' Ionic Conductivity

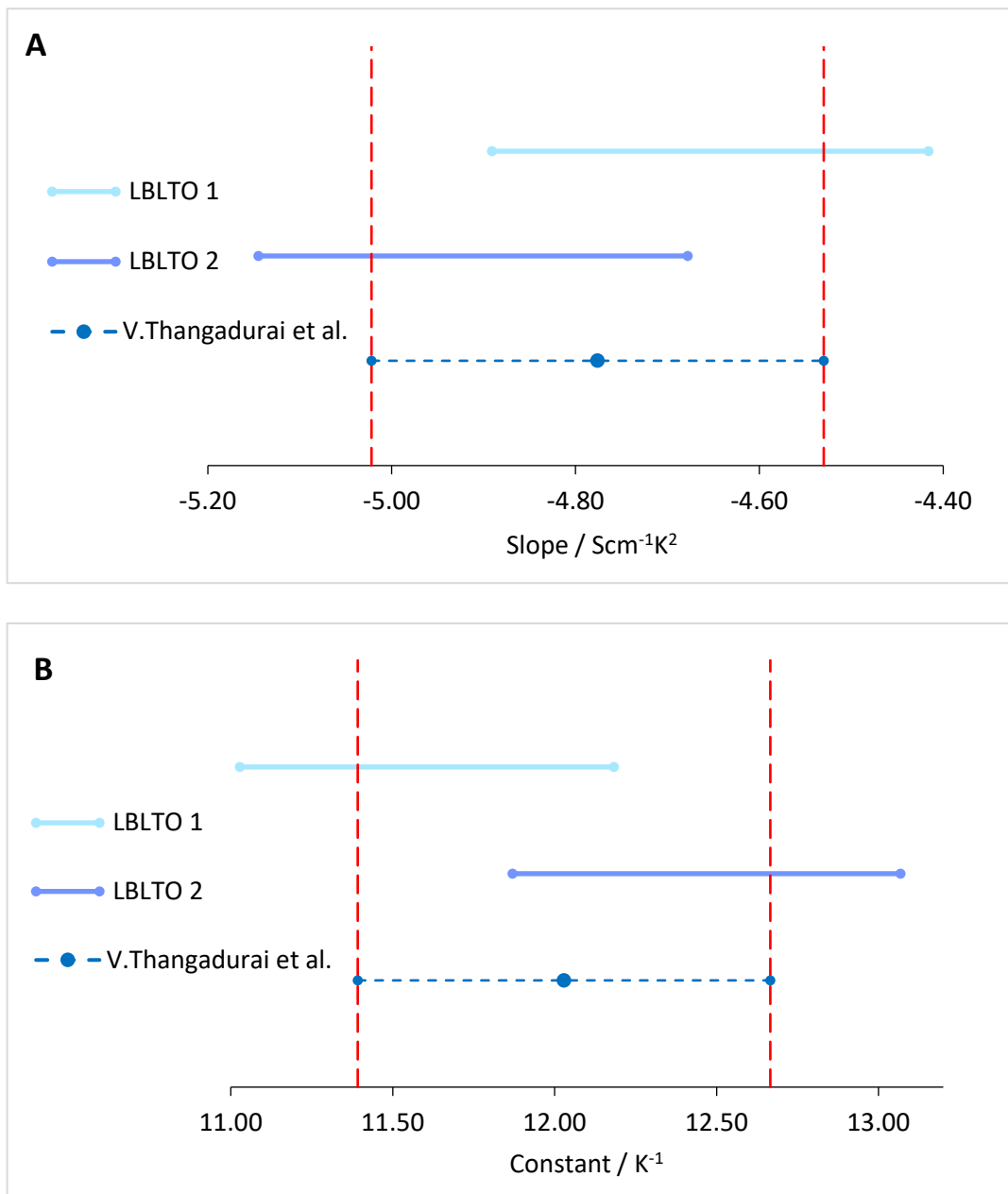


Figure 7.3. Confidence intervals of the A) slope and B) constant term of each obtained linear correlation from two LBLTO pellets and bibliographic data [87].

ANNEX 4: Statistical Study of the Three Different Strategies on LLTYO Ionic Conductivity Results

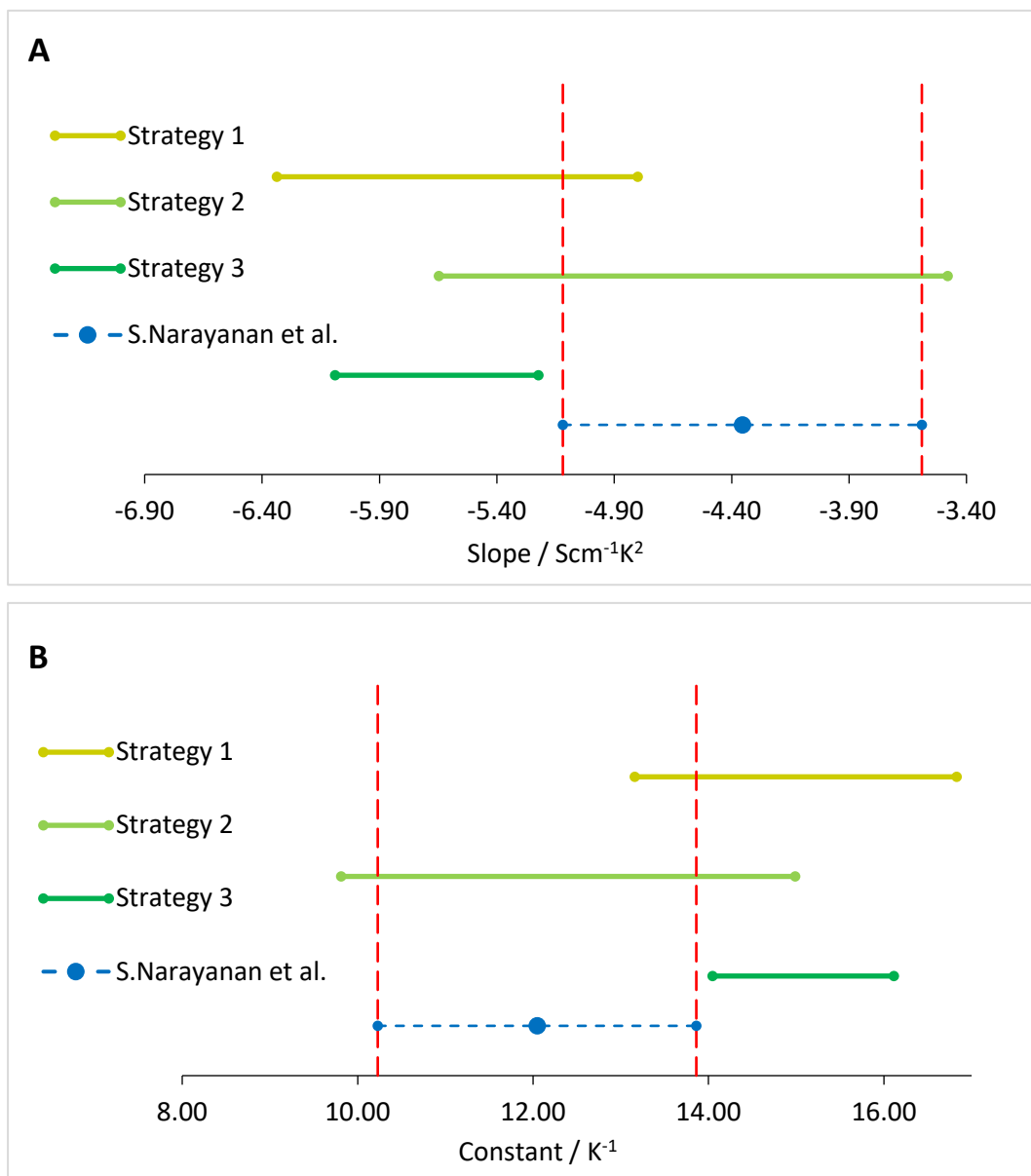


Figure 7.4. Confidence intervals of the A) slope and B) constant term of each obtained linear correlation from the different strategies and bibliographic data [157].

ANNEX 5: Statistical Study of the Two LLTYO Replicates' Ionic Conductivity

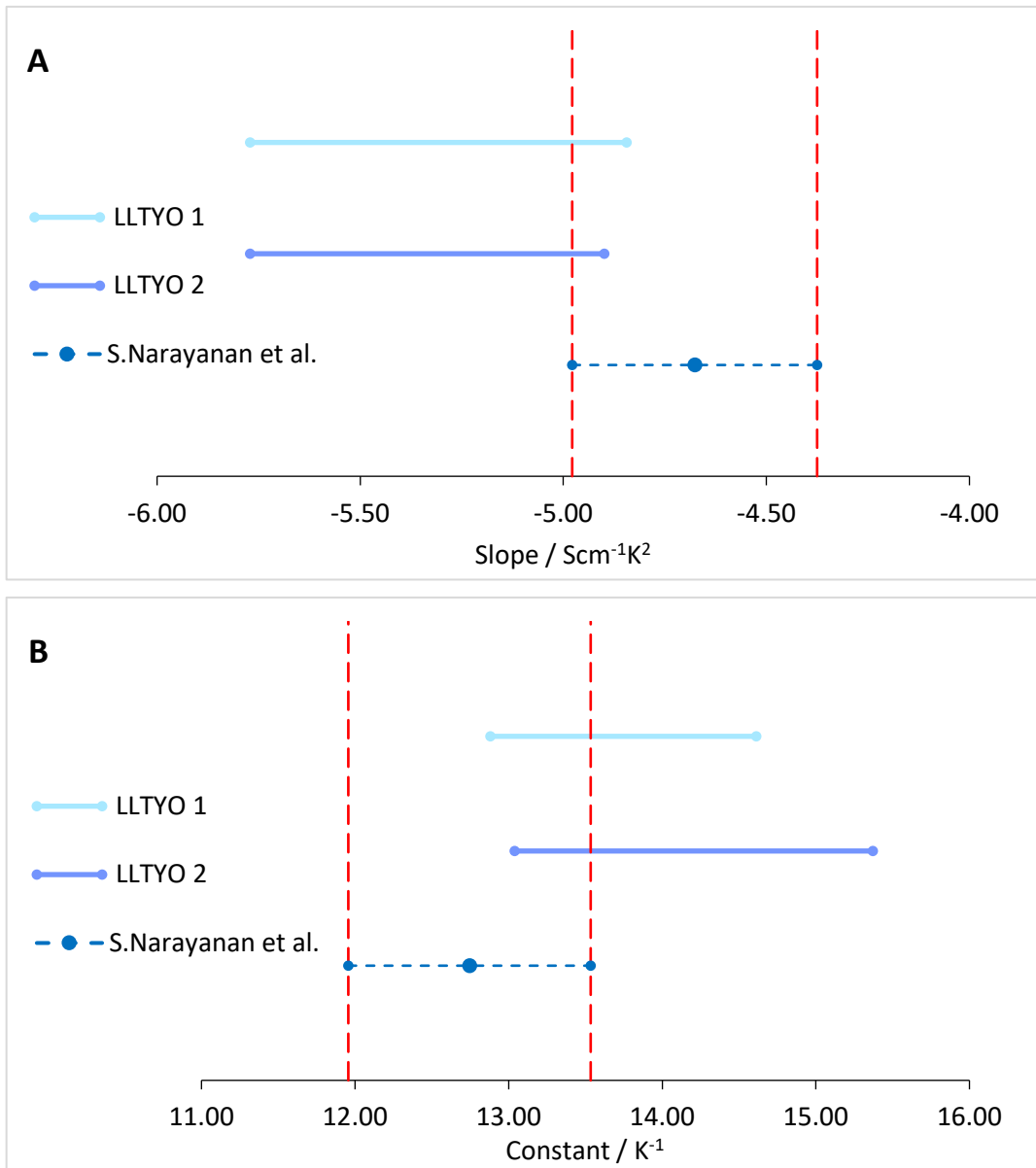


Figure 7.5. Confidence intervals of the A) slope and B) constant term of each obtained linear correlation from two LLTYO pellets and bibliographic data [157].

ANNEX 6: Lithium Calibration Curve for the AAS-Flame Analysis

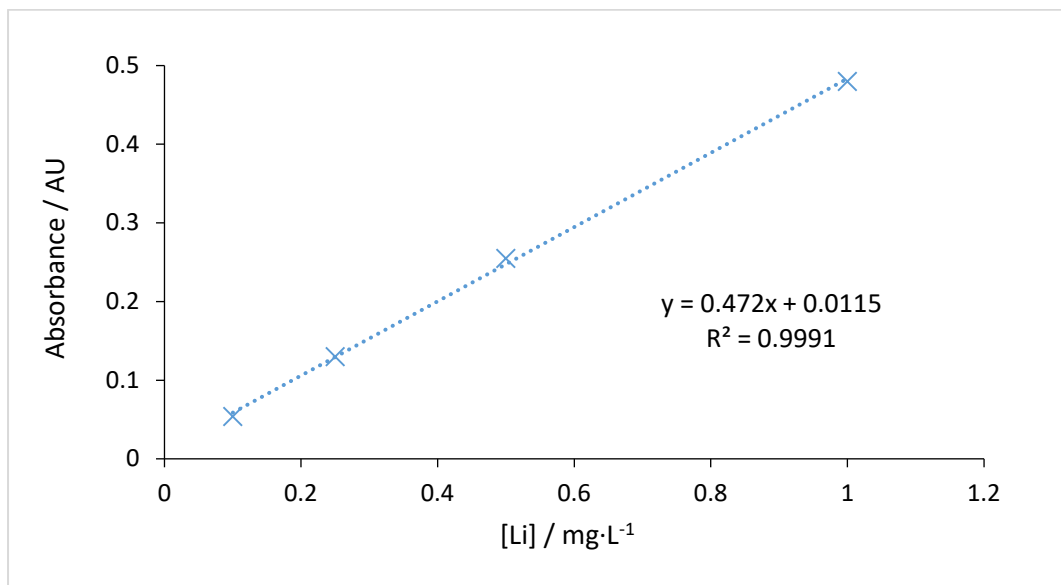


Figure 7.6. Lithium calibration curve for the AAS-Flame analysis.

ANNEX 7: Statistical Study of the Lithium Quantification Results In Pb-Li Samples

To be able to perform the statistical analysis, the first step was to determine if the data followed a normal distribution. For this objective, a probability plot testing normal distribution was done (Figure 7.7).

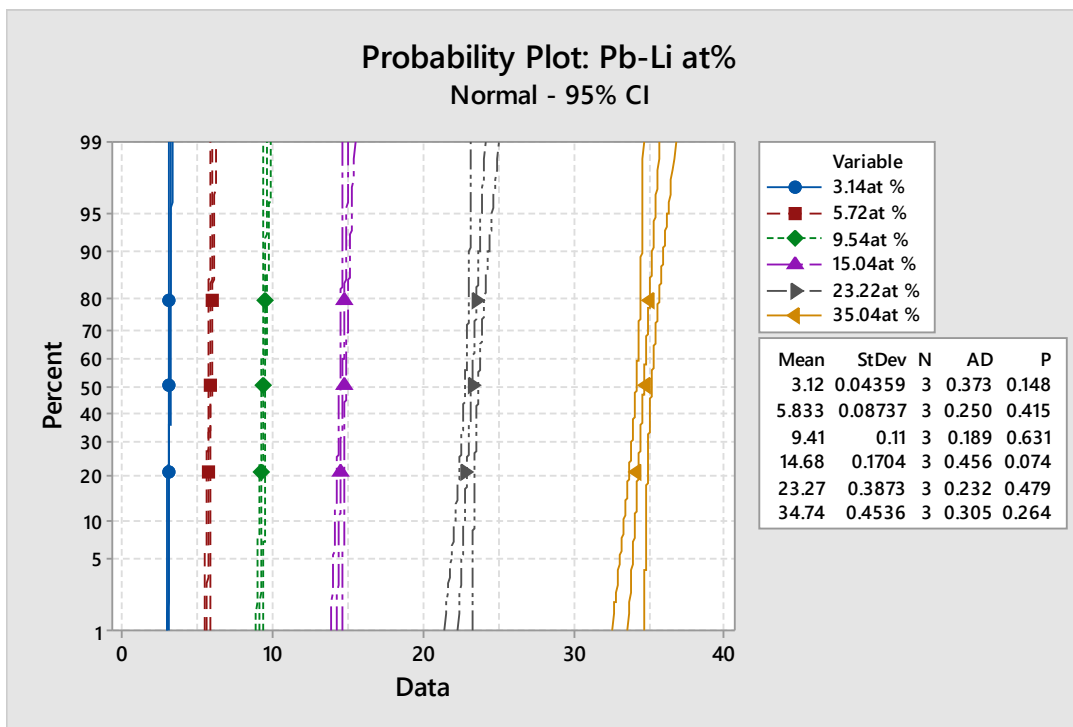


Figure 7.7. Probability plot of each of the analyzed Pb-Li ingots.

To determine if values in each group followed a normal distribution, the P-value showed in the plot had to be compared to the significance level (α), which was set as 5% or 0.05. A significance level of 0.05 means that the risk of values not following a normal distribution when they do follow, is 5%. If $P\text{-value} > \alpha$, it cannot be concluded that data values do not follow the distribution. As shown in Figure 7.7, for each at% Li concentration the P-value was higher than the significance level and hence, all values followed a normal distribution.

Once assumed that the data followed a normal distribution, it was possible to perform a Grubbs test for outliers. With this test, it was possible to check if any of the ingots' parts (upper, middle, and lower) for each of the Li concentrations were significantly different from the rest. The resulting P-values of the test are shown in Table 7.1.

Table 7.1. Grubb's test results for outliers for each of the analyzed Pb-Li ingots.

Pb-Li at%	P-Value
3.14%	0.324
5.72%	0.591
9.54%	0.998
15.04%	0.080
23.22%	0.627
35.04%	0.379

The significance level (α) of the test was set again as 5% or 0.05. In this case, the significance level of 0.05 means the risk of whether the most external value in the list is an outlier. If the $P\text{-value} > \alpha$, it cannot be concluded that the most external value is an outlier. As shown in Table 7.1, for each at% Li concentration the P-value was higher than the significance level and hence, there were no differences between the different ingot parts for each Li concentration.

Once it was determined that all the quantified values at each ingot belonged to a similar statistical population, a final T-student test ($\alpha = 0.05$) was performed to check whether the mean of the values was not significantly different from its reported at% Li concentration. The resulting P-values of the test are shown in Table 7.2.

Table 7.2. T-student's test results for each of the analyzed Pb-Li ingots.

Pb-Li at%	P-Value
3.14%	0.510
5.72%	0.154
9.54%	0.177
15.04%	0.066
23.22%	0.834
35.04%	0.375

ANNEX 8: Statistical Study of the Pb-Li Preparation Method

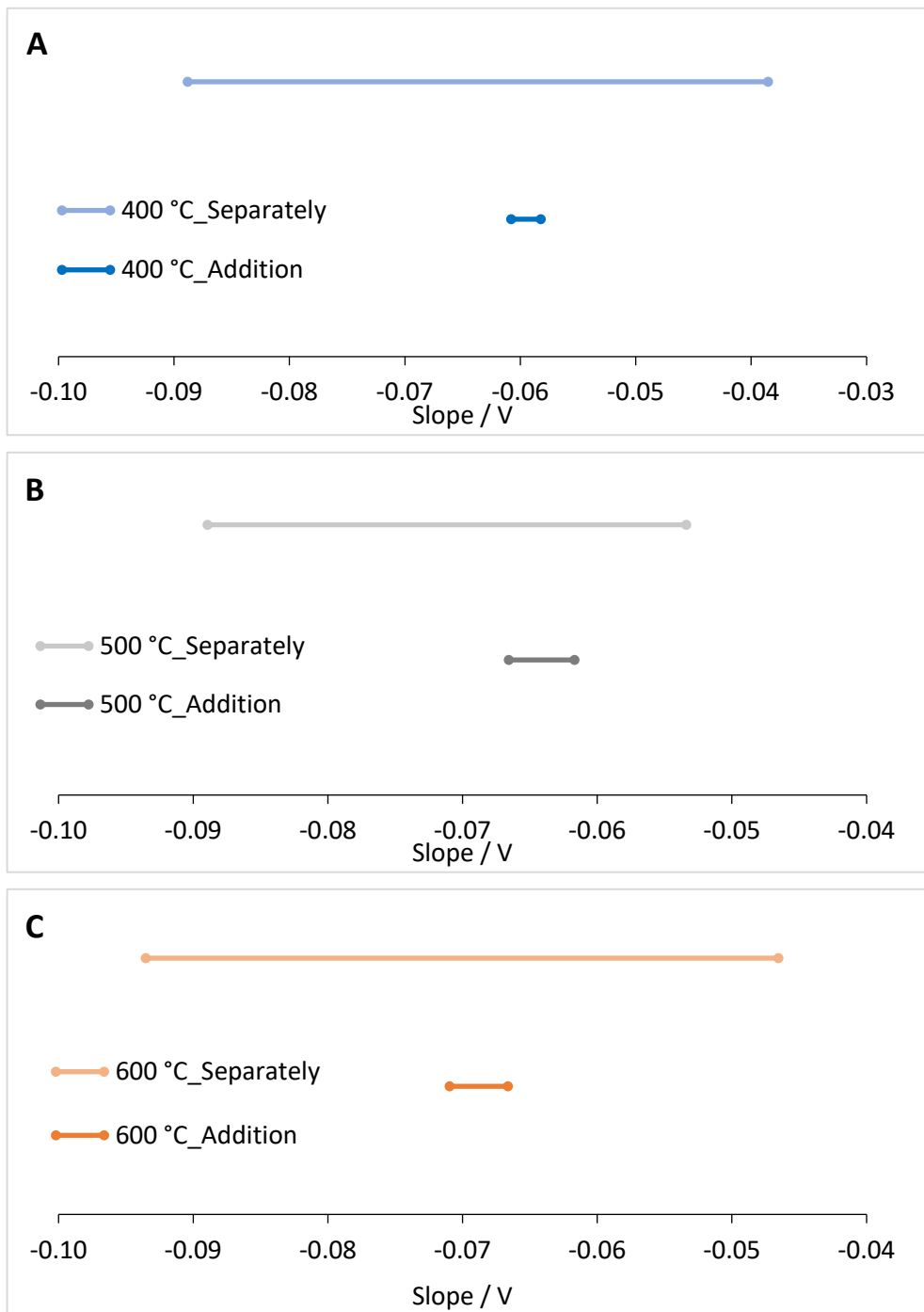


Figure 7.8. Confidence intervals of the linear correlations' slopes for each preparation method at A) 400 °C, B) 500 °C, and C) 600 °C.

ANNEX 9: Statistical Study of the Eutectic Pb-Li and Pb-3Li Reference Systems

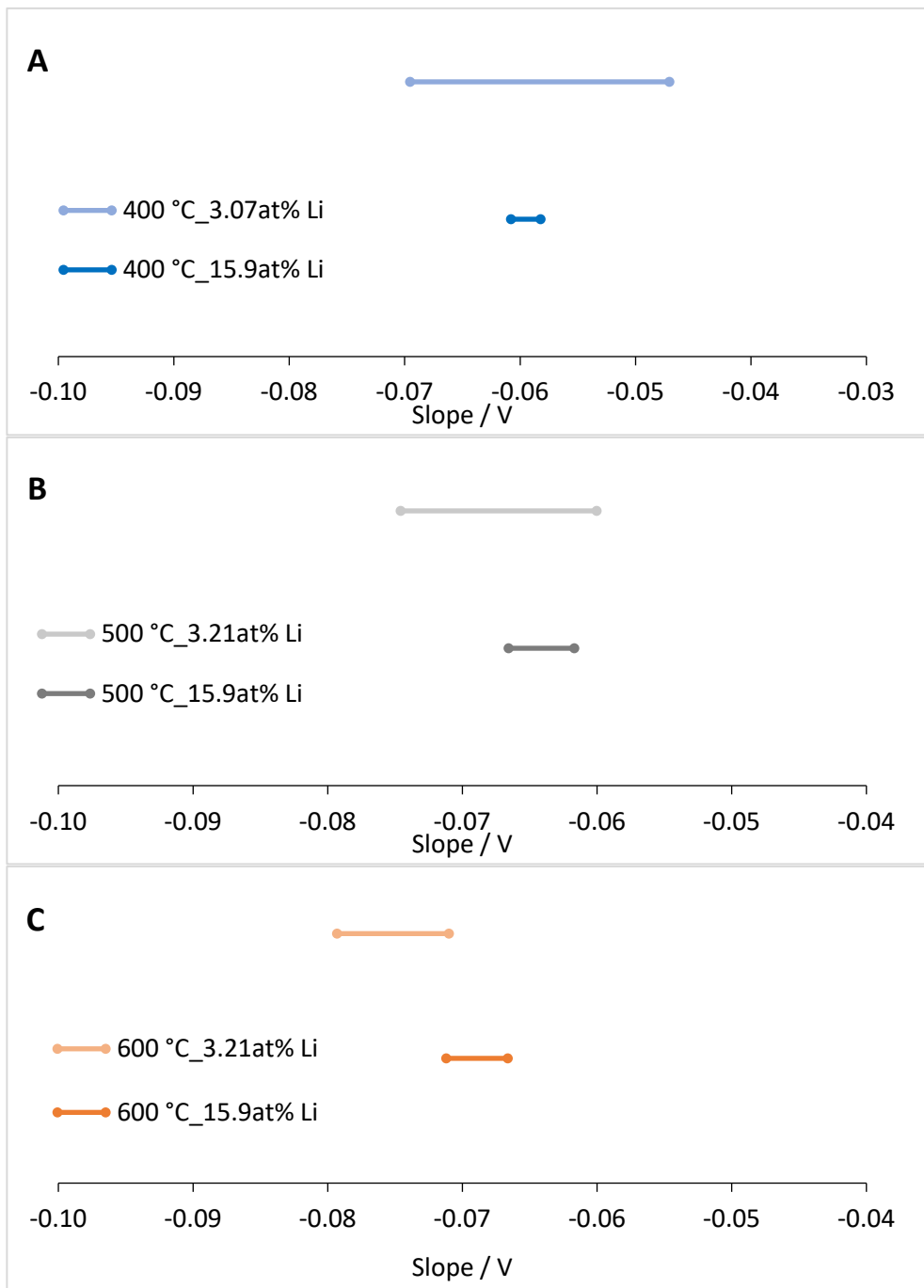


Figure 7.9. Confidence intervals of the linear correlations' slopes for each reference system at A) 400 °C, B) 500 °C and C) 600 °C.

